ON A TENSOR-BASED FINITE ELEMENT MODEL FOR THE ANALYSIS OF SHELL STRUCTURES

A Dissertation

by

ROMAN AUGUSTO ARCINIEGA ALEMAN

Submitted to the Office of Graduate Studies of
Texas A&M University
in partial fulfillment of the requirements for the degree of

DOCTOR OF PHILOSOPHY

December 2005

Major Subject: Mechanical Engineering

ON A TENSOR-BASED FINITE ELEMENT MODEL FOR THE ANALYSIS OF SHELL STRUCTURES

A Dissertation

by

ROMAN AUGUSTO ARCINIEGA ALEMAN

Submitted to the Office of Graduate Studies of
Texas A&M University
in partial fulfillment of the requirements for the degree of

DOCTOR OF PHILOSOPHY

Approved by:

Chair of the Committee,	J.N. Reddy
Committee Members,	Harry A. Hogan
	Arun R. Srinivasa
	Jay R. Walton
Head of the Department,	Dennis L. O'Neal

December 2005

Major Subject: Mechanical Engineering

ABSTRACT

On a Tensor-Based Finite Element Model for
the Analysis of Shell Structures. (December 2005)

Roman Augusto Arciniega Aleman, B.E., University of Ricardo Palma, Lima;
M.E., Catholic University of Rio de Janeiro
Chair of Advisory Committee: Dr. J.N. Reddy

In the present study, we propose a computational model for the linear and nonlinear analysis of shell structures. We consider a tensor-based finite element formulation which describes the mathematical shell model in a natural and simple way by using curvilinear coordinates. To avoid membrane and shear locking we develop a family of high-order elements with Lagrangian interpolations.

The approach is first applied to linear deformations based on a novel and consistent third-order shear deformation shell theory for bending of composite shells. No simplification other than the assumption of linear elastic material is made in the computation of stress resultants and material stiffness coefficients. They are integrated numerically without any approximation in the shifter. Therefore, the formulation is valid for thin and thick shells. A conforming high-order element was derived with C^0 continuity across the element boundaries.

Next, we extend the formulation for the geometrically nonlinear analysis of multilayered composites and functionally graded shells. Again, Lagrangian elements with high-order interpolation polynomials are employed. The flexibility of these elements mitigates any locking problems. A first-order shell theory with seven parameters is derived with exact nonlinear deformations and under the framework of the

Lagrangian description. This approach takes into account thickness changes and, therefore, 3D constitutive equations are utilized. Finally, extensive numerical simulations and comparisons of the present results with those found in the literature for typical benchmark problems involving isotropic and laminated composites, as well as functionally graded shells, are found to be excellent and show the validity of the developed finite element model. Moreover, the simplicity of this approach makes it attractive for future applications in different topics of research, such as contact mechanics, damage propagation and viscoelastic behavior of shells.

To the beloved memory of my father
Alejandro Angel Arciniega Arciniega
(2.VII.1927 - 2.VII.1998)

ACKNOWLEDGMENTS

I would like to express my sincere gratitude to Dr. J.N. Reddy, the advisor of this dissertation, not only for his guidance and support during the course of this work but also for his philosophical attitude which allowed me to pursue my own research interest.

I am also grateful to Dr. H. Hogan, Dr. A. Srinivasa and Dr. J. Walton for serving on this dissertation committee. In particular, I would like to thank Dr. Walton for his lectures on Tensor Analysis and Continuum Mechanics, so important for shell theories.

I owe special thanks to Dr. G. Paulino at the University of Illinois, Urbana-Champaign, Dr. R. Rosas and Dr. P. Gonçalves at Catholic University of Rio de Janeiro in Brazil for their recommendation and support to admission at Texas A&M University.

Finally, my heartfelt appreciation goes to my aunt Aida Alemán de Arciniega for her love and encouragement through my whole life. Without her devotion and care, I could not have accomplished so much. I am also indebted to Tatiana Mejía for her help and support during my four years at College Station.

TABLE OF CONTENTS

LIST OF FIGURES

FIGURE Page

FIGURE Page

FIGURE Page

FIGURE Page

FIGURE Page

LIST OF TABLES

TABLE Page

CHAPTER I

INTRODUCTION

A. General

Shell structures have always been a fascinating area of research. Their unpredictable behavior and difficulties in their mathematical as well as numerical modeling make these structures a challenge for researchers and engineers. Since shells abound in nature, it is not surprising that they have been widely used as efficient load-carrying members in many engineering structures. Shells can sustain large loads with remarkably little material. Examples of shell applications include storage tanks, roofs, lenses, and helmets, and they are also found in automobile, aircraft and off-shore structures.

Shells are three-dimensional bodies in which one topological dimension is much smaller than the other two. They occupy a narrow neighborhood of a two-dimensional manifold. The behavior of the shell can be captured by solving directly the three-dimensional elasticity differential equations. However, due to the complexity of the numerical simulations of a three-dimensional body (even for the most powerful computers and computational techniques, solutions are restricted to simple cases), it is suitable to represent the problem as a two-dimensional model leading to the construction of shell theories. Such theories enable an insight into the structure of the equations involved, independently and prior to the computation itself. Based on them, powerful computational methods can be formulated. Shell theory is, of course, subject to the faults and limitations of any mathematical model of a physical system and posses many layers of approximations. Difficulties in modeling shell structures are illustrated by the

---

The journal model is Computer Methods in Applied Mechanics and Engineering.

following three excerpts from prominent researches of the area:

> *Shell theory attempts the impossible: to provide a two-dimensional representation of an intrinsically three-dimensional phenomenon.*
>
> W.T. Koiter and J.G. Simmonds [1]
>
> *The theory of shells is by definition an approximate one and, generally, neither complete nor exact information as to the stress and strain state in a thin three-dimensional body can be provided by this theory.*
>
> W. Pietraszkiewicz [2]
>
> *Shell structures may be called the prima donnas of structures. Their behavior is difficult to analyze and … apparently small changes of geometry or support conditions can result into a totally different response.*
>
> D. Chapelle and K.J. Bathe [3]

In the past decades, the development of efficient computational models for the analysis of shells has been one of the most important research activities. This has been motivated by the advent of materials such as composite laminates and functionally graded shells. In particular, shells made of laminated composites continue to be of great interest in many engineering applications. In some applications these structures can experience large elastic deformations and finite rotations. Consequently, geometric nonlinearities play an essential role in the behavior of the shell. In that sense, the choice of appropriate mathematical models together with reliable computational procedures that can accurately represent nonlinear deformations and stresses in shell structures is of vital importance.

Most significant advances in shell analyses have been made using the finite element method. Finite elements used for shells can be grouped into four kinds: flat facet element, solid 3D element, continuum based shell element (or degenerated shell element) and a 2D element based on a shell theory. Among these, the last two elements are the most common ones. The degenerated shell element was first developed by Ahmad et al. [4] from a three-dimensional solid element by a process which discretizes the 3D elasticity equations in terms of midsurface nodal variables. It is based on isoparametric interpolations in Cartesian coordinates that imposes the same kinematical constraints as those of the Reissner-Mindlin approach. Therefore, a first-order shear deformation theory can be implicitly identified. On the other hand, elements based on shell theories began to appear in the late sixties. These elements are based on convected curvilinear coordinates and are capable of capturing the membrane-bending coupling correctly. Even though degenerated solid elements have dominated shell analysis during the seventies and eighties, beginning with the work of Simo and Fox [5], shell elements have been increasingly used in the last decade. Examples of these formulations can be found in Chinosi et al. [6], Cho and Roh [7] and Chapelle et al. [8]. A comparison between both methodologies, presented by Büchter and Ramm [9], reveals that they have come very close to each other in the meantime.

Finite elements based on shell theories describe, in a natural way, the behavior of the shell since they are written in terms of curvilinear coordinates. For this case, two different approaches can be identified whether or not there is an approximation of the geometry of the midsurface (i.e., finite element domain in the parametric space of the midsurface $\mathscr{A}$). Formulations in which the midsurface is represented by a chart and that interpolate the covariant components of the kinematic variables are called tensor-based finite element models. It is often heard the argument that this kind of interpolation automatically causes difficulties with the rigid body modes of curved structures because they cannot be properly represented [9, 10]. That point of view is not shared herein. We shall demonstrate in this dissertation (from a heuristic perspective) that with the help of an appropriate element, these problems never occur.

It is well-known that the standard displacement-based type of element for shells is too stiff and suffers from locking phenomena. Locking problem arises due to inconsistencies in modeling the transverse shear energy and membrane energy. In other words, the convergence property of the element for some specific problems becomes worse as the thickness tends to zero. The dominant trend in computational mechanics for shells over the last decades is the use of low-order finite element formulations with mixed interpolations to overcome locking. A mixed interpolation approach can be considered as a special case of mixed finite element models that are usually modeled by the Hu-Washizu functional. To propose a reliable mixed finite element, we should satisfy the inf-sup condition property. This condition means optimal convergence in shell analyses. Despite of its importance, it is generally not possible to prove analytically whether or not a shell element satisfies this condition. Examples of efficient low-order elements are the assumed strain elements (Hinton and Huang [11], Dvorkin and Bathe [12]) and the enhanced strain elements (Simo and Rifai [13]).

Alternatively, high-order elements have been proposed for the analysis of shells. The claim of this approach is to use finite elements of sufficiently high degree to recover the convergence property within an optimal order. This is called *p*-version finite element (where *p* is the degree of the interpolation polynomial). In that case, there is no need to use mixed formulations and displacement-based finite elements can be applied.

As compared with standard low-order elements, high-order finite elements appear far more complicated. However, we will see in this dissertation that raising the *p*-level frequently results in better accuracy. Moreover, high-order finite elements are more reliable because of their applicability in a diversity of shell problems. Finite elements with high-order interpolations have been utilized by Pitkäranta and co-workers [14-16] for linear analysis of isotropic shells. Further applications of high-order elements to shells (with hierarchical modal basis) can be found in Refs. [6, 17].

The use of tensor-based finite element formulations together with high-order elements for the analysis of shell structures leads to an efficient computational approach which is straightforward to implement. Such model can be applied to linear and nonlinear analyses of shells made of isotropic, laminated composite and functionally graded materials as we will see in this dissertation.

B. Motivation and objectives

After an assessment of previous studies in the literature for the analysis of shells, we find that most shell formulations are based on mixed functionals with low-order finite elements (under the isoparametric concept, which is directly inherited from degenerated finite elements). Moreover, finite element models for shells are limited to the analysis of isotropic materials with few applications to laminated composites [18-20]. Having motivated the use of tensor-based finite element models with high-order expansion, we propose in this dissertation a reliable computational model for the linear and nonlinear analysis of shell structures. Specifically, our aim in this work is the following:

- To develop of a mathematical model and its finite element implementation for the linear analysis of shell structures. The formulation is based on the third-order shear deformation theory (Reddy [21], Reddy and Liu [22]) which can captures the basic kinematic response of laminated composite materials.
- To develop a refined mathematical model to simulate finite displacements and rotations of shell structures. The model is based on an improved first-order shear deformation theory with seven independent parameters (Sansour [23], Bischoff and Ramm [24]) under the Lagrangian framework. The use of a rotation tensor is

avoided and the additive update procedure of the shell configuration is preserved. Since thickness stretching is considered in the formulation, three-dimensional constitutive equations are required.

The formulation is original in the following aspects:

- The finite element formulation is tensor-based (domain in the parametric space of the midsurface and interpolation of the covariant components of the kinematic variables).
- First to introduce high-order finite elements together with a displacement-based finite element model to mitigate locking in geometrically nonlinear analysis of shells.
- Broad range of applications for different geometries (beams, plates, cylindrical shells, spherical shells, etc.) as well as different type of materials (isotropic, laminated composite and functionally graded shells).

The mathematical shell model is beautifully and consistently derived using absolute tensor notation and the finite element model is developed in a straightforward way. The simplicity of this approach makes it attractive for future applications in different topics of research such as contact mechanics, damage propagation and viscoelastic behavior of shells. Previous works of the author for linear analysis of laminated shells can be found in Refs. [25, 26].

C. Outline of the research

This dissertation is organized in six chapters. Chapter II and III are concerned with the linear shell analysis while Chapter IV and V deal with the nonlinear analysis.

In Chapter II, we discuss the linear shell theory. After a brief bibliographical review, we introduce some mathematical concepts for shell analyses. Next, we develop the kinematics of deformation of the shell based on the third-order theory. Reduced constitutive equations for linear elastic materials are derived and then utilized in the principle of virtual work.

Chapter III presents the abstract finite element implementation for the shell model described in Chapter II. We start by defining the configuration of the shell and deriving the variational formulation. The discrete finite element model is introduced and the interpolations of the kinematic variables are described. The problem of locking in shell structures is amply discussed. Two asymptotic behavior of the shell that causes locking are identified. The use of high-order elements is justified. Finally, we present numerical examples for static linear analysis of plates, cylindrical shells and spherical shells. Specifically we consider several well-known benchmark problems such as the barrel vault, the pinched cylinder, the pinched hemispherical shell, etc.

Chapter IV is concerned with the development of the nonlinear shell theory for finite displacements and rotations. We review some mathematical preliminaries related to shell theories. The deformation of the shell is examined under the Lagrangian description. The kinematics of the shell is presented in vector form. An alternative tensor component form for these equations is also given. The stress power is derived and the stress resultant tensors are defined. For the sake of completeness, the equilibrium equations are obtained in absolute tensor notation by applying the principle of virtual work. Next, we present the constitutive equations for the formulation based on hyperelastic materials. In particular, constitutive matrices for multilayered composites and functionally graded shells are considered. Finally, a brief description of the geometrically exact shell theory is presented.

Chapter V addresses the finite element model for the nonlinear shell theory derived before. We apply the principle of virtual work to obtain the weak form of the equilibrium equations. A consistent linearization is derived that yields the symmetric tangent operator. The discrete finite element model is introduced by approximating the parametric space of the midsurface and interpolating the covariant components of the kinematic variables. Solution procedures based on the Newton-Raphson method and the cylindrical arc-length method are examined. Finally, numerical simulations are performed for finite deformation analyses of benchmark problems that include plates, cylindrical, spherical and hyperboloidal shells under static loading.

Chapter VI gives the closure of our work. It starts with a summary of the study, followed by the concluding remarks and comments on the direction of future research.

CHAPTER II

LINEAR SHELL THEORY[*]

The aim of this chapter is to develop a consistent third-order shear deformation theory for the linear analysis of multilayered composite and functionally graded shells. The theory, based on the ideas of Reddy and Liu [22], has five independent parameters and satisfies the tangential traction-free condition on the inner and outer surfaces of the shell (this condition can be relaxed by using a seven-parameter formulation which will be described in the finite element formulation in Chapter III). In addition, no simplification is made in the computation of stress resultants other than the assumption of linear elastic material. Material stiffness coefficients of the laminate are integrated numerically without any approximation in the shifter. The principle of virtual work is applied in terms of stress resultants and provides a basis for the finite element implementation.

For the derivation of the shell theory we utilize concepts and notions of tensor analysis and tensor calculus in curvilinear coordinates, and differential geometry. Except for section B that deals with the mathematical background of the shell theory, these concepts are accepted outright and are not further discussed.

A. Preliminaries

We discuss briefly a bibliographical review for shear deformable theories. The derivation of shear deformable shell theories has been one of the most prominent

---

[*] Copyright © 2004 From Shear deformation plate and shell theories: From Stavsky to present by J.N. Reddy, R.A. Arciniega. Mech. Advanced Mater. Struct. 11 (6-II), 535-582. Reproduced by permission of Taylor & Francis Group, LLC., http://www.taylorandfrancis.com; Copyright © 2005 From Consistent third-order shell theory with application to composite circular cylinders by R.A. Arciniega, J.N. Reddy. AIAA J. 43 (9), 2024-2038. Reprinted by permission of the American Institute of Aeronautics and Astronautics, Inc.

challenges in solid mechanics for many years. The basic idea is to develop appropriate models that can accurately simulate the effects of shear deformations and transverse normal strains in laminated shells.

Shear deformable shell theories are intrinsically related to the advent of laminated structures. The importance of including these effects comes from the fact that composite materials have very high ratios of inplane Young's moduli to transverse shear moduli. Consequently, shear deformation plays an important role in the global behavior of these materials. The first such theory for laminated isotropic plates is due to Stavsky [27]. The theory was generalized to laminated anisotropic plates by Yang et al. [28] and it is known as the YNS theory (which stands for Yang, Norris and Stavsky). This theory represents an extension of Reissner-Mindlin plate theory for homogeneous isotropic plates to arbitrarily laminated anisotropic plates and includes shear deformation and rotatory inertia effects.

Comparisons of closed-form elasticity solutions of laminated plates with those of the classical plate theory (under Kirchhoff assumptions) have been conducted by Pagano [29, 30] and Pagano and Hatfield [31]. These papers are well-known benchmarks for evaluation of laminated plate theories. The effect of boundary conditions in vibration and buckling responses of composite plates was investigated by Whitney [32].

The classical Reissner-Mindlin theory used in most of the work cited above assumes linear variation of the in-plane displacements with the thickness coordinate. High-order theories have then been required for a better description of shear deformations and transverse normal strains in laminated shells. Most of the high-order theories are derived based on assuming a displacement field. The displacement field is expanded as a quadratic or higher-order functions of the thickness coordinate. These theories are computationally more demanding. An additional independent variable is introduced in the theory with each additional power of the thickness coordinate.

These limitations were overcame back in the 80s with a simpler third-order shear deformation laminate theory proposed by Reddy [21] for composite plates and by Reddy and Liu [22] for laminated shells. The theory is based on assuming membrane displacements as cubic functions of the thickness coordinate, and the transverse displacement as constant through the thickness. The theory contains the same independent unknowns as the Reissner-Mindlin theory which is usually called the first-order theory. This is achieved by enforcing the free-traction condition on the top and bottom surfaces of the shell. The significant feature of the Reddy's theory is that the assumed displacement field leads to a parabolic distribution of the transverse shear strain, hence, it removes the need for using a shear correction factor. The theory has been amply used for computation of deflections, natural frequencies, buckling loads, etc. of laminated plates and shells [33-38]. In general, third-order shear deformation theories are capable of predicting accurately the global behavior of plates and shells.

An important question arises regarding the adoption of a kinematical model to analyze composite shells: which model can better describe the shell behavior? It has been demonstrated that the classical shell theory is not able to predict the deformation behavior with sufficient accuracy in composite shells [39]. However, the benefits in using high-order theories instead of first-order theories are not clearly established.

Disadvantages of the refined third-order theory can be attributed to the numerical solution rather than the theory itself. The presence of first partial derivatives of the transverse displacement in the displacement field leads to finite element formulations with Hermite interpolations functions. However, this drawback can be overcome by relaxing the continuity of the displacement field. This point will be amply discussed in Chapter III.

To complete the present literature review we mention two additional refined theories which are available to evaluate detailed local stress analysis: the layer-wise theory and the zig-zag theory. In the layer-wise plate theory, proposed by Reddy [40] and Reddy et al. [41, 42], the 3D displacement field is expanded as a linear combination of the thickness coordinate and undetermined functions of the position of each layer. The continuity of the transverse normal and shear stresses is not enforced. On the other hand, we have the zigzag theory [43-45] in which the displacement field fulfills a priori the static and geometric continuity conditions between contiguous layers. The reduction of the three-dimensional problem to the two-dimensional one is accomplished by assuming a displacement field which allows piecewise linear variation of the membrane displacements and a constant value of the transverse displacement through the thickness of the laminate. Thus, the boundary conditions on the external surfaces are not fulfilled, as well as in the first-order shear deformation theories.

Even though these theories described above are superior to the third-order theory in predicting local stresses, we will adopt the latter because of its simplicity (less computational effort) and accurate results for global analysis which is the goal in the present research. We will also show that the developed third-order theory is able to represent complex through-the-thickness distributions of insurface displacements and stresses of laminated shells.

B. Mathematical background

In this section, we present the mathematical preliminaries of the shell theory. A general description of tensor algebra can be found in [46-50]. Figure 2.1 shows the undeformed state of an arbitrary shell continuum. Let V be the volume of the undeformed (reference) configuration. Let S^{+} and S^{-} denote the outer and inner surfaces of the volume V, and Ω

be the undeformed midsurface of the shell such that

$$V=\Omega\times\left[-h/2,h/2\right]. \tag{2.1}$$

The point P in V (surface $\bar{\Omega}$) is defined by a set of convected curvilinear coordinates $\left(\theta^1,\theta^2,\theta^3\right)$ attached to the shell body and the point P_0 in Ω by $\left(\theta^1,\theta^2\right)$, where θ^3 denotes the normal coordinate. Covariant and contravariant base vectors at P_0 in Ω are denoted by $\mathbf{a}_\alpha,\mathbf{a}^\alpha$ with metric $a_{\alpha\beta},a^{\alpha\beta}$. We also define a normal vector to the midsurface $\mathbf{a}_3=\mathbf{a}^3$ such that $\mathbf{a}_3\cdot\mathbf{a}_3=1$. As usual, the Einstein summation convention is applied to repeated indices of tensor components where Greek indices represent the numbers 1, 2 and Latin ones the numbers 1, 2, 3. Then

$$\begin{gathered}a_{\alpha\beta}=\mathbf{a}_\alpha\cdot\mathbf{a}_\beta,\quad a^{\alpha\beta}=\mathbf{a}^\alpha\cdot\mathbf{a}^\beta,\quad \mathbf{a}^\alpha\cdot\mathbf{a}_\beta=\delta^\alpha_\beta,\quad \mathbf{a}_\alpha\cdot\mathbf{a}_3=0\\ \mathbf{a}_\alpha=\frac{\partial\mathbf{r}}{\partial\theta^\alpha}=\mathbf{r},_\alpha,\quad \mathbf{r}=\mathbf{r}\left(\theta^1,\theta^2\right)\end{gathered} \tag{2.2}$$

where $\mathbf{r}$ is the position vector of the point P_0 in Ω, and δ^α_β is the mixed Kronecker delta function.

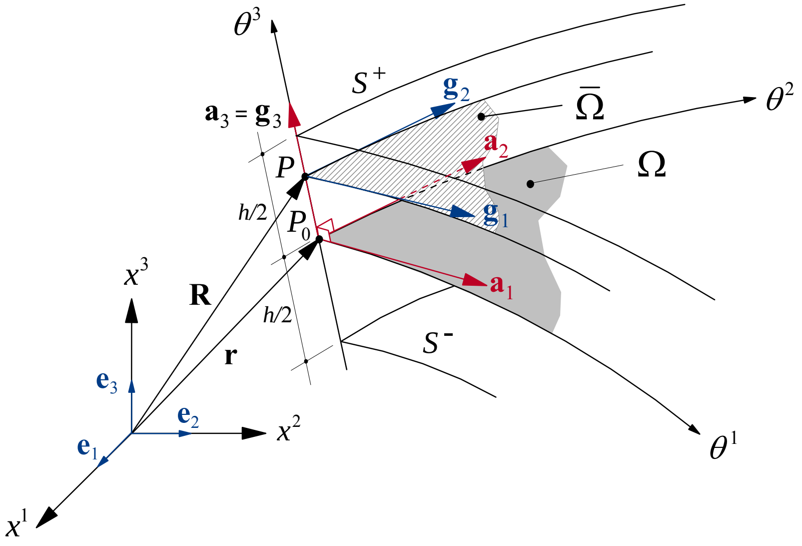

Fig. 2.1. Reference state of an arbitrary shell continuum.

The components of the metric tensor $a_{\alpha\beta}$ are known as the first fundamental form of the surface. In the following developments, $(\circ)_{,i}$ denotes partial derivatives with respect to the corresponding space coordinate, while $(\circ)_{\|i}$ and $(\circ)_{|\alpha}$ designate covariant derivatives with respect to space and surface metrics, respectively. In a similar fashion, covariant and contravariant base vectors at points of *V* are denoted by $\mathbf{g}_i, \mathbf{g}^i$ with corresponding metrics g_{ij}, g^{ij}. Thus

$$\begin{gathered} g_{ij} = \mathbf{g}_i \cdot \mathbf{g}_j, \quad g^{ij} = \mathbf{g}^i \cdot \mathbf{g}^j, \quad \mathbf{g}^i \cdot \mathbf{g}_j = \delta^i_j \\ \mathbf{g}_i = \frac{\partial \mathbf{R}}{\partial \theta^i} = \mathbf{R}_{,i}, \quad \mathbf{R} = \mathbf{R}\left(\theta^1, \theta^2, \theta^3\right) \end{gathered} \tag{2.3}$$

where **R** is the position vector of a typical point *P* in *V* (see Fig. 2.1).

The description of the 3D shell continuum can be obtained by expressing the position vector **R** at the point *P* in terms of **r** and the unit vector $\mathbf{a}_3$. Namely

$$\mathbf{R} = \mathbf{r} + \theta^3 \mathbf{a}_3. \tag{2.4}$$

In view of (2.4), the covariant vectors $\mathbf{g}_\alpha$ and $\mathbf{a}_\alpha$ are related according to the expression

$$\begin{aligned} \mathbf{g}_\alpha &= \mathbf{a}_\alpha + \theta^3 \mathbf{a}_{3,\alpha} \\ \mathbf{g}_3 &= \mathbf{a}_3. \end{aligned} \tag{2.5}$$

It follows that

$$g_{\alpha 3} = g^{\alpha 3} = 0, \quad g_{33} = g^{33} = 1. \tag{2.6}$$

The covariant components of the curvature tensor (second fundamental form of the surface) are defined by

$$\begin{aligned} b_{\alpha\beta} &= -\Gamma^3_{\alpha\beta|\Omega} = \mathbf{r}_{,\alpha\beta} \cdot \mathbf{a}_3 \\ &= \mathbf{a}_{\alpha,\beta} \cdot \mathbf{a}_3 = -\mathbf{a}_\alpha \cdot \mathbf{a}_{3,\beta} \end{aligned} \tag{2.7}$$

and the mixed components of the curvature tensor by

$$\begin{aligned} b^\alpha_\beta &= -\Gamma^\alpha_{\beta 3|\Omega} \\ &= a^{\alpha\mu} b_{\mu\beta} \end{aligned} \tag{2.8}$$

where $\Gamma^{i}_{jk|\Omega}$ denotes the Christoffel symbol of the second kind with respect to Ω. We also define the components of the third fundamental form of the surface as

$$c_{\alpha\beta} = b^{\lambda}_{\alpha} b_{\lambda\beta}. \tag{2.9}$$

Now, we use the well-known Weingarten formula

$$\mathbf{a}_{3,\alpha} = -b^{\lambda}_{\alpha}\,\mathbf{a}_{\lambda}. \tag{2.10}$$

The first equation of expression (2.5) can be transformed into

$$\begin{gathered} \mathbf{g}_{\alpha} = \mu^{\beta}_{\alpha}\mathbf{a}_{\beta} \\ \mu^{\beta}_{\alpha} = \delta^{\beta}_{\alpha} - \theta^{3} b^{\beta}_{\alpha} \end{gathered} \tag{2.11}$$

with μ^{β}_{α} as the shifter tensor components of the shell continuum.

The following additional definitions and relationships are needed in the sequel

$$\begin{gathered} a = \det\left(a_{\alpha\beta}\right), \quad g = \det\left(g_{ij}\right), \quad \mu = \det\left(\mu^{\beta}_{\alpha}\right) \\ \mu = \sqrt{g/a} = 1 - 2H\theta^{3} + K(\theta^{3})^{2} \end{gathered} \tag{2.12}$$

where *H* and *K*, respectively, denote the mean and Gaussian curvatures of the surface.

Finally, the differential volume of an element is given by

$$\begin{aligned} dV &= \sqrt{g}\, d\theta^{1} d\theta^{2} d\theta^{3} \\ &= \mu\, d\Omega\, d\theta^{3} \end{aligned} \tag{2.13}$$

where g and μ are related by (2.12) and the surface element is defined by

$$d\Omega = \sqrt{a}\, d\theta^{1} d\theta^{2}. \tag{2.14}$$

C. Kinematics of deformation of shells

Let **v** be the displacement vector associated with a point *P* in *V*. It can be expressed in terms of either the space base vectors $\mathbf{g}_{i}$ (or $\mathbf{g}^{i}$) in *V* or the surface base vectors $\mathbf{a}_{\alpha}$ and $\mathbf{a}_{3}$ in Ω. Namely

$$\begin{aligned}\mathbf{v} &= V^i \mathbf{g}_i = V_i \mathbf{g}^i \\ &= v^\alpha \mathbf{a}_\alpha + v^3 \mathbf{a}_3 = v_\alpha \mathbf{a}^\alpha + v_3 \mathbf{a}^3\end{aligned} \tag{2.15}$$

where $\left(V^i, V_i\right)$ and $\left(v^i, v_i\right)$ are the contravariant and covariant components of the vector **v** in V and Ω, respectively.

Similarly, the Green-Lagrange strain tensor **E** can be expressed in terms of the space or surface base vectors. Then

$$\begin{aligned}\mathbf{E} &= E_{ij}\, \mathbf{g}^i \otimes \mathbf{g}^j \\ &= \bar{E}_{ij}\, \mathbf{a}^i \otimes \mathbf{a}^j\end{aligned} \tag{2.16}$$

where E_{ij} and $\bar{E}_{ij}$ denote the covariant components of the tensor **E**. The tensor components E_{ij} measure the difference of metrics between the deformed and undeformed configurations. It can be shown that

$$\begin{aligned}E_{ij} &= \frac{1}{2}(\mathbf{g}_i \cdot \mathbf{v}_{,j} + \mathbf{g}_j \cdot \mathbf{v}_{,i} \underline{+ \mathbf{v}_{,i} \cdot \mathbf{v}_{,j}}) \\ &= \frac{1}{2}(V_{i\|j} + V_{j\|i} \underline{+ V^k_{\|i} V_{k\|j}}).\end{aligned} \tag{2.17}$$

Since we are considering only infinitesimal deformations, the underlined terms of (2.17) may be dropped. Then, the linear strain components are

$$\varepsilon_{ij} = \frac{1}{2}(V_{i\|j} + V_{j\|i}). \tag{2.18}$$

The space and surface components of the displacement vector are connected by the following equations

$$\begin{aligned}V_\alpha &= \mu_\alpha^\beta v_\beta \\ V_3 &= v_3\end{aligned} \tag{2.19}$$

and the covariant derivatives of the vector **v** in V are related to the covariant derivatives in Ω by the following expression (see Naghdi [48] and Librescu [49])

$$\begin{gathered} V_{\alpha\|\beta} = \mu_\alpha^\lambda\,(v_{\lambda|\beta} - b_{\lambda\beta} v_3), \quad V_{\alpha\|3} = \mu_\alpha^\lambda\, v_{\lambda,3} \\ V_{3\|\alpha} = v_{3,\alpha} + b_\alpha^\lambda v_\lambda, \quad V_{3\|3} = v_{3,3}. \end{gathered} \tag{2.20}$$

Eq. (2.18) can be written as

$$\begin{aligned} \varepsilon_{\alpha\beta} &= \frac{1}{2}(V_{\alpha\|\beta} + V_{\beta\|\alpha}) \\ \varepsilon_{\alpha 3} &= \frac{1}{2}(V_{\alpha\|3} + V_{3\|\alpha}) \\ \varepsilon_{33} &= V_{3\|3}. \end{aligned} \tag{2.21}$$

Finally, substituting (2.20) into (2.21), we obtain the exact 3D strain-displacement relations of the shell

$$\begin{aligned} \varepsilon_{\alpha\beta} &= \frac{1}{2}\Big(\mu_\alpha^\lambda (v_{\lambda|\beta} - b_{\lambda\beta} v_3) + \mu_\beta^\lambda (v_{\lambda|\alpha} - b_{\lambda\alpha} v_3) \Big) \\ &= \left(\frac{1}{2}(v_{\alpha|\beta} + v_{\beta|\alpha}) - b_{\alpha\beta} v_3 \right) + \left(c_{\alpha\beta} v_3 - \frac{1}{2}(b_\alpha^\lambda v_{\lambda|\beta} + b_\beta^\lambda v_{\lambda|\alpha}) \right) (\theta^3) \\ \varepsilon_{\alpha 3} &= \frac{1}{2}(\mu_\alpha^\lambda v_{\lambda,3} + v_{3,\alpha} + b_\alpha^\lambda v_\lambda) \\ &= \frac{1}{2}(v_{\alpha,3} + v_{3,\alpha} + b_\alpha^\lambda v_\lambda) + \frac{1}{2}(-b_\alpha^\lambda v_{\lambda,3})\,(\theta^3) \\ \varepsilon_{33} &= v_{3,3}. \end{aligned} \tag{2.22}$$

Next, we introduce the following assumptions for the present formulation:

Assumption 1: The displacement field is based on a cubic expansion of the thickness coordinate around the midsurface and the transverse displacement is assumed to be constant through the thickness.

Assumption 2: Fourth or higher-order terms in the strain-displacement relations of the shell are neglected.

Assumption 3: The normal stresses perpendicular to the midsurface are neglected.

The first two are kinematic assumptions while the last one is commonly used [9] in shell theories. Assumption 1 was originally proposed by Reddy [21] and Reddy and Liu

[22] in which, a nine-parameter formulation obtained initially is reduced to a five-parameter one imposing the tangential traction-free conditions on S^+ and S^-. In addition, the second part of assumption 1 asserts the "unstretched" condition of the material line normal to the midsurface. Then, the displacement field can be written as

$$\begin{aligned} v_\alpha\left(\theta^i\right) &= u_\alpha + \varphi_\alpha\,\theta^3 + \gamma_\alpha(\theta^3)^2 + \eta_\alpha(\theta^3)^3 \\ v_3\left(\theta^i\right) &= u_3. \end{aligned} \tag{2.23}$$

The stress tensor $\boldsymbol{\sigma}$ and the stress vector $\mathbf{t}$ can be expressed in terms of the covariant space vectors $\mathbf{g}_i$ as

$$\begin{aligned} \boldsymbol{\sigma} &= \sigma^{ij}\,\mathbf{g}_i \otimes \mathbf{g}_j \\ \mathbf{t} &= t^\alpha \mathbf{g}_\alpha + t^3 \mathbf{g}_3. \end{aligned} \tag{2.24}$$

The absence of tangential tractions on S^+ and S^- implies that $t^\alpha = 0$. Using the Cauchy formula on the outer and inner surfaces with $\mathbf{n} = \mathbf{g}_3$ and $\mathbf{n} = -\mathbf{g}_3$ respectively, we arrive to the following condition

$$t^\alpha = \sigma^{3\alpha}\,|_{S^+,S^-} = 0. \tag{2.25}$$

Note that for anisotropic materials the generalized Hooke's law is written as

$$\sigma^{ij} = E^{ijkl}\varepsilon_{kl} \tag{2.26}$$

where E^{ijkl} are contravariant space components of the elasticity tensor associated with a linear elastic body. Substituting (2.26) into (2.25), we obtain

$$\varepsilon_{3\alpha}\,|_{S^+,S^-} = 0 \tag{2.27}$$

for orthotropic materials. In case of anisotropic or monoclinic materials (one material plane of symmetry), Eq. (2.27) does not hold.

The displacement field (2.23) is substituted into the second equation of (2.22) and the result into (2.27). It gives

$$\begin{aligned} \gamma_\alpha &= -\frac{1}{3} b_\alpha^\lambda (d^{-1})_\lambda^\beta (\varphi_\beta + u_{3,\beta} + b_\beta^\kappa u_\kappa) \\ \eta_\alpha &= -\frac{4}{3h^2} (d^{-1})_\alpha^\beta (\varphi_\beta + u_{3,\beta} + b_\beta^\kappa u_\kappa) \end{aligned} \tag{2.28}$$

where $(d^{-1})_\alpha^\beta$ denotes the inverse of d_α^β and is defined as

$$\begin{gathered} d_\beta^\alpha = \delta_\beta^\alpha \left(1 - \frac{h^2}{12} K\right) - \frac{h^2}{6} b_\beta^\alpha H \\ (d^{-1})_\alpha^\lambda \, d_\lambda^\beta = \delta_\alpha^\beta . \end{gathered} \tag{2.29}$$

Taking into account (2.28), the displacement field (2.23) becomes

$$\begin{aligned} v_\alpha\left(\theta^i\right) &= u_\alpha + \varphi_\alpha \, \theta^3 \underline{+ h_\alpha^\lambda (d^{-1})_\lambda^\beta (\varphi_\beta + u_{3,\beta} + b_\beta^\kappa u_\kappa)} \\ v_3\left(\theta^i\right) &= u_3 \end{aligned} \tag{2.30}$$

where

$$h_\alpha^\beta = \left(-\frac{1}{3} b_\alpha^\beta (\theta^3)^2 - \frac{4}{3h^2} \delta_\alpha^\beta (\theta^3)^3\right). \tag{2.31}$$

The nine-parameter theory given by equation (2.23) is now reduced to a five-parameter one (with variables u_i and φ_α), which has the same number of variables as the first-order shell theory [48]. We denote TSDT the present third-order shear deformation theory and FSDT the present first-order shear deformation theory. The latter theory can be obtained from (2.30) by neglecting the underlined terms and is also known as the Reissner-Mindlin theory. Substituting equation (2.30) into the strain-displacement equations given in (2.22), we obtain the following relations

$$\begin{aligned} \varepsilon_{\alpha\beta} &= \varepsilon_{\alpha\beta}^{(0)} + \varepsilon_{\alpha\beta}^{(1)} (\theta^3) + \varepsilon_{\alpha\beta}^{(2)} (\theta^3)^2 + \varepsilon_{\alpha\beta}^{(3)} (\theta^3)^3 \underline{+ \varepsilon_{\alpha\beta}^{(4)} (\theta^3)^4} \\ \varepsilon_{\alpha 3} &= \varepsilon_{\alpha 3}^{(0)} + \varepsilon_{\alpha 3}^{(1)} (\theta^3) + \varepsilon_{\alpha 3}^{(2)} (\theta^3)^2 + \varepsilon_{\alpha 3}^{(3)} (\theta^3)^3 \end{aligned} \tag{2.32}$$

with $\varepsilon_{33} = 0$. The underlined term is neglected by assumption 2.

On the other hand, assumption 3 implies the normal stress is zero. However, the second part of assumption 1 states the strain component $\varepsilon_{33} = 0$ in evident contradiction to the constitutive equations. A justification for this assumption can be found in Koiter [51]. Shell formulations that include a linear variation of the thickness stretch have been proposed by Büchter and Ramm [52] and Simo et al. [53].

Finally, the coefficients $\varepsilon_{\alpha\beta}^{(i)}$ and $\varepsilon_{\alpha 3}^{(i)}$ of (2.32) are given by

$$\begin{aligned}
\varepsilon_{\alpha\beta}^{(0)} &= \frac{1}{2}(u_{\alpha|\beta} + u_{\beta|\alpha}) - b_{\alpha\beta}u_3 \\
\varepsilon_{\alpha\beta}^{(1)} &= \frac{1}{2}(\varphi_{\alpha|\beta} + \varphi_{\beta|\alpha} - b_\alpha^\lambda u_{\lambda|\beta} - b_\beta^\lambda u_{\lambda|\alpha}) + c_{\alpha\beta}u_3 \\
\varepsilon_{\alpha\beta}^{(2)} &= \frac{1}{2}(\gamma_{\alpha|\beta} + \gamma_{\beta|\alpha} - b_\alpha^\lambda \varphi_{\lambda|\beta} - b_\beta^\lambda \varphi_{\lambda|\alpha}) \\
\varepsilon_{\alpha\beta}^{(3)} &= \frac{1}{2}(\eta_{\alpha|\beta} + \eta_{\beta|\alpha} - b_\alpha^\lambda \gamma_{\lambda|\beta} - b_\beta^\lambda \gamma_{\lambda|\alpha}) \\
\varepsilon_{\alpha\beta}^{(4)} &= \frac{1}{2}(-b_\alpha^\lambda \eta_{\lambda|\beta} - b_\beta^\lambda \eta_{\lambda|\alpha}) \\
\varepsilon_{\alpha 3}^{(0)} &= \frac{1}{2}(\varphi_\alpha + u_{3,\alpha} + b_\alpha^\lambda u_\lambda) \\
\varepsilon_{\alpha 3}^{(1)} &= \gamma_\alpha \\
\varepsilon_{\alpha 3}^{(2)} &= \frac{1}{2}(3\eta_\alpha - b_\alpha^\lambda \gamma_\lambda) \\
\varepsilon_{\alpha 3}^{(3)} &= -b_\alpha^\lambda \eta_\lambda
\end{aligned} \tag{2.33}$$

where γ_α and η_α are defined by (2.28). Full expressions of the strain-displacement relations for plates, cylindrical shells and spherical shells (for the TSDT and FSDT) are shown in appendix A.

D. Constitutive equations

This section addresses the constitutive equations for a laminated shell. A more detailed explanation, which includes functionally graded materials, can be found in Chapter IV section F.

Consider a composite shell built of a finite number N of laminae which are made of an arbitrary linear elastic orthotropic material (Fig. 2.2). It is also assumed that layers are perfectly bonded together without any slip among their interfaces. The principal material axes are allowed to be oriented differently from layer to layer. At each point of the layer $L\ (L=1,N)$, we set a local orthonormal coordinate system $\bar{\theta}^{\alpha}$ such that the corresponding base vectors $\bar{\mathbf{g}}_{\alpha}$ coincide at P with the principal material directions and are, furthermore, of unit length. The third coordinate $\theta^3=\bar{\theta}^3$ remains unchanged. The constitutive equations with respect to this system are given by

$$\bar{\sigma}^{ij}=\bar{E}_L^{ijkl}\,\bar{\varepsilon}_{kl} \tag{2.34}$$

where $\bar{E}_L^{mnkl}$ are the components of the elasticity tensor referred to $\bar{\theta}^i$ and identical at P with the physical ones (since $\bar{\mathbf{g}}_i$ are orthonormal basis). Therefore, these coefficients can be calculated in terms of the engineering elastic constants which can be found in several textbooks of composite materials (see Reddy [54]).

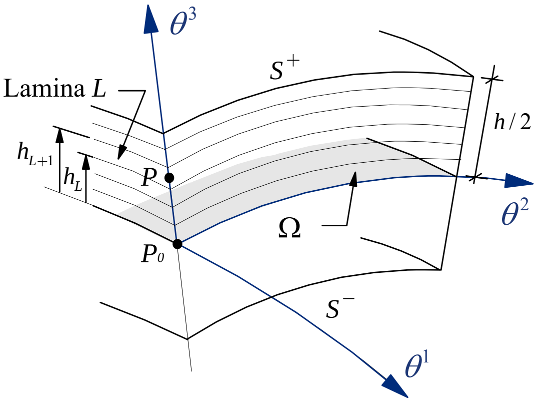

Fig. 2.2. Arbitrary laminated shell.

Writing (2.34) in terms of the laminate coordinates θ^i gives

$$\sigma^{ij}=E_L^{ijkl}\,\varepsilon_{kl} \tag{2.35}$$

where

$$E_L^{ijkl} = \frac{\partial \theta^i}{\partial \bar{\theta}^m} \frac{\partial \theta^j}{\partial \bar{\theta}^n} \frac{\partial \theta^k}{\partial \bar{\theta}^p} \frac{\partial \theta^l}{\partial \bar{\theta}^q} \bar{E}_L^{mnpq}. \tag{2.36}$$

The base vectors in coordinates $\bar{\theta}^i$ and θ^i are related by

$$\bar{\mathbf{g}}_m = \frac{\partial \theta^j}{\partial \bar{\theta}^m} \mathbf{g}_j \tag{2.37}$$

which implies

$$E_L^{ijkl} = (\mathbf{g}^i \cdot \bar{\mathbf{g}}_m)(\mathbf{g}^j \cdot \bar{\mathbf{g}}_n)(\mathbf{g}^k \cdot \bar{\mathbf{g}}_p)(\mathbf{g}^l \cdot \bar{\mathbf{g}}_q) \bar{E}_L^{mnpq}. \tag{2.38}$$

Finally, we use assumption 3 of zero stress condition in the thickness direction. It leads to

$$\begin{aligned} \sigma^{\alpha\beta} &= C_L^{\alpha\beta\omega\rho} \varepsilon_{\omega\rho} \\ \sigma^{\alpha 3} &= 2 C_L^{\alpha 3 \omega 3} \varepsilon_{\omega 3} \end{aligned} \tag{2.39}$$

with the reduced elasticity tensor

$$\begin{aligned} C_L^{\alpha\beta\omega\rho} &= E_L^{\alpha\beta\omega\rho} - E_L^{\alpha\beta 33} \frac{E_L^{33\omega\rho}}{E_L^{3333}} \\ C_L^{\alpha 3 \omega 3} &= E_L^{\alpha 3 \omega 3}. \end{aligned} \tag{2.40}$$

Note that C_L^{ijkl} are no longer components of a tensor.

E. Principle of virtual work and stress resultants

For the displacement finite element formulation, the virtual work principle of the laminated continuum is utilized. It asserts that: *If a continuum body is in equilibrium then the virtual work of the total forces is zero under a virtual displacement* (see Reddy [55]). It is expressed in terms of the stress and strain tensor as

$$\begin{aligned} \delta\mathcal{W} &= \delta\mathcal{W}_{\text{int}} + \delta\mathcal{W}_{\text{ext}} \\ &= \int_V \sigma^{ij} \delta\varepsilon_{ij} \, dV - \int_\Omega P^j \delta V_j \, d\Omega = 0 \end{aligned} \tag{2.41}$$

where $\delta\mathcal{W}_{\text{int}}$ is the virtual work of the internal forces, $\delta\mathcal{W}_{\text{ext}}$ the virtual work of external forces and δ is the variational operator.

Substituting equation (2.13) into the expression above, we obtain

$$\delta \mathcal{W}_{\text{int}} = \int_V \mu \sigma^{ij} \delta \varepsilon_{ij} \, d\Omega d\theta^3. \tag{2.42}$$

The decisive step in defining the stress resultants is to split (2.42) into a surface integral and a line integral in the transverse direction using (2.32). Furthermore, in view of the condition $\varepsilon_{33} = 0$ we obtain

$$\delta \mathcal{W}_{\text{int}} = \int_V \left(\sigma^{\alpha\beta} \sum_{n=0}^{3} (\theta^3)^{(n)} \delta \varepsilon^{(n)}_{\alpha\beta} + 2\sigma^{\alpha 3} \sum_{n=0}^{3} (\theta^3)^{(n)} \delta \varepsilon^{(n)}_{\alpha 3} \right) \mu \, d\Omega d\theta^3. \tag{2.43}$$

The pre-integration along the thickness of the laminate leads to a two-dimensional virtual work principle, i.e.

$$\delta \mathcal{W} = \int_\Omega \left(\sum_{n=0}^{3} \overset{(n)}{N}{}^{\alpha\beta} \delta \varepsilon^{(n)}_{\alpha\beta} + 2 \sum_{n=0}^{3} \overset{(n)}{Q}{}^{\alpha 3} \delta \varepsilon^{(n)}_{\alpha 3} \right) d\Omega - \int_\Omega P^j \delta V_j \, d\Omega = 0. \tag{2.44}$$

The stress resultants $\overset{(n)}{N}{}^{\alpha\beta}$ and $\overset{(n)}{Q}{}^{\alpha 3}$ are denoted by

$$\begin{aligned} \overset{(n)}{N}{}^{\alpha\beta} &= \int_{-h/2}^{h/2} \mu \sigma^{\alpha\beta} (\theta^3)^n \, d\theta^3 \\ \overset{(n)}{Q}{}^{\alpha 3} &= \int_{-h/2}^{h/2} \mu \sigma^{\alpha 3} (\theta^3)^n \, d\theta^3, \quad n = 0,1,2,3. \end{aligned} \tag{2.45}$$

The scalar quantity μ, which is the determinant of the shell shifter tensor, contains information about changes of differential geometry, i.e. the size and the shape of a differential volume element throughout the shell thickness. We can now expand expression (2.45) by using (2.39) with (2.32)

$$\begin{aligned} \overset{(n)}{N}{}^{\alpha\beta} &= \int_{-h/2}^{h/2} \mu \sigma^{\alpha\beta} (\theta^3)^n \, d\theta^3 = \sum_{L=1}^{N} \int_{h_L}^{h_{L+1}} \mu C_L^{\alpha\beta\omega\rho} \left(\sum_{k=0}^{3} (\theta^3)^k \varepsilon^{(k)}_{\omega\rho} \right) (\theta^3)^n \, d\theta^3 \\ &= \sum_{k=0}^{3} \overset{k+n}{C}{}^{\alpha\beta\omega\rho} \varepsilon^{(k)}_{\omega\rho}, \quad n = 0,1,2,3 \end{aligned} \tag{2.46}$$

and

$$\overset{(n)}{Q}{}^{\alpha 3} = \int_{-h/2}^{h/2} \mu \sigma^{\alpha 3} (\theta^3)^n d\theta^3 = 2\sum_{L=1}^{N} \int_{h_L}^{h_{L+1}} \mu C_L^{\alpha 3\beta 3} \left(\sum_{k=0}^{3} (\theta^3)^k \overset{(k)}{\varepsilon}_{\beta 3} \right) (\theta^3)^n d\theta^3$$
$$= 2\sum_{k=0}^{3} \overset{k+n}{C}{}^{\alpha 3\beta 3} \overset{(k)}{\varepsilon}_{\beta 3}, \quad n = 0,1,2,3 \tag{2.47}$$

where material stiffness coefficients of the laminate are given by

$$\overset{k}{C}{}^{\alpha\beta\omega\rho} = \sum_{L=1}^{N} \left(\int_{h_L}^{h_{L+1}} \mu C_L^{\alpha\beta\omega\rho} (\theta^3)^k d\theta^3 \right)$$
$$\overset{k}{C}{}^{\alpha 3\beta 3} = \sum_{L=1}^{N} \left(\int_{h_L}^{h_{L+1}} \mu C_L^{\alpha 3\beta 3} (\theta^3)^k d\theta^3 \right), \quad k = 0,1,\ldots,6. \tag{2.48}$$

Integration shown in equation (2.48) of the material law through the thickness direction is fundamental in reducing the three-dimensional theory into the two-dimensional one. The actual process of computation of (2.48) is carried out numerically using the Gaussian integration formula with 50 Gauss points per layer.

CHAPTER III

ABSTRACT FINITE ELEMENT MODEL AND RESULTS*

This chapter is devoted firstly to the development of the displacement finite element model for laminated shells based on the principle of virtual work and secondly to numerical applications of the present approach.

It is well-known [39] that first-order shear deformable models require the use of Lagrange interpolation functions for all generalized displacements for the finite element implementation. This is called C^0 elements since it is required that the kinematic variables be continuous through the boundary of the elements. On the other hand, because of the presence of first partial derivatives of the variable u_3 in the displacement field (2.30), the finite element model for the third-order theory requires Hermite interpolation for the transverse deflection (C^1 elements) and Lagrange interpolation for other displacements.

It has been shown that finite element models for shells based on C^1 continuity elements are numerically inconvenient as they involve second partial derivatives of the interpolation functions. They cannot account for all rigid body modes of a curved element (Cantin and Clough [56]). Furthermore, C^1 continuity elements can be only used for mapping rectangular meshes not distorted ones since the constant curvature criterion could be violated (Zienkiewicz [57]). Therefore, the use of displacement finite element models with C^0 continuity across the element boundary is computationally

---

* Copyright © 2004 From Shear deformation plate and shell theories: From Stavsky to present by J.N. Reddy, R.A. Arciniega. Mech. Advanced Mater. Struct. 11 (6-II), 535-582. Reproduced by permission of Taylor & Francis Group, LLC., http://www.taylorandfrancis.com; Copyright © 2005 From Consistent third-order shell theory with application to composite circular cylinders by R.A. Arciniega, J.N. Reddy. AIAA J. 43 (9), 2024-2038. Reprinted by permission of the American Institute of Aeronautics and Astronautics, Inc.

advantageous.

In that sense, we relax the continuity in the displacement field (2.30) by introducing two auxiliary variables ψ_α, i.e.

$$\psi_\alpha = \varphi_\alpha + u_{3,\alpha} \tag{3.1}$$

which was utilized by Nayak et al. [38] for the analysis of composite plates. In order to satisfy Eq. (3.1), we have to incorporate in the weak formulation the corresponding displacement constraints $\mathcal{K}_\alpha \equiv \psi_\alpha - (\varphi_\alpha + u_{3,\alpha})$. Substituting (3.1) into (2.30), we have

$$\begin{aligned} v_\alpha\left(\theta^i\right) &= u_\alpha + \varphi_\alpha\, \theta^3 + h_\alpha^\lambda\, (d^{-1})_\lambda^\beta\, (\psi_\beta + b_\beta^\kappa u_\kappa) \\ v_3\left(\theta^i\right) &= u_3 \end{aligned} \tag{3.2}$$

which requires only C^0 continuity in the kinematic variables. In vector notation Eq. (3.2) becomes

$$\mathbf{v}\left(\theta^i\right) = \mathbf{u}\left(\theta^\alpha\right) + \theta^3\, \underline{\boldsymbol{\varphi}}\left(\theta^\alpha\right) + (\theta^3)^2\, \underline{\boldsymbol{\gamma}}\left(\theta^\alpha\right) + (\theta^3)^3\, \underline{\boldsymbol{\eta}}\left(\theta^\alpha\right) \tag{3.3}$$

where $\mathbf{u}$ denotes displacement vector of the midsurface; and $\underline{\boldsymbol{\varphi}}, \underline{\boldsymbol{\gamma}}$ and $\underline{\boldsymbol{\eta}}$ are in-surface rotation vectors defined by

$$\begin{gathered} \mathbf{u}\left(\theta^\alpha\right) = u_i \mathbf{a}^i, \quad \underline{\boldsymbol{\varphi}}\left(\theta^\alpha\right) = \varphi_\beta \mathbf{a}^\beta, \quad \underline{\boldsymbol{\gamma}}\left(\theta^\alpha\right) = -\frac{1}{3} b_\mu^\lambda\, (d^{-1})_\lambda^\beta\, (\psi_\beta + b_\beta^\kappa u_\kappa)\, \mathbf{a}^\mu \\ \underline{\boldsymbol{\eta}}\left(\theta^\alpha\right) = -\frac{4}{3h^2}\, (d^{-1})_\mu^\beta\, (\psi_\beta + b_\beta^\kappa u_\kappa)\, \mathbf{a}^\mu . \end{gathered} \tag{3.4}$$

Note that the displacement field (3.3), which defines the configuration of the shell, can be written in terms of the triple $\left(u_i, \varphi_\alpha, \psi_\alpha\right)$ with seven independent variables. Equation (3.3) is then used to obtain the new kinematic relations of the shell and, hence, the variational formulation for the finite element model. As a result of (3.1), the number of kinematic variables for the TSDT and FSDT formulations is seven and five respectively.

A. Abstract configuration of the shell

The displacement field (3.3) is a three dimensional vector depending on three curvilinear coordinates $\left(\theta^1,\theta^2,\theta^3\right)$. However, all kinematic variables are functions of the parametric space of the midsurface $\left(\theta^1,\theta^2\right)$. The third coordinate, normal to the midsurface, is used to complete the description of the configuration of the shell. The interval $\left[-h/2, h/2\right]$ is considered constant everywhere. Consequently, the configuration of the shell in uniquely determined by the triple $\left(\mathbf{u},\underline{\varphi},\underline{\psi}\right)$ or in component form by the triple $\left(u_i,\varphi_\alpha,\psi_\alpha\right)$.

Let $\left(\theta^1,\theta^2\right)\in\mathscr{A}$ be the parametric space of the midsurface. The vectors $\mathbf{u},\underline{\varphi}$ and $\underline{\psi}$ can be interpreted as mappings from the two-dimensional chart $\mathscr{A}$ to $\mathbb{R}^n$ (Fig. 3.1).

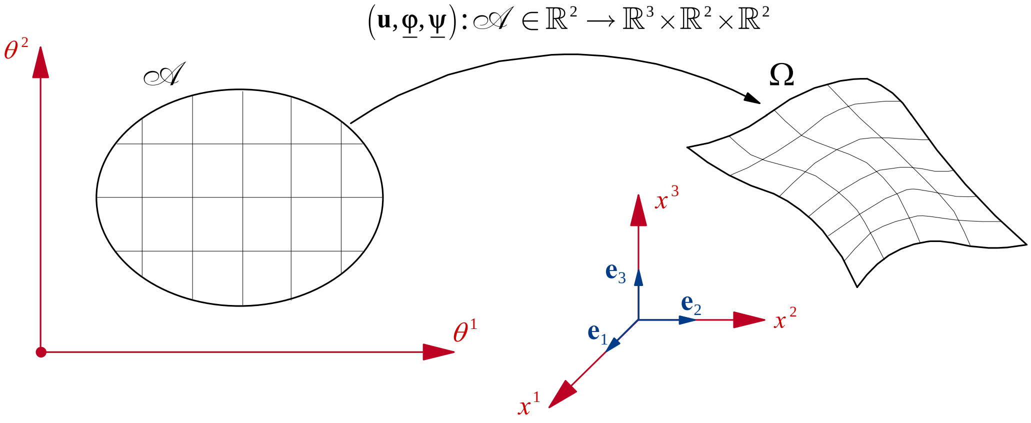

Fig. 3.1. Parametrization of the midsurface.

The abstract configuration of the shell is then defined by the set

$$\mathscr{C}=\left\{\Phi\equiv\left(\mathbf{u},\underline{\varphi},\underline{\psi}\right)\middle|\Phi:\mathscr{A}\rightarrow\mathbb{R}^3\times\mathbb{R}^2\times\mathbb{R}^2\right\}. \tag{3.5}$$

Note that elements $\Phi\in\mathscr{C}$ contain the same amount of three-dimensional information as Eq. (3.3) to locate arbitrary points in the three-dimensional shell.

The set $\mathscr{C}$ is also interpreted as a configuration manifold. Shell theories can be written in terms of tensors on an abstract manifold. That approach is preferred by mathematicians who are well-trained in analysis and calculus on manifolds (see books of do Carmo [58] and Bishop and Goldberg [59]). A typical example of this kind of notation is given by the so called “geometrically exact shell theory” based on the Cosserat continuum (see dissertations of Fox [60] and Rifai [61]). However, for most engineers, general tensor analysis is more suitable to develop shell theories since problems in elasticity occur in the Euclidean manifold $\mathcal{E}$.

B. The variational formulation

The weak form can be easily constructed from the principle of virtual work given in equation (2.41). Let $\Phi \equiv \left(\mathbf{u}, \underline{\boldsymbol{\varphi}}, \underline{\boldsymbol{\psi}}\right)$ be a configuration solution of the shell. We start by introducing the space of test functions $\mathcal{V}$ (space of admissible variations) defined by

$$\mathcal{V} = \left\{ \Theta \equiv \left(\mathbf{w}, \underline{\boldsymbol{\vartheta}}, \underline{\boldsymbol{\kappa}}\right) \in \left[H^1(\Omega)\right]^3 \times \left[H^1(\Omega)\right]^2 \times \left[H^1(\Omega)\right]^2 \,\middle|\, \mathbf{w}\,|_{\Gamma_D} = 0, \underline{\boldsymbol{\vartheta}}\,|_{\Gamma_D} = 0, \underline{\boldsymbol{\kappa}}\,|_{\Gamma_D} = 0 \right\} \quad (3.6)$$

where $H^1(\Omega)$ is the Sobolev space of degree 1 and Γ_D is the Dirichlet boundary (see Brenner and Scott [62]). The test function Θ can be seen as virtual displacements and rotations of the midsurface. Notice that we have chosen the space $H^1(\Omega)$ since only C^0 continuity is required for the functions on the finite element space $\mathcal{V}^{hp}$.

The weak form $\mathcal{G}$ can be written in the following form

$$\mathcal{G}\left(\Theta;\Phi\right) \equiv \mathcal{A}_{mb}\left(\Theta;\Phi\right) + \mathcal{A}_{s}\left(\Theta;\Phi\right) \underline{+\mathcal{B}\left(\Theta;\Phi\right)} - \mathcal{F}\left(\Theta\right) = 0 \quad (3.7)$$

where $\mathcal{A}_{mb}$, $\mathcal{A}_s$ and $\mathcal{B}$ are bilinear forms given by

$$\mathcal{A}_{mb}\left(\Theta;\Phi\right) = \int_\Omega \left(\sum_{k=0}^{3} \sum_{l=0}^{3} \overset{k+l}{C}{}^{\alpha\beta\omega\rho}\, \varepsilon^{(l)}_{\omega\rho}\left(\Phi\right) \varepsilon^{(k)}_{\alpha\beta}\left(\Theta\right) \right) d\Omega$$

$$\mathcal{A}_{s}\left(\Theta;\Phi\right) = \int_\Omega \left(4 \sum_{k=0}^{3} \sum_{l=0}^{3} \overset{k+l}{C}{}_{\alpha 3 \omega 3}\, \varepsilon^{(l)}_{\omega 3}\left(\Phi\right) \varepsilon^{(k)}_{\alpha 3}\left(\Theta\right) \right) d\Omega$$

$$\mathcal{B}\left(\Theta;\Phi\right)=\gamma\int_{\Omega}\mathcal{K}_{\alpha}(\Phi)\mathcal{K}_{\alpha}(\Theta)\,d\Omega \tag{3.8}$$

and $\mathcal{F}$ is a linear form denoted by

$$\mathcal{F}\left(\Theta\right)=\int_{\Omega}(P^{\alpha}w_{\alpha}+P^{3}w_{3})\,d\Omega \tag{3.9}$$

for external distributed loading. The terms $\varepsilon_{\alpha\beta}^{(n)}\left(\circ\right)$ and $\varepsilon_{\alpha 3}^{(n)}\left(\circ\right)$ are components of the strain tensor given by Eq. (2.33) while $\overset{n}{C}{}^{ijkl}$ are material stiffness coefficients. Note that a penalty term for the constraints (3.1) is incorporated in (3.7) where γ denotes the penalty parameter (very large value). Nevertheless, it can be shown that the influence of the underlined term in (3.7) on the numerical results is negligible. Therefore, this term is not included in the numerical results unless it is stated otherwise.

The variational formulation of the boundary value problem can be now stated as follows

$$\text{Find } \Phi=\left(\mathbf{u},\underline{\boldsymbol{\varphi}},\underline{\boldsymbol{\psi}}\right)\in\mathcal{V} \text{ such that } \forall\,\Theta=\left(\mathbf{w},\underline{\boldsymbol{\vartheta}},\underline{\boldsymbol{\kappa}}\right)\in\mathcal{V}$$

$$\mathcal{A}_{mb}\left(\Theta;\Phi\right)+\mathcal{A}_{s}\left(\Theta;\Phi\right)=\mathcal{F}\left(\Theta\right). \tag{3.10}$$

It can be easily demonstrated that $\mathcal{A}_{mb}$ and $\mathcal{A}_{s}$ are symmetric and bounded. On the other hand, proving ellipticity (or coercivity) on $\mathcal{V}$ of the bilinear forms is far more complicated. Since this issue goes beyond the goals of the present dissertation, we will not attempt to do it. However, for the sake of completeness we refer the paper of Bernadou et al. [63] which provides complete proofs of the ellipticity of the strain energies in two shell models: Koiter’s model and Naghdi’s model (see also Ciarlet [64] and Chapelle and Bathe [65, 66]). Under the conditions discussed above, existence and uniqueness in the solution of the variational problem (3.10) follows from the Lax-Milgram theorem [62, 66].

C. Discrete finite element model

Let $\mathscr{A}$ be the computational domain of the shell which is discretized into NEL elements such that

$$\mathscr{A} = \bigcup_{e=1}^{\mathrm{NEL}} \mathscr{A}^{e} \tag{3.11}$$

where the closure of $\mathscr{A}$ is obviously understood. Next, we construct the finite-dimensional space of $\mathcal{V}$ called $\mathcal{V}^{hp}$ such that $\mathcal{V}^{hp} \subset \mathcal{V}$. The symbol *h* represents the maximum of all element sizes (we shall be careful with this symbol because *h* is also used in the numerical examples as the thickness of the shell) and *p* the degree of the polynomials utilized to interpolate the kinematic variables. In order to obtain a better approximation of the solution, we can either reduce *h* (i.e. refine the mesh) or increase the polynomial degree *p*.

The discrete finite element model of the problem (3.10) is now written as

$$\text{Find } \Phi^{hp} = \left(\mathbf{u}^{hp}, \underline{\boldsymbol{\varphi}}^{hp}, \underline{\boldsymbol{\psi}}^{hp}\right) \in \mathcal{V}^{hp} \text{ such that } \forall\, \Theta^{hp} = \left(\mathbf{w}^{hp}, \underline{\boldsymbol{\vartheta}}^{hp}, \underline{\boldsymbol{\kappa}}^{hp}\right) \in \mathcal{V}^{hp}$$

$$\mathcal{A}_{mb}^{(e)}\left(\Theta^{hp}; \Phi^{hp}\right) + \mathcal{A}_{s}^{(e)}\left(\Theta^{hp}; \Phi^{hp}\right) = \mathcal{F}^{(e)}\left(\Theta^{hp}\right). \tag{3.12}$$

Similar to the variational problem (3.10), uniqueness of the discrete problem follows from the condition $\mathcal{V}^{hp} \subset \mathcal{V}$ and the Lax-Milgram theorem.

Under the isoparametric concept, the same interpolation functions for the coordinates and variables are utilized [67]. Let $\hat{\Omega}^{e} \equiv [-1,1] \times [-1,1]$ be a parent domain in (ξ, η)-space (i.e., the closed, biunit square in $\mathbb{R}^2$). We first map the parametric coordinates $\underline{\boldsymbol{\theta}}(\cdot,\cdot) : \hat{\Omega}^{e} \in \mathbb{R}^2 \rightarrow \mathscr{A}^{e}$ such that

$$\underline{\boldsymbol{\theta}}(\xi, \eta) = \left(\sum_{j=1}^{m} (\theta^{\alpha})^{(j)} N^{(j)}(\xi, \eta) \right) \mathbf{e}_{\alpha} \tag{3.13}$$

where $\underline{\boldsymbol{\theta}} = \theta^{\alpha} \mathbf{e}_{\alpha}$. The vectors $\mathbf{e}_{\alpha}$ are orthonormal basis of $\mathbb{R}^2$.

We shall point out that the isoparametric concept used here should not be confused with the isoparametric formulations for shells which are directly inherited from the degenerated element models (so-called continuum-based formulations [4, 68]). In our case the map $\underline{\boldsymbol{\theta}}(\xi,\eta)$ just scales a rectangular element to the master element instead of a total approximation of the midsurface.

Next, the kinematic variables are interpolated. As we know the present finite element model requires only C^0 continuity in all variables. The finite element equations are obtained by interpolating the covariant components of the kinematic variables of the midsurface in terms of base vectors $\mathbf{a}^\alpha$. Namely

$$\mathbf{u}^{hp}(\underline{\boldsymbol{\theta}}) = \left(\sum_{j=1}^{m} u_k{}^{(j)} N^{(j)}(\xi,\eta)\right)\mathbf{a}^k, \qquad \underline{\boldsymbol{\varphi}}^{hp}(\underline{\boldsymbol{\theta}}) = \left(\sum_{j=1}^{m} \varphi_\alpha{}^{(j)} N^{(j)}(\xi,\eta)\right)\mathbf{a}^\alpha$$
$$\underline{\boldsymbol{\psi}}^{hp}(\underline{\boldsymbol{\theta}}) = \left(\sum_{j=1}^{m} \psi_\alpha{}^{(j)} N^{(j)}(\xi,\eta)\right)\mathbf{a}^\alpha \tag{3.14}$$

where *m* is the number of nodes of the element, $N^{(j)}(\xi,\eta)$ are interpolation functions at the node *j* and $\left(u_i^{(j)}, \varphi_\alpha^{(j)}, \psi_\alpha^{(j)}\right)$ denote the nodal values of the kinematic variables.

The present finite element model is called “tensor-based formulation” because of the following two conditions: no approximation of the midsurface (the computational domain lies in $\mathscr{A}$) and interpolation of the covariant components of the kinematic variables. We believe that tensor-based models describe in a natural and better way the actual behavior of the shell.

1. The problem of locking and its implications

The variational problem (3.10) and the discrete problem (3.12) are well-posed in the sense that their solution exist, are unique, and depend continuously on the external data $\mathcal{F}$. Moreover, the Céa’s Lemma ensures that the finite element solution is optimal with respect to the approximation capabilities of the finite element space $\mathcal{V}^{hp}$ [62, 66]. Namely

$$\left\| \Phi - \Phi^{hp} \right\|_{\mathcal{V}} \leq C \inf_{\Theta \in \mathcal{V}^{hp}} \left\| \Phi - \Theta \right\|_{\mathcal{V}} . \tag{3.15}$$

The error $\left\| \Phi - \Phi^{hp} \right\|_{\mathcal{V}}$ is proportional to the best it can be using the discrete space $\mathcal{V}^{hp}$.

The approximation theory and Eq. (3.15) yield an error estimate for the present boundary value problem, i.e.

$$\left\| \Phi - \Phi^{hp} \right\|_{\mathcal{V}} \leq C \mathcal{O}\left(h^{p} \right) \tag{3.16}$$

for smooth solutions Φ, with the constant C independent of h but dependent on the geometry and material properties. For plates and shells C depend on the thickness t. For small values of t the constant C becomes very large and the order of convergence given in (3.16) results impractical. This phenomenon is known as *locking* (see Babuška and Suri [69]).

Locking may arise if there are concealed constraints in the physical model that are not well represented in the finite element approximation of the model (see Pitkäranta [70]). In shells structures the constraints that cause numerical locking are inherited from the asymptotic theory as the thickness tens to zero. Two different asymptotic behaviors can be identified: membrane dominated and bending dominated states. This classification depends on whether the membrane or bending energy component dominates the total energy [3, 14-16].

Standard low-order finite element approximations perform well for membrane dominated shell problems. The bending dominated case is far more complex to handle. In the limit as t tends to zero the asymptotic behavior of the shell corresponds to the inextensional shell theory. This constraint causes a numerical overstiffness in finite element models. This is called *membrane locking*. Yet another type of locking, called *shear locking*, can appear in plates and shells. This is caused by the Kirchhoff-Love constraints of vanishing transverse shear strain as the thickness becomes small [14].

Many finite element techniques have been proposed over the past decades to remediate shear and membrane locking. The locking is avoided in many cases by using uniformly reduced integration or selective integration in the numerical evaluation of the stiffness coefficients (Zienkiewicz et al. [71], Stolarski and Belytschko [72]). Alternatively, mixed formulations with lower-order elements have been proposed to mitigate the effects of shear and membrane locking. Among them, we can cite the assumed strain elements (Hinton and Huang [11], Dvorkin and Bathe [12]) and the enhanced strain elements (Simo and Rifai [13]).

On the other hand, higher-order finite elements show less sensitivity to membrane and shear locking and for a particular high p level, problems associated with locking disappear [17]. Pitkäranta and co-workers [14-16] verified that increasing the element p level is far a more effective way of improving the quality of the numerical approximation than refining the finite element mesh at a fixed p level. When the comparison between implementation cost and accuracy is taken into account, high-order finite elements need a smaller computational effort to achieve the desired accuracy without any tricky techniques. Applications of higher-order elements to plates and shells can be found in Chinosi et al. [6] and Pontaza and Reddy [14, 73].

In spite of the many proposed “simple”, “efficient” or “free-locking” finite elements found in the literature, there is not such a perfect shell element. We strongly agree with the concluding remarks of J. Pitkäranta [74] in a recent paper and quote: *The combined effort of the engineer and mathematician can bring out the ultimate dream element for shells, it could achieve another important goal. It could raise the art of finite element modeling of shells from occultism to science*.

In this dissertation a family of high-order Lagrange elements is developed (Fig. 3.2). These elements seem to be free of membrane and shear locking. Basically, we use elements labeled $Q25$ and $Q81$ (p levels equal to 4 and 8 respectively), yet the program is developed for any p level element. Table 3.1 shows the family of higher-order Lagrange elements utilized here and the corresponding number of degrees of freedom for the FSDT and TSDT while Figure 3.3 depicts the shape functions $N^{(13)}$, $N^{(25)}$ and $N^{(41)}$ associate with elements $Q25$, $Q49$ and $Q81$ respectively.

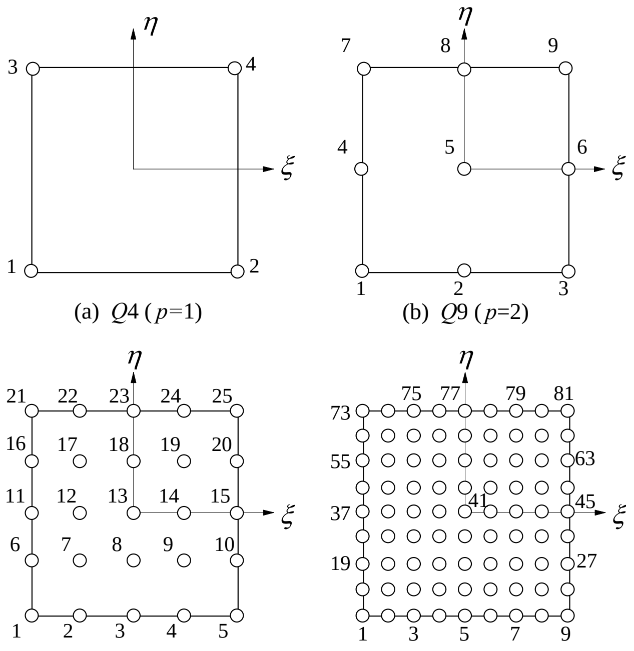

(a) $Q4$ (p=1)
(b) $Q9$ (p=2)
(c) $Q25$ (p=4)
(d) $Q81$ (p=8)

Fig. 3.2. Basic p-elements used in the present formulation.

Table 3.1. Number of degrees of freedom per element for different *p* levels.

Element	*p* level	FSDT (DOF)	TSDT (DOF)
$Q4$	1	20	28
$Q9$	2	45	63
$Q25$	4	125	175
$Q49$	6	245	343
$Q81$	8	405	567

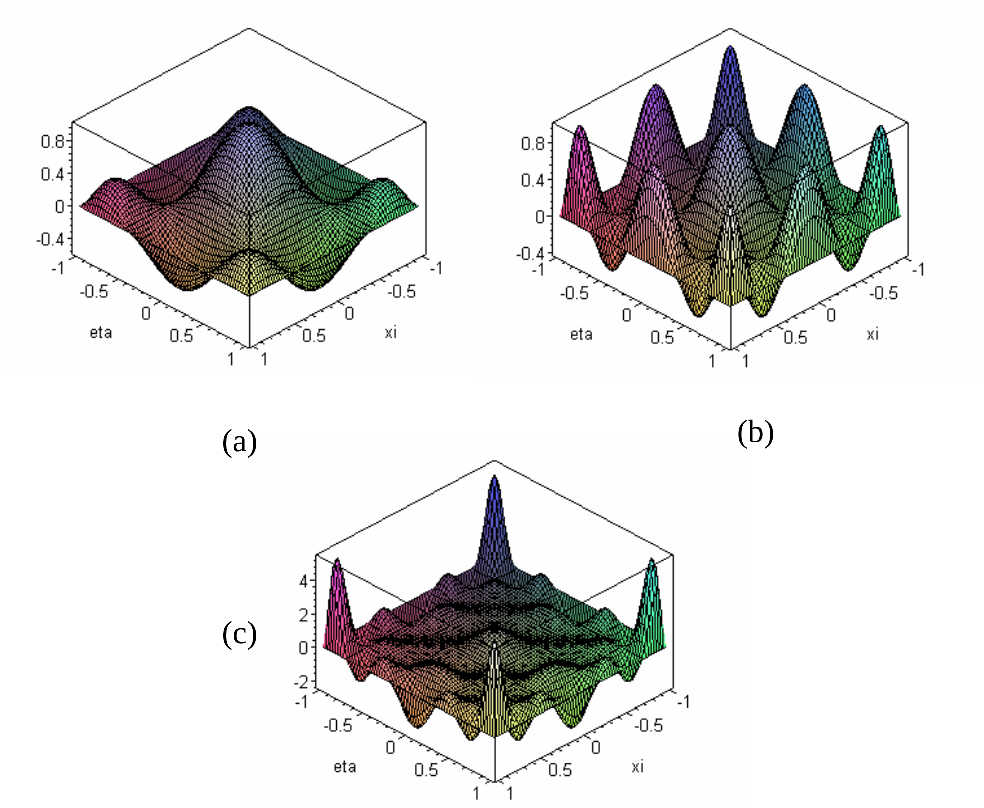

(a)

(b)

(c)

Fig. 3.3. Interpolation functions: (a) $N^{(13)}$ - $Q25$, (b) $N^{(25)}$ - $Q49$, (c) $N^{(41)}$ - $Q81$.

For the sake of completeness we present formulas to compute Lagrange polynomials in natural coordinates [67, 68], i.e.

$$L_i^1(\xi)=\prod_{\substack{k=1\\k\neq i}}^{p+1}\frac{(\xi-\xi_k)}{(\xi_i-\xi_k)},\quad L_i^2(\eta)=\prod_{\substack{k=1\\k\neq i}}^{p+1}\frac{(\eta-\eta_k)}{(\eta_i-\eta_k)},\qquad i=1,\dots,p+1 \tag{3.17}$$

where p is the polynomial degree. Finally, the shape functions mapped in the biunit square are of the form

$$N^{(k)}(\xi,\eta)=L_i^1(\xi)L_j^2(\eta),\qquad k=(j-1)(p+1)+i \tag{3.18}$$

for the node k of the element.

2. Solution procedure

Substituting Eq. (3.14) with interpolation functions (3.18) into the finite element approximation (3.12) we obtain the following matrix equations

$$\boldsymbol{k}^{(e)}\boldsymbol{r}^{(e)}=\boldsymbol{f}^{(e)} \tag{3.19}$$

where $\boldsymbol{k}^{(e)}$ is the element stiffness matrix which is symmetric and positive definite, $\boldsymbol{r}^{(e)}$ is the nodal vector displacement of the element and $\boldsymbol{f}^{(e)}$ is the load vector.

The assembly of the NEL matrices is then carried out over the domain $\mathscr{A}$. This leads to a global system

$$\boldsymbol{K}\boldsymbol{d}=\boldsymbol{F} \tag{3.20}$$

with

$$\boldsymbol{K}=\underset{e=1}{\overset{\text{NEL}}{\mathbb{A}}}\boldsymbol{k}^{(e)},\quad \boldsymbol{F}=\underset{e=1}{\overset{\text{NEL}}{\mathbb{A}}}\boldsymbol{f}^{(e)} \tag{3.21}$$

where $\mathbb{A}$ denotes the finite element assembly operator and $\boldsymbol{d}$ are the displacements of the global degrees of freedom.

Finally, Eq. (3.20) is solved by employing a direct method such as Gauss elimination for symmetric and banded matrices which is suitable for linear shell problems.

D. Numerical examples

We present in this section the numerical examples obtained with the formulation developed herein. The performance of the developed elements together with the FSDT and TSDT formulations are evaluated by solving several benchmark problems for plates, cylindrical shells and spherical shells (see Fig. 3.4). A parametric study for bending of functionally graded plates is presented as well.

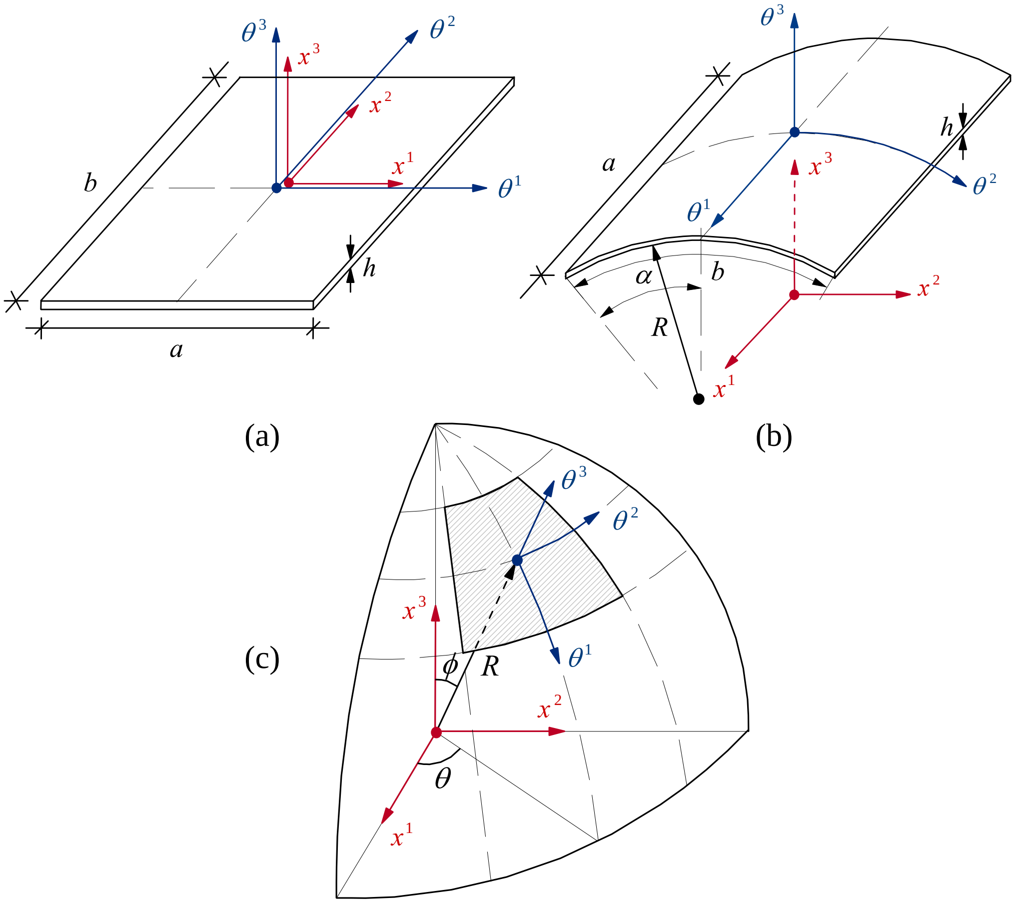

Fig. 3.4. Geometries: (a) Plate, (b) Cylindrical shell, (c) Spherical shell.

Regular meshes of Lagrange elements (*Q*4, *Q*9, *Q*25 and *Q*81) with five and seven degrees of freedom per node for the FSDT and TSDT respectively are utilized in the finite element analysis. The flexibility of higher-order elements (using polynomials of fourth and eighth degree) precludes any presence of shear and membrane locking in the numerical computation. Consequently, full Gauss integration rule is employed in the evaluation of the stiffness coefficients. For comparison reasons, reduced and selective integration techniques have also been implemented.

The numerical integration rule (Gauss quadrature) utilized in this formulation is shown in Table 3.2. The last number denotes the number of Gauss points used to evaluate transverse shear terms, the middle one denotes the number of Gauss points used to evaluate the bending-membrane coupling terms, and the first one denotes the number of Gauss points used to evaluate the remaining terms in the stiffness matrix. The code allows using full integration for all terms, reduced integration (one point less than full integration) for all terms, or selective integration in which reduced integration is used for both shear and bending-membrane terms and full integration for all other terms.

Table 3.2. Gauss integration rule for different *p* levels used in the present formulation.

p level	Geometry*	Full Integration	Selective Integration	Reduced Integration
1	P	2×-×2	2×-×1	1×-×1
	C	2×2×2	2×1×1	1×1×1
	S	2×2×2	2×2×1	-
2	P	3×-×3	3×-×2	2×-×2
	C	3×3×3	3×2×2	2×2×2
	S	3×3×3	3×3×2	-
4	P	5×-×5	5×-×4	4×-×4
	C	5×5×5	5×4×4	4×4×4
	S	5×5×5	5×5×4	-
8	P	9×-×9	9×-×8	8×-×8
	C	9×9×9	9×8×8	8×8×8
	S	9×9×9	9×9×8	-

* P, C and S stand for plates, cylindrical shell and spherical shell respectively.

1. Plates

a. Comparisons with analytical solutions

First, we compare our numerical results with those obtained by Pagano [30]. The solutions of Pagano are amply used for assessment of the accuracy of plate theories because they represent one of the few analytical 3D solutions for bending cross-ply laminated plates.

In Tables 3.3 and 3.4 we show dimensionless central deflections and in-plane stresses for symmetric cross-ply plates (0°/90°/0°) under sinusoidal loading with two plate aspect ratios, $a/b = 1$ and 1/3 respectively. The following dimensionless parameters are employed

$$\bar{v}_{<3>} = \frac{100\,E_2}{q_0\,h\,S^4}\,v_{<3>}, \quad \bar{v}_{<\alpha>} = \frac{100\,E_2}{q_0\,h\,S^3}\,v_{<\alpha>}, \quad \bar{\sigma}_{<\alpha\beta>} = \frac{1}{q_0\,S^2}\,\sigma_{<\alpha\beta>}, \quad S = \frac{a}{h}$$

and lamina properties

$$E_1/E_2 = 25, \quad G_{13} = G_{12} = 0.5E_2, \quad G_{23} = 0.2E_2, \quad \nu_{12} = 0.25\,.$$

The simply-supported boundary conditions are

$$\text{At } \theta^1 = \pm\, a/2 \qquad u_{<2>} = u_{<3>} = \varphi_{<2>} = \psi_{<2>} = 0$$

$$\text{At } \theta^2 = \pm\, b/2 \qquad u_{<1>} = u_{<3>} = \varphi_{<1>} = \psi_{<1>} = 0$$

and loading $P^3 = q_0 \cos\left(\pi\theta^1/a\right)\cos\left(\pi\theta^2/b\right)$.

It is noticed that the results for the present FSDT and TSDT are in close agreement with those of Pagano [30]. However, when we increase the thickness of the plate the results diverge. This is clearly understood and expected since the equivalent single-layer formulation adopted here, is a 2D approximation of the 3D continuum. It is also verified once again that the TSDT shows more accurate results than the FSTD for thick plates.

Table 3.3. Central deflection and stresses of a three-ply (0°/90°/0°) laminated square plate under sinusoidal loading (4×4Q25).

S		Pagano [30]	Present TSDT	Present FSDT
4	$\bar{\sigma}_{<11>}\left(0,0,\frac{h}{2}\right)$	0.801	0.76692	0.43697
10		0.590	0.58472	0.51341
20		0.552	0.55070	0.53183
50		0.541	0.54064	0.53757
100		0.539	0.53919	0.53841
4	$\bar{\sigma}_{<22>}\left(0,0,-\frac{h}{6}\right)$	-0.556	-0.50786	-0.47744
10		-0.288	-0.27123	-0.25361
20		-0.210	-0.20500	-0.19967
50		-0.185	-0.18376	-0.18286
100		-0.181	-0.18063	-0.18040
4	$\bar{\sigma}_{<12>}\left(\frac{a}{2},\frac{b}{2},\frac{h}{2}\right)$	-0.0511	-0.04993	-0.03692
10		-0.0289	-0.02807	-0.02517
20		-0.0234	-0.02312	-0.02234
50		-0.0216	-0.02158	-0.02145
100		-0.0213	-0.02136	-0.02132

Table 3.4. Central deflections and stresses of a three-ply (0°/90°/0°) laminated rectangular plate $(b = 3a)$ under sinusoidal loading (4×4*Q*25).

S		Pagano [30]	Present TSDT	Present FSDT
4	$\bar{v}_{<3>}\left(0,0,\,0\right)$	2.820	2.64838	2.36256
10		0.919	0.86904	0.80301
20		0.610	0.59580	0.57838
50		0.520	0.51821	0.51539
100		0.508	0.50709	0.50638
4	$\bar{\sigma}_{<11>}\left(0,0,\frac{h}{2}\right)$	1.140	1.08110	0.61299
10		0.726	0.71216	0.62141
20		0.650	0.64618	0.62279
50		0.628	0.62697	0.62319
100		0.624	0.62420	0.62325
4	$\bar{\sigma}_{<22>}\left(0,0,-\frac{h}{6}\right)$	-0.1190	-0.10389	-0.09342
10		-0.0435	-0.04011	-0.03746
20		-0.0299	-0.02898	-0.02827
50		-0.0259	-0.02576	-0.02564
100		-0.0253	-0.02529	-0.02526
4	$\bar{\sigma}_{<12>}\left(\frac{a}{2},\frac{b}{2},\frac{h}{2}\right)$	-0.0269	-0.02631	-0.02047
10		-0.0120	-0.01167	-0.01048
20		-0.0093	-0.00915	-0.00884
50		-0.0084	-0.00842	-0.00837
100		-0.0083	-0.00832	-0.00830

Another comparison of the dimensionless central deflections of three cross-ply rectangular plates is given in Table 3.5 (with the same geometry, material properties and boundary conditions). In addition to the results of Pagano we include the MDT and SDT7 results of Braun [75] and Braun et al. [76]. The MDT is a layer-wise theory (C^0 continuous displacement field) so-called multidirector theory, while the SDT7 is an improved first-order theory with thickness stretching and 7 parameters (with enhanced assumed strain, EAS). The percentage of error computed for the TSDT and FSDT (case $S = 4$) with respect to Pagano's solutions are 6% and 16% respectively. Naturally, the MDT gives better results for thick plates than other theories. On the other hand, remarkably, the present FSDT shows more accurate than the SDT7, although Braun's formulation uses thickness stretching with EAS. These results are illustrated in Fig. 3.5 as well.

Table 3.5. Comparison of the central deflection $\bar{v}_{<3>}$ of a (0°/90°/0°) laminated rectangular plate $(b = 3a)$ under sinusoidal loading (4×4Q25).

Formulation	Ratio $S = a/h$				
	4	10	20	50	100
Pagano [30]	2.820	0.919	0.610	0.520	0.508
MDT [75]	2.78334	0.90797	0.60512	0.52000	0.50800
	1.3%	1.2%	0.8%	0.0%	0.0%
SDT7[75]	2.06142	0.75358	0.56608	0.51376	0.50597
	26.9%	18.0%	7.2%	1.2%	0.4%
Present TSDT	2.64838	0.86904	0.59580	0.51821	0.50709
	6.0857%	5.4360%	2.3286%	0.3434%	0.1788%
Present FSDT	2.36256	0.80301	0.57838	0.51539	0.50638
	16.2211%	12.6212%	5.1840%	0.8875%	0.3183%

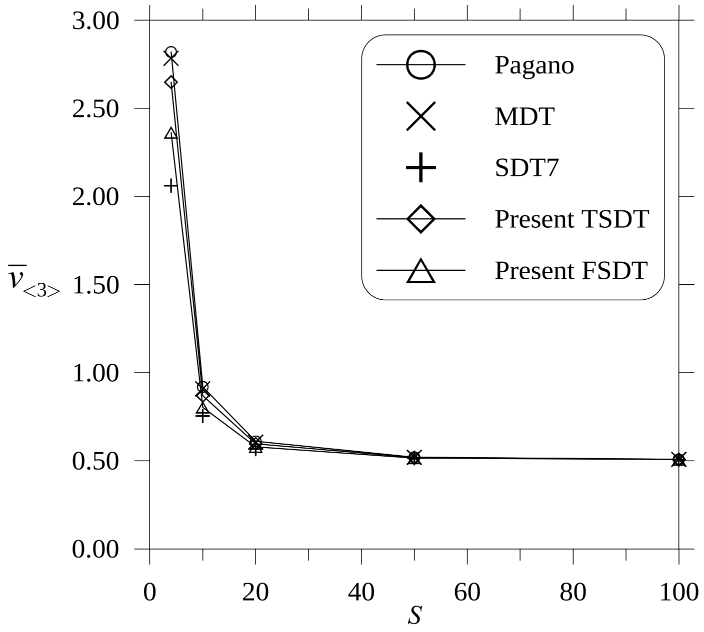

Fig. 3.5. Central deflection of a three-ply (0°/90°/0°) laminated rectangular plate vs. ratio *S*.

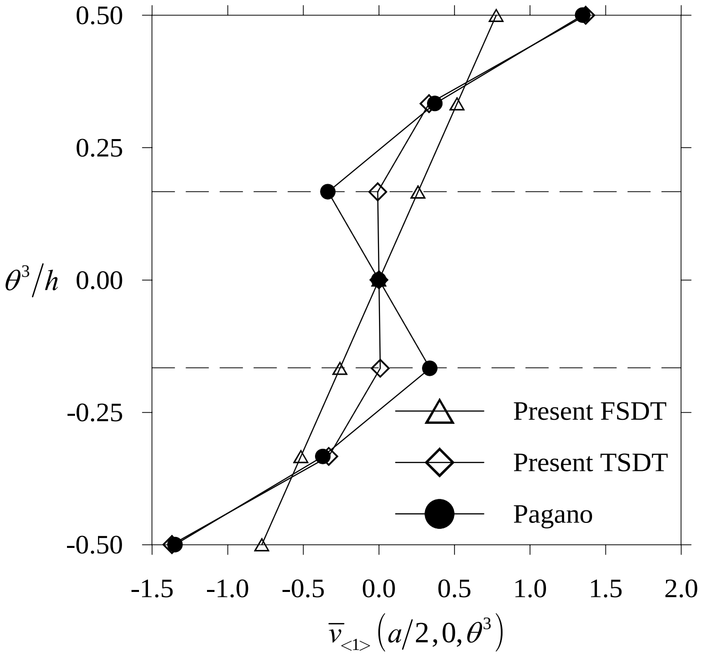

Fig. 3.6. Displacement distribution through the thickness $\bar{v}_{<1>}$ of a symmetric three-ply (0°/90°/0°) laminated rectangular plate (4×4*Q*25, *S* = 4).

Figure 3.6 shows through-the-thickness distribution of the in-plane dimensionless displacement $\bar{v}_{<1>}$ for the problem discussed above. We should point out two important facts from these results: first the zigzag effect arises visibly in thick cross-ply plates and second the TSDT (not the FSDT) can reproduce that effect with some degree of accuracy.

b. Cross-ply rectangular plates

Here we present finite element solutions for cross-ply laminated rectangular plates. This problem was analyzed analytically and numerically by Khdeir and Reddy [33]. They compared Lévy-type solutions with finite element results using different theories. Figure 3.7 shows the computational domain of the rectangular plate with its corresponding boundary conditions.

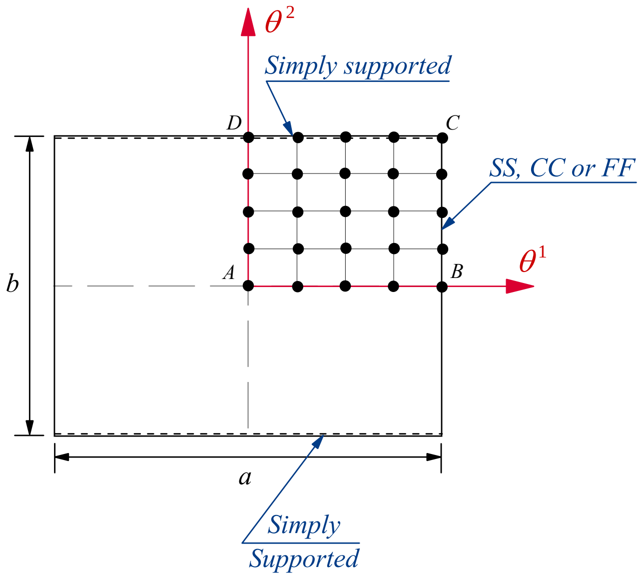

Fig. 3.7. Cross-ply laminated plate under sinusoidal load.

The edges $\theta^2 = \pm b/2$ are simply supported, while the remaining ones ($\theta^1 = \pm a/2$) may have arbitrary combination of free, clamped and simply supported edge conditions. For the purpose of comparison, the following lamina properties, typical of graphite-epoxy material, are used in the numerical examples

$$E_1/E_2 = 25, \quad G_{13} = G_{12} = 0.5E_2, \quad G_{23} = 0.2E_2, \quad \nu_{12} = 0.25\,.$$

The loading, in all cases, is assumed to be sinusoidal along each surface coordinate direction, i.e.

$$P^3 = q_0 \cos\left(\frac{\pi\theta^1}{a}\right)\cos\left(\frac{\pi\theta^2}{b}\right).$$

In the finite element analysis, meshes of 4×4 of Q25 and 2×2 of Q81 elements are used for the FSDT (with shear correction factor of $5/6$) and the TSDT. The notation *SS*, *CC* and *FF* stand for simply supported, clamped and free boundary conditions at the edge $\theta^1 = \pm a/2$. Because of the symmetry conditions of the problem, a quarter of the plate is chosen as computational domain. The boundary conditions are

At $\theta^1 = 0$ $\quad u_{<1>} = \varphi_{<1>} = \psi_{<1>} = 0$ (Symmetry)

At $\theta^2 = 0$ $\quad u_{<2>} = \varphi_{<2>} = \psi_{<2>} = 0$ (Symmetry)

At $\theta^2 = b/2$ $\quad u_{<1>} = u_{<3>} = \varphi_{<1>} = \psi_{<1>} = 0$ (SS)

At $\theta^1 = a/2$ $\quad u_{<2>} = u_{<3>} = \varphi_{<2>} = \psi_{<2>} = 0$ (SS)

At $\theta^1 = a/2$ $\quad u_{<1>} = u_{<2>} = u_{<3>} = \varphi_{<1>} = \varphi_{<2>} = \psi_{<1>} = \psi_{<2>} = 0$ (CC)

At $\theta^1 = a/2$ $\quad$ Free (FF).

Tables 3.6 to 3.9 show numerical results for deflections and stresses of cross-ply square plates for different number of layers, thickness and boundary conditions. The following dimensionless variables are utilized

$$\bar{v}_{<3>} = \frac{10^2 E_2}{q_0 b S^3} v_{<3>}(0,0,0), \qquad \bar{\sigma}_{<11>} = -\frac{10}{q_0 S^2} \sigma_{<11>}(0,0,-h/2)$$

$$\bar{\sigma}_{<22>} = \frac{10}{q_0 S^2} \sigma_{<22>}(0,0,h/2), \qquad \bar{\sigma}_{<23>} = -\frac{10}{q_0 S} \sigma_{<23>}(0,b/2,0)$$

where $S = b/h$.

In all cases finite element results are in good agreement with the corresponding analytical solutions specially the FSDT. It is also noticed that there is no presence of shear locking for meshes of 4×4*Q*25 or 2×2*Q*81 elements.

Table 3.6. Dimensionless central deflection $\bar{v}_{<3>}$ of cross-ply laminated square plates under sinusoidal loading (4×4*Q*25 and 2×2*Q*81, full integration).

Scheme	*S*	Theory	Type*	4×4*Q*25			2×2*Q*81		
				SS	CC	FF	SS	CC	FF
(0°/90°)	5	TSDT	NR	1.6852	1.1619	2.6597	1.6852	1.1619	2.6597
			AR	1.6670	1.0880	2.6240	1.6670	1.0880	2.6240
		FSDT	NR	1.7584	1.2565	2.7770	1.7584	1.2565	2.7770
			AR	1.7580	1.2570	2.7770	1.7580	1.2570	2.7770
	10	TSDT	NR	1.2197	0.6308	1.9996	1.2197	0.6308	1.9996
			AR	1.2160	0.6170	1.9920	1.2160	0.6170	1.9920
		FSDT	NR	1.2373	0.6563	2.0282	1.2373	0.6563	2.0282
			AR	1.2370	0.6560	2.0280	1.2370	0.6560	2.0280
(0°/90°)$_5$	5	TSDT	NR	1.1300	0.9159	1.6532	1.1300	0.9159	1.6532
			AR	1.1290	0.8790	1.6510	1.1290	0.8790	1.6510
		FSDT	NR	1.1365	0.9446	1.6628	1.1365	0.9446	1.6628
			AR	1.1370	0.9450	1.6630	1.1370	0.9450	1.6630
	10	TSDT	NR	0.6160	0.3817	0.9156	0.6160	0.3817	0.9156
			AR	0.6160	0.3750	0.9160	0.6160	0.3750	0.9160
		FSDT	NR	0.6154	0.3852	0.9148	0.6154	0.3852	0.9148
			AR	0.6150	0.3850	0.9150	0.6150	0.3850	0.9150

* NR corresponds to the present finite element solution and AN to the analytical solution obtained by Khdeir and Reddy [33].

Table 3.7. Dimensionless axial stress $\bar{\sigma}_{<11>}$ of cross-ply laminated square plates under sinusoidal loading (4×4Q25 and 2×2Q81, full integration).

Scheme	S	Theory	Type*	4×4Q25			2×2Q81		
				SS	CC	FF	SS	CC	FF
(0°/90°)	5	TSDT	NR	7.9285	4.8709	2.8488	7.9286	4.8709	2.8490
			AR	8.3850	5.6790	3.1710	8.3850	5.6790	3.1710
		FSDT	NR	7.1574	3.9104	2.4689	7.1575	3.9105	2.4691
			AR	7.1570	3.9110	2.4690	7.1570	3.9110	2.4690
	10	TSDT	NR	7.3630	4.7582	2.5530	7.3630	4.7583	2.5532
			AR	7.4680	4.9520	2.6240	7.4680	4.9520	2.6240
		FSDT	NR	7.1574	4.4504	2.4415	7.1575	4.4505	2.4417
			AR	7.1570	4.4500	2.4420	7.1570	4.4500	2.4420
$(0°/90°)_5$	5	TSDT	NR	6.2544	3.7551	2.3456	6.2545	3.7551	2.3458
			AR	6.3400	4.0250	2.4820	6.3400	4.0250	2.4820
		FSDT	NR	5.0091	2.2750	1.7118	5.0091	2.2750	1.7119
			AR	5.0090	2.2750	1.7120	5.0090	2.2750	1.7120
	10	TSDT	NR	5.3452	3.1691	1.9156	5.3453	3.1692	1.9157
			AR	5.3460	3.1930	1.9240	5.3460	3.1930	1.9240
		FSDT	NR	5.0091	2.6916	1.7225	5.0091	2.6917	1.7226
			AR	5.0090	2.6920	1.7230	5.0090	2.6920	1.7230

* NR corresponds to the present finite element solution and AN to the analytical solution obtained by Khdeir and Reddy [33].

Table 3.8. Dimensionless axial stress $\bar{\sigma}_{<22>}$ of cross-ply laminated square plates under sinusoidal loading (4×4*Q*25 and 2×2*Q*81, full integration).

Scheme	*S*	Theory	Type*	4×4*Q*25			2×2*Q*81		
				SS	CC	FF	SS	CC	FF
(0°/90°)	5	TSDT	NR	7.9285	5.5102	12.868	7.9286	5.5103	12.868
			AR	8.3850	5.5050	13.551	8.3850	5.5050	13.551
		FSDT	NR	7.1574	5.1525	11.907	7.1575	5.1525	11.907
			AR	7.1570	5.1530	11.907	7.1570	5.1530	11.907
	10	TSDT	NR	7.3630	3.8223	12.135	7.3630	3.8223	12.135
			AR	7.4680	3.8030	12.295	7.4680	3.8030	12.295
		FSDT	NR	7.1574	3.7991	11.884	7.1575	3.7992	11.884
			AR	7.1570	3.7990	11.884	7.1570	3.7990	11.884
$(0°/90°)_5$	5	TSDT	NR	6.2544	5.1043	9.3494	6.2545	5.1044	9.3496
			AR	6.3400	4.9630	9.4540	6.3400	4.9630	9.4540
		FSDT	NR	5.0091	4.2116	7.5824	5.0091	4.2116	7.5825
			AR	5.0090	4.2120	7.5830	5.0090	4.2120	7.5830
	10	TSDT	NR	5.3452	3.3132	8.0054	5.3453	3.3132	8.0055
			AR	5.3460	3.2600	8.0050	5.3460	3.2600	8.0050
		FSDT	NR	5.0091	3.1354	7.5330	5.0091	3.1355	7.5331
			AR	5.0090	3.1350	7.5330	5.0090	3.1350	7.5330

* NR corresponds to the present finite element solution and AN to the analytical solution obtained by Khdeir and Reddy [33].

Table 3.9. Dimensionless transverse shear stress $\bar{\sigma}_{<23>}$ of cross-ply laminated square plates under sinusoidal loading (4×4*Q*25 and 2×2*Q*81, full integration).

Scheme	*S*	Theory	Type*	4×4*Q*25			2×2*Q*81		
				SS	CC	FF	SS	CC	FF
(0°/90°)	5	TSDT	NR	2.9339	2.0425	4.1098	2.9340	2.0425	4.1100
			AR	3.1550	2.0950	4.4570	3.1550	2.0950	4.4570
		FSDT	NR	2.7283	1.9579	3.9008	2.7284	1.9580	3.9010
			AR	2.7290	1.9280	3.9010	2.7290	1.9280	3.9010
	10	TSDT	NR	2.9775	1.6412	4.1435	2.9778	1.6413	4.1439
			AR	3.1900	1.7250	4.4890	3.1900	1.7250	4.4890
		FSDT	NR	2.7281	1.5228	3.8818	2.7284	1.5230	3.8822
			AR	2.7290	1.5230	3.8820	2.7290	1.5230	3.8820
(0°/90°)$_5$	5	TSDT	NR	3.3222	2.6696	4.7348	3.3223	2.6697	4.7349
			AR	3.3620	2.6010	4.7840	3.3620	2.6010	4.7840
		FSDT	NR	2.7283	2.2472	3.8836	2.7284	2.2472	3.8836
			AR	2.7290	2.2480	3.8830	2.7290	2.2480	3.8830
	10	TSDT	NR	3.4057	2.1112	4.8136	3.4059	2.1112	4.8138
			AR	3.4080	2.0830	4.8140	3.4080	2.0830	4.8140
		FSDT	NR	2.7282	1.7079	3.8530	2.7284	1.7080	3.8532
			AR	2.7290	1.7080	3.8530	2.7290	1.7080	3.8530

* NR corresponds to the present finite element solution and AN to the analytical solution obtained by Khdeir and Reddy [33].

c. Functionally graded square plates

Next, we consider some bending solutions for functionally graded square plates. The boundary conditions are the same as those of the last example (simply-supported). For this problem the underlined term in (3.7) is taken into account in the formulation. Young's modulus and Poisson's ratio for zirconia (ceramic material) and aluminium (metal material) are the following

$$E_c = 151\,GPa, \quad \nu_c = 0.3, \quad E_m = 70\,GPa, \quad \nu_m = 0.3$$

respectively. The non-dimensional quantities are given by

$$\bar{v}_{<3>} = \frac{E_m}{q_0\,h\,S^4}\,v_{<3>}, \qquad \bar{v}_{<\alpha>} = \frac{E_m}{q_0\,h\,S^3}\,v_{<\alpha>}$$

$$\bar{\sigma}_{<\alpha\beta>} = \frac{1}{q_0\,S^2}\,\sigma_{<\alpha\beta>}, \quad \bar{\sigma}_{<\alpha 3>} = \frac{1}{q_0\,S}\,\sigma_{<\alpha 3>}\,.$$

In Table 3.10, central deflection and in-plane stress results for functionally graded plates under sinusoidal loading are tabulated for different side-to-thickness ratios S and two volume fraction exponents. It is observed slight differences between the present FSDT and TSDT results. They increase when ratio S decreases (thick plates). We also illustrate, in Figures 3.8 and 3.9, the effect of the volume fraction exponent on the central deflection of FGM square plates for different ratios S under sinusoidal and uniformly loading respectively. Again, small differences between both formulations increases for thick plates (S = 4) and volume fraction exponents 4 to 8.

Finally, Figures 3.10 to 3.17 show through-the-thickness distributions of in-plane displacements, membrane and transverse shear stresses for FGM square plates under sinusoidal loading for various volume fraction exponents and ratios S = 4, 100.

Table 3.10. Central deflection and in-plane stresses of FGM square plates under sinusoidal loading (4×4Q25).

S		Present TSDT		Present FSDT	
		$n = 0.5$	$n = 2.0$	$n = 0.5$	$n = 2.0$
4	$\bar{v}_{<3>}(0,0,0)$	0.022114	0.027577	0.022189	0.027404
10		0.017496	0.021448	0.017505	0.021415
20		0.016834	0.020568	0.016836	0.020560
50		0.016648	0.020321	0.016648	0.020320
100		0.016622	0.020286	0.016622	0.020286
4	$\bar{\sigma}_{<11>}\left(0,0,\frac{h}{2}\right)$	0.244374	0.283599	0.230626	0.265405
10		0.232874	0.268379	0.230627	0.265406
20		0.231193	0.266155	0.230628	0.265407
50		0.230727	0.265536	0.230635	0.265414
100		0.230666	0.265454	0.230642	0.265423
4	$\bar{\sigma}_{<22>}\left(0,0,-\frac{h}{6}\right)$	-0.046763	-0.063841	-0.049238	-0.067535
10		-0.048834	-0.066931	-0.049238	-0.067535
20		-0.049137	-0.067383	-0.049238	-0.067535
50		-0.049223	-0.067512	-0.049240	-0.067537
100		-0.049237	-0.067533	-0.049241	-0.067539
4	$\bar{\sigma}_{<12>}\left(\frac{a}{2},\frac{b}{2},\frac{h}{2}\right)$	-0.131586	-0.152707	-0.124183	-0.142910
10		-0.125393	-0.144511	-0.124183	-0.142910
20		-0.124487	-0.143312	-0.124183	-0.142910
50		-0.124232	-0.142975	-0.124184	-0.142911
100		-0.124197	-0.142928	-0.124185	-0.142912

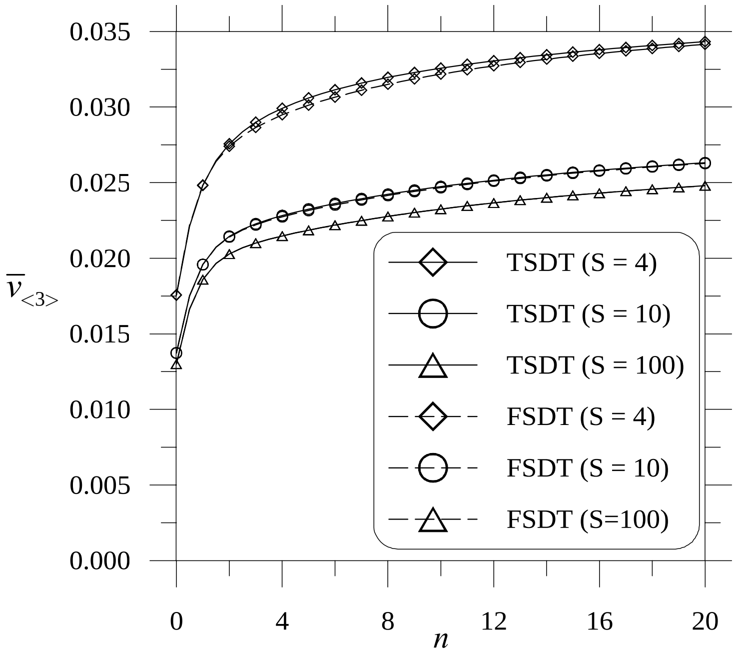

Fig. 3.8. Central deflection $\bar{v}_{<3>}$ versus the volume fraction exponent n for FGM square plates under sinusoidal load.

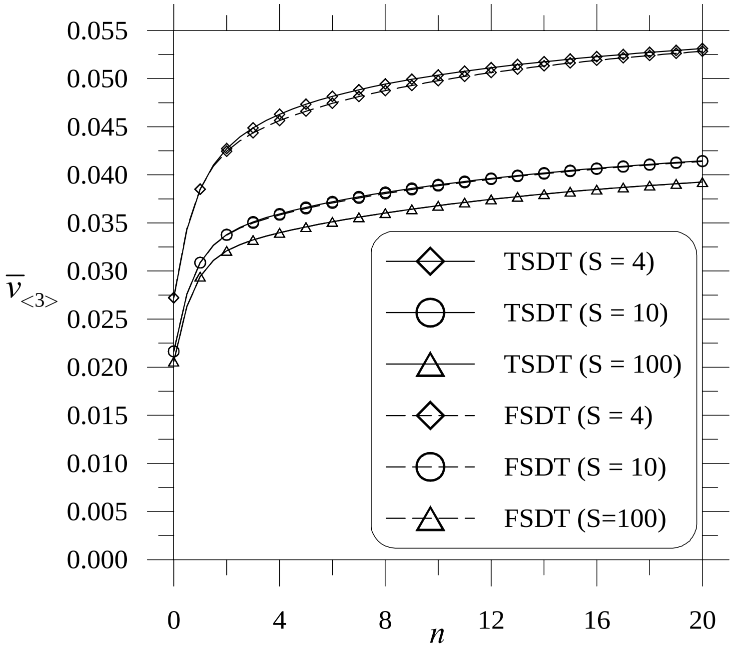

Fig. 3.9. Central deflection $\bar{v}_{<3>}$ versus the volume fraction exponent n for FGM square plates under uniform load.

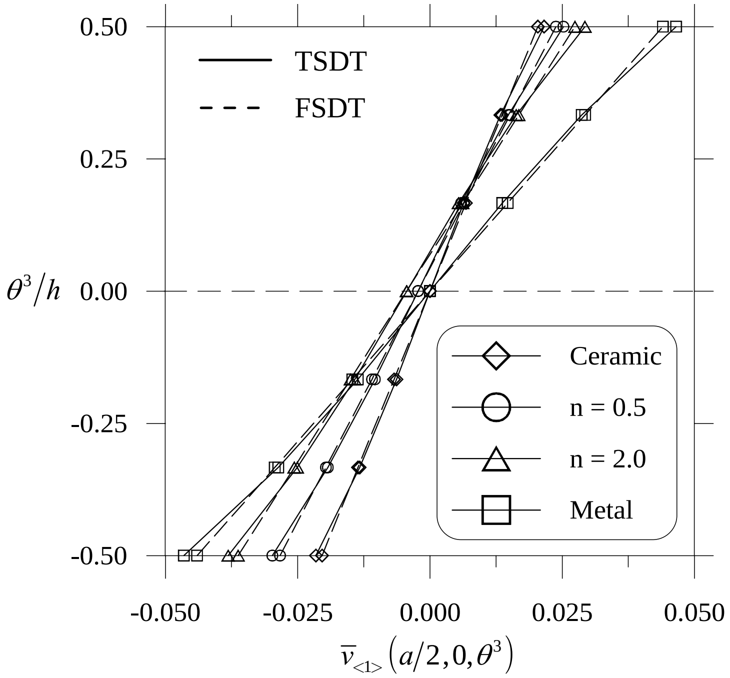

Fig. 3.10. Displacement distribution through the thickness $\bar{v}_{<1>}$ for FGM plates ($S = 4$).

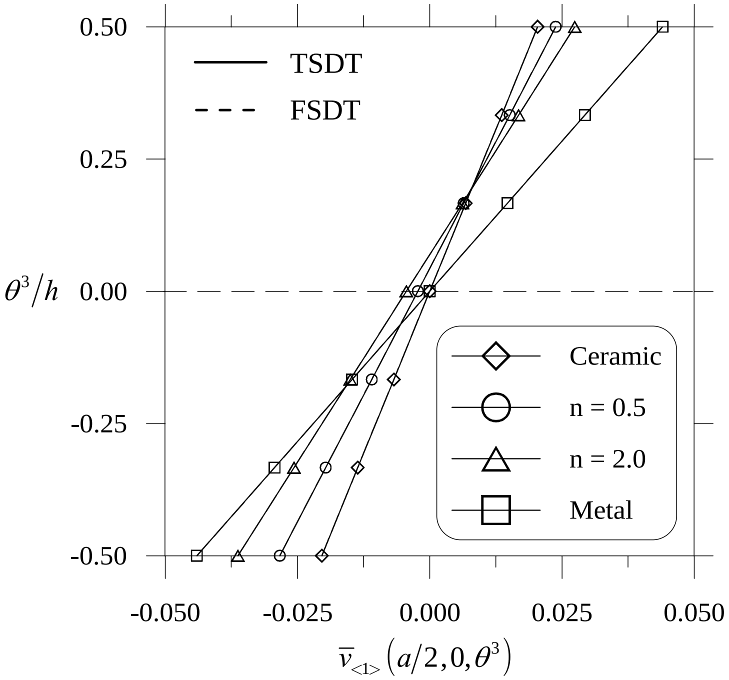

Fig. 3.11. Displacement distribution through the thickness $\bar{v}_{<1>}$ for FGM plates (S=100).

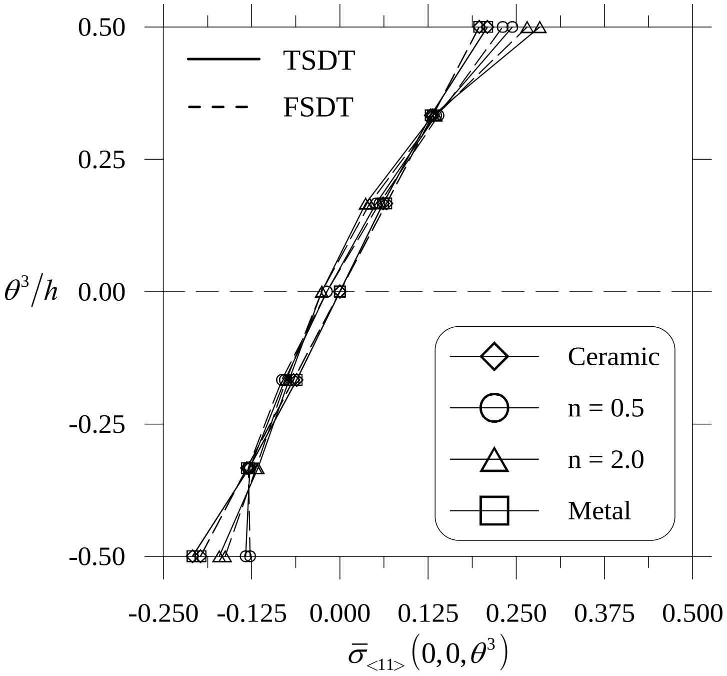

Fig. 3.12. Stress distribution through the thickness $\bar{\sigma}_{<11>}$ for FGM plates (S = 4).

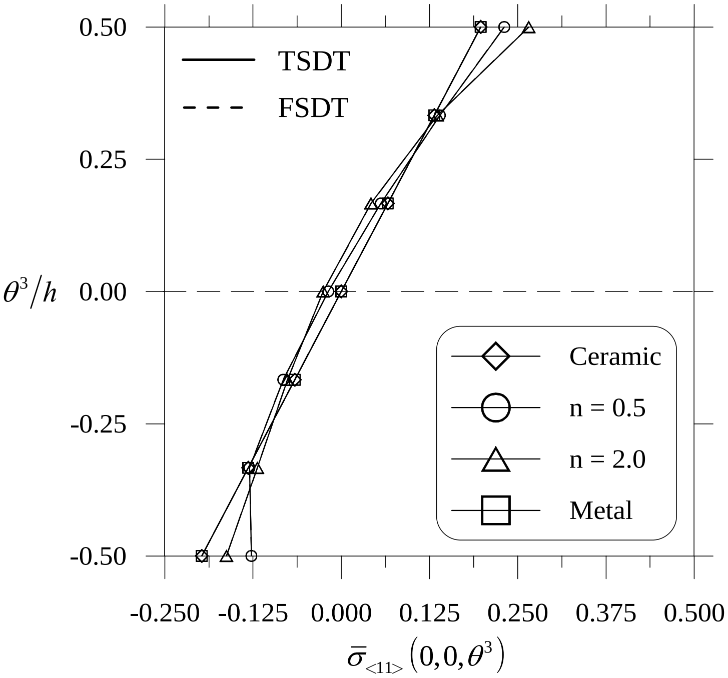

Fig. 3.13. Stress distribution through the thickness $\bar{\sigma}_{<11>}$ for FGM plates (S = 100).

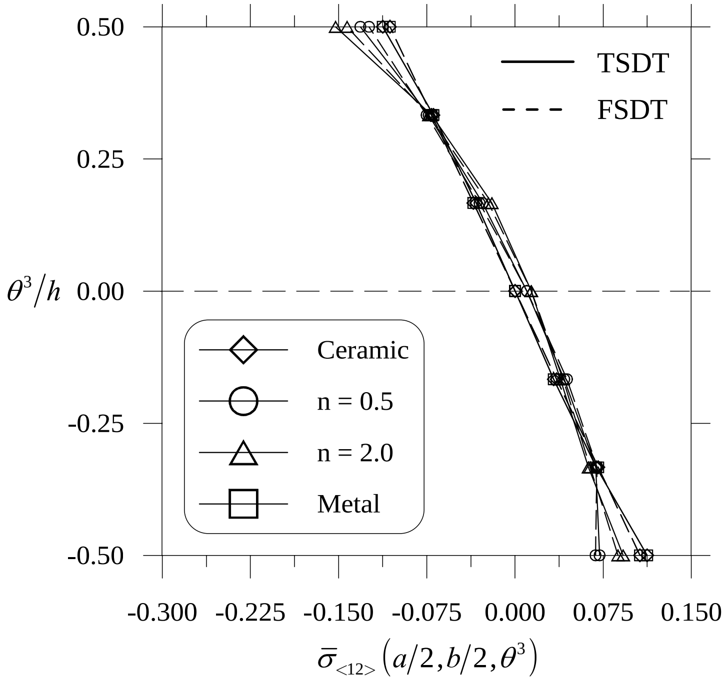

Fig. 3.14. Stress distribution through the thickness $\bar{\sigma}_{<12>}$ for FGM plates (S = 4).

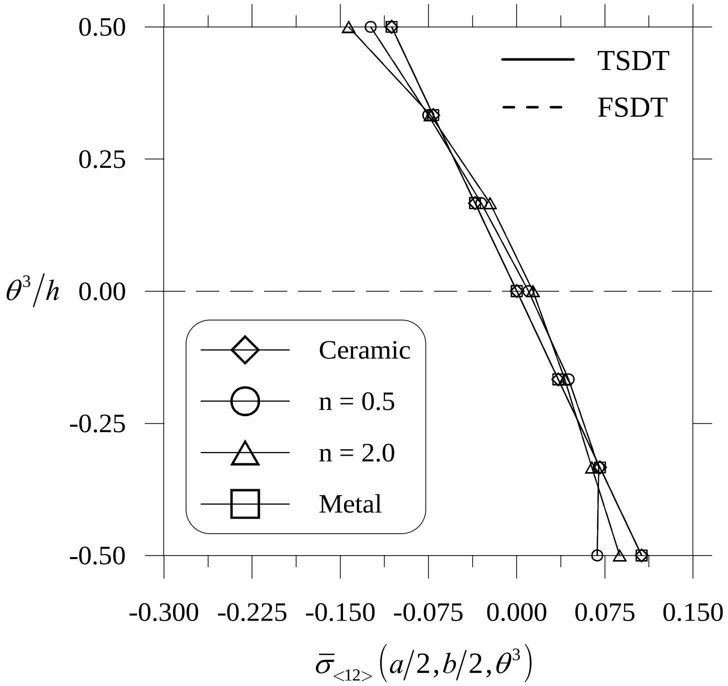

Fig. 3.15. Stress distribution through the thickness $\bar{\sigma}_{<12>}$ for FGM plates (S = 100).

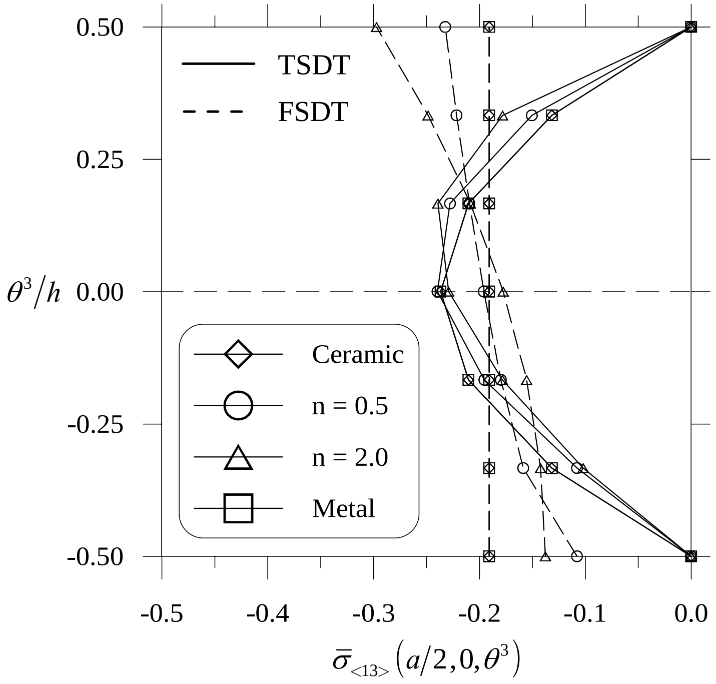

Fig. 3.16. Stress distribution through the thickness $\bar{\sigma}_{<13>}$ for FGM plates (S = 4).

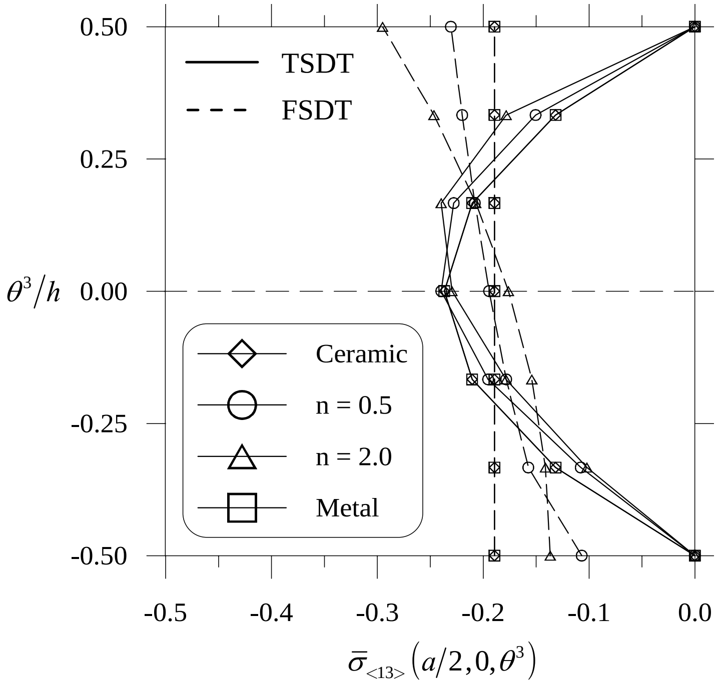

Fig 3.17. Stress distribution through the thickness $\bar{\sigma}_{<13>}$ for FGM plates (S = 100).

We notice that both theories converge to each other when the ratio S increases. Also, there is no presence of the zigzag effect in the through-the-thickness distribution of the in-plane displacement even for thick plates. Both cases, thin and thick plates (S = 4 and 100 respectively) show similar pattern of curves. In-plane stress distribution through the thickness does not exhibit, as expected, any discontinuity (stress concentration like laminated plates). Major differences between the FSDT and TSDT are observed in the transverse shear stress through-the-thickness distributions as illustrated in Figures 3.16 and 3.17. Definitely, the FSDT cannot neither reproduce the quasi-parabolic behavior of the transverse shear stress nor satisfy the tangential traction-free conditions in the bottom and top planes of the plate. This is one of the main advantages of the TSDT over the FSDT. In all through-the-thickness distributions of stresses we note that fully metal and fully ceramic plates give the same results. This is understandable since we are considering linear behavior. Stresses depend on the loading and geometry but not material properties.

2. Cylindrical shells

a. Clamped shallow panel

The first cylindrical shell problem to be considered is a clamped shallow panel under pressure load (Palazotto and Dennis [77]). This problem exhibits strong shear locking (ratio R/h = 800). Because of the symmetry of the problem, a quarter of the panel is considered as computational domain (Fig. 3.18). The geometric and material data for the problem are

$$\begin{aligned}&E = 0.45\times10^{6}\ psi, \quad \nu = 0.3\\ &a = 20\,in, \quad R = 100\,in, \quad h = 0.125\,in, \quad \alpha = 0.1 rad\ .\end{aligned}$$

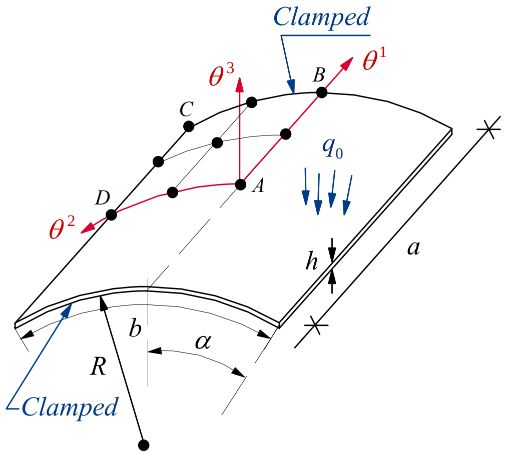

Fig. 3.18. Clamped cylindrical shell under uniformly transverse load.

The panel is subjected to uniform transverse load $q_0 = 0.04\,psi$ with the following boundary conditions

At $\theta^1 = 0$ $\quad u_{<1>} = \varphi_{<1>} = \psi_{<1>} = 0$ (Symmetry)

At $\theta^2 = 0$ $\quad u_{<2>} = \varphi_{<2>} = \psi_{<2>} = 0$ (Symmetry)

At $\theta^1 = a/2,\ \theta^2 = \alpha$ $\quad u_{<i>} = \varphi_{<\alpha>} = \psi_{<\alpha>} = 0$.

Two sets of uniform meshes are used in the analysis (one with 81 nodes and other with 289 nodes). Vertical displacements at the center of the shell for various p levels and integration rules are tabulated in Table 3.11 for the TSDT as well as the FSDT. For this problem, Palazotto and Dennis [77] reported the vertical deflection at the center as $0.01144\,in$ and Brebbia and Connor [78] reported $0.011\,in$. The results obtained for the $Q4$ element with full integration show strong presence of shear locking. Selective or reduced integrations for these cases are, in general, in good agreement with those cited before. On the other hand, high-order elements ($Q25$ and $Q81$) perform very well under shear locking and give excellent results using full integration.

Table 3.11. Vertical deflection at the center of the clamped cylindrical panel under uniformly transverse load ($-u_{<3>} \times 10^{2}$ *in*).

p level		Mesh of 81 nodes			Mesh of 289 nodes		
		Full integration	Selective integration	Reduced integration	Full integration	Selective integration	Reduced integration
1	TSDT	0.294404	1.156251	1.157727	0.690335	1.140095	1.140459
	FSDT	0.337791	1.156233	1.157720	0.745615	1.140085	1.140457
2	TSDT	1.172442	1.135172	1.135228	1.142842	1.134908	1.134908
	FSDT	1.172160	1.135157	1.135219	1.142721	1.134901	1.134906
4	TSDT	1.134782	1.134897	1.134896	1.134892	1.134894	1.134892
	FSDT	1.134775	1.134888	1.134885	1.134888	1.134889	1.134890
8	TSDT	1.134895	1.134883	1.134889	1.134892	1.134892	1.134893
	FSDT	1.134888	1.134878	1.134876	1.134890	1.134889	1.134889

b. Barrel vault

This benchmark is also well-known as the Scordelis-Lo roof (Fig. 3.19). The first authors to present a solution for this problem appear to be Cantin and Clough [56] (using $\nu = 0.3$ instead of zero). They compared their results with those obtained by the program of Scordelis and Lo [79] for cylindrical shallow shells. An analytical solution was obtained by Gibson [80] who reported the vertical displacement at the center of the free edge as $3.70331\,in$ (see also Ashwell [81]). For deep shell, other authors give a value of $3.6288\ in$ for the vertical deflection (see Simo et al. [82]). We adopt the latter result as the reference solution for this example (w_{ref}). The geometric and material data for the problem are the following

$$E = 3\times10^{6}\ psi, \quad \nu = 0.0$$
$$a = 600\,in, \quad R = 300\,in, \quad h = 3\,in, \quad \alpha = 0.6981\,rad.$$

The dead weight loading $(q_0 = 0.625\,psi)$ can be expressed in components of θ^2 as

$$P^2 = q_0 \sin\left(\theta^2\right), \qquad P^3 = -q_0 \cos\left(\theta^2\right).$$

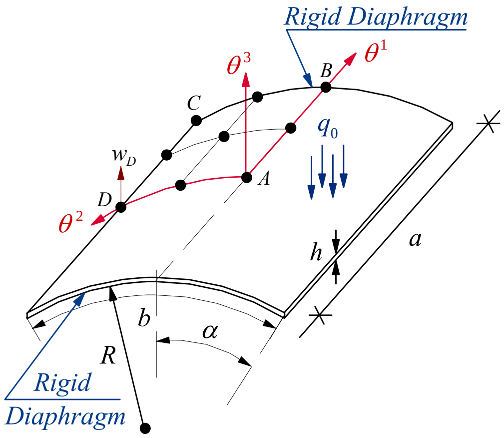

Fig. 3.19. Barrel vault benchmark with dead weight load.

Finally, the boundary conditions on the computational domain are

$$\text{At } \theta^1 = 0 \qquad u_{<1>} = \varphi_{<1>} = \psi_{<1>} = 0 \quad \text{(Symmetry)}$$

$$\text{At } \theta^2 = 0 \qquad u_{<2>} = \varphi_{<2>} = \psi_{<2>} = 0 \quad \text{(Symmetry)}$$

$$\text{At } \theta^1 = a/2 \qquad u_{<2>} = u_{<3>} = \varphi_{<2>} = 0\,.$$

Here, we are considering free boundary conditions at $\theta^2 = \alpha$.

The vertical deflection at the point *D* for uniform meshes of 289 nodes and 1089 nodes with different *p* levels is reported in Table 3.12. The analysis is carried out for the TSDT and FSDT with various integration rules. It is clearly shown that shear and membrane locking is avoided by using high-order elements (*Q*25 and *Q*81). Again, results obtained with selective and reduced integration are in close agreement with those with meshes of 8×8*Q*25 and 4×4*Q*81 with full integration.

The vertical deflection of the line *AD* and axial displacement of the line *BC* are depicted in Figures 3.20 and 3.21 and compared with those of Gibson [80].

Table 3.12. Vertical deflection at the center of the free edge ($-w_D\, in$) of the Barrel vault.

p level		Mesh of 289 nodes Full integration	Mesh of 289 nodes Selective integration	Mesh of 289 nodes Reduced integration	Mesh of 1089 nodes Full integration	Mesh of 1089 nodes Selective integration	Mesh of 1089 nodes Reduced integration
1	TSDT	0.838487	3.247487	3.622260	1.726715	3.517603	3.620960
	FSDT	0.897689	3.247861	3.618373	1.830634	3.517676	3.617874
2	TSDT	3.591876	3.613964	3.622168	3.611742	3.617631	3.620785
	FSDT	3.591688	3.614232	3.617881	3.611326	3.617452	3.617682
4	TSDT	3.612094	3.617789	3.622350	3.615259	3.618267	3.620811
	FSDT	3.611798	3.617730	3.617731	3.614648	3.617669	3.617670
8	TSDT	3.614360	3.618341	3.622618	3.617565	3.618798	3.620846
	FSDT	3.613857	3.617779	3.617780	3.616582	3.617669	3.617670

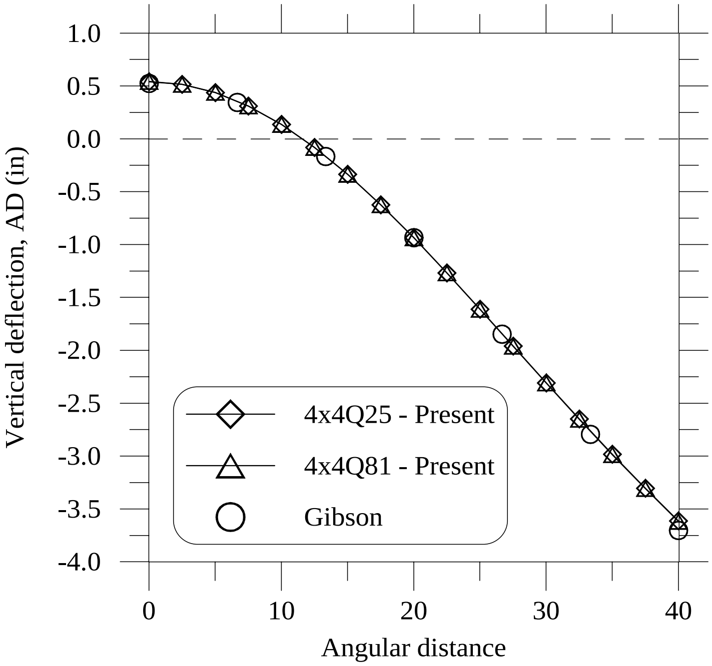

Fig. 3.20. Vertical deflection of the curve *AD* of the Barrel vault.

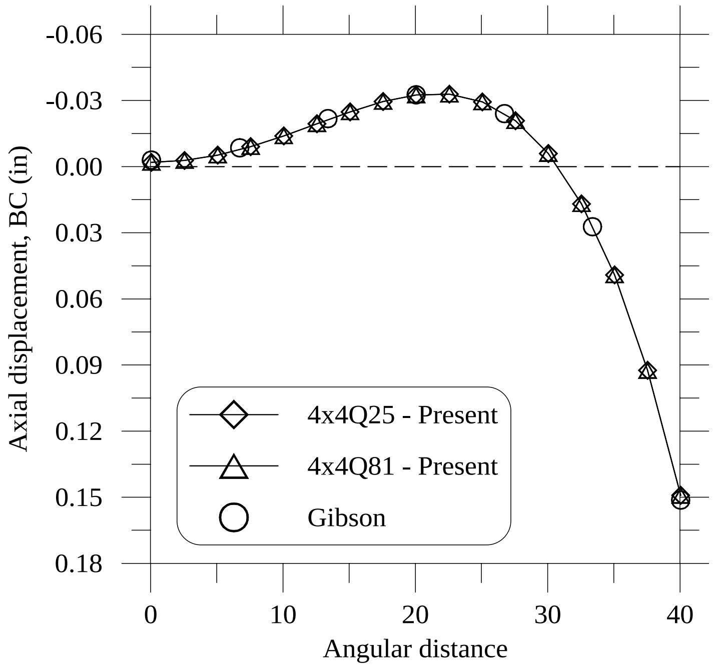

Fig. 3.21. Axial displacement $u_{<1>}$ of the curve *BC* of the Barrel vault.

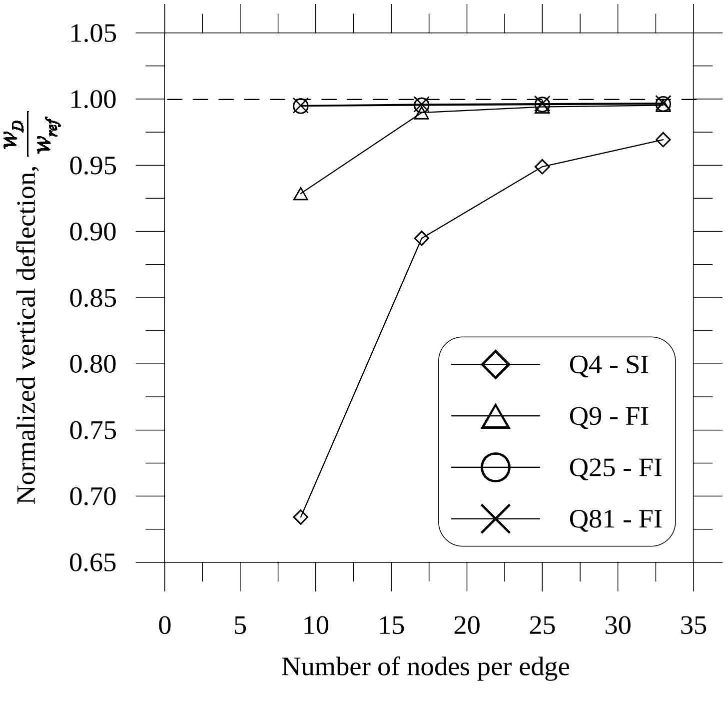

Fig. 3.22. Convergence of the vertical deflection w_D at the center of the free edge of the Barrel vault.

To illustrate the performance of the elements *Q*25 and *Q*81, we show in Fig. 3.22 the convergence analysis of the vertical deflection at the center of the free edge for different *p* levels (all results for the TSDT). We note that an excellent rate of convergence is achieved if high-order elements are employed.

c. *Pinched cylinder with rigid diaphragms*

Another well-known isotropic benchmark for cylindrical shells is the pinched cylinder with end diaphragms depicted in Figure 3.23. It has been used by many researchers and is identified as one of the most severe tests for both inextensional bending and complex membrane states. The pinched shell is supported at each end by rigid diaphragms and loaded by two opposed forces acting at midpoint of the shell. Due to the symmetry condition of the structure, an octant of the cylinder is considered as computational domain.

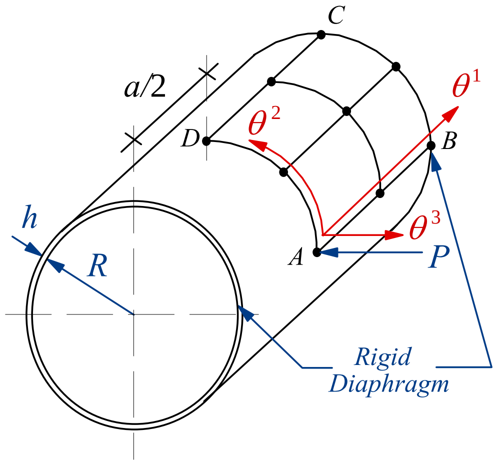

Fig. 3.23. Geometry of the pinched circular cylinder with end diaphragms.

The following geometrical data and material properties are used

$$E = 3\times10^6\ psi, \quad \nu = 0.3$$
$$a = 600\,in, \quad R = 300\,in, \quad h = 3\,in, \quad \alpha = \pi/2\ rad$$

with load $P = 1.0\ lb$ and boundary conditions as shown

$$\text{At } \theta^1 = 0 \qquad u_{<1>} = \varphi_{<1>} = \psi_{<1>} = 0 \quad \text{(Symmetry)}$$

$$\text{At } \theta^2 = 0,\ \alpha \qquad u_{<2>} = \varphi_{<2>} = \psi_{<2>} = 0 \quad \text{(Symmetry)}$$

$$\text{At } \theta^1 = a/2 \qquad u_{<2>} = u_{<3>} = \varphi_{<2>} = 0\,.$$

In Table 3.13 we present results for the radial displacement at the point A with meshes of 289 nodes and 1089 nodes and different p levels. The analytical solution given by Flügge [83] is -1.8248×10^{-5} *in*. However, because Flügge neglected the shear deformation (classical shell theory) in contrast with the present formulation, we adopt as the reference solution (w_{ref}) the value reported by Cho and Roh [7] which is -1.8541×10^{-5} *in*. It is observed that the rate of convergence is slower than those obtained for the Barrel vault. Results for $Q4$ and $Q9$ elements with full integration are far from the reference solution cited before, even for meshes with 1089 nodes. Conversely, we see very good convergence ratios for the $Q25$ and $Q81$ elements. In all cases, selective and reduced integrations overestimate the displacement at the point load.

Figures 3.24 and 3.25 show a convergence study for the radial displacement at the point A and the axial displacement u_B ($u_{ref} = -4.5711\times10^{-7}$ *in*) using different p levels and elements. Again, all results are obtained using the TSDT. In both cases, the locking is overcome by using high-order elements. It is also noted that the convergence of the axial displacement u_B is faster than w_A.

Finally, Fig. 3.26 shows a comparison between the radial deflection distribution of the line DC with meshes of $4\times4Q25$ and $4\times4Q81$ for the present TSDT formulation and the element 8-URI of Kreja et al. [84]. This particular example can be treated as the most severe one for the problem considered and is rarely noted in the literature. We note that full integration with high p levels gives, in general, excellent results minimizing the membrane and shear locking. The result reported for the displacement w_D is 5.22×10^{-8} *in* [85]. All results suggest using at least meshes of 4×4Q25 elements to avoid locking.

Table 3.13. Radial displacement at A ($-u_{<3>}\times10^{5}$ *in*) of the pinched cylinder.

		Mesh of 289 nodes			Mesh of 1089 nodes		
p level		Full integration	Selective integration	Reduced integration	Full integration	Selective integration	Reduced integration
1	TSDT	0.251812	1.774684	1.858685	0.550182	1.840790	1.866632
	FSDT	0.278551	1.779810	1.861183	0.601829	1.846633	1.870120
2	TSDT	1.216584	1.836614	1.858427	1.678857	1.859622	1.865619
	FSDT	1.224521	1.841271	1.860786	1.685528	1.864953	1.868865
4	TSDT	1.755459	1.848284	1.857482	1.832276	1.861194	1.864758
	FSDT	1.758577	1.852522	1.859767	1.834672	1.866060	1.867858
8	TSDT	1.831581	1.852502	1.856828	1.846517	1.862194	1.864251
	FSDT	1.833630	1.856177	1.859076	1.848246	1.866501	1.867271

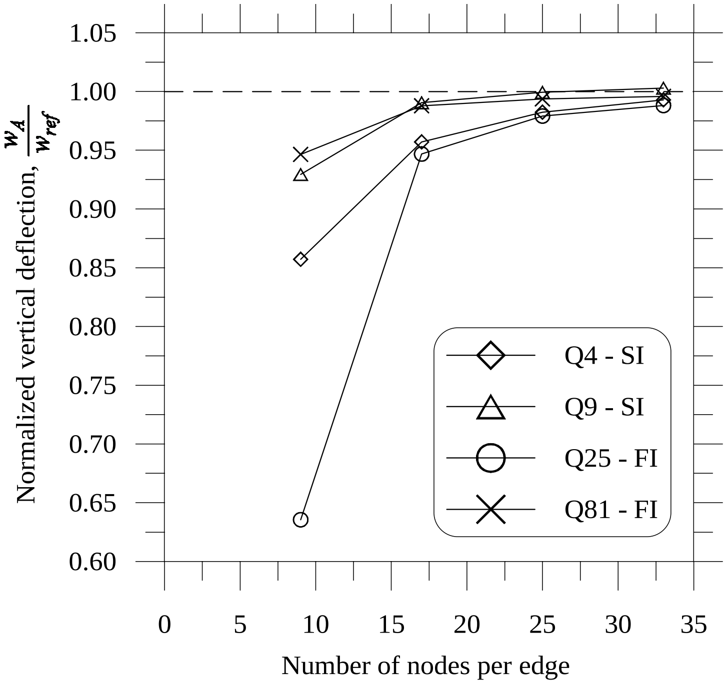

Fig. 3.24. Convergence of the radial displacement $u_{<3>}$ at the point *A* of the pinched cylinder.

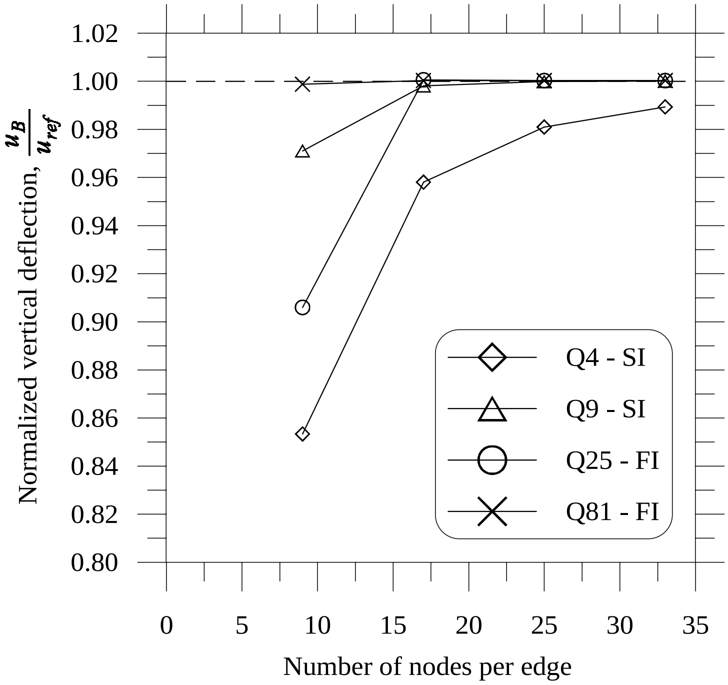

Fig. 3.25. Convergence of the axial displacement u_B of the pinched cylinder.

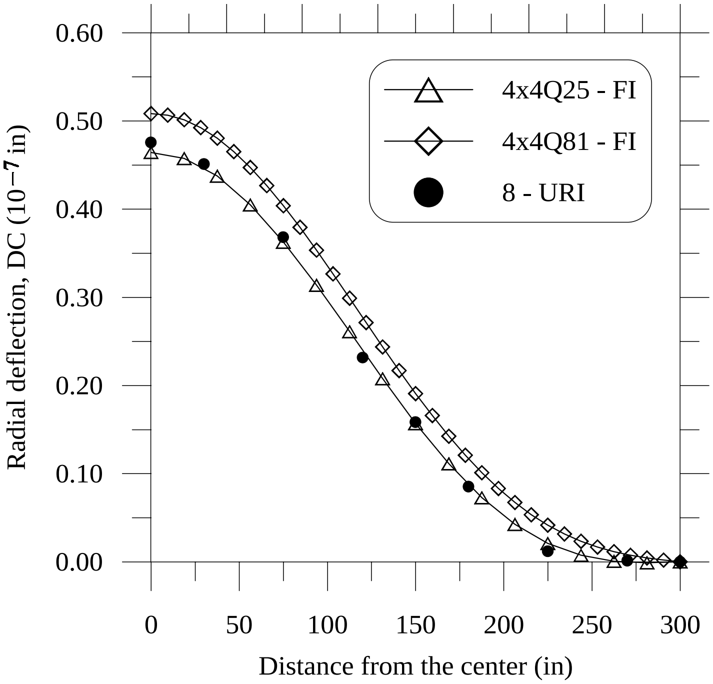

Fig. 3.26. Radial displacement distribution of the line *DC* of the pinched cylinder.

d. Cross-ply laminated cylinder

Now, bending behavior of laminated cylindrical shells is studied. We consider a simply-supported cross-ply cylinder under internal sinusoidal pressure (Fig. 3.27). The problem was solved analytically by Varadan and Bhaskar [86] using the 3D elasticity theory. Because of symmetry conditions, a panel of length *a*, angle 2α and radius *R* is analyzed with simply supported boundary conditions at edges $\theta^1 = 0, a$ and $\theta^2 = 0, 2\alpha$.

The dimensionless material properties and geometrical data are the following

$$
\begin{aligned}
&E_1/E_2 = 25, \quad G_{13} = G_{12} = 0.5E_2 \\
&G_{23} = 0.2E_2, \quad \nu_{12} = 0.25 \\
&a/R = 4, \quad R/h = S, \quad \alpha = \pi/8.
\end{aligned}
$$

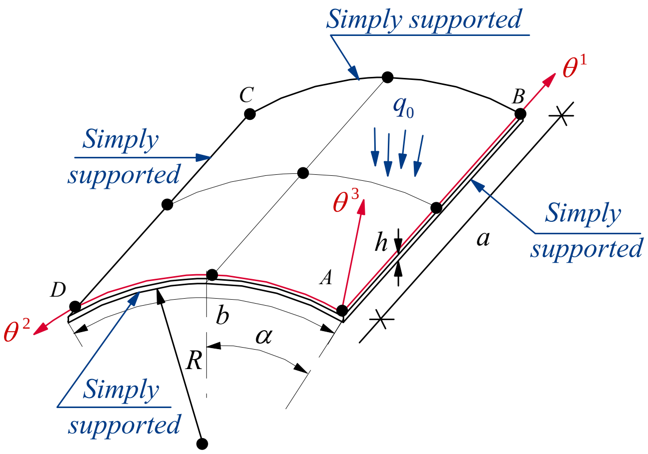

Fig. 3.27. Cross-ply cylinder with simply-supported ends.

The sinusoidal load can be expressed as

$$P^3 = q_0 \sin\left(\frac{\pi\theta^1}{a}\right)\sin\left(\frac{\pi\theta^2}{2\alpha}\right).$$

Since the effect of the laminate in bending response is unknown, full panel is considered as computational domain. The imposed simply-supported boundary conditions are

At $\theta^1 = 0, a$ $\quad u_{<2>} = u_{<3>} = \varphi_{<2>} = \psi_{<2>} = 0$

At $\theta^2 = 0, 2\alpha$ $\quad u_{<1>} = u_{<3>} = \varphi_{<1>} = \psi_{<1>} = 0$.

Tables 3.14 to 3.17 show results of the present FSDT and TSDT formulations compared with the 3D analytical solutions of Varadan and Bhaskar [86] and the exact closed-form bending solutions of Cheng et al. [87] (for perfectly bonded layers). The results are tabulated for the dimensionless central deflection and stresses of cross-ply panels (four different kinds of laminates) and considering ratios $S = 4, 10, 50, 100, 500$. The following quantities are introduced

$$\bar{v}_{<\alpha>} = \frac{10\,E_1}{q_0\,R\,S^2}\,v_{<\alpha>}, \qquad \bar{v}_{<3>} = \frac{10\,E_1}{q_0\,R\,S^3}\,v_{<3>}$$

$$\bar{\sigma}_{<\alpha\beta>} = \frac{10}{q_0\,S^2}\,\sigma_{<\alpha\beta>}\,.$$

A mesh of 4×4*Q*25 is used in the full panel and the stiffness coefficients are evaluated using full integration. We observe that both theories give good results compared to the 3D solutions. As we expected, these results diverge from the analytical solution when we have lower ratio *S*. In general, the TSDT appears to be more accurate than the FSDT especially for thick shells.

Figures 3.28 to 3.36 show through-the-thickness distributions of in-surface displacements and bending stresses for the three-ply ($90^o/0^o/90^o$) laminated shell with ratios $S = 4, 10, 100$. Three theories, present FSDT and TSDT, and the 3D solutions of Varadan, are compared. Again, we note a better performance of the TSDT over the FSDT (thickness distributions of displacements and stresses) for thick panels with $S = 4, 10$; as it is clearly seen in figures 3.28 and 3.31.

Table 3.14. Central deflection and stresses of a single-ply (90°) laminated circular cylindrical panel under sinusoidal loading (4×4*Q*25, full integration).

S		Ref. [86]	Present TSDT	Present FSDT
4	$\bar{v}_{<3>}\left(\frac{a}{2},\alpha,0\right)$	2.7830	2.98884	3.13878
10		0.9189	0.94796	0.94958
50		0.5385	0.54275	0.54262
100		0.5170	0.51883	0.51879
500		0.3060	0.30606	0.30606
4	$\bar{\sigma}_{<11>}\left(\frac{a}{2},\alpha,\frac{h}{2}\right)$	0.0981	0.09229	0.07940
10		0.0663	0.06647	0.06112
50		0.0845	0.08500	0.08451
100		0.1190	0.11943	0.11924
500		0.2459	0.24640	0.24639
4	$\bar{\sigma}_{<11>}\left(\frac{a}{2},\alpha,-\frac{h}{2}\right)$	-0.2295	-0.09150	-0.05780
10		-0.0656	-0.04530	-0.04021
50		-0.0086	-0.00791	-0.00795
100		0.0288	0.02905	0.02898
500		0.1924	0.19250	0.19249
4	$\bar{\sigma}_{<22>}\left(\frac{a}{2},\alpha,\frac{h}{2}\right)$	4.8590	4.50830	3.12988
10		4.0510	4.17300	3.64722
50		3.9020	3.94390	3.89663
100		3.8430	3.87300	3.85435
500		2.3060	2.35160	2.34976
4	$\bar{\sigma}_{<22>}\left(\frac{a}{2},\alpha,-\frac{h}{2}\right)$	-6.9690	-8.03680	-4.75957
10		-4.5090	-4.79990	-4.30457
50		-3.9790	-4.01090	-4.01432
100		-3.8760	-3.88490	-3.89186
500		-2.2930	-2.28300	-2.28437
4	$\bar{\sigma}_{<12>}\left(0,0,\frac{h}{2}\right)$	-0.0925	-0.07165	-0.07330
10		-0.0436	-0.03910	-0.03745
50		-0.0243	-0.02379	-0.02362
100		-0.0161	-0.01586	-0.01579
500		0.0249	0.02498	0.02498
4	$\bar{\sigma}_{<12>}\left(0,0,-\frac{h}{2}\right)$	0.0840	0.09652	0.09529
10		0.0412	0.04697	0.04570
50		0.0383	0.03929	0.03932
100		0.0447	0.04515	0.04518
500		0.0611	0.06110	0.06111

Table 3.15. Central deflection and stresses of a two-ply (0°/90°) laminated circular cylindrical panel under sinusoidal loading (4×4Q25, full integration).

S		Ref. [86]	Ref. [87]	Present TSDT	Present FSDT
4	$\bar{v}_{<3>}\left(\frac{a}{2},\alpha,0\right)$	6.1000	5.09696	6.66980	7.32821
10		3.3300	3.16576	3.44978	3.67150
50		2.2420	2.23717	2.26272	2.28648
100		1.3670	1.36665	1.37380	1.37812
500		0.1005	0.10049	0.10060	0.10061
4	$\bar{\sigma}_{<11>}\left(\frac{a}{2},\alpha,\frac{h}{2}\right)$	0.2120	0.20710	0.24272	0.23042
10		0.1930	0.19098	0.20242	0.20389
50		0.2189	0.21866	0.22122	0.22223
100		0.1871	0.18708	0.18838	0.18860
500		0.0449	0.04491	0.04509	0.04508
4	$\bar{\sigma}_{<11>}\left(\frac{a}{2},\alpha,-\frac{h}{2}\right)$	-0.9610	-0.71888	-0.93037	-0.90572
10		-0.1689	-0.15665	-0.17017	-0.17541
50		1.6100	1.60510	1.62290	1.63873
100		2.3000	2.29788	2.30920	2.31605
500		0.9436	0.94359	0.94424	0.94427
4	$\bar{\sigma}_{<22>}\left(\frac{a}{2},\alpha,\frac{h}{2}\right)$	10.310	12.07122	12.57100	10.38730
10		10.590	10.95205	11.32900	10.92150
50		8.9370	8.95433	9.06240	9.02585
100		5.5600	5.56430	5.62630	5.60604
500		0.4345	0.43460	0.44868	0.44816
4	$\bar{\sigma}_{<22>}\left(\frac{a}{2},\alpha,-\frac{h}{2}\right)$	-1.7890	-1.11616	-1.68620	-1.79515
10		-1.3430	-1.20498	-1.32470	-1.42100
50		-0.9670	-0.96152	-0.97207	-0.98588
100		-0.5759	-0.57495	-0.57771	-0.58073
500		-0.0339	-0.03392	-0.03428	-0.03430
4	$\bar{\sigma}_{<12>}\left(0,0,\frac{h}{2}\right)$	-0.20070	-0.16858	-0.20324	-0.21694
10		-0.12470	-0.11819	-0.12606	-0.13019
50		0.07840	0.07842	0.07938	0.08080
100		0.18190	0.18187	0.18279	0.18354
500		0.09250	0.09245	0.09252	0.09253
4	$\bar{\sigma}_{<12>}\left(0,0,-\frac{h}{2}\right)$	0.28120	0.22653	0.29249	0.32172
10		0.23250	0.22105	0.24039	0.25724
50		0.34490	0.34440	0.34835	0.35231
100		0.34520	0.34514	0.34690	0.34809
500		0.10450	0.10448	0.10457	0.10457

Table 3.16. Central deflection and stresses of a three-ply (90°/0°/90°) laminated circular cylindrical panel under sinusoidal loading (4×4*Q*25, full integration).

S		Ref. [86]	Ref. [87]	Present TSDT	Present FSDT
4	$\bar{v}_{<3>}\left(\frac{a}{2},\alpha,0\right)$	4.0090	3.60671	4.08163	3.79904
10		1.2230	1.20335	1.18349	1.07135
50		0.5495	0.54862	0.55044	0.54574
100		0.4715	0.47110	0.47273	0.47180
500		0.1027	0.10269	0.10280	0.10280
4	$\bar{\sigma}_{<11>}\left(\frac{a}{2},\alpha,\frac{h}{2}\right)$	0.1270	0.12126	0.11545	0.08576
10		0.0739	0.07231	0.07156	0.06040
50		0.0712	0.07097	0.07147	0.07061
100		0.0838	0.08370	0.08414	0.08387
500		0.0559	0.05585	0.05604	0.05603
4	$\bar{\sigma}_{<11>}\left(\frac{a}{2},\alpha,-\frac{h}{2}\right)$	-0.2701	-0.12923	-0.13848	-0.07216
10		-0.0791	-0.05632	-0.05790	-0.04695
50		-0.0225	-0.02167	-0.02192	-0.02189
100		0.0018	0.00197	0.00199	0.00191
500		0.0379	0.03788	0.03796	0.03795
4	$\bar{\sigma}_{<22>}\left(\frac{a}{2},\alpha,\frac{h}{2}\right)$	6.5450	7.01022	5.72740	3.30200
10		4.6830	4.69967	4.66530	3.80004
50		3.9300	3.92646	3.96520	3.90776
100		3.5070	3.50478	3.53300	3.51579
500		0.7895	0.78973	0.80447	0.80400
4	$\bar{\sigma}_{<22>}\left(\frac{a}{2},\alpha,-\frac{h}{2}\right)$	-9.3230	-10.5280	-11.08700	-4.84184
10		-5.2240	-5.30760	-5.46550	-4.41580
50		-3.9870	-3.98701	-4.01660	-3.99775
100		-3.5070	-3.50626	-3.51520	-3.51627
500		-0.7542	-0.75451	-0.74965	-0.75001
4	$\bar{\sigma}_{<12>}\left(0,0,\frac{h}{2}\right)$	-0.1081	-0.08998	-0.09025	-0.07419
10		-0.0374	-0.03343	-0.03287	-0.02784
50		0.0118	0.01228	0.01225	0.01225
100		0.0478	0.04798	0.04812	0.04808
500		0.0766	0.07660	0.07665	0.07665
4	$\bar{\sigma}_{<12>}\left(0,0,-\frac{h}{2}\right)$	0.1609	0.16242	0.17924	0.14534
10		0.0729	0.07569	0.07525	0.06597
50		0.0760	0.07639	0.07670	0.07613
100		0.1038	0.10393	0.10428	0.10412
500		0.0889	0.08886	0.08892	0.08892

Table 3.17. Central deflection and stresses of a ten-ply (90°/0°/90°/0°/90°)$_s$ laminated circular cylindrical panel under sinusoidal loading (4×4Q25, full integration).

S		Ref. [86]	Present TSDT	Present FSDT
4	$\bar{v}_{<3>}\left(\frac{a}{2},\alpha,0\right)$	4.2060	3.90209	4.18634
10		1.3800	1.31414	1.34037
50		0.7622	0.76468	0.76546
100		0.6261	0.62806	0.62820
500		0.1006	0.10067	0.10067
4	$\bar{\sigma}_{<11>}\left(\frac{a}{2},\alpha,\frac{h}{2}\right)$	0.1243	0.11134	0.10011
10		0.0877	0.08637	0.08160
50		0.0971	0.09769	0.09719
100		0.1076	0.10812	0.10793
500		0.0516	0.05181	0.05180
4	$\bar{\sigma}_{<11>}\left(\frac{a}{2},\alpha,-\frac{h}{2}\right)$	-0.2674	-0.12408	-0.09510
10		-0.0927	-0.07205	-0.06844
50		-0.0340	-0.03355	-0.03370
100		-0.0015	-0.00137	-0.00147
500		0.0340	0.03408	0.03408
4	$\bar{\sigma}_{<22>}\left(\frac{a}{2},\alpha,\frac{h}{2}\right)$	6.6350	5.92790	4.66730
10		5.8750	5.97930	5.46968
50		5.5290	5.58740	5.53463
100		4.6770	4.71560	4.69626
500		0.7770	0.79232	0.79177
4	$\bar{\sigma}_{<22>}\left(\frac{a}{2},\alpha,-\frac{h}{2}\right)$	-8.9700	-9.87600	-7.04297
10		-6.4620	-6.77990	-6.42938
50		-5.6060	-5.65260	-5.66983
100		-4.6700	-4.68270	-4.69327
500		-0.7351	-0.73172	-0.73215
4	$\bar{\sigma}_{<12>}\left(0,0,\frac{h}{2}\right)$	0.0972	0.06956	0.07571
10		0.0406	0.03619	0.03508
50		-0.0223	-0.02273	-0.02297
100		-0.0734	-0.07373	-0.07382
500		-0.0829	-0.08298	-0.08298
4	$\bar{\sigma}_{<12>}\left(0,0,-\frac{h}{2}\right)$	-0.1652	-0.15202	-0.16168
10		-0.0869	-0.08689	-0.08766
50		-0.1120	-0.11292	-0.11311
100		-0.1479	-0.14855	-0.14863
500		-0.0949	-0.09501	-0.09501

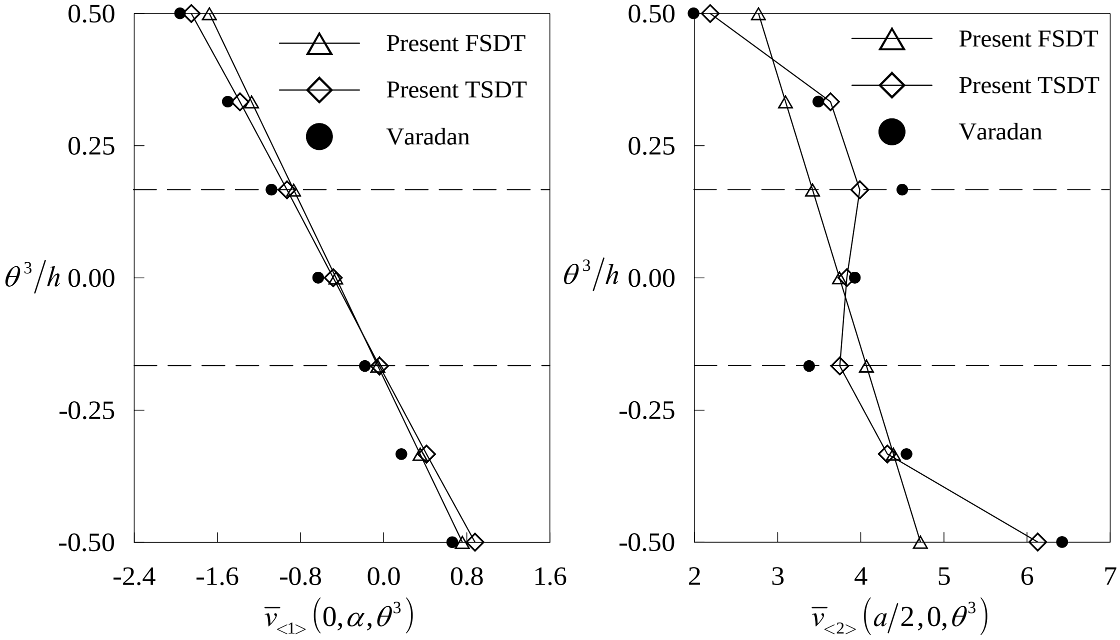

Fig. 3.28. Displacement distribution through the thickness $\bar{v}_{<1>}$ and $\bar{v}_{<2>}$ of a three-ply (90°/0°/90°) laminated circular cylindrical panel (4×4*Q*25, *S* = 4).

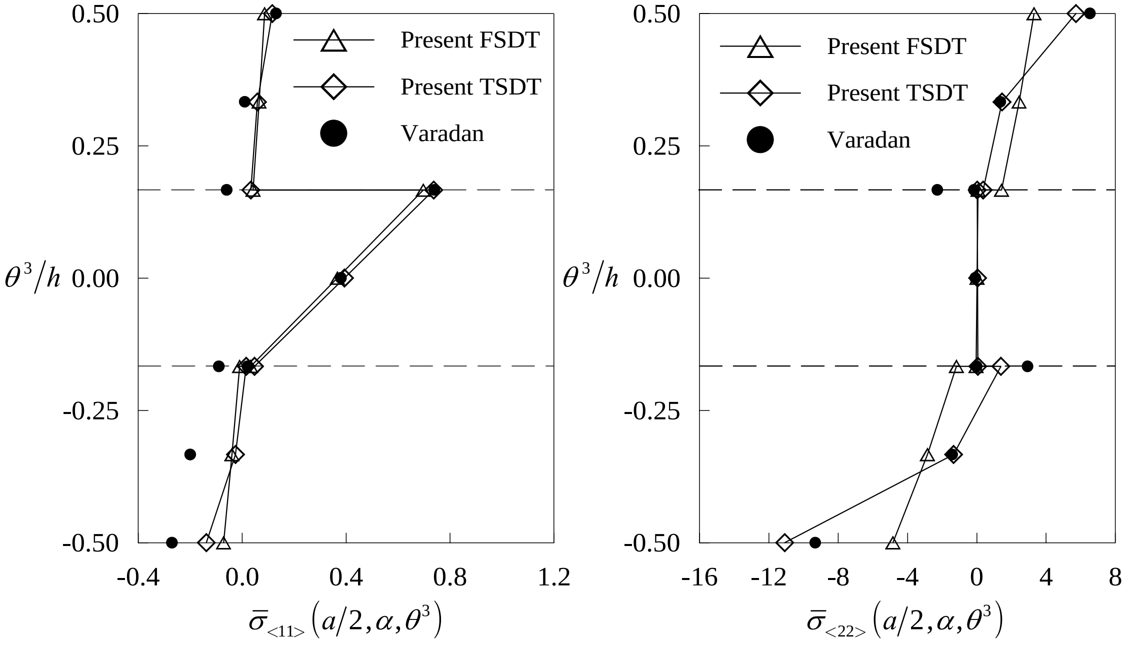

Fig. 3.29. Stress distribution through the thickness $\bar{\sigma}_{<11>}$ and $\bar{\sigma}_{<22>}$ of a three-ply (90°/0°/90°) laminated circular cylindrical panel (4×4*Q*25, *S* = 4).

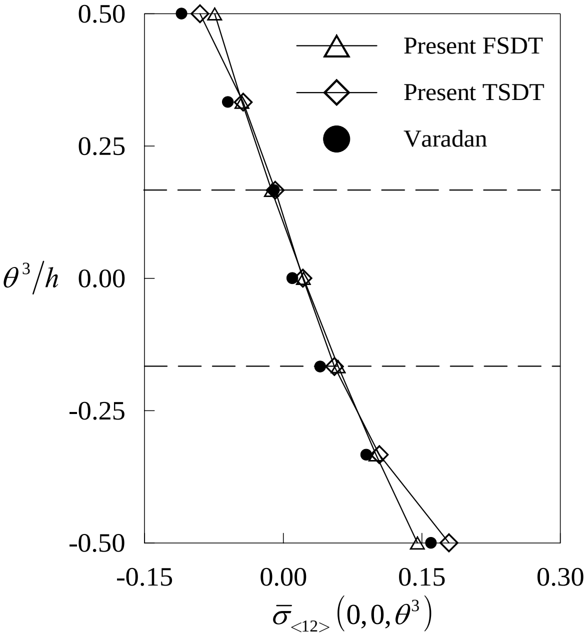

Fig. 3.30. Stress distribution through the thickness $\bar{\sigma}_{<12>}$ of a three-ply (90°/0°/90°) laminated circular cylindrical panel (4×4*Q*25, *S* = 4).

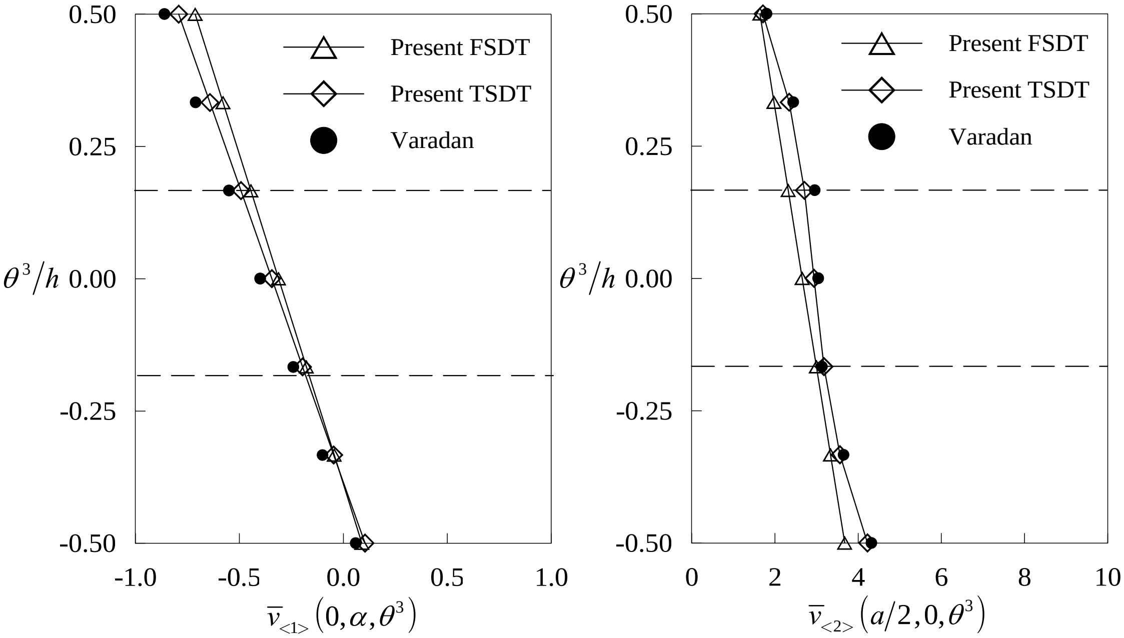

Fig. 3.31. Displacement distribution through the thickness $\bar{v}_{<1>}$ and $\bar{v}_{<2>}$ of a three-ply (90°/0°/90°) laminated circular cylindrical panel (4×4*Q*25, *S* = 10).

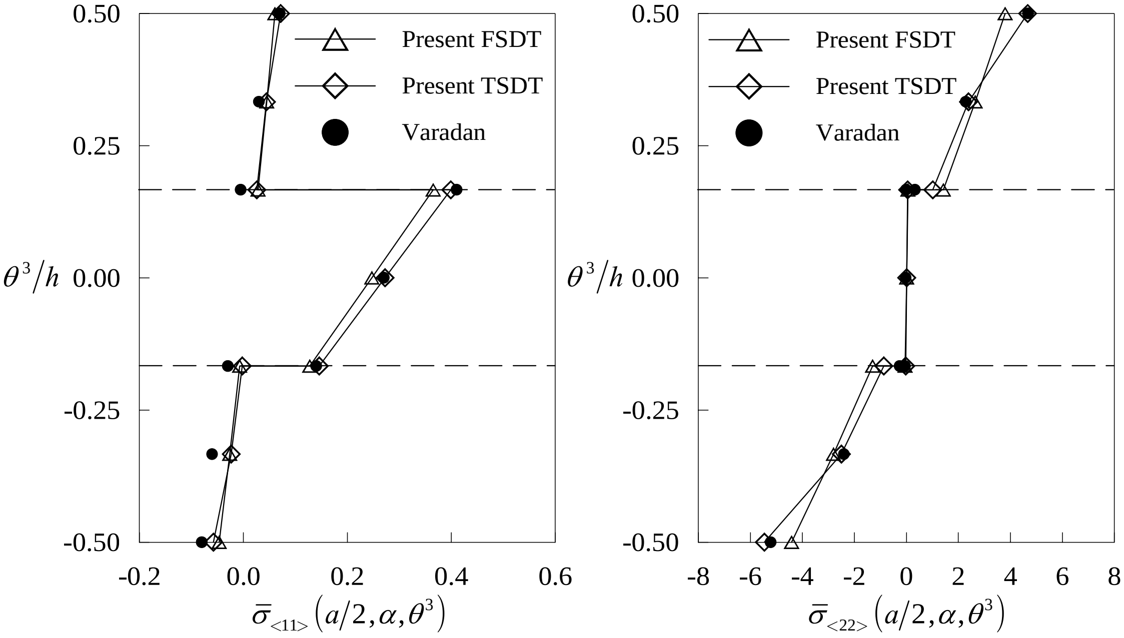

Fig. 3.32. Stress distribution through the thickness $\bar{\sigma}_{<11>}$ and $\bar{\sigma}_{<22>}$ of a three-ply (90°/0°/90°) laminated circular cylindrical panel (4×4*Q*25, *S* = 10).

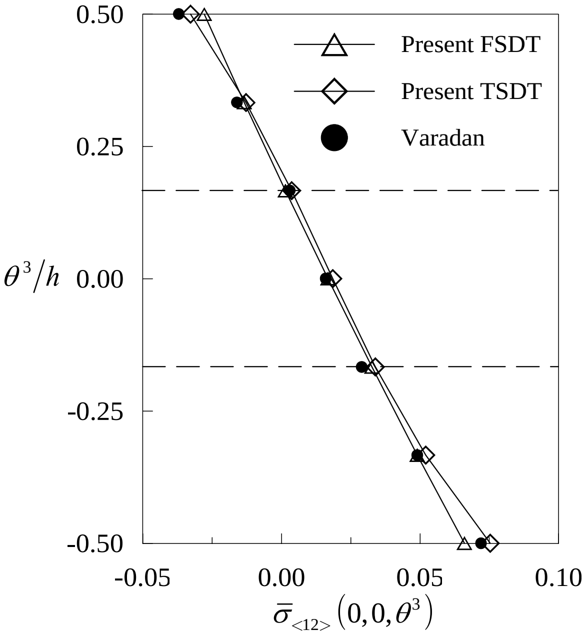

Fig. 3.33. Stress distribution through the thickness $\bar{\sigma}_{<12>}$ of a three-ply (90°/0°/90°) laminated circular cylindrical panel (4×4*Q*25, *S* = 10).

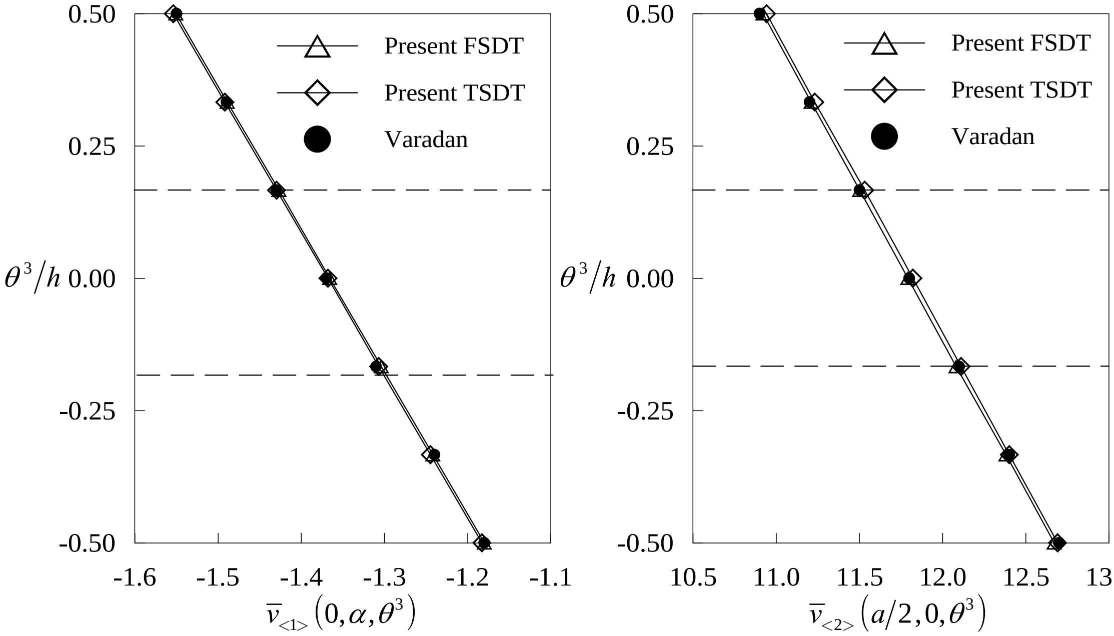

Fig. 3.34. Displacement distribution through the thickness $\bar{v}_{<1>}$ and $\bar{v}_{<2>}$ of a three-ply (90°/0°/90°) laminated circular cylindrical panel (4×4*Q*25, *S* = 100).

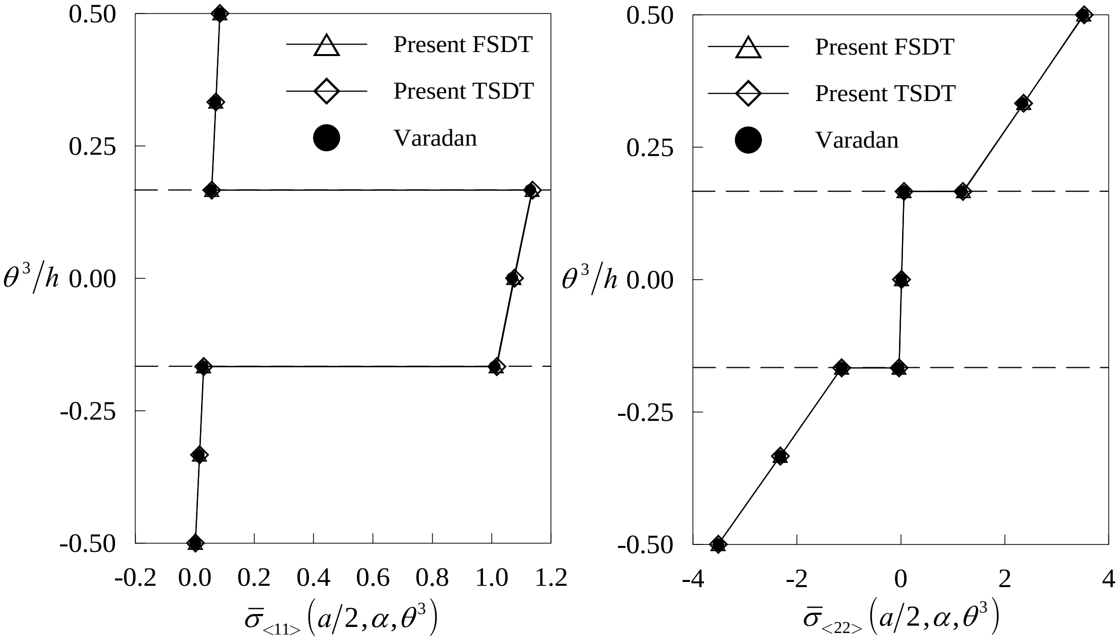

Fig. 3.35. Stress distribution through the thickness $\bar{\sigma}_{<11>}$ and $\bar{\sigma}_{<22>}$ of a three-ply (90°/0°/90°) laminated circular cylindrical panel (4×4*Q*25, *S* = 100).

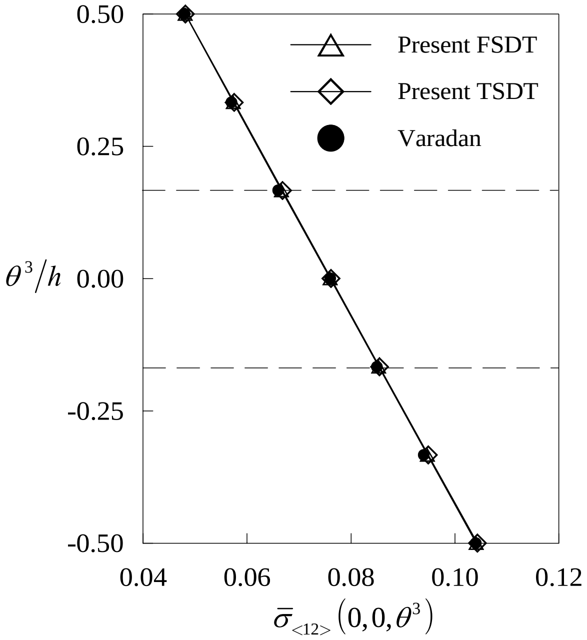

Fig. 3.36. Stress distribution through the thickness $\bar{\sigma}_{<12>}$ of a three-ply (90°/0°/90°) laminated circular cylindrical panel (4×4*Q*25, *S* = 100).

e. Simply-supported and clamped laminated panel

In this example simply-supported and clamped laminated cylindrical shells are studied. Cross-ply and angle-ply for 2, 4 and 10 layers are used in the analysis. In similar way as the last example, full panel is taken as computational domain. The physical and geometrical features of the problem are the following

$$E_1/E_2 = 25, \quad G_{13} = G_{12} = 0.5E_2, \quad G_{23} = 0.2E_2, \quad \nu_{12} = 0.25$$
$$a/R = 2, \quad R/h = S, \quad \alpha = \pi/4$$

with two kinds of external loads: uniform transverse load (UL) and sinusoidal load (SL)

$$P^3 = q_0$$
$$P^3 = q_0 \sin\left(\frac{\pi\theta^1}{a}\right)\sin\left(\frac{\pi\theta^2}{2\alpha}\right)$$

respectively. The boundary conditions are

Simply supported:

At $\theta^1 = 0, a$ $\quad u_{<2>} = u_{<3>} = \varphi_{<2>} = \psi_{<2>} = 0$ (cross-ply)

$u_{<1>} = u_{<3>} = \varphi_{<2>} = \psi_{<2>} = 0$ (angle-ply)

At $\theta^2 = 0, 2\alpha$ $\quad u_{<1>} = u_{<3>} = \varphi_{<1>} = \psi_{<1>} = 0$ (cross-ply)

$u_{<2>} = u_{<3>} = \varphi_{<1>} = \psi_{<1>} = 0$ (angle-ply) .

Clamped:

At $\theta^1 = 0, a$ $\quad u_{<i>} = \varphi_{<\alpha>} = \psi_{<\alpha>} = 0$

At $\theta^2 = 0, 2\alpha$ $\quad u_{<i>} = \varphi_{<\alpha>} = \psi_{<\alpha>} = 0$.

Tables 3.18 to 3.21 show the present TSDT results for central deflections and stresses of cylindrical panels with various laminate schemes. Figures 3.37 to 3.40 show central deflection curves vs. *S* for cross-ply and angle-ply laminates with simply-supported and clamped boundary conditions. Both cases are tabulated for dimensionless central deflections and stresses of the panel. The following parameters are utilized

$$\bar{v}_{<3>} = \frac{10\,E_1}{q_0\,R\,S^3}\; v_{<3>}\left(a/2, \alpha, 0\right), \qquad \bar{\sigma}_{<11>} = \frac{10}{q_0\,S^2}\; \sigma_{<11>}\left(a/2, \alpha, -h/2\right)$$

$$\bar{\sigma}_{<22>} = \frac{10}{q_0\,S^2}\; \sigma_{<22>}\left(a/2, \alpha, h/2\right)$$

and

$$\bar{\sigma}_{<12>} = \frac{10}{q_0\,S^2}\; \sigma_{<12>}\left(0, 0, -h/2\right) \qquad \text{for simply-supported}$$

$$\bar{\sigma}_{<12>} = \frac{10}{q_0\,S^2}\; \sigma_{<12>}\left(a/2, \alpha, h/2\right) \qquad \text{for clamped panels .}$$

These results can be utilized as a benchmark for other laminated shell formulations.

Table 3.18. Central deflection and stresses of simply-supported cross-ply laminated circular cylindrical panels under uniform and sinusoidal loading (4×4Q25, full integration).

Scheme	S	Load	$\bar{v}_{<3>}$	$\bar{\sigma}_{<11>}$	$\bar{\sigma}_{<22>}$	$\bar{\sigma}_{<12>}$
(0°/90°)	20	UL	3.09815	0.42197	1.86990	1.53390
		SL	2.12361	0.05022	2.54050	0.72257
	50	UL	0.33826	0.50095	-0.97074	0.72642
		SL	0.35165	0.38107	0.66125	0.27258
	100	UL	-0.02976	0.09916	-1.22470	0.45458
		SL	0.08813	0.25099	0.26264	0.13212
(0°/90°)$_s$	20	UL	2.78534	-1.03020	0.10667	1.35710
		SL	1.93798	-0.98612	0.18218	0.66473
	50	UL	0.29863	0.32039	-0.09678	0.67785
		SL	0.34396	0.17660	0.04550	0.26789
	100	UL	-0.04298	0.09624	-0.10258	0.43364
		SL	0.08742	0.19865	0.01692	0.13138
(0°/90°)$_5$	20	UL	2.92651	-0.76981	3.84210	1.29250
		SL	1.92153	-0.80674	3.31950	0.65870
	50	UL	0.45636	0.38013	0.02537	0.60142
		SL	0.34385	0.21493	0.83929	0.26757
	100	UL	0.06140	0.22628	-0.73242	0.35598
		SL	0.08745	0.20878	0.31011	0.13137

Table 3.19. Central deflection and stresses of clamped cross-ply laminated circular cylindrical panel under uniform and sinusoidal loading (4×4Q25, full integration).

Scheme	S	Load	$\bar{v}_{<3>}$	$\bar{\sigma}_{<11>}$	$\bar{\sigma}_{<22>}$	$\bar{\sigma}_{<12>} \times 10^3$
(0°/90°)	20	UL	0.09035	0.00722	1.08520	0.03557
		SL	0.20933	-0.12113	1.79480	0.00689
	50	UL	0.01390	0.00265	0.40195	-0.01856
		SL	0.10763	-0.02519	1.11330	-0.01511
	100	UL	0.00288	0.00020	0.19273	-0.00380
		SL	0.06656	0.02517	0.72040	-0.00979
$(0°/90°)_s$	20	UL	0.08887	-0.02444	0.04782	-0.00051
		SL	0.21752	-0.26960	0.11451	0.31333
	50	UL	0.01338	-0.00035	0.01635	0.00485
		SL	0.11444	-0.10857	0.07679	0.02073
	100	UL	0.00271	0.00047	0.00750	-0.01168
		SL	0.06875	-0.01526	0.04892	-0.00934
$(0°/90°)_5$	20	UL	0.08757	0.00257	1.14260	0.04814
		SL	0.14195	-0.14821	1.57720	0.04752
	50	UL	0.01434	0.00389	0.41959	-0.00980
		SL	0.05440	-0.03731	0.88472	0.00042
	100	UL	0.00336	0.00075	0.19856	-0.00952
		SL	0.03561	-0.00265	0.62712	-0.00604

Table 3.20. Central deflection and stresses of simply-supported angle-ply laminated circular cylindrical panels under uniform and sinusoidal loading (4×4Q25, full integration).

Scheme	S	Load	$\bar{v}_{<3>}$	$\bar{\sigma}_{<11>}$	$\bar{\sigma}_{<22>}$	$\bar{\sigma}_{<12>}$
(-45°/45°)	20	UL	0.13966	0.42055	0.51643	-0.20266
		SL	0.36941	-0.03431	0.91395	-0.75741
	50	UL	0.018741	0.17481	0.19543	-0.10457
		SL	0.13268	0.02124	0.41867	-0.65970
	100	UL	0.00400	0.08685	0.09696	-0.05563
		SL	0.05607	0.04550	0.19322	-0.52936
$(45°/-45°)_s$	20	UL	0.14755	0.38923	0.55008	1.18090
		SL	0.28093	-0.02296	0.85549	-0.15872
	50	UL	0.02037	0.171490	0.20088	0.39054
		SL	0.09159	-0.01608	0.41657	-0.70010
	100	UL	0.00437	0.08747	0.09769	0.17200
		SL	0.04109	0.00983	0.21487	-0.70202
$(-45°/45°)_5$	20	UL	0.14952	0.39288	0.54280	-0.15640
		SL	0.26489	-0.05495	0.83155	-0.49712
	50	UL	0.02061	0.17033	0.20022	-0.09383
		SL	0.08804	-0.01229	0.39538	-0.45589
	100	UL	0.00445	0.08713	0.09759	-0.05190
		SL	0.03994	0.01846	0.20427	-0.39402

Table 3.21. Central deflection and stresses of clamped angle-ply laminated circular cylindrical panel under uniform and sinusoidal loading (4×4Q25, full integration).

Scheme	S	Load	$\bar{v}_{<3>}$	$\bar{\sigma}_{<11>}$	$\bar{\sigma}_{<22>}$	$\bar{\sigma}_{<12>}$
(-45°/45°)	20	UL	0.12723	0.45180	0.50271	0.42787
		SL	0.23908	0.09751	0.75783	0.59470
	50	UL	0.01211	0.19479	0.17793	0.15407
		SL	0.06995	0.06649	0.33903	0.27758
	100	UL	0.00121	0.09335	0.08797	0.07482
		SL	0.02386	0.06710	0.15520	0.13541
(45°/-45°)$_s$	20	UL	0.13560	0.41205	0.54496	0.46241
		SL	0.20302	0.08501	0.73805	0.60845
	50	UL	0.01650	0.19064	0.18860	0.16172
		SL	0.05332	0.04328	0.33333	0.28345
	100	UL	0.00219	0.09790	0.08757	0.07414
		SL	0.02037	0.04133	0.17104	0.15199
(-45°/45°)$_5$	20	UL	0.13867	0.40936	0.54298	0.45801
		SL	0.19347	0.06487	0.72295	0.59930
	50	UL	0.01683	0.18898	0.18890	0.16159
		SL	0.05136	0.04003	0.32252	0.27396
	100	UL	0.00233	0.09725	0.08821	0.07451
		SL	0.02001	0.04060	0.16609	0.14714

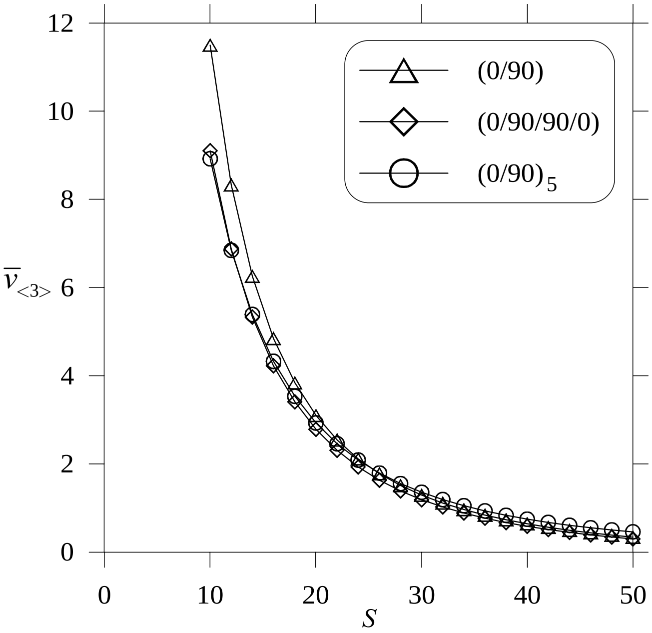

Fig. 3.37. Central deflection of simply-supported cross-ply panels under uniform load vs. ratio *S*.

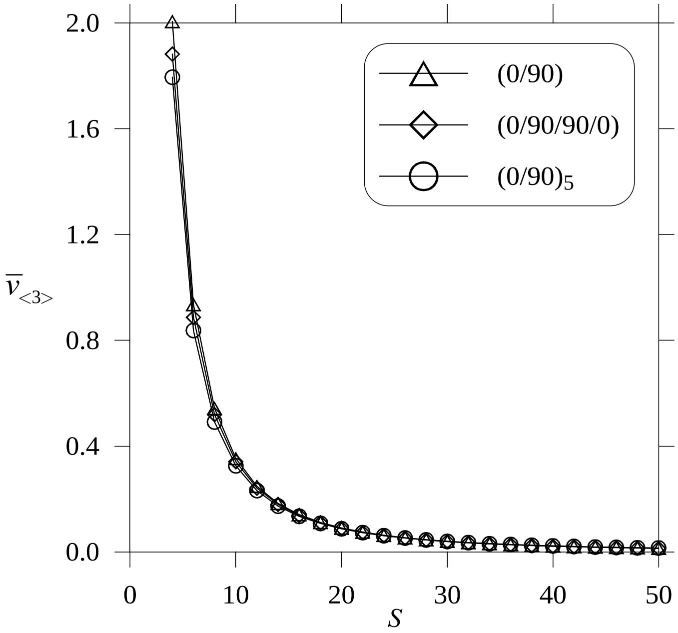

Fig. 3.38. Central deflection of clamped cross-ply panels under uniform load vs. ratio *S*.

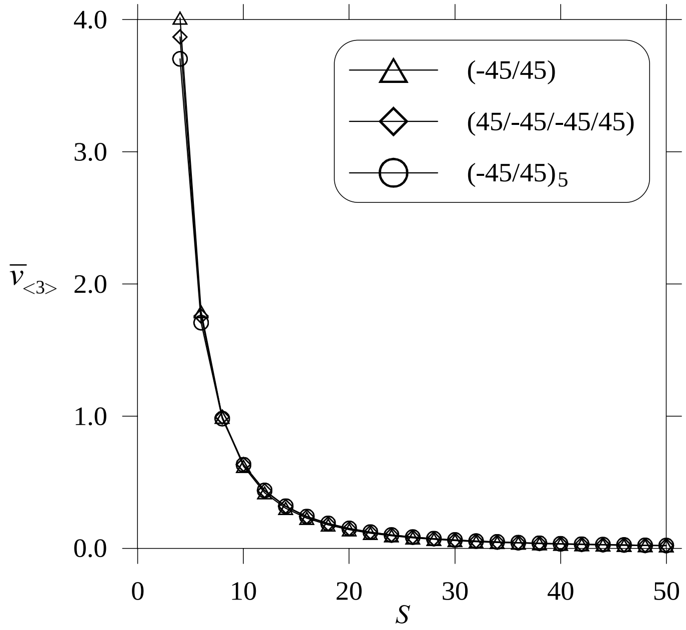

Fig. 3.39. Central deflection of simply-supported angle-ply panels under uniform load vs. ratio *S*.

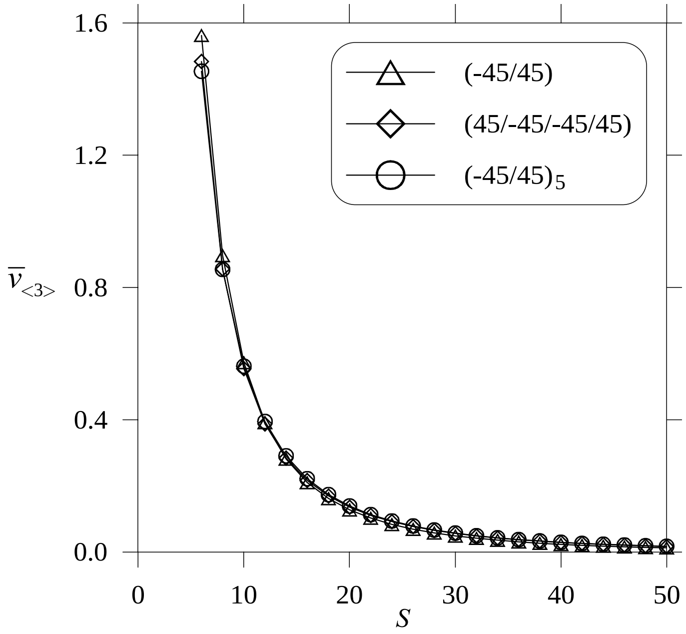

Fig. 3.40. Central deflection of clamped angle-ply panels under uniform load vs. ratio *S*.

3. Spherical shells

a. Pinched hemispherical shell with 18° hole

Next, we examine the behavior of a pinched hemispherical shell with 18° hole. This is a challenging test for the representation of rigid body motions and it has been chosen from the list of standard test problems proposed for shell elements by MacNeal and Harder [88]. The example considers a closed isotropic hemispherical shell with two inward and two outward forces perpendicular to each other. The hole at the outer and the equator are supposed to be free edges so that the problem represents a hemisphere with four point loads. Due to the symmetry of the problem, only one quarter of the shell has been modeled by a regular mesh as shown in Fig. 3.41.

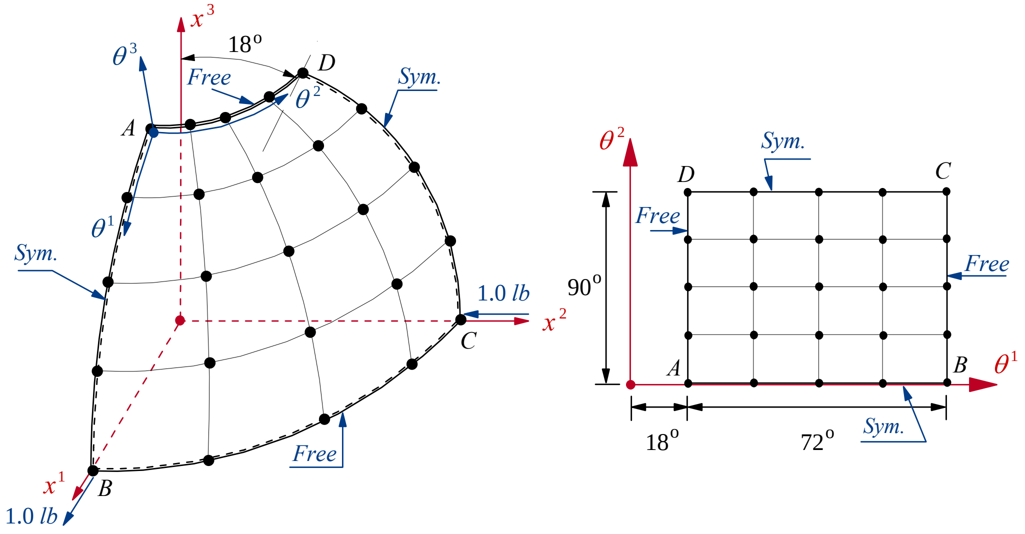

(a)

(b)

Fig. 3.41. Pinched hemispherical shell with 18° hole: (a) Mesh in Cartesian coordinates, (b) Mesh in curvilinear coordinates.

The material properties are

$$E = 6.825\times10^{7}\,psi,\quad \nu = 0.3,\quad R = 10\,in,\quad h = 0.04\,in$$

and a load of $P^{3} = 1.0\,lb$. The imposed boundary conditions for the computational domain are

At θ^{1} = 18°, 90° Free

At θ^{2} = 0°, 90° $u_{<2>} = \varphi_{<2>} = \psi_{<2>} = 0$ (Symmetry) .

The radial deflection at the point B for uniform meshes of 81, 289 nodes and 1089 nodes with different p levels is reported in Table 3.22. The reference solution given by MacNeal and Harder [88] is 0.094 *in*. Simo et al. [82] also report a value of 0.093 *in* for the deflection at B. We adopt the former value as a reference solution (u_{ref}) for this example. The present results correspond to the TSDT and FSDT with full and selective integration rules. It is found that using selective integration rule tends to overestimate displacements (more flexible). However, meshes of 8×8Q25 and 4×4Q81 with full integration are in good agreement with the reference solution. Also, the TSDT and FSDT do not present significant difference in the numerical solutions.

Table 3.22. Radial displacement at B ($u_{<3>}\times10^{2}$ *in*) of the pinched hemisphere with 18° hole.

		Mesh of 81 nodes		Mesh of 289 nodes		Mesh of 1089 nodes	
p level		Full integratio	Selective integratio	Full integration	Selective integration	Full integration	Selective integration
2	TSDT	0.44746	0.75629	4.18446	4.41420	8.64079	8.72217
	FSDT	0.44850	0.75640	4.18582	4.41518	8.64105	8.72344
4	TSDT	8.87609	9.20607	9.30302	9.35750	9.35372	9.37242
	FSDT	8.87643	9.20610	9.30302	9.35789	9.35370	9.37358
8	TSDT	9.28833	9.49682	9.35157	9.39702	9.35881	9.37378
	FSDT	9.28834	9.49675	9.35154	9.39717	9.35876	9.37458

The performance of the present elements: $Q25$ and $Q81$ is investigated in Figure 3.42 through a comparison with the 8-URI element of Kreja et al. [84] and the mixed element of Simo et al. [82]. It is shown a convergence analysis of the radial deflection at the point B for different number of nodes. We notice an excellent rate of convergence for our $Q25$ and $Q81$ elements. It is also observed no presence of membrane or shear locking.

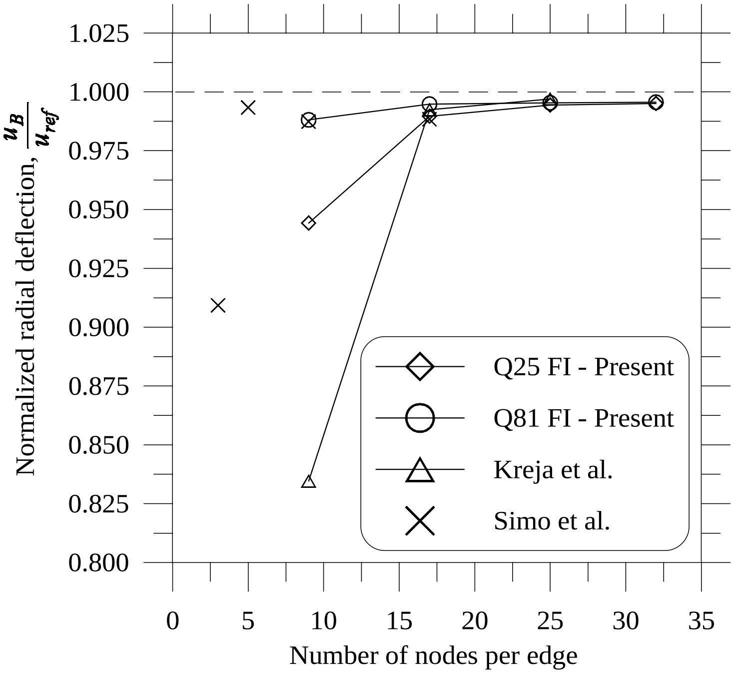

Fig. 3.42. Convergence of the radial displacement $u_{<3>}$ at the point B of the pinched hemisphere with 18° hole.

b. Full pinched hemispherical shell

In this example, we study a similar pinched hemispherical shell with no hole on the outer. It has the same material properties and geometry as the last problem. The equator is to be assumed a free edge and the apex is fixed (see Fig. 3.43). We exploit the symmetry of the problem and only one quarter of the shell has been modeled by rectangular meshes. Note that an edge is shrunk to a point (the apex) when it is mapped from the parametric space to the Euclidean space. However, it does not cause any singularity problems in the numerical solution.

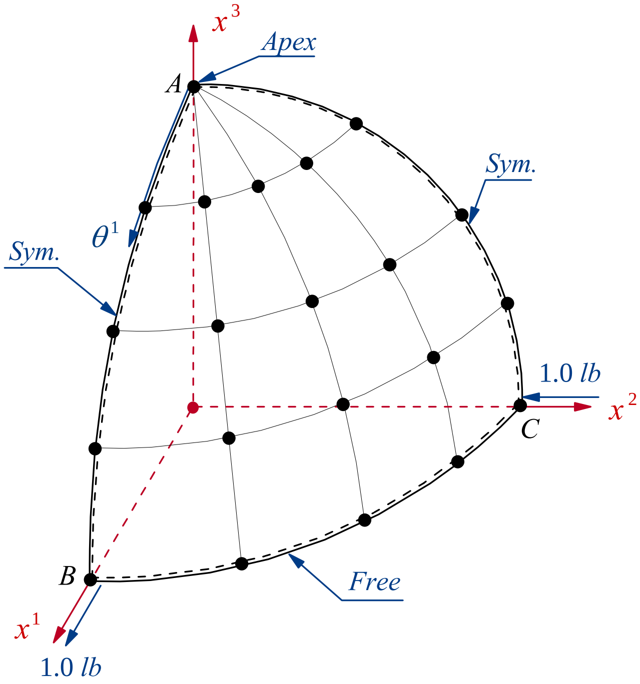

Fig. 3.43. Full pinched hemispherical shell

The imposed boundary conditions for the computational domain are

At $\theta^1 = 0°$ $\quad u_{<1>} = u_{<2>} = \varphi_{<1>} = \varphi_{<2>} = \psi_{<1>} = \psi_{<2>} = 0$

At $\theta^1 = 90°$ $\quad$ Free

At $\theta^2 = 0°, 90°$ $\quad u_{<2>} = \varphi_{<2>} = \psi_{<2>} = 0$ (Symmetry) .

The radial deflection at the point *B* for uniform meshes of 81, 289 nodes and 1089 nodes with different *p* levels is reported in Table 3.23. The analytical solution given by MacNeal and Harder [88] is 0.0924 *in*. which is adopted as a reference solution (u_{ref}).

We tabulate values corresponding to the TSDT and FSDT with full and selective integration rules. Conclusions similar to those of the last example are obtained from these results.

Finally, we illustrate in Fig. 3.44 the performance of our elements *Q*25 and *Q*81 with the element of Balah and Al-Ghamedy [18] and the mixed element of Simo et al. [82] which could be considered among the best shell elements. Remarkably, we notice a slightly better rate of convergence for our *Q*81 than those from Simo and Balah. There is also no presence of membrane and shear locking for the studied elements.

Table 3.23. Radial displacement at B ($u_{<3>} \times 10^{2}$ in) of the full pinched hemisphere.

p level		Mesh of 81 nodes		Mesh of 289 nodes		Mesh of 1089 nodes	
		Full integratio	Selective integratio	Full integration	Selective integration	Full integration	Selective integration
2	TSDT	0.38478	0.62816	3.81108	4.05657	8.43507	8.53111
	FSDT	0.38572	0.62832	3.81255	4.05747	8.43538	8.53216
4	TSDT	8.71692	9.07403	9.15037	9.23943	9.24059	9.26234
	FSDT	8.71734	9.07429	9.15037	9.23973	9.24056	9.26325
8	TSDT	9.12865	9.41446	9.23867	9.30633	9.24627	9.26610
	FSDT	9.12869	9.41470	9.23863	9.30644	9.24623	9.26669

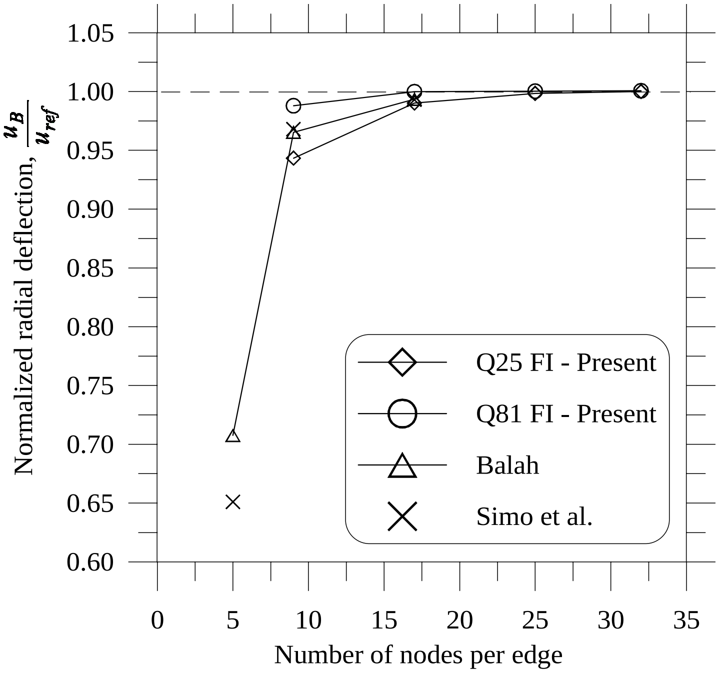

Fig. 3.44. Convergence of the radial displacement $u_{<3>}$ at the point B of the full pinched hemisphere.

CHAPTER IV

NONLINEAR SHELL THEORY

This chapter is concerned with the theoretical development of geometrically nonlinear shells for finite deformations. The formulation is based on an improved first-order theory with seven independent parameters. The shell theory takes thickness changes into account (no plane stress assumption) and circumvents the use of a rotation tensor. The following brief review, which focuses on studies that have appeared in the open literature in the last three decades about nonlinear shear deformation shell theories, provides a fine background for the derivation of the present approach.

Shell theories are by no means new; studies on deflection of elastic membranes can be traced as far back as the first part of the nineteenth century. Since then, the theory of shells has been amply researched. It was Naghdi [48] who first incorporated the Reissner-Mindlin assumptions to isotropic shells. In a later development, Naghdi [46] presented a complete treatise of shell theories in the well-known Encyclopedia of Physics. There, he derived two approaches for nonlinear shell theories: the direct approach based on the Cosserat continuum theory and the derivation from the 3D continuum theory; so-called single-layer theories.

The direct approach considers the shell from the beginning as a two-dimensional manifold, called Cosserat continuum. The possibility of employing a 2D model for a thin shell presents itself in a natural way. Such an approach was conceived of and dealt with by the brothers E. and F. Cosserat but remained largely unknown or unnoticed until the 1950s. It was Ericksen and Truesdell [89] who first rediscovered the theory and Green and Naghdi [90] and Green et al. [91] who initiated it. Working along similar lines, Simo and co-workers [5, 82, 92] proposed *the stress-resultant geometrically exact shell model* which is formulated entirely in terms of stress resultants and is essentially equivalent to the single director inextensible Cosserat surface. It was denominated “geometrically exact” because there was no approximation error in the geometric equations. However, it only illustrates the fact that the approximation error is concentrated in the material law. Additional applications of the direct approach can be found in references [93, 94].

Regarding the single-layer theories, it seems that the first shear deformation theory for geometrically nonlinear laminated shells was given Librescu [95] and Librescu and Schmidt [96]. They proposed a refined geometrically nonlinear theory for anisotropic composite shallow shells by incorporating transverse shear deformation and transverse normal stress effects. The Lagrangian formulation was used to derive the theory and the 3D strain-displacement relations include some degree of geometric nonlinearity. The theory is well-known as the *moderate rotation shell theory*. Applications of the theory can be found in Librescu and Stein [97] and Librescu and Chang [98] to study the postbuckling behavior with sensitivity to imperfections of laminated panels. The theory was particularized to the first-order theory by Schmidt and Reddy [50] and it was utilized by Palmerio et al. [99, 100] and Kreja et al. [84] for finite element applications to anisotropic shells.

Another important group of shell theories that deal with assumed magnitudes of strains and rotations in full nonlinear equations are the *finite rotation theories*. It was Pietraszkiewicz [2, 101] and Pietraszkiewicz and Badur [102] who introduced the idea in a formal manner. The set of governing equations and boundary conditions can be obtained from a variational principle. Pietraszkiewicz [103] also developed both total Lagrangian and update Lagrangian formulations for geometrically nonlinear shells based on the Kirchhoff-Love assumptions. Strains and rotations about the normal to the surface are assumed to be of the order ϑ, where ϑ is small compared to unity. Rotations about tangents to the surface are organized in a consistent classification where for each range of magnitude of rotations specific shell equations are obtained. The finite rotation theory was then applied to composite shells by Başar [104, 105]. Refined high-order shear deformation models for composite shells using finite rotations can be found in Başar et al. [106] and Balah and Al-Ghamedy [18]. Both approaches utilize the third-order shell theory for the analysis of composite shells via finite element methods.

Recently, considerable attention has been given to the development of 3D constitutive shell models with thickness stretching. These models are able to approximately represent three-dimensional effects, in comparison to formulations which use reduced elasticity tensor components. The use of unmodified and complete 3D material laws within shell analysis has been the major motivation for the development of such models. Among the most important works, we can refer to Büchter and Ramm [52], Sansour [23] and Simo et al. [53]. Improvements of shell theories to 7-independent-parameter models have been presented by Braun et al. [76], Büchter et al. [107], and Bischoff and Ramm [24, 108]. Further applications of this refined shell theory can be found in references [109, 110].

In geometrically exact shell theories thickness change is neglected and hence the plane stress assumption has to be introduced. For finite rotation analyses this restriction leads to the use of a rotation tensor in order to enforce the inextensibility constraint. The rotation tensor is then parametrized by mean of rotational degrees of freedom. Depending on the kind of parametrization singularities or other rank-deficiency problems can arise during the deformation (see Betsch et al. [111]).

On the other hand, the application of 3D constitutive equations in shell theories is of special importance (specifically when material nonlinearities are considered) since problems related to the incorporation of the plane stress assumption can be automatically avoided. The use of rotational degrees of freedom is circumvented and the plane stress condition is achieved numerically. As the thickness becomes small, numerical solutions must coincide with those resulting from geometrically exact shell theories using parametrizations of a rotation tensor together with the plane stress assumption [112]. All these features make shell theories with 3D constitutive laws attractive for applications to finite deformations of shells and, therefore, it will be adopted in the present dissertation.

Most formulations of finite rotation shell theories are restricted to isotropic materials with few cases of multilayered composite materials [18-20, 106]. However until now, no applications for functionally graded shells with finite deformations are found in the literature. The finite element implementation of this approach is given in Chapter V.

A. Notation and geometric relations

The term *Euclidean point space* applies to a set $\mathcal{E}$, with elements called *points*, which is related to a *Euclidean vector space* $\mathscr{V}$. The space $\mathcal{E}$ is also a *Euclidean manifold* if it is equipped with a family of C^r-charts [113]. The space $\mathscr{V}$ can be seen as a translation (or tangent) space of $\mathcal{E}$. The set $\mathbb{R}^3$ is the triple Cartesian product of the space $\mathbb{R}$.

Let $\mathscr{B}$ be an open set in some topological space defining a *body* and consisting of material particles $X, Y, \ldots \in \mathscr{B}$. The body $\mathscr{B}$ is considered in a reference configuration $\kappa_R : \mathscr{B} \rightarrow \mathscr{B}_R \subset \mathcal{E}$ and a current configuration $\kappa_t : \mathscr{B} \rightarrow \mathscr{B}_t \subset \mathcal{E}$, where $\mathscr{B}_R$ and $\mathscr{B}_t$ are regions (also called placements) of the Euclidean point space $\mathcal{E}$ that is occupied by the body $\mathscr{B}$ [114, 115].

We denote by **X** the place given to the point X by the reference configuration. Then

$$\mathbf{X} = \kappa_R\left(X\right). \tag{4.1}$$

Since κ_R is, by assumption, continuous and invertible

$$X = \kappa_R^{-1}\left(\mathbf{X}\right). \tag{4.2}$$

We define a motion of $\mathscr{B}$ as a mapping of the points comprised by $\mathscr{B}$ onto points of a three-dimensional Euclidean space $\mathcal{E}$ at the time *t*, i.e.

$$\mathbf{x} = \kappa_t\left(X, t\right) \qquad \forall\, X \in \mathscr{B}, \quad \forall\, t \in \mathbb{R}. \tag{4.3}$$

Substituting equation (4.2) into (4.3) we obtain

$$\mathbf{x} = \kappa_t\left(\kappa_R^{-1}\left(\mathbf{X}\right), t\right) := \chi\left(\mathbf{X}, t\right). \tag{4.4}$$

Note that the motion χ also denotes a composition of mappings $\chi = \kappa_t \circ \kappa_R^{-1}$.

In this dissertation we consider a body in which at any time *t* one dimension of the region $\mathscr{B}_R$ as well as of the family of regions $\mathscr{B}_t$ is always much smaller than the other two. Such a body $\mathscr{B}$ will be called a *shell* (or shell-like body).

Let us introduce in the region $\mathscr{B}_R(\mathscr{B}_t)$ a *convected* curvilinear coordinate system $\{\theta^i\}$, $i = 1,2,3$, such that the surface $\theta^3 = 0$ define the midsurface $\mathscr{M}_R(\mathscr{M}_t)$ of the region $\mathscr{B}_R(\mathscr{B}_t)$. The coordinate θ^3 is the measure of distance between points $P \in \mathscr{B}_R$ $(\bar{P} \in \mathscr{B}_t)$ and $M \in \mathscr{M}_R$ $(\bar{M} \in \mathscr{M}_t)$, with $-h/2 \leq \theta^3 \leq h/2$, where *h* is the thickness of the shell (Fig. 4.1).

We can think that the convected coordinate system moves and deforms continuously with the shell as it passes from the reference placement $\mathscr{B}_R$ to the deformed one $\mathscr{B}_t$. The values of these coordinates, defining a generic point $P \in \mathscr{B}_R$, remain constant as *P* moves to its new position denoted by $\bar{P} \in \mathscr{B}_t$. Fibers are lines of particles in θ^3 direction extending from the bottom surface to its top surface. Thus, these fibers are represented by θ^3 lines in the reference configuration and θ^3 curves in the current configuration. Initially, they are normal to the midsurface but, after deformation, they become, in general, curved and no longer orthogonal to the midsurface $(\mathscr{M}_t)$ because of the shear deformation (see Naghdi [46] and Pietraszkiewicz [2]).

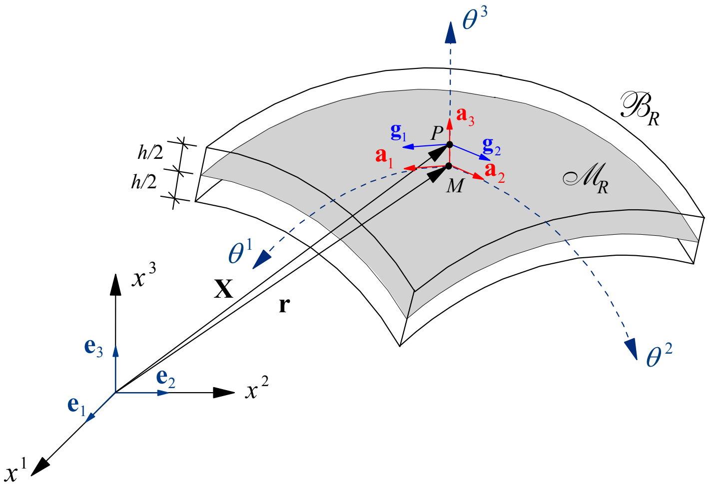

Fig. 4.1. Shell continuum in the reference configuration.

Geometric quantities of the region $\mathscr{B}_R$ are denoted by the position vector $\mathbf{X}(\theta^i)$, which is used to define the natural (or covariant) base vectors $\mathbf{g}_i$, dual (or contravariant) base vectors $\mathbf{g}^i$, components $g_{ij}, \delta_i^j, g^{ij}$ of the metric tensor, Christoffel symbols $\Gamma_{ij}^k, \Gamma_{ijk}$, spatial covariant derivative operation $(\circ)_{\|i}$ as well as other quantities discussed in detail in Refs. [46, 47, 49]. Some of these relations are presented below

$$
\begin{gathered}
\mathbf{g}_i = \frac{\partial \mathbf{X}}{\partial \theta^i} = \mathbf{X}_{,i}, \quad \mathbf{X} = \mathbf{X}\left(\theta^1, \theta^2, \theta^3\right) \\
g_{ij} = \mathbf{g}_i \cdot \mathbf{g}_j, \quad g^{ij} = \mathbf{g}^i \cdot \mathbf{g}^j, \quad \mathbf{g}^i \cdot \mathbf{g}_j = \delta_j^i \\
\mathbf{g}_{i,j} = \Gamma_{ijk}\, \mathbf{g}^k = \Gamma_{ij}^k\, \mathbf{g}_k, \quad \mathbf{g}^i{}_{,j} = -\Gamma_{jk}^i\, \mathbf{g}^k \\
\Gamma_{ijk} = g_{mk} \Gamma_{ij}^m = \frac{1}{2}(g_{ik,j} + g_{jk,i} - g_{ij,k}) = \mathbf{g}_{i,j} \cdot \mathbf{g}_k \\
\Gamma_{ij}^m = g^{ml} \Gamma_{lij} = \mathbf{g}_{i,j} \cdot \mathbf{g}^k, \quad g = \det\left(g_{ij}\right).
\end{gathered}
\tag{4.5}
$$

On the other hand, quantities describing the surface $\mathscr{M}_R$ are defined by the position vector $\mathbf{r}(\theta^\alpha)$ of the surface points. With the aid of this vector we define the natural (or covariant) base vectors $\mathbf{a}_\alpha$, dual (or contravariant) base vectors $\mathbf{a}^\alpha$, unit vector $\mathbf{a}_3 = \mathbf{a}^3$ normal to $\mathscr{M}_R$, coefficients $a_{\alpha\beta}$ and $b_{\alpha\beta}$ of the first and second fundamental forms, Christoffel symbols $\overline{\Gamma}^{\lambda}_{\alpha\beta}, \overline{\Gamma}_{\alpha\beta\lambda}$ with respect to the midsurface ($\theta^3 = 0$), surface covariant derivative operation $(\circ)_{|i}$ and also other quantities that can be utilized in this dissertation and that we show below

$$
\begin{gathered}
\mathbf{a}_{\alpha} = \frac{\partial \mathbf{r}}{\partial \theta^{\alpha}} = \mathbf{r}_{,\alpha}, \quad \mathbf{r} = \mathbf{r}\left(\theta^1, \theta^2\right) \\
a_{\alpha\beta} = \mathbf{a}_{\alpha} \cdot \mathbf{a}_{\beta}, \quad a^{\alpha\beta} = \mathbf{a}^{\alpha} \cdot \mathbf{a}^{\beta}, \quad \mathbf{a}^{\alpha} \cdot \mathbf{a}_{\beta} = \delta^{\alpha}_{\beta} \\
\mathbf{a}_{\alpha,\beta} = \overline{\Gamma}_{\alpha\beta\lambda}\, \mathbf{a}^{\lambda} = \overline{\Gamma}^{\lambda}_{\alpha\beta}\, \mathbf{a}_{\lambda}, \quad \mathbf{a}^{\alpha}{}_{,\beta} = -\overline{\Gamma}^{\alpha}_{\beta\mu}\, \mathbf{a}^{\mu} \\
\overline{\Gamma}_{\alpha\beta\gamma} = a_{\mu\gamma} \overline{\Gamma}^{\mu}_{\alpha\beta} = \frac{1}{2}(a_{\alpha\gamma,\beta} + a_{\beta\lambda,\alpha} - a_{\alpha\beta,\lambda}) = \mathbf{a}_{\alpha,\beta} \cdot \mathbf{a}_{\lambda} \\
\overline{\Gamma}^{\mu}_{\alpha\beta} = a^{\lambda\mu}\, \overline{\Gamma}_{\lambda\alpha\beta} = \mathbf{a}_{\alpha,\beta} \cdot \mathbf{a}^{\mu}, \quad a = \det\left(a_{\alpha\beta}\right) \\
b_{\alpha\beta} = \mathbf{a}_{\alpha,\beta} \cdot \mathbf{a}_3 = -\mathbf{a}_{\alpha} \cdot \mathbf{a}_{3,\beta}, \quad b^{\alpha}_{\beta} = \overline{\Gamma}^{\alpha}_{\beta 3} = a^{\alpha\mu} b_{\mu\beta}.
\end{gathered}
\tag{4.6}
$$

We also observe that for shell theories the convected coordinates system θ^i can always be chosen in the reference configuration in an appropriate way (Naghdi [46]). Hence, without loss of generality we may write the position vector in the region $\mathscr{B}_R$ as

$$
\mathbf{X} = \mathbf{r} + \theta^3 \mathbf{a}_3. \tag{4.7}
$$

In what follows we shall use some concepts and relations of tensor algebra and tensor analysis in the three-dimensional Euclidean point space $\mathcal{E}$ expressed directly in an absolute notation (see Refs. [116, 117]). The absolute tensor notation is independent of any coordinate system and it makes possible to present many known relations in a very simple and compact way.

Now we define the tensor product $\otimes$ of two vectors $\mathbf{u}, \mathbf{v} \in \mathscr{V}$ which gives a three-dimensional Euclidean tensor $\mathbf{u} \otimes \mathbf{v} \in \mathscr{T}^2 \equiv \mathscr{V} \otimes \mathscr{V}$ of second order. We can express this product as

$$
(\mathbf{u} \otimes \mathbf{v})\mathbf{w} = \mathbf{u}(\mathbf{v} \cdot \mathbf{w}) \tag{4.8}
$$

for each $\mathbf{w} \in \mathscr{V}$. If $\mathbf{g}_i, \mathbf{g}^i, \mathbf{a}_i, \ldots (i = 1,2,3)$ are bases of $\mathscr{V}$ then any set of nine tensors of the type $\mathbf{g}_i \otimes \mathbf{g}_j, \mathbf{g}_i \otimes \mathbf{a}_j, \mathbf{a}_i \otimes \mathbf{g}^j, \ldots \in \mathscr{T}^2$ are bases of the space $\mathscr{T}^2$. Hence, any tensor $\mathbf{T} \in \mathscr{T}^2$ can be represented in the form

$$\mathbf{T} = T^{ij}\mathbf{g}_i \otimes \mathbf{g}_j = T^{ia}\mathbf{g}_i \otimes \mathbf{a}_a = T^a_j \mathbf{a}_a \otimes \mathbf{g}^j = \cdots. \tag{4.9}$$

The metric tensor $\mathbf{1} \in \mathscr{T}^2$ in the region $\mathscr{B}_R$ can be conveniently represented in three different ways

$$\begin{aligned} \mathbf{1} &= g_{ij}\mathbf{g}^i \otimes \mathbf{g}^j = \mathbf{g}_i \otimes \mathbf{g}^i \\ &= a_{kl}\mathbf{a}^k \otimes \mathbf{a}^l = \mathbf{a}_k \otimes \mathbf{a}^k \\ &= \mu^a_i \mathbf{a}_a \otimes \mathbf{g}^i = \mu^j_b \mathbf{g}_j \otimes \mathbf{a}^b. \end{aligned} \tag{4.10}$$

We also use the notation $\mathbf{G}$ for *the Riemannian metric* in the reference configuration such that

$$\mathbf{G} = g_{ij}\mathbf{g}^i \otimes \mathbf{g}^j. \tag{4.11}$$

Note that the distinction between $\mathbf{G}$ and $\mathbf{1}$ is purely formal since $\mathbf{G} = \mathbf{1}$ (see Başar and Weichert [118]). Taking the derivative of Eq. (4.7) with respect to θ^i and using Eqs. (4.5), (4.6) and (4.10) we obtain the following relations

$$\begin{gathered} \mathbf{g}_i = \mu^a_i \mathbf{a}_a, \quad \mathbf{g}^j = \mu^j_b \mathbf{a}^b \\ g_{ij} = \mu^a_i \mu^b_j a_{ab}, \quad g^{ij} = \mu^i_a \mu^j_b a^{ab} \end{gathered} \tag{4.12}$$

where

$$\begin{gathered} g_{33} = g^{33} = a_{33} = a^{33} = \mu^3_3 = 1 \\ g_{\varphi 3} = g^{\varphi 3} = a_{\alpha 3} = a^{\alpha 3} = \mu^3_\beta = \mu^\beta_3 = 0 \\ \mathbf{g}_3 = \mathbf{g}^3 = \mathbf{a}_3 = \mathbf{a}^3 \\ \mu^\alpha_\varphi = \mathbf{a}^\alpha \cdot \mathbf{g}_\varphi = \delta^\alpha_\varphi - \theta^3 b^\alpha_\varphi. \end{gathered} \tag{4.13}$$

Symbols of the type μ^a_i, μ^j_b are called “shifters” or “translators”. It is obvious from (4.10) that they are components of the metric tensor $\mathbf{1} \in \mathscr{T}^2$ in mixed basis.

Next we define the symmetric shifter tensor $\boldsymbol{\mu} \in \mathscr{T}^2$, which is a two-point tensor that transforms bases from the surface $\mathscr{M}_R$ to the region $\mathscr{B}_R$. It can be written as follows

$$\begin{gathered}\boldsymbol{\mu} = \mathbf{g}_i \otimes \mathbf{a}^i, \quad \boldsymbol{\mu}^{-1} = \mathbf{a}_i \otimes \mathbf{g}^i \\ \boldsymbol{\mu} = \mu_a^b \mathbf{a}_b \otimes \mathbf{a}^a\end{gathered} \tag{4.14}$$

and

$$\mathbf{g}_i = \boldsymbol{\mu}\,\mathbf{a}_i, \quad \mathbf{g}^j = \boldsymbol{\mu}^{-T}\mathbf{a}^j, \quad \mathbf{a}_a = \boldsymbol{\mu}^{-1}\mathbf{g}_a, \quad \mathbf{a}^b = \boldsymbol{\mu}^T\,\mathbf{g}^b. \tag{4.15}$$

In addition, let us introduce the metric tensor $\mathbf{A}$ and the curvature tensor $\mathbf{B}$ of the surface $\mathscr{M}_R$ as

$$\begin{gathered}\mathbf{A} = a_{\alpha\beta}\mathbf{a}^\alpha \otimes \mathbf{a}^\beta = \mathbf{a}_\alpha \otimes \mathbf{a}^\alpha \\ \mathbf{B} = b_{\alpha\beta}\mathbf{a}^\alpha \otimes \mathbf{a}^\beta = -\mathbf{a}_{3,\alpha} \otimes \mathbf{a}^\alpha.\end{gathered} \tag{4.16}$$

Notice that the shifter tensor can be expressed in absolute tensor notation as

$$\boldsymbol{\mu} = \mathbf{1} - \theta^3\mathbf{B} \tag{4.17}$$

which can be easily verified. Using equation (4.14) together with (4.13) we obtain

$$\begin{aligned}\boldsymbol{\mu} = \mu_j^i \mathbf{a}_i \otimes \mathbf{a}^j &= \mu_\alpha^\beta \mathbf{a}_\beta \otimes \mathbf{a}^\alpha + \mathbf{a}_3 \otimes \mathbf{a}^3 \\ &= (\delta_\alpha^\beta - \theta^3 b_\alpha^\beta)\,\mathbf{a}_\beta \otimes \mathbf{a}^\alpha + \mathbf{a}^3 \otimes \mathbf{a}^3.\end{aligned}$$

Since $\delta_\alpha^\beta = a_{\alpha\lambda}a^{\lambda\beta}$ and $b_\alpha^\beta = a^{\lambda\beta}b_{\lambda\alpha}$ equation above becomes

$$\begin{aligned}\boldsymbol{\mu} &= (a_{\alpha\lambda}a^{\lambda\beta} - \theta^3 b_{\lambda\alpha}a^{\lambda\beta})\,\mathbf{a}_\beta \otimes \mathbf{a}^\alpha + \mathbf{a}^3 \otimes \mathbf{a}^3 \\ &= (a_{\alpha\lambda} - \theta^3 b_{\lambda\alpha})(a^{\lambda\beta}\mathbf{a}_\beta) \otimes \mathbf{a}^\alpha + \mathbf{a}^3 \otimes \mathbf{a}^3 \\ &= (a_{\alpha\lambda}\mathbf{a}^\lambda \otimes \mathbf{a}^\alpha + \mathbf{a}^3 \otimes \mathbf{a}^3) - \theta^3(b_{\lambda\alpha}\mathbf{a}^\lambda \otimes \mathbf{a}^\alpha).\end{aligned}$$

Finally, using equations (4.10) and (4.16) we obtain

$$\boldsymbol{\mu} = \mathbf{1} - \theta^3\mathbf{B}$$

and the proof is completed.

B. Deformation of the shell

Consider the motion $\chi(\mathbf{X},t)$ of the shell $\mathscr{B}$ from the reference configuration $\mathscr{B}_R$ to the current configuration $\mathscr{B}_t$. Since a convected coordinate system $\{\theta^i\}$ has been adopted, geometric quantities of the region $\mathscr{B}_t$ are analogous to those defined in $\mathscr{B}_R$ (see Fig. 4.2). In order to avoid the introduction of new symbols we shall distinguish these geometric quantities by putting, in general, and additional bar: $\mathbf{x}, \bar{\mathbf{g}}_i, \bar{\mathbf{g}}^j, \bar{g}_{ij}, \bar{g}^{ij}, \bar{\mu}_\alpha^\beta$, $G_{ijk}, G_{ij}^k, (\circ)_{;\|i}, \bar{\mathbf{1}}, \bar{\mathbf{G}}, \bar{\boldsymbol{\mu}}, \ldots \text{etc}$. For these quantities, formulae analogous to (4.5) hold true. Similarly, geometric quantities for the surface $\mathscr{M}_t$ analogous to those defined for $\mathscr{M}_R$ will also be distinguished by an additional bar: $\bar{\mathbf{r}}, \bar{\mathbf{a}}_\alpha, \bar{\mathbf{a}}^\beta, \bar{\mathbf{a}}_3, \bar{a}_{ab}, \bar{a}^{ab}, \bar{b}_{\alpha\beta}, \bar{G}_{ijk}, \bar{G}_{ij}^k, (\circ)_{;|i}$, $\bar{\mathbf{A}}, \bar{\mathbf{B}}, \ldots \text{etc}$. Again relations similar to (4.6), (4.10), (4.14) and (4.16) still hold true (Pietraszkiewicz [2]).

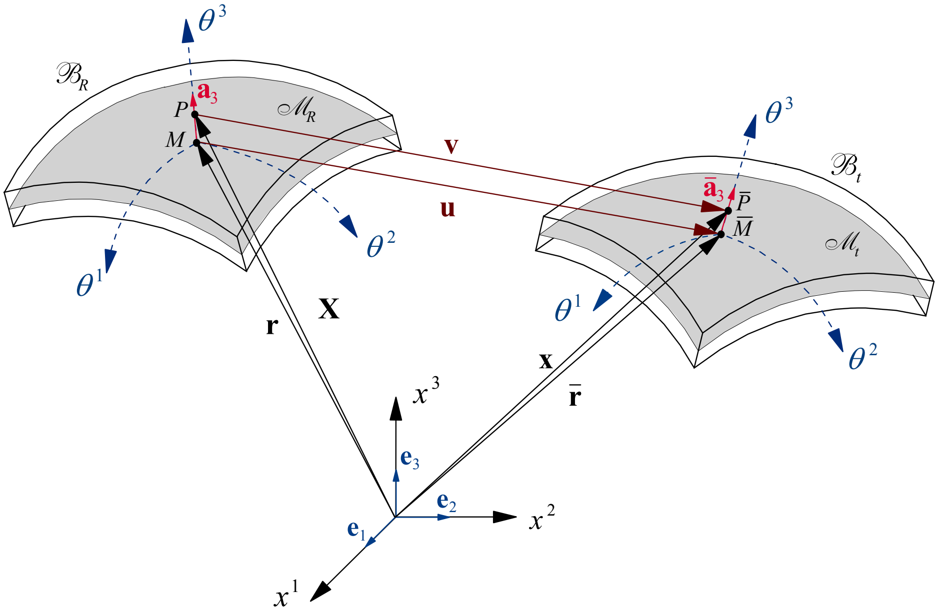

Fig. 4.2. Deformation of the shell.

In the Lagrangian description the displacement of the particle X from the reference configuration to the current configuration is given by the vector $\mathbf{v}(\mathbf{X},t)$, i.e.

$$\begin{aligned}\mathbf{v}(\mathbf{X},t) &= \chi(\mathbf{X},t) - \mathbf{X} = \mathbf{x} - \mathbf{X} \\ &= V^{i}\mathbf{g}_{i} = V_{j}\,\mathbf{g}^{j}\end{aligned} \tag{4.18}$$

given in component form with respect to the region $\mathscr{B}_R$. Taking the derivative of equation (4.18) with respect to θ^i and using relations (4.5) we obtain

$$\overline{\mathbf{g}}_i = \mathbf{g}_i + \mathbf{v}_{,i}\,. \tag{4.19}$$

The deformation gradient is defined as the tangent map of the motion $\chi(\mathbf{X},t)$ such that $\mathbf{F} := \mathcal{T}\chi : \mathcal{T}\mathscr{B}_R \rightarrow \mathcal{T}\mathscr{B}_t$. From (4.18) we have

$$\mathbf{F}(\mathbf{X},t) = \operatorname{Grad}\chi(\mathbf{X},t) = \mathbf{1} + \operatorname{Grad}\mathbf{v} \tag{4.20}$$

with $\operatorname{Grad}\mathbf{v}(\mathbf{X},t)$ being the material gradient relative to the reference configuration $\mathbf{X}$ at a fixed time t [119].

The deformation gradient is a two-point tensor which may be written as

$$\mathbf{F} = \overline{\mathbf{g}}_i \otimes \mathbf{g}^i. \tag{4.21}$$

The proof of this statement is quite simple. Since $\mathbf{1} = \mathbf{g}_i \otimes \mathbf{g}^i$ and $\operatorname{Grad}\mathbf{v} = \mathbf{v}_{,i} \otimes \mathbf{g}^i$ (see Ref. [118]) we can write Eq. (4.20) as

$$\begin{aligned}\mathbf{F} = \mathbf{1} + \operatorname{Grad}\mathbf{v} &= \mathbf{g}_i \otimes \mathbf{g}^i + \mathbf{v}_{,i} \otimes \mathbf{g}^i \\ &= (\mathbf{g}_i + \mathbf{v}_{,i}) \otimes \mathbf{g}^i = \overline{\mathbf{g}}_i \otimes \mathbf{g}^i\end{aligned}$$

where (4.19) was used in the last step.

Let the displacement vector $\mathbf{v}(\mathbf{X},t)$ be expanded into a Taylor series in the vicinity of the point $M \in \mathscr{M}_R$. Thus

$$\begin{aligned}\mathbf{v}(\theta^i) &= \sum_{k=0}^{\infty} \frac{(\theta^3)^k}{k!}\mathbf{v}^{(k)}|_{\theta^3=0} \\ &= \mathbf{v}^{(0)}|_{\theta^3=0} + \theta^3\mathbf{v}^{(1)}|_{\theta^3=0} + \frac{(\theta^3)^2}{2}\mathbf{v}^{(2)}|_{\theta^3=0} + \cdots\end{aligned} \tag{4.22}$$

where $\mathbf{v}^{(k)} = \partial^k \mathbf{v} / \partial(\theta^3)^k$. Without loss of generality this equation may also be written as follow

$$\mathbf{v}\left(\theta^i\right) = \mathbf{u}^0\left(\theta^\alpha\right) + \theta^3\mathbf{u}^1\left(\theta^\alpha\right) + (\theta^3)^2\mathbf{u}^2\left(\theta^\alpha\right) + (\theta^3)^3\mathbf{u}^3\left(\theta^\alpha\right) + \cdots. \qquad (4.23)$$

Some researchers utilize the Taylor expansion of the position vector of the current configuration instead of the displacement field, i.e.

$$\mathbf{x}\left(\theta^i\right) = \mathbf{x}^0\left(\theta^\alpha\right) + \theta^3\mathbf{x}^1\left(\theta^\alpha\right) + (\theta^3)^2\mathbf{x}^2\left(\theta^\alpha\right) + (\theta^3)^3\mathbf{x}^3\left(\theta^\alpha\right) + \cdots. \qquad (4.24)$$

Both approaches are equivalent since $\mathbf{x}$ and $\mathbf{v}$ are related by (4.18) and (4.7).

Equation (4.23) or its equivalent (4.24) is, indeed, a reduction from a 3D continuum theory to a 2D one. Shell equations are now governed by the position vector of the midsurface $\mathscr{M}_t$ and denoted by $\mathbf{x}^0$ (in this dissertation we call it $\bar{\mathbf{r}}$), and some directors $\mathbf{x}^i\,(i = 1,\, k)$, where k is the order of approximation considered in the formulation. It is argued (see Naghdi [46]) that as $k \to \infty$ the exact motion of the three-dimensional body is recovered.

Next we introduce the first assumption for the shell model:

Assumption 1: The displacement field is considered as a linear expansion of the thickness coordinate around the midsurface ($k = 1$). The transverse displacement is parabolic through the thickness of the shell.

This assumption implies that

$$\mathbf{v}\left(\theta^\alpha\right) = \mathbf{u}\left(\theta^\alpha\right) + \theta^3\boldsymbol{\varphi}\left(\theta^\alpha\right) \underline{+ (\theta^3)^2\underline{\boldsymbol{\psi}}\left(\theta^\alpha\right)} \qquad (4.25a)$$

where $\mathbf{u}^0$ and $\mathbf{u}^1$ have been renamed $\mathbf{u}$ and $\boldsymbol{\varphi}$ respectively, and

$$\mathbf{u}\left(\theta^\alpha\right) = u_i\mathbf{a}^i, \quad \boldsymbol{\varphi}\left(\theta^\alpha\right) = \varphi_i\mathbf{a}^i, \quad \underline{\boldsymbol{\psi}}\left(\theta^\alpha\right) = \psi_3\,\mathbf{a}^3. \qquad (4.25b)$$

The underlined term of (4.25a) is included to avoid undesired stiffening effects. The 6-parameter formulation has a severe deficiency in bending dominated cases with nonvanishing Poisson's ratio *v*. The linear displacement field in the thickness direction results in a constant normal strain which in turn causes artificial stresses in that direction. This problem is called Poisson locking (Bischoff and Ramm [24]).

In contrast to other locking problems, errors caused by Poisson locking do not diminish with mesh refinement. This is due to the fact that the origin of the stiffening lies in the theory itself rather than the numerical solution. To remedy this effect we can either use enhanced strain methods or include an additional variable in the formulation assuming a quadratically distributed transverse displacement. For the present approach we adopt the latter case. Hence, the improvement in the approach is carried out in the shell theory, not in the numerical approximation (Sansour and Kollmann [112]).

The position vector of the deformed shell can be obtained substituting equations (4.7) and (4.25a) into (4.18). Thus

$$\begin{aligned}\mathbf{x} &= (\mathbf{r}+\mathbf{u}) + \theta^3(\mathbf{a}_3 + \boldsymbol{\varphi}) + (\theta^3)^2 \underline{\boldsymbol{\psi}} \\ &= \bar{\mathbf{r}} + \theta^3 \bar{\mathbf{a}}_3 + (\theta^3)^2 \underline{\boldsymbol{\psi}}\end{aligned} \tag{4.26}$$

where $\bar{\mathbf{r}} = \mathbf{r} + \mathbf{u}$ and $\bar{\mathbf{a}}_3 = \mathbf{a}_3 + \boldsymbol{\varphi}$. The vector $\boldsymbol{\varphi}$ is also called difference vector (change of the director of the midsurface). It is worthy to point out that the vector $\bar{\mathbf{a}}_3$ is, in general, neither a unit vector nor orthogonal to $\mathscr{M}_t$.

Note that the configuration of the shell is uniquely determined by the displacement vector $\mathbf{u}$ of the midsurface together with the difference vector $\boldsymbol{\varphi}$ and the additional variable $\underline{\boldsymbol{\psi}}$, i.e. by seven independent components of these vectors.

The deformation gradient $\mathbf{F}$ can be decomposed through equations (4.15) and (4.21) as follows

$$\begin{aligned}\mathbf{F} &= \bar{\mathbf{g}}_i \otimes \mathbf{g}^i = \bar{\mathbf{g}}_i \otimes (\boldsymbol{\mu}^{-T}\mathbf{a}^i) \\ &= (\bar{\mathbf{g}}_i \otimes \mathbf{a}^i)\boldsymbol{\mu}^{-1} = \bar{\boldsymbol{\mu}}(\bar{\mathbf{a}}_i \otimes \mathbf{a}^i)\boldsymbol{\mu}^{-1} \\ &= \bar{\boldsymbol{\mu}}\mathbf{F}^0\boldsymbol{\mu}^{-1}\end{aligned} \tag{4.27}$$

where $\mathbf{F}^0$ is the surface deformation gradient tensor and is defined by

$$\mathbf{F}^0 := \mathbf{F}|_{\theta^3=0} = \overline{\mathbf{a}}_i \otimes \mathbf{a}^i. \tag{4.28}$$

The tensor $\mathbf{F}^0$ can be seen as a tangent map of the motion of the midsurface $\mathscr{M}$. Using equation (4.27) we can obtain

$$\mathbf{F} = (\overline{\mathbf{g}}_i \otimes \mathbf{a}^i)\boldsymbol{\mu}^{-1} = \hat{\mathbf{F}}\,\boldsymbol{\mu}^{-1} \tag{4.29}$$

which will be used in the next section.

C. Lagrangian description

In the Lagrangian formulation all kinematic variables are referred to initial configuration (that the body occupies at time $t = 0$). On the contrary, Eulerian formulations use the final configuration to this end (usually utilized in fluid mechanics).

Next we define the *right Cauchy-Green tensor* $\mathbf{C}$ and the *right stretch tensor* $\mathbf{U}$ as

$$\mathbf{C} = \mathbf{F}^T\mathbf{F}, \quad \mathbf{U}^2 = \mathbf{C}. \tag{4.30}$$

Both tensors are symmetric and positive definite.

We now introduce the Green strain tensor $\mathbf{E}$ as a measure of the strain which is suitable for a material description. That is

$$\begin{aligned} \mathbf{E} &= \frac{1}{2}(\mathbf{C} - \mathbf{G}) \\ &= \frac{1}{2}(\mathbf{F}^T\mathbf{F} - \mathbf{G}) \end{aligned} \tag{4.31}$$

which is a symmetric tensor by definition.

One interpretation of the right Cauchy-Green tensor $\mathbf{C}$ is as the convected metric tensor (Marsden and Hughes [120], Fox [60]). The convected metric tensor can be seen as the *pull-back* of the covariant metric tensor $\overline{\mathbf{G}}$. Thus

$$\begin{aligned}\mathbf{C} &= \Phi^{*}\left(\overline{\mathbf{G}}\right) = \mathbf{F}^{T}\overline{\mathbf{G}}\mathbf{F} \\ &= \mathbf{F}^{T}(\overline{g}_{ij}\,\overline{\mathbf{g}}^{i}\otimes\overline{\mathbf{g}}^{j})\,\mathbf{F} \\ &= \overline{g}_{ij}\,\mathbf{g}^{i}\otimes\mathbf{g}^{j}\end{aligned} \tag{4.32}$$

where $\Phi^{*}\left(\circ\right)$ is the pull-back operator.

For the definition of the pull-back and push-forward operators the reader can consult the books of Başar and Weichert [118] and Holzapfel [119]. The intrinsic meaning of the Green strain tensor is one haft of the difference between the convected metric tensor and reference metric tensor. Since $\mathbf{G} = g_{ij}\,\mathbf{g}^{i}\otimes\mathbf{g}^{j}$ the Green strain tensor can be expressed in components relative to the reference dual basis as

$$\mathbf{E} = \frac{1}{2}\,(\overline{g}_{ij} - g_{ij})\,\mathbf{g}^{i}\otimes\mathbf{g}^{j} \tag{4.33}$$

usually used in shell theories.

Another suitable measure of the strain in the material description is the *Biot* strain tensor [118] which is given by

$$\mathbf{H} = \mathbf{U} - \mathbf{G} \tag{4.34}$$

where $\mathbf{U}$ is denoted in (4.30). This tensor is closer to the engineering definition of the strain tensor.

For the Eulerian description the strain state is described by the *Euler-Almansi* strain tensor $\mathbf{e}$ defined as

$$\mathbf{e} = \frac{1}{2}\,(\overline{\mathbf{G}} - \mathbf{b}^{-1}) \tag{4.35}$$

where $\mathbf{b} = \mathbf{F}\mathbf{F}^{T}$ is the *left Cauchy-Green tensor* which is symmetric and positive definite. The Almansi strain tensor can be seen as the push-forward of the covariant tensor $\mathbf{E}$, i.e.

$$\begin{aligned}\mathbf{e} &= \frac{1}{2}(\overline{\mathbf{G}} - \mathbf{F}^{-T}\mathbf{F}^{-1}) \\ &= \mathbf{F}^{-T}\left[\frac{1}{2}(\mathbf{F}^{T}\mathbf{F} - \mathbf{G})\right]\mathbf{F}^{-1} \\ &= \mathbf{F}^{-T}\mathbf{E}\mathbf{F}^{-1} = \Phi_{*}\left(\mathbf{E}\right)\end{aligned} \tag{4.36}$$

and the Green tensor as the pull-back of the covariant tensor $\mathbf{e}$

$$\mathbf{E} = \mathbf{F}^{T}\mathbf{e}\,\mathbf{F} = \Phi^{*}\left(\mathbf{e}\right). \tag{4.37}$$

An equivalent expression of (4.33) can be obtained for the Almansi strain tensor by using the base vectors $\overline{\mathbf{g}}^{i}$ in the current configuration.

Let equation (4.33) be expanded by the components of the Green strain tensor

$$E_{ij} = \frac{1}{2}(\overline{g}_{ij} - g_{ij}) = \frac{1}{2}(\overline{\mathbf{g}}_{i}\cdot\overline{\mathbf{g}}_{j} - \mathbf{g}_{i}\cdot\mathbf{g}_{j}) \tag{4.38}$$

as follows

$$\begin{aligned}E_{\alpha\beta} &= \frac{1}{2}(\overline{\mathbf{g}}_{\alpha}\cdot\overline{\mathbf{g}}_{\beta} - \mathbf{g}_{\alpha}\cdot\mathbf{g}_{\beta}) \\ E_{\alpha 3} = E_{3\alpha} &= \frac{1}{2}(\overline{\mathbf{g}}_{3}\cdot\overline{\mathbf{g}}_{\alpha} - \mathbf{g}_{3}\cdot\mathbf{g}_{\alpha}) \\ E_{33} &= \frac{1}{2}(\overline{\mathbf{g}}_{3}\cdot\overline{\mathbf{g}}_{3} - \mathbf{g}_{3}\cdot\mathbf{g}_{3}).\end{aligned} \tag{4.39}$$

Since $\overline{\mathbf{g}}_{i}$ and $\mathbf{g}_{i}$ are functions of θ^{3} we can write E_{ij} as

$$\begin{aligned}E_{\alpha\beta} &= \sum_{k=0}^{4}(\theta^{3})^{k}\varepsilon_{\alpha\beta}^{(k)} \\ E_{\alpha 3} &= \sum_{k=0}^{3}(\theta^{3})^{k}\varepsilon_{\alpha 3}^{(k)} \\ E_{33} &= \sum_{k=0}^{2}(\theta^{3})^{k}\varepsilon_{33}^{(k)}.\end{aligned} \tag{4.40}$$

By means of the identities $\mathbf{a}_{3}\cdot\mathbf{a}_{3,\alpha} = 0$ and $\mathbf{a}_{\alpha}\cdot\mathbf{a}_{3,\beta} = \mathbf{a}_{\beta}\cdot\mathbf{a}_{3,\alpha}$ we finally obtain the component form of the Green strain tensor, namely

$$
\begin{aligned}
\varepsilon_{\alpha\beta}^{(0)} &= \frac{1}{2}(\bar{\mathbf{a}}_{\alpha}\cdot\bar{\mathbf{a}}_{\beta} - \mathbf{a}_{\alpha}\cdot\mathbf{a}_{\beta}) \\
\varepsilon_{\alpha\beta}^{(1)} &= \frac{1}{2}(\bar{\mathbf{a}}_{\alpha}\cdot\bar{\mathbf{a}}_{3,\beta} + \bar{\mathbf{a}}_{\beta}\cdot\bar{\mathbf{a}}_{3,\alpha} - 2\,\mathbf{a}_{3,\alpha}\cdot\mathbf{a}_{\beta}) \\
\varepsilon_{\alpha\beta}^{(2)} &= \frac{1}{2}(\bar{\mathbf{a}}_{3,\alpha}\cdot\bar{\mathbf{a}}_{3,\beta} + \underline{\boldsymbol{\psi}}_{,\alpha}\cdot\bar{\mathbf{a}}_{\beta} + \underline{\boldsymbol{\psi}}_{,\beta}\cdot\bar{\mathbf{a}}_{\alpha} - \mathbf{a}_{3,\alpha}\cdot\mathbf{a}_{3,\beta}) \\
\varepsilon_{\alpha\beta}^{(3)} &= \frac{1}{2}(\underline{\boldsymbol{\psi}}_{,\alpha}\cdot\bar{\mathbf{a}}_{3,\beta} + \underline{\boldsymbol{\psi}}_{,\beta}\cdot\bar{\mathbf{a}}_{3,\alpha}) \\
\varepsilon_{\alpha\beta}^{(4)} &= \frac{1}{2}(\underline{\boldsymbol{\psi}}_{,\alpha}\cdot\underline{\boldsymbol{\psi}}_{,\beta}) \\
\varepsilon_{\alpha 3}^{(0)} &= \frac{1}{2}(\bar{\mathbf{a}}_{\alpha}\cdot\bar{\mathbf{a}}_{3}) \\
\varepsilon_{\alpha 3}^{(1)} &= \frac{1}{2}(\bar{\mathbf{a}}_{3,\alpha}\cdot\bar{\mathbf{a}}_{3} + 2\,\bar{\mathbf{a}}_{\alpha}\cdot\underline{\boldsymbol{\psi}}) \\
\varepsilon_{\alpha 3}^{(2)} &= \frac{1}{2}(\underline{\boldsymbol{\psi}}_{,\alpha}\cdot\bar{\mathbf{a}}_{3} + 2\,\bar{\mathbf{a}}_{3,\alpha}\cdot\underline{\boldsymbol{\psi}}) \\
\varepsilon_{\alpha 3}^{(3)} &= (\underline{\boldsymbol{\psi}}_{,\alpha}\cdot\underline{\boldsymbol{\psi}}) \\
\varepsilon_{33}^{(0)} &= \frac{1}{2}(\bar{\mathbf{a}}_{3}\cdot\bar{\mathbf{a}}_{3} - 1) \\
\varepsilon_{33}^{(1)} &= (2\,\bar{\mathbf{a}}_{3}\cdot\underline{\boldsymbol{\psi}}) \\
\varepsilon_{33}^{(2)} &= (2\,\underline{\boldsymbol{\psi}}\cdot\underline{\boldsymbol{\psi}})
\end{aligned}
\tag{4.41}
$$

where equations $\bar{\mathbf{g}}_{\alpha} = \bar{\mathbf{a}}_{\alpha} + \theta^{3}\,\bar{\mathbf{a}}_{3,\alpha} + (\theta^{3})^{2}\,\underline{\boldsymbol{\psi}}_{,\alpha}$ and $\mathbf{g}_{\alpha} = \mathbf{a}_{\alpha} + \theta^{3}\,\mathbf{a}_{3,\alpha}$ were utilized.

The displacement of the midsurface $\mathbf{u}$, the difference vector $\boldsymbol{\varphi}$ and $\underline{\boldsymbol{\psi}}$ can be written in terms of the contravariant base vectors $\mathbf{a}^{i}$ as

$$
\begin{aligned}
\mathbf{u} &= u_{\lambda}\mathbf{a}^{\lambda} + u_{3}\mathbf{a}^{3} \\
\boldsymbol{\varphi} &= \varphi_{\lambda}\mathbf{a}^{\lambda} + \varphi_{3}\mathbf{a}^{3} \\
\underline{\boldsymbol{\psi}} &= \psi_{3}\mathbf{a}^{3}.
\end{aligned}
\tag{4.42}
$$

Furthermore, their respective surface covariant derivatives are

$$
\begin{aligned}
\mathbf{u}_{,\alpha} &= (u_{\lambda|\alpha} - b_{\alpha\lambda}u_{3})\,\mathbf{a}^{\lambda} + (u_{3,\alpha} + b_{\alpha}^{\lambda}u_{\lambda})\,\mathbf{a}^{3} \\
\boldsymbol{\varphi}_{,\alpha} &= (\varphi_{\lambda|\alpha} - b_{\alpha\lambda}\varphi_{3})\,\mathbf{a}^{\lambda} + (\varphi_{3,\alpha} + b_{\alpha}^{\lambda}\varphi_{\lambda})\,\mathbf{a}^{3} \\
\underline{\boldsymbol{\psi}}_{,\alpha} &= -b_{\alpha\lambda}\psi_{3}\,\mathbf{a}^{\lambda} + \psi_{3,\alpha}\,\mathbf{a}^{3}
\end{aligned}
\tag{4.43}
$$

with components of the surface covariant derivative defined as

$$\begin{aligned} u_{\lambda|\alpha} &= u_{\lambda,\alpha} - \overline{\Gamma}^{\mu}_{\lambda\alpha} u_{\mu} \\ \varphi_{\lambda|\alpha} &= \varphi_{\lambda,\alpha} - \overline{\Gamma}^{\mu}_{\lambda\alpha} \varphi_{\mu} . \end{aligned} \tag{4.44}$$

The second assumption for the shell model is the following:

Assumption 2: Quadratic and higher-order terms in θ^3 of the Green strain tensor components are neglected.

This implies that the underlined terms of the following equation are disregarded

$$\begin{aligned} E_{\alpha\beta} &= \varepsilon^{(0)}_{\alpha\beta} + \theta^3 \varepsilon^{(1)}_{\alpha\beta} \underline{+ (\theta^3)^2 \varepsilon^{(2)}_{\alpha\beta} + (\theta^3)^3 \varepsilon^{(3)}_{\alpha\beta} + (\theta^3)^4 \varepsilon^{(4)}_{\alpha\beta}} \\ E_{\alpha 3} &= \varepsilon^{(0)}_{\alpha 3} + \theta^3 \varepsilon^{(1)}_{\alpha 3} \underline{+ (\theta^3)^2 \varepsilon^{(2)}_{\alpha 3} + (\theta^3)^3 \varepsilon^{(3)}_{\alpha 3}} \\ E_{33} &= \varepsilon^{(0)}_{33} + \theta^3 \varepsilon^{(1)}_{33} \underline{+ (\theta^3)^2 \varepsilon^{(2)}_{33}} \end{aligned} \tag{4.45}$$

i.e. we consider only linear variation through θ^3 of the Green strain tensor.

Another way to express (4.41) is in terms of the triple $\left(\mathbf{u}, \boldsymbol{\varphi}, \underline{\boldsymbol{\psi}}\right)$. In fact, using equations $\overline{\mathbf{a}}_{\alpha} = \mathbf{a}_{\alpha} + \mathbf{u}_{,\alpha}$ and $\overline{\mathbf{a}}_3 = \mathbf{a}_3 + \boldsymbol{\varphi}$ we obtain

$$\begin{aligned} \varepsilon^{(0)}_{\alpha\beta} &= \frac{1}{2} (\mathbf{a}_{\alpha} \cdot \mathbf{u}_{,\beta} + \mathbf{a}_{\beta} \cdot \mathbf{u}_{,\alpha} + \mathbf{u}_{,\alpha} \cdot \mathbf{u}_{,\beta}) \\ \varepsilon^{(1)}_{\alpha\beta} &= \frac{1}{2} (\mathbf{a}_{3,\alpha} \cdot \mathbf{u}_{,\beta} + \mathbf{a}_{3,\beta} \cdot \mathbf{u}_{,\alpha} + \mathbf{a}_{\alpha} \cdot \boldsymbol{\varphi}_{,\beta} + \mathbf{a}_{\beta} \cdot \boldsymbol{\varphi}_{,\alpha} + \boldsymbol{\varphi}_{,\beta} \cdot \mathbf{u}_{,\alpha} + \boldsymbol{\varphi}_{,\alpha} \cdot \mathbf{u}_{,\beta}) \\ \varepsilon^{(0)}_{\alpha 3} &= \frac{1}{2} (\boldsymbol{\varphi} \cdot \mathbf{u}_{,\alpha} + \mathbf{a}_3 \cdot \mathbf{u}_{,\alpha} + \boldsymbol{\varphi} \cdot \mathbf{a}_{\alpha}) \\ \varepsilon^{(1)}_{\alpha 3} &= \frac{1}{2} (\mathbf{a}_{3,\alpha} \cdot \boldsymbol{\varphi} + \mathbf{a}_3 \cdot \boldsymbol{\varphi}_{,\alpha} + \boldsymbol{\varphi} \cdot \boldsymbol{\varphi}_{,\alpha} + 2 \mathbf{a}_{\alpha} \cdot \underline{\boldsymbol{\psi}} + 2 \mathbf{u}_{,\alpha} \cdot \underline{\boldsymbol{\psi}}) \\ \varepsilon^{(0)}_{33} &= \frac{1}{2} (2 \mathbf{a}_3 \cdot \boldsymbol{\varphi} + \boldsymbol{\varphi} \cdot \boldsymbol{\varphi}) \\ \varepsilon^{(1)}_{33} &= (2 \mathbf{a}_3 \cdot \underline{\boldsymbol{\psi}} + 2 \boldsymbol{\varphi} \cdot \underline{\boldsymbol{\psi}}) . \end{aligned} \tag{4.46}$$

With the help of (4.42) and (4.43), Eq. (4.46) is written directly in terms of the seven components of the displacement field. This leads to (see Habip [121, 122])

$$
\begin{aligned}
\varepsilon_{\alpha\beta}^{(0)} &= \frac{1}{2}\Big(u_{\alpha|\beta} + u_{\beta|\alpha} - 2b_{\alpha\beta}u_3 + a^{\lambda\gamma}u_{\lambda|\alpha}u_{\gamma|\beta} - b_\beta^\lambda u_3 u_{\lambda|\alpha} - b_\alpha^\lambda u_3 u_{\lambda|\beta} \\
&\quad + c_{\alpha\beta}(u_3)^2 + u_{3,\alpha}u_{3,\beta} + b_\alpha^\lambda u_\lambda u_{3,\beta} + b_\beta^\lambda u_\lambda u_{3,\alpha} + b_\alpha^\lambda b_\beta^\gamma u_\lambda u_\gamma\Big) \\
\varepsilon_{\alpha\beta}^{(1)} &= \frac{1}{2}\Big(\varphi_{\alpha|\beta} + \varphi_{\beta|\alpha} - 2b_{\alpha\beta}\varphi_3 - b_\beta^\lambda u_{\lambda|\alpha} - b_\alpha^\lambda u_{\lambda|\beta} + 2c_{\alpha\beta}u_3 + a^{\lambda\gamma}u_{\lambda|\alpha}\varphi_{\gamma|\beta} \\
&\quad + a^{\lambda\gamma}u_{\lambda|\beta}\varphi_{\gamma|\alpha} - b_\beta^\lambda \varphi_3 u_{\lambda|\alpha} - b_\alpha^\lambda \varphi_3 u_{\lambda|\beta} - b_\beta^\lambda u_3 \varphi_{\lambda|\alpha} - b_\alpha^\lambda u_3 \varphi_{\lambda|\beta} + 2c_{\alpha\beta}u_3\varphi_3 \\
&\quad + u_{3,\alpha}\varphi_{3,\beta} + u_{3,\beta}\varphi_{3,\alpha} + b_\alpha^\lambda \varphi_\lambda u_{3,\beta} + b_\beta^\lambda \varphi_\lambda u_{3,\alpha} + b_\alpha^\lambda u_\lambda \varphi_{3,\beta} + b_\beta^\lambda u_\lambda \varphi_{3,\alpha} \\
&\quad + b_\alpha^\lambda b_\beta^\gamma u_\lambda \varphi_\gamma + b_\beta^\lambda b_\alpha^\gamma u_\lambda \varphi_\gamma\Big) \\
\varepsilon_{\alpha 3}^{(0)} &= \frac{1}{2}\Big(\varphi_\alpha + u_{3,\alpha} + b_\alpha^\lambda u_\lambda + a^{\lambda\gamma}u_{\lambda|\alpha}\varphi_\gamma - b_\alpha^\lambda \varphi_\lambda u_3 + \varphi_3 u_{3,\alpha} + b_\alpha^\lambda u_\lambda \varphi_3\Big) \\
\varepsilon_{\alpha 3}^{(1)} &= \frac{1}{2}\Big(\varphi_{3,\alpha} + a^{\lambda\gamma}\varphi_{\lambda|\alpha}\varphi_\gamma + \varphi_3 \varphi_{3,\alpha} + 2\psi_3 u_{3,\alpha} + 2\psi_3 b_\alpha^\lambda u_\lambda\Big) \\
\varepsilon_{33}^{(0)} &= \frac{1}{2}\Big(2\varphi_3 + a^{\lambda\gamma}\varphi_\lambda\varphi_\gamma + (\varphi_3)^2\Big) \\
\varepsilon_{33}^{(1)} &= 2\left(\psi_3 + \varphi_3\psi_3\right)
\end{aligned} \tag{4.47}
$$

where $c_{\alpha\beta} = b_{\alpha\mu}b_\beta^\mu$ is the covariant third fundamental form of the reference surface. Note that the component $\varepsilon_{33}^{(1)}$ vanishes when $\psi_3 = 0$ (6-parameter formulation).

The Green strain tensor $\mathbf{E}$ can be also represented in a different way. This can be done utilizing equation (4.29). First we write the right Cauchy-Green strain tensor as

$$
\begin{aligned}
\mathbf{C} &= \mathbf{F}^T\mathbf{F} \\
&= \boldsymbol{\mu}^{-T}(\hat{\mathbf{F}}^T\hat{\mathbf{F}})\,\boldsymbol{\mu}^{-1}.
\end{aligned} \tag{4.48}
$$

The tensor $\hat{\mathbf{F}}$ can be expanded as a function of the thickness coordinate θ^3, i.e.

$$
\begin{aligned}
\hat{\mathbf{F}} &= \overline{\mathbf{g}}_i \otimes \mathbf{a}^i \\
&= \overline{\mathbf{a}}_i \otimes \mathbf{a}^i + \theta^3(\overline{\mathbf{a}}_{3,\alpha} \otimes \mathbf{a}^\alpha + 2\underline{\boldsymbol{\psi}} \otimes \mathbf{a}^3) + (\theta^3)^2(\underline{\boldsymbol{\psi}}_{,\alpha} \otimes \mathbf{a}^\alpha) \\
&= \mathbf{F}^0 + \theta^3\mathbf{F}^1 + (\theta^3)^2\mathbf{F}^2.
\end{aligned} \tag{4.49}
$$

The tensor $\mathbf{F}^0$ was defined in (4.28).

Hence, the Green strain tensor is given by

$$\begin{aligned}\mathbf{E} &= \boldsymbol{\mu}^{-T}\frac{1}{2}(\hat{\mathbf{F}}^T\hat{\mathbf{F}} - \boldsymbol{\mu}^T\mathbf{G}\boldsymbol{\mu})\boldsymbol{\mu}^{-1} \\ &= \boldsymbol{\mu}^{-T}\hat{\mathbf{E}}\boldsymbol{\mu}^{-1}.\end{aligned} \tag{4.50}$$

The shifter $\boldsymbol{\mu}$ is a two-point tensor which relates the region $\mathscr{B}_R$ to the reference midsurface $\mathscr{M}_R$. On the other hand, the tensor $\hat{\mathbf{E}}$ denotes the pull-back (to the configuration $\mathscr{M}_R$) of the covariant Green strain tensor $\mathbf{E}$. Then

$$\hat{\mathbf{E}} = \Phi^*\left(\mathbf{E}\right) = \boldsymbol{\mu}^T\mathbf{E}\boldsymbol{\mu}. \tag{4.51}$$

Note that the tensor $\hat{\mathbf{E}}$ is a covariant tensor and it is written in terms of the contravariant base vectors $\mathbf{a}^i \otimes \mathbf{a}^j$. However, the components of $\hat{\mathbf{E}}$ are exactly the same as the Green strain tensor $\mathbf{E}$ (with basis $\mathbf{g}^i \otimes \mathbf{g}^j$).

The tensor $\hat{\mathbf{E}}$ can be expanded as a function of the coordinate θ^3, i.e.

$$\hat{\mathbf{E}} = \boldsymbol{\varepsilon}^0 + \theta^3\boldsymbol{\varepsilon}^1 \underline{+(\theta^3)^2\boldsymbol{\varepsilon}^2 + (\theta^3)^3\boldsymbol{\varepsilon}^3 + (\theta^3)^4\boldsymbol{\varepsilon}^4}. \tag{4.52}$$

The underlined terms are neglected by assumption 2. Substituting (4.17) and (4.49) into (4.50), we obtain

$$\begin{aligned}\boldsymbol{\varepsilon}^0 &= \frac{1}{2}(\mathbf{F}^{0^T}\mathbf{F}^0 - \mathbf{1}), \quad \boldsymbol{\varepsilon}^1 = \frac{1}{2}(\mathbf{F}^{0^T}\mathbf{F}^1 + \mathbf{F}^{1^T}\mathbf{F}^0 + 2\mathbf{B}) \\ \boldsymbol{\varepsilon}^2 &= \frac{1}{2}(\mathbf{F}^{0^T}\mathbf{F}^2 + \mathbf{F}^{2^T}\mathbf{F}^0 + \mathbf{F}^{1^T}\mathbf{F}^1 - \mathbf{B}^2) \\ \boldsymbol{\varepsilon}^3 &= \frac{1}{2}(\mathbf{F}^{1^T}\mathbf{F}^2 + \mathbf{F}^{2^T}\mathbf{F}^1), \quad \boldsymbol{\varepsilon}^4 = \frac{1}{2}(\mathbf{F}^{2^T}\mathbf{F}^2)\end{aligned} \tag{4.53}$$

where $\mathbf{B}$ is the symmetric curvature tensor given in (4.16).

We now consider the following decomposition

$$\begin{aligned}\boldsymbol{\varepsilon}^0 &= \varepsilon^{(0)}_{\alpha\beta}\,\mathbf{a}^\alpha \otimes \mathbf{a}^\beta + \varepsilon^{(0)}_{\alpha 3}(\mathbf{a}^\alpha \otimes \mathbf{a}^3 + \mathbf{a}^3 \otimes \mathbf{a}^\alpha) + \varepsilon^{(0)}_{33}\mathbf{a}^3 \otimes \mathbf{a}^3 \\ \boldsymbol{\varepsilon}^1 &= \varepsilon^{(1)}_{\alpha\beta}\,\mathbf{a}^\alpha \otimes \mathbf{a}^\beta + \varepsilon^{(1)}_{\alpha 3}(\mathbf{a}^\alpha \otimes \mathbf{a}^3 + \mathbf{a}^3 \otimes \mathbf{a}^\alpha) + \varepsilon^{(1)}_{33}\mathbf{a}^3 \otimes \mathbf{a}^3\end{aligned} \tag{4.54}$$

where $\varepsilon^{(i)}_{\alpha\beta}, \varepsilon^{(i)}_{\alpha 3}$ and $\varepsilon^{(i)}_{33}$ are given by (4.46) and (4.47).

D. Stress resultants and stress power

Let $\boldsymbol{\sigma}$ and $\mathbf{S}$ be the (true) *Cauchy* stress tensor and the *second Piola-Kirchhoff* stress tensor respectively. We can relate both stresses using the following equation

$$\mathbf{S} = j\,\mathbf{F}^{-1}\boldsymbol{\sigma}\mathbf{F}^{-T} \tag{4.55}$$

where $j = \det(\mathbf{F})$. The second Piola-Kirchhoff stress tensor is commonly used in Lagrangian formulations for geometrically nonlinear analysis.

The rate of internal mechanical work (*stress power*), denoted by $\mathscr{P}_{\text{int}}(t)$, in a continuum medium in the region $\mathscr{B}_t$ can be expressed as

$$\mathscr{P}_{\text{int}}(t) := \int_{\mathscr{B}_t} \boldsymbol{\sigma}\cdot\mathbf{D}\,d\bar{V}. \tag{4.56}$$

The tensor $\mathbf{D}$ is the symmetric part of the velocity gradient $\mathbf{L}$ which are denoted by

$$\begin{aligned} \mathbf{L} &:= \frac{\partial\dot{\mathbf{x}}(\mathbf{x},t)}{\partial\mathbf{x}} = \operatorname{grad}\dot{\mathbf{v}}(\mathbf{x},t) \\ \mathbf{D} &= \frac{1}{2}(\mathbf{L}+\mathbf{L}^T). \end{aligned} \tag{4.57}$$

The operator $\operatorname{grad}\dot{\mathbf{v}}$ is the spatial gradient relative to the current configuration $\mathbf{x}$ at a fixed time t.

The pair $(\boldsymbol{\sigma},\mathbf{D})$ is said to be energetically-conjugate since it produces the energy stored in the deformable body. It can be shown that the second Piola-Kirchhoff stress tensor is also energetically-conjugate to the rate of Green strain tensor $\dot{\mathbf{E}}$ (Başar and Weichert [118], Reddy [123])

$$\mathscr{P}_{\text{int}}(t) := \int_{\mathscr{B}_R} \mathbf{S}\cdot\dot{\mathbf{E}}\,dV. \tag{4.58}$$

Note that $d\bar{V} = j\,dV$. Like $\mathbf{E}$, the second Piola-Kirchhoff stress tensor $\mathbf{S}$ is transformed to the midsurface $\mathscr{M}_R$ by

$$\begin{aligned}\hat{\mathbf{S}} &= \boldsymbol{\mu}^{-1}\mathbf{S}\boldsymbol{\mu}^{-T} \\ &= \Phi^{*}\left(\mathbf{S}\right)\end{aligned} \tag{4.59}$$

which is the pull-back operator of the contravariant tensor $\mathbf{S}$.

The stress power of the three-dimensional theory may be expressed in the equivalent form

$$\begin{aligned}\mathscr{P}_{\text{int}}(t) &= \int_{\mathscr{B}_R} \mathbf{S}\cdot\dot{\mathbf{E}}\,dV \\ &= \int_{\mathscr{M}_R} (\mathbf{M}^0\cdot\dot{\boldsymbol{\varepsilon}}^0 + \mathbf{M}^1\cdot\dot{\boldsymbol{\varepsilon}}^1)\,d\Omega\end{aligned} \tag{4.60}$$

where $\mathbf{M}^n$ denote the *pseudo-stress resultant tensor* (or just stress resultant tensor) which is symmetric (whenever $\hat{\mathbf{S}}$ be symmetric) opposite to its physical counterpart. The tensor $\mathbf{M}^n$ is defined as

$$\left[\mathbf{M}^0,\mathbf{M}^1\right] = \int_{-h/2}^{h/2}\left[1,\theta^3\right]\hat{\mathbf{S}}\mu\,d\theta^3. \tag{4.61}$$

The scalar μ is the determinant of the shifter tensor $\boldsymbol{\mu}$.

To prove (4.60) we consider the inner product $\mathbf{S}\cdot\dot{\mathbf{E}} = \text{tr}\left(\mathbf{S}^T\dot{\mathbf{E}}\right)$ in $\mathscr{T}^2$. Then

$$\begin{aligned}\text{tr}\left(\mathbf{S}^T\dot{\mathbf{E}}\right) &= \text{tr}\left(\boldsymbol{\mu}\hat{\mathbf{S}}^T\boldsymbol{\mu}^T\boldsymbol{\mu}^{-T}\dot{\hat{\mathbf{E}}}\boldsymbol{\mu}^{-1}\right) \\ &= \text{tr}\left(\hat{\mathbf{S}}^T\dot{\hat{\mathbf{E}}}\right) = \hat{\mathbf{S}}\cdot\dot{\hat{\mathbf{E}}} \\ &= \hat{\mathbf{S}}\cdot(\dot{\boldsymbol{\varepsilon}}^0 + \theta^3\dot{\boldsymbol{\varepsilon}}^1).\end{aligned}$$

Since $dV = \mu\,d\theta^3 d\Omega$ and using the definition (4.61) we obtain

$$\begin{aligned}\mathscr{P}_{\text{int}} &= \int_{\mathscr{B}_R} \hat{\mathbf{S}}\cdot(\dot{\boldsymbol{\varepsilon}}^0 + \theta^3\dot{\boldsymbol{\varepsilon}}^1)\mu\,d\theta^3 d\Omega \\ &= \int_{\mathscr{M}_R} (\mathbf{M}^0\cdot\dot{\boldsymbol{\varepsilon}}^0 + \mathbf{M}^1\cdot\dot{\boldsymbol{\varepsilon}}^1)\,d\Omega\end{aligned}$$

and the proof is completed.

Note that the pseudo-stress resultant tensors in Eq. (4.60) are energetically-conjugate to the strain resultants $\boldsymbol{\varepsilon}^i$. The stress resultant tensors may be decomposed in component form as

$$\begin{aligned}\mathbf{M}^0 &= \overset{(0)}{N}{}^{\alpha\beta}\,\mathbf{a}_\alpha \otimes \mathbf{a}_\beta + \overset{(0)}{Q}{}^{\alpha 3}(\mathbf{a}_\alpha \otimes \mathbf{a}_3 + \mathbf{a}_3 \otimes \mathbf{a}_\alpha) + \overset{(0)}{T}{}^{33}\,\mathbf{a}_3 \otimes \mathbf{a}_3 \\ \mathbf{M}^1 &= \overset{(1)}{N}{}^{\alpha\beta}\,\mathbf{a}_\alpha \otimes \mathbf{a}_\beta + \overset{(1)}{Q}{}^{\alpha 3}(\mathbf{a}_\alpha \otimes \mathbf{a}_3 + \mathbf{a}_3 \otimes \mathbf{a}_\alpha) + \overset{(1)}{T}{}^{33}\,\mathbf{a}_3 \otimes \mathbf{a}_3\end{aligned} \tag{4.62}$$

where $\overset{(n)}{N}{}^{\alpha\beta}, \overset{(n)}{Q}{}^{\alpha 3}$ and $\overset{(n)}{T}{}^{33}$ are membrane, shear and stretching components of the stress resultant tensor respectively.

E. Equilibrium equations

To obtain the equilibrium equations we apply the principle of virtual work. It states that: *A continuum body is in equilibrium if and only if the virtual work of all forces acting on the body under a virtual displacement is zero* (see Reddy [55]). Thus

$$\delta\mathcal{W} = \delta\mathcal{W}_{\text{int}} + \delta\mathcal{W}_{\text{ext}} = 0\,. \tag{4.63}$$

The first term is the virtual work due to internal forces and the second term is the virtual work due to external forces. For the Lagrangian formulation, the conjugate tensors giving the internal virtual work are the second Piola-Kirchhoff stress tensor $\mathbf{S}$ and the variation of the Green strain tensor $\delta\mathbf{E}$. Thus

$$\delta\mathcal{W} = \int_{\mathcal{B}_R} \mathbf{S}\cdot\delta\mathbf{E}\,dV - \int_{\mathcal{B}_R} \rho_0 \mathbf{f}\cdot\delta\mathbf{v}\,dV - \int_{\partial\mathcal{B}_R} \mathbf{t}\cdot\delta\mathbf{v}\,dS = 0\,. \tag{4.64}$$

The internal virtual work can be reduced in similar fashion to the stress power (see section D). Then, we have

$$\begin{aligned}\delta\mathcal{W}_{\text{int}} &= \int_{\mathcal{B}_R} \mathbf{S}\cdot\delta\mathbf{E}\,dV = \int_{\mathcal{B}_R} \hat{\mathbf{S}}\cdot\delta\hat{\mathbf{E}}\,dV \\ &= \int_{\mathcal{B}_R} \hat{\mathbf{S}}\cdot\delta(\boldsymbol{\varepsilon}^0 + \theta^3\boldsymbol{\varepsilon}^1)\mu d\theta^3 d\Omega \\ &= \int_{\mathcal{M}_R} (\mathbf{M}^0\cdot\delta\boldsymbol{\varepsilon}^0 + \mathbf{M}^1\cdot\delta\boldsymbol{\varepsilon}^1)\,d\Omega\end{aligned} \tag{4.65}$$

and using (4.53) we obtain

$$\delta\mathcal{W}_{\text{int}} = \int_{\mathcal{M}_R} \left\{ (\mathbf{F}^0\mathbf{M}^0 + \mathbf{F}^1\mathbf{M}^1)\cdot\delta\mathbf{F}^0 + (\mathbf{F}^0\mathbf{M}^1)\cdot\delta\mathbf{F}^1 \right\} d\Omega\,. \tag{4.66}$$

Finally, we compute the variation of $\mathbf{F}^0$ and $\mathbf{F}^1$ from (4.49) as

$$\begin{aligned} \delta\mathbf{F}^0 &= \delta\mathbf{u}_{,\alpha}\otimes\mathbf{a}^\alpha + \delta\boldsymbol{\varphi}\otimes\mathbf{a}^3 \\ \delta\mathbf{F}^1 &= \delta\boldsymbol{\varphi}_{,\alpha}\otimes\mathbf{a}^\alpha + 2\delta\underline{\boldsymbol{\psi}}\otimes\mathbf{a}^3 \end{aligned} \tag{4.67}$$

and we obtain

$$\begin{aligned} \delta\mathcal{W}_{\text{int}} = \int_{\mathcal{M}_R} \big\{ &(\mathbf{F}^0\mathbf{M}^0 + \mathbf{F}^1\mathbf{M}^1)\mathbf{a}^\alpha\cdot\delta\mathbf{u}_{,\alpha} + (\mathbf{F}^0\mathbf{M}^0 + \mathbf{F}^1\mathbf{M}^1)\mathbf{a}^3\cdot\delta\boldsymbol{\varphi} \\ &+ (\mathbf{F}^0\mathbf{M}^1)\mathbf{a}^\alpha\cdot\delta\boldsymbol{\varphi}_{,\alpha} + 2(\mathbf{F}^0\mathbf{M}^1)\mathbf{a}^3\cdot\delta\underline{\boldsymbol{\psi}} \big\}\, d\Omega\,. \end{aligned} \tag{4.68}$$

Consider next the external virtual work $\delta\mathcal{W}_{\text{ext}}$ (Sansour [23]). We assume that the midsurface $\mathcal{M}_R$ has a smooth curve $\partial\mathcal{M}_R$ as a boundary with parameter length s, differential length ds and normal vector $\mathbf{n}$. The boundary of the shell consists of three parts: an upper, a lower, and a lateral surface denoted by $\partial\mathcal{B}_R{}^+$, $\partial\mathcal{B}_R{}^-$ and $\partial\mathcal{B}_R{}^s$ respectively. We make use of the notation $\mu^+ = \mu|_{\theta^3=h/2}$, $\mu^- = \mu|_{\theta^3=-h/2}$ and μ^s for μ at the lateral surface. Then, the surface elements can be written as

$$dS^+ = \mu^+ d\Omega, \quad dS^- = \mu^- d\Omega, \quad dS^s = \mu^s d\theta^3 ds\,. \tag{4.69}$$

Introducing these equations in (4.64), we obtain

$$\begin{aligned} \delta\mathcal{W}_{\text{ext}} &= -\int_{\mathcal{B}_R} \rho_0\mathbf{f}\cdot\delta\mathbf{v}\, dV - \int_{\partial\mathcal{B}_R} \mathbf{t}\cdot\delta\mathbf{v}\, dS \\ &= -\int_{\mathcal{B}_R} \rho_0\mathbf{f}\cdot\delta\left(\mathbf{u} + \theta^3\boldsymbol{\varphi} + (\theta^3)^2\underline{\boldsymbol{\psi}}\right) dV - \int_{\partial\mathcal{B}_R{}^+} \mathbf{t}^+\cdot\delta\left(\mathbf{u} + \frac{h}{2}\boldsymbol{\varphi} + \frac{h^2}{4}\underline{\boldsymbol{\psi}}\right) dS^+ \\ &\quad - \int_{\partial\mathcal{B}_R{}^-} \mathbf{t}^-\cdot\delta\left(\mathbf{u} - \frac{h}{2}\boldsymbol{\varphi} + \frac{h^2}{4}\underline{\boldsymbol{\psi}}\right) dS^- - \int_{\partial\mathcal{B}_R{}^s} \mathbf{t}^s\cdot\delta\left(\mathbf{u} + \theta^3\boldsymbol{\varphi} + (\theta^3)^2\underline{\boldsymbol{\psi}}\right) dS^s \\ &= -\int_{\mathcal{M}_R} (\mathbf{p}\cdot\delta\mathbf{u} + \mathbf{l}\cdot\delta\boldsymbol{\varphi} + \mathbf{k}\cdot\delta\underline{\boldsymbol{\psi}})\, d\Omega - \int_{\partial\mathcal{M}_R} (\mathbf{p}^s\cdot\delta\mathbf{u} + \mathbf{l}^s\cdot\delta\boldsymbol{\varphi} + \mathbf{k}^s\cdot\delta\underline{\boldsymbol{\psi}})\, ds \end{aligned} \tag{4.70}$$

with the definitions

$$\begin{aligned}
&\mathbf{p} := \int_{-h/2}^{h/2} \rho_0 \mathbf{f} \mu d\theta^3 + \mu^+ \mathbf{t}^+ + \mu^- \mathbf{t}^- \\
&\mathbf{l} := \int_{-h/2}^{h/2} \rho_0 \mathbf{f} \mu \theta^3 d\theta^3 + \frac{h}{2} \mu^+ \mathbf{t}^+ - \frac{h}{2} \mu^- \mathbf{t}^- \\
&\mathbf{k} := \int_{-h/2}^{h/2} \rho_0 \mathbf{f} \mu (\theta^3)^2 d\theta^3 + \frac{h^2}{4} \mu^+ \mathbf{t}^+ + \frac{h^2}{4} \mu^- \mathbf{t}^- \\
&\mathbf{p}^s := \int_{-h/2}^{h/2} \mathbf{t}^s \mu^s d\theta^3, \quad \mathbf{l}^s := \int_{-h/2}^{h/2} \mathbf{t}^s \mu^s \theta^3 d\theta^3 \\
&\mathbf{k}^s := \int_{-h/2}^{h/2} \mathbf{t}^s \mu^s (\theta^3)^2 d\theta^3 \, .
\end{aligned} \tag{4.71}$$

We may now write $\delta\mathcal{W}_{\text{ext}}$ as

$$\begin{aligned}
\delta\mathcal{W}_{\text{ext}} = &-\int_{\mathcal{M}_R} (\mathbf{p} \cdot \delta\mathbf{u} + \mathbf{l} \cdot \delta\boldsymbol{\varphi} + \mathbf{k} \cdot \delta\underline{\boldsymbol{\psi}}) \, d\Omega \\
&-\int_{\partial\mathcal{M}_R} (\mathbf{p}^s \cdot \delta\mathbf{u} + \mathbf{l}^s \cdot \delta\boldsymbol{\varphi} + \mathbf{k}^s \cdot \delta\underline{\boldsymbol{\psi}}) \, ds \, .
\end{aligned} \tag{4.72}$$

The virtual work done is obtained substituting (4.68) and (4.72) into (4.63) as follows

$$\begin{aligned}
&\int_{\mathcal{M}_R} \Big\{ (\mathbf{F}^0\mathbf{M}^0 + \mathbf{F}^1\mathbf{M}^1)\mathbf{a}^\alpha \cdot \delta\mathbf{u}_{,\alpha} + (\mathbf{F}^0\mathbf{M}^0 + \mathbf{F}^1\mathbf{M}^1)\mathbf{a}^3 \cdot \delta\boldsymbol{\varphi} \\
&+ (\mathbf{F}^0\mathbf{M}^1)\mathbf{a}^\alpha \cdot \delta\boldsymbol{\varphi}_{,\alpha} + 2(\mathbf{F}^0\mathbf{M}^1)\mathbf{a}^3 \cdot \delta\underline{\boldsymbol{\psi}} - (\mathbf{p} \cdot \delta\mathbf{u} + \mathbf{l} \cdot \delta\boldsymbol{\varphi} + \mathbf{k} \cdot \delta\underline{\boldsymbol{\psi}}) \Big\} \, d\Omega \\
&- \int_{\partial\mathcal{M}_R} (\mathbf{p}^s \cdot \delta\mathbf{u} + \mathbf{l}^s \cdot \delta\boldsymbol{\varphi} + \mathbf{k}^s \cdot \delta\underline{\boldsymbol{\psi}}) ds = 0 \, .
\end{aligned} \tag{4.73}$$

Integrating by part over $\mathcal{M}_R$ and considering arbitrary variations $\delta\mathbf{u}$, $\delta\boldsymbol{\varphi}$ and $\delta\underline{\boldsymbol{\psi}}$, we obtain the following equilibrium equations

$$\begin{aligned}
&\delta\mathbf{u}: \ \frac{1}{\sqrt{a}} \Big\{ \sqrt{a} \, (\mathbf{F}^0\mathbf{M}^0 + \mathbf{F}^1\mathbf{M}^1) \mathbf{a}^\alpha \Big\}_{,\alpha} - \mathbf{p} = \mathbf{0} && \text{in } \mathcal{M}_R \\
&\delta\boldsymbol{\varphi}: \ (\mathbf{F}^0\mathbf{M}^0 + \mathbf{F}^1\mathbf{M}^1)\mathbf{a}^3 + \frac{1}{\sqrt{a}} \Big\{ \sqrt{a} \, (\mathbf{F}^0\mathbf{M}^1 + \mathbf{F}^1\mathbf{M}^2) \mathbf{a}^\alpha \Big\}_{,\alpha} - \mathbf{l} = \mathbf{0} && \text{in } \mathcal{M}_R \\
&\delta\psi_3: \ \Big\{ 2\,(\mathbf{F}^0\mathbf{M}^1)\mathbf{a}^3 - \mathbf{k} \Big\} \cdot \mathbf{a}^3 = 0 && \text{in } \mathcal{M}_R
\end{aligned} \tag{4.74a}$$

and natural boundary conditions

$$\begin{aligned}
&\delta\mathbf{u}: \quad (\mathbf{F}^0\mathbf{M}^0 + \mathbf{F}^1\mathbf{M}^1)\mathbf{a}^\alpha n_\alpha - \mathbf{p}^s = \mathbf{0} && \text{on } \partial\mathcal{M}_R \\
&\delta\boldsymbol{\varphi}: \quad (\mathbf{F}^0\mathbf{M}^1)\mathbf{a}^\alpha n_\alpha - \mathbf{l}^s = \mathbf{0} && \text{on } \partial\mathcal{M}_R \\
&\delta\psi_3: \quad \mathbf{k}^s \cdot \mathbf{a}^3 = 0 && \text{on } \partial\mathcal{M}_R
\end{aligned} \tag{4.74b}$$

for a Neumann boundary problem. In other cases, the natural boundary conditions should be applied to a part of the boundary $\partial\mathcal{M}_R$, i.e. Γ_N. Note that $\Gamma_D \equiv \partial\mathcal{M}_R / \Gamma_N$ is the Dirichlet boundary.

F. Constitutive equations

This section addresses the particular case of hyperelastic constitutive equations. The shell structure can undergo finite deformations (finite rotations and displacements) while the material response remains in the elastic regime. Therefore, no elasto-plastic behavior is discussed in this dissertation.

The main characteristic of hyperelastic materials (or Green-elastic material [124]) is that postulate the existence of a strain energy function Ψ depending on the deformation gradient (or in the present case on the Green strain tensor). The function Ψ is called *Helmholtz free energy* and describes by definition strain energy per unit of undeformed mass.

If we have a perfectly elastic material which produces no locally entropy and for the specific case of purely mechanical process (isothermal), we can equal the rate of mechanical work (or stress power) per unit reference volume to $\rho_0 \dot{e}$. We make use of the pointwise statement of the first law of thermodynamics [118, 119]

$$\rho_0 \dot{e} = \mathbf{S} \cdot \dot{\mathbf{E}} \underline{+ \rho_0 r_0 - \operatorname{Div} \mathbf{q}_0} \tag{4.75}$$

where the underlined terms vanish because of the isothermal conditions. We also know

$$\Psi = e - \eta \Theta \tag{4.76}$$

for constant entropy η and temperature Θ. As a result of (4.76) we have $\dot{\Psi} = \dot{e}$. On the other hand, the chain rule yields

$$\rho_0 \dot{\Psi} := \rho_0 \dot{\Psi}(\mathbf{E}) = \rho_0 \frac{\partial \Psi}{\partial \mathbf{E}} \cdot \dot{\mathbf{E}}\,. \tag{4.77}$$

For arbitrary values of $\dot{\mathbf{E}}$ we obtain

$$\mathbf{S} := \mathbf{S}(\mathbf{E}) = \rho_0 \frac{\partial \Psi(\mathbf{E})}{\partial \mathbf{E}}\,. \tag{4.78}$$

Let us now apply the linearization of the tensor-value function $\mathbf{S}(\mathbf{E})$ with respect to $\mathbf{E}$ at a point $\mathbf{x}$. Thus

$$\mathcal{L}\mathbf{S}(\mathbf{E}, \Delta\mathbf{E}) = \mathbf{S}(\mathbf{E}) + D\mathbf{S}(\mathbf{E})[\Delta\mathbf{E}] + o(\Delta\mathbf{E}) \tag{4.79}$$

where $\mathcal{L}$ denotes the linearization operator. The second term of the right-hand side is the *Gâteaux derivative* or directional derivative of $\mathbf{S}(\mathbf{E})$ defined by

$$D\mathbf{S}(\mathbf{E})[\Delta\mathbf{E}] = \left.\frac{d\,\mathbf{S}_\varepsilon}{d\varepsilon}\right|_{\varepsilon=0} = \left.\frac{d}{d\varepsilon}\mathbf{S}(\mathbf{E} + \varepsilon\,\Delta\mathbf{E})\right|_{\varepsilon=0} \tag{4.80}$$

which is linear in $\Delta\mathbf{E}$. Note that the Gâteaux derivative of $\mathbf{S}(\mathbf{E})$ can also be written as

$$\begin{aligned} D\mathbf{S}(\mathbf{E})[\Delta\mathbf{E}] = \mathcal{D}\mathbf{S}(\mathbf{E}) \cdot \Delta\mathbf{E} &= \frac{\partial \mathbf{S}(\mathbf{E})}{\partial \mathbf{E}} \cdot \Delta\mathbf{E} \\ &= \rho_0 \frac{\partial^2 \Psi(\mathbf{E})}{\partial \mathbf{E}\,\partial \mathbf{E}} \cdot \Delta\mathbf{E} \\ &= \mathbb{C} \cdot \Delta\mathbf{E} \end{aligned} \tag{4.81}$$

where $\mathbb{C} \in \mathscr{T}^4$ is the fourth-order elasticity tensor. Note that the elasticity tensor can be obtained by applying the time derivative of $\mathbf{S}$, i.e.

$$\dot{\mathbf{S}} = \mathbb{C} \cdot \dot{\mathbf{E}}\,. \tag{4.82}$$

We introduce now an assumption related to the constitutive equations of the shell. Some authors consider this conjecture as small strain shell behavior. However, we will see that moderate and large strains may still occur.

Assumption 3: We consider linear relation between the second Piola-Kirchhoff stress tensor $\mathbf{S}$ and the Green strain tensor $\mathbf{E}$.

It implies that

$$\mathbf{S} = \mathbb{C} \cdot \mathbf{E} . \tag{4.83}$$

This expression is easy to derive. We neglect higher-order terms in (4.79) and apply the linearization of $\mathbf{S}(\mathbf{E})$ at the point $\mathbf{x} = \mathbf{X}$ (undeformed configuration). Then, we obtain

$$\mathcal{L}\mathbf{S}(\mathbf{0}, \Delta\mathbf{E}) = \mathbb{C} \cdot \Delta\mathbf{E} \tag{4.84}$$

since $\mathbf{S}(\mathbf{0}) = \mathbf{0}$. Finally, we change the notation $\Delta\mathbf{E}$ to $\mathbf{E}$ and equation (4.84) becomes (4.83). Furthermore

$$\rho_0 \Psi = \frac{1}{2} \mathbf{E} \cdot \mathbb{C} \cdot \mathbf{E} \tag{4.85}$$

which is called linear quadratic constitutive model [60].

The tensor $\mathbb{C}$ can be written in terms of convected basis vectors $\{\mathbf{g}_i\}$ in the region $\mathscr{B}_R$ as

$$\mathbb{C} = C^{ijkl} \mathbf{g}_i \otimes \mathbf{g}_j \otimes \mathbf{g}_k \otimes \mathbf{g}_l \tag{4.86}$$

where the components of $\mathbb{C}$ satisfy the following symmetry conditions

$$C^{ijkl} = C^{jikl} = C^{ijlk} = C^{klij} . \tag{4.87}$$

The number of independent components of the elasticity tensor $\mathbb{C}$ for an arbitrarily anisotropic material is 21, for a monoclinic material with symmetry respect to the midsurface is 13, for an orthotropic material is 9, for a transversely isotropic material is 5, and finally for an isotropic material is 2.

For isotropic materials equations (4.83) and (4.85) are well-defined in the literature. In that particular case we have

$$\begin{aligned} \mathbf{S} &= \lambda \operatorname{tr}(\mathbf{E})\,\mathbf{G} + 2\mu\mathbf{E} \\ \rho_0 \Psi &= \frac{\lambda}{2} \operatorname{tr}(\mathbf{E})^2 + \mu \operatorname{tr}(\mathbf{E}^2) \end{aligned} \tag{4.88}$$

which characterizes the so-called *Saint-Venant-Kirchhoff material*. Here, λ and μ denote the *Lamé* constants.

1. Multilayered composite shells

Fiber-reinforced composites are composed of oriented fibers embedded in a matrix. The basic feature of composites with oriented fibers is their anisotropic behavior. When a shell consists of several laminae with varying material properties and fiber orientations, it is called a laminated composite shell.

We assume that layers are perfectly bonded together without any slip among their interfaces. It supports the continuity of the displacement field across lamina boundaries. It is common practice to represent mechanical behavior of the laminated shell on the macroscopic level as a piece-wise homogeneous and anisotropic continuum. The behavior of the laminate at a particular layer can be assumed as purely elastic and described with a simple hyperelastic orthotropic material law.

We first focus our attention to a single lamina L made of an orthotropic material (Fig. 4.3). To calculate at a point P the components of the elasticity tensor $\mathbb{C}$ associated with the convected coordinates $\{\theta^i\}$ in terms of given orthotropic constants, we postulate a coordinate system $\{\vartheta^i\}$ such that the corresponding base vectors $\{\hat{\mathbf{e}}_i\}$ coincide at P with the principal material directions (see Refs. [19, 20, 104, 125]). The base vectors $\{\hat{\mathbf{e}}_i\}$ form an orthonormal basis and are oriented differently from layer to layer. The third coordinate $\theta^3 = \vartheta^3$ remains unchanged.

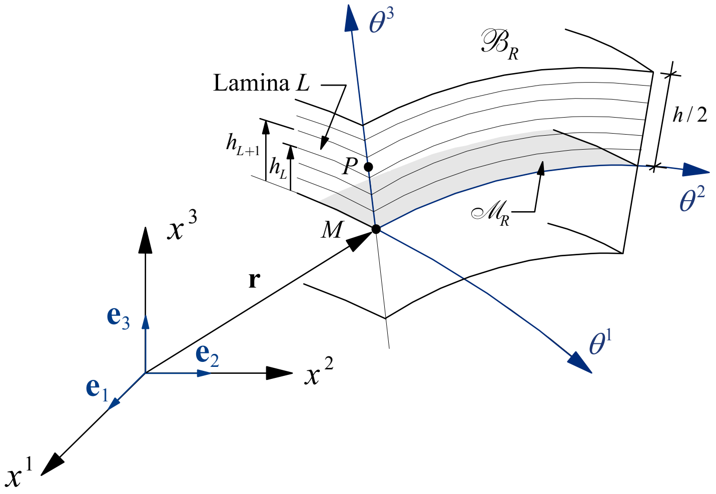

Fig. 4.3. A multilayered composite shell.

In the coordinate system $\{\vartheta^i\}$ we express the elasticity tensor in terms of its components $\breve{C}^{ijkl}$ relative to the fiber reference axis of a lamina L, i.e.

$$\mathbb{C}_L = \breve{C}_L^{abcd}\,\hat{\mathbf{e}}_a \otimes \hat{\mathbf{e}}_b \otimes \hat{\mathbf{e}}_c \otimes \hat{\mathbf{e}}_d \tag{4.89}$$

which can be arranged in a matrix $\left[\breve{C}_L^{ijkl}\right] \in \mathbb{M}^{6\times 6}$. Here we use the Voigt ordering for the components in matrix form. Thus

$$\left[\breve{C}_L^{ijkl}\right] = \begin{bmatrix} \breve{C}_L^{1111} & \breve{C}_L^{1122} & \breve{C}_L^{1133} & 0 & 0 & 0 \\ \breve{C}_L^{1122} & \breve{C}_L^{2222} & \breve{C}_L^{2233} & 0 & 0 & 0 \\ \breve{C}_L^{1133} & \breve{C}_L^{2233} & \breve{C}_L^{3333} & 0 & 0 & 0 \\ 0 & 0 & 0 & \breve{C}_L^{2323} & 0 & 0 \\ 0 & 0 & 0 & 0 & \breve{C}_L^{1313} & 0 \\ 0 & 0 & 0 & 0 & 0 & \breve{C}_L^{1212} \end{bmatrix}_{6\times 6} \tag{4.90}$$

where the components $\breve{C}_L^{ijkl}$ are given by (Reddy [54, p. 30])

$$\begin{aligned} &\breve{C}_L^{1111} = \frac{E_1(1-\nu_{23}\nu_{32})}{\Delta}, \quad \breve{C}_L^{2222} = \frac{E_2(1-\nu_{13}\nu_{31})}{\Delta}, \quad \breve{C}_L^{3333} = \frac{E_3(1-\nu_{12}\nu_{21})}{\Delta} \\ &\breve{C}_L^{1122} = \frac{E_1(\nu_{21}+\nu_{31}\nu_{23})}{\Delta}, \quad \breve{C}_L^{1133} = \frac{E_3(\nu_{13}+\nu_{12}\nu_{23})}{\Delta}, \quad \breve{C}_L^{2233} = \frac{E_2(\nu_{32}+\nu_{12}\nu_{31})}{\Delta} \\ &\breve{C}_L^{1212} = G_{12}, \quad \breve{C}_L^{2323} = G_{23}, \quad \breve{C}_L^{1313} = G_{13} \end{aligned} \tag{4.91}$$

in which $\Delta = 1 - \nu_{12}\nu_{21} - \nu_{23}\nu_{32} - \nu_{13}\nu_{31} - 2\nu_{21}\nu_{32}\nu_{13}$. Note that the tensor $\mathbb{C}_L$ is computed from (4.91) in terms of nine independent engineering elastic constants.

Since we are developing the formulation in convective coordinates associated with the basis $\{\mathbf{g}_i\}$, we have to express the elasticity tensor $\mathbb{C}_L$ in the same convective coordinates by mean of the following transformation (Fig. 4.4)

$$\mathbb{C}_L = \breve{C}_L^{abcd}\,\hat{\mathbf{e}}_a \otimes \hat{\mathbf{e}}_b \otimes \hat{\mathbf{e}}_c \otimes \hat{\mathbf{e}}_d = C_L^{ijkl}\,\mathbf{g}_i \otimes \mathbf{g}_j \otimes \mathbf{g}_k \otimes \mathbf{g}_l \tag{4.92}$$

which leads to

$$C_L^{ijkl} = (\mathbf{g}^i \cdot \hat{\mathbf{e}}_a)(\mathbf{g}^j \cdot \hat{\mathbf{e}}_b)(\mathbf{g}^k \cdot \hat{\mathbf{e}}_c)(\mathbf{g}^l \cdot \hat{\mathbf{e}}_d)\breve{C}_L^{abcd}. \tag{4.93}$$

The base vectors in coordinates ϑ^i and θ^i are related by

$$\hat{\mathbf{e}}_a = \frac{\partial \theta^i}{\partial \vartheta^a}\mathbf{g}_i\,. \tag{4.94}$$

Thus, equation (4.93) becomes

$$C_L^{ijkl} = \frac{\partial \theta^i}{\partial \vartheta^a}\frac{\partial \theta^j}{\partial \vartheta^b}\frac{\partial \theta^k}{\partial \vartheta^c}\frac{\partial \theta^l}{\partial \vartheta^d}\breve{C}_L^{abcd} \tag{4.95}$$

for a lamina L.

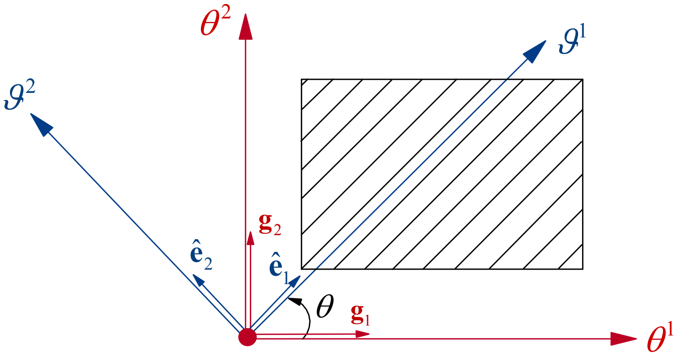

Fig. 4.4. Principal material coordinates $\{\vartheta^i\}$ and convective coordinates $\{\theta^i\}$.

The coordinate θ^3 is always orthogonal to the midsurface. Since $\theta^3 = \vartheta^3$ we obtain

$$\mathbf{g}^3 \cdot \hat{\mathbf{e}}_\alpha = 0, \quad \mathbf{g}^\alpha \cdot \hat{\mathbf{e}}_3 = 0, \quad \mathbf{g}^3 \cdot \hat{\mathbf{e}}_3 = 1. \tag{4.96}$$

For the particular case when the basis vectors $\{\mathbf{g}_i\}$ are orthogonal, we have

$$\mathbf{g}^1 \cdot \hat{\mathbf{e}}_1 = \frac{\cos\theta}{\sqrt{g_{11}}}, \quad \mathbf{g}^2 \cdot \hat{\mathbf{e}}_1 = \frac{\sin\theta}{\sqrt{g_{22}}}, \quad \mathbf{g}^1 \cdot \hat{\mathbf{e}}_2 = -\frac{\sin\theta}{\sqrt{g_{11}}}, \quad \mathbf{g}^2 \cdot \hat{\mathbf{e}}_2 = \frac{\cos\theta}{\sqrt{g_{22}}} \tag{4.97}$$

where $g_{\alpha\alpha}$ (no sum) are components of the metric tensor at $\mathscr{B}_R$ and θ is the fiber direction angle relative to the convective coordinates (Fig. 4.4).

We specialize the constitutive equations (4.86) to convected curvilinear coordinates with basis $\{\mathbf{g}_i\}$. For orthotropic materials we have $C_L^{\alpha\beta\gamma3} = 0$ and $C_L^{\alpha333} = 0$, hence

$$\begin{aligned} S^{\alpha\beta} &= C_L^{\alpha\beta\lambda\mu} E_{\lambda\mu} + C_L^{\alpha\beta33} E_{33} \\ S^{\alpha3} &= 2C_L^{\alpha3\lambda3} E_{\lambda3} \\ S^{33} &= C_L^{\lambda\mu33} E_{\lambda\mu} + C_L^{3333} E_{33}\,. \end{aligned} \tag{4.98}$$

The above relation can be arranged in matrix form by defining the matrices $\{S^{ij}\} \in \mathbb{M}^{6\times1}$ and $\{E_{ij}\} \in \mathbb{M}^{6\times1}$. Then, we obtain

$$\begin{Bmatrix} S^{11} \\ S^{22} \\ S^{33} \\ S^{23} \\ S^{13} \\ S^{12} \end{Bmatrix} = \begin{bmatrix} C_L^{1111} & C_L^{1122} & C_L^{1133} & 0 & 0 & C_L^{1112} \\ C_L^{1122} & C_L^{2222} & C_L^{2233} & 0 & 0 & C_L^{2212} \\ C_L^{1133} & C_L^{2233} & C_L^{3333} & 0 & 0 & C_L^{3312} \\ 0 & 0 & 0 & C_L^{2323} & C_L^{2313} & 0 \\ 0 & 0 & 0 & C_L^{2313} & C_L^{1313} & 0 \\ C_L^{1112} & C_L^{2212} & C_L^{3312} & 0 & 0 & C_L^{1212} \end{bmatrix} \begin{Bmatrix} E_{11} \\ E_{22} \\ E_{33} \\ 2E_{23} \\ 2E_{13} \\ 2E_{12} \end{Bmatrix}. \tag{4.99}$$

The constitutive matrix $\left[C_L^{ijkl}\right] \in \mathbb{M}^{6\times6}$ in the convective coordinates may also be obtained by mean of the transformation matrix $[T]$, i.e.

$$\left[C_L^{ijkl}\right] = [T]\left[\breve{C}_L^{ijkl}\right][T]^T \tag{4.100}$$

where $[T] \in \mathbb{M}^{6\times6}$ is denoted by

$$[T]=\begin{bmatrix} (c_{11})^2 & (c_{12})^2 & 0 & 0 & 0 & 2c_{11}c_{12} \\ (c_{21})^2 & (c_{22})^2 & 0 & 0 & 0 & 2c_{21}c_{22} \\ 0 & 0 & 1 & 0 & 0 & 0 \\ 0 & 0 & 0 & c_{22} & c_{21} & 0 \\ 0 & 0 & 0 & c_{12} & c_{11} & 0 \\ c_{11}c_{21} & c_{12}c_{22} & 0 & 0 & 0 & c_{11}c_{22}+c_{21}c_{12} \end{bmatrix}_{6\times 6} \tag{4.101}$$

and $c_{ij} = \mathbf{g}^i \cdot \hat{\mathbf{e}}_j$ is given in (4.96) and (4.97).

2. Functionally graded shells

Functionally graded materials (FGMs) are a special kind of composites in which the material properties vary smoothly and continuously from one surface to the other. These materials are microscopically inhomogeneous and are typically made from isotropic components. One of the main advantages of FGMs is that it mitigates severe stress concentrations and singularities at intersections between interfaces usually presented in laminate composites due to their abrupt transitions in material compositions and properties. Applications of FGMs are extensive especially in high-temperature environments such as nuclear reactors, chemical plants and high-speed spacecrafts.

Functionally graded materials (FGMs) considered here are made from a mixture of ceramics and metals. It is known that these materials withstand high-temperature gradient environments while maintaining their structural integrity. The ceramic constituent of the material provides the high-temperature resistance due to its low thermal conductivity. On the other hand, the ductility of the metal constituent prevents fracture cause by stresses due to high-temperature gradient in a very short period of time. Additionally, ceramic-metal FGMs with continuously varying volume fraction can be easily manufactured.

In this two-phase functionally graded material, the properties are assumed to vary through the thickness of the shell. The materials in the bottom and top surfaces are metal and ceramic respectively (Fig. 4.5). Material properties at a point $\mathbf{X}$ are given by a combination between metal and ceramic constituents.

The symmetry group of this isotropic material body is given by the set $\mathcal{G}_{\theta^3}$ (inhomogeneous through the thickness) such that the second Piola-Kirchhoff stress tensor $\mathbf{S}$ is invariant under $\mathcal{G}_{\theta^3}$, i.e.

$$\mathbf{S}\left(\mathbf{E}\right)=\mathbf{S}\left(\mathbf{Q}^T\mathbf{E}\mathbf{Q}\right) \qquad \forall\mathbf{Q}\in\mathcal{G}_{\theta^3} \tag{4.102}$$

for $\mathcal{G}_{\theta^3}=\mathrm{SO}(3)$. The set $\mathrm{SO}(3)$ is the proper orthogonal group in the Euclidean three-dimensional vector space (positive determinant).

We also assume a rule of mixtures based on the Voigt model (Ref. [126]). Hence, any material property is given by the weighted average of the moduli of the constituents, namely

$$\varpi\left(\theta^3\right)=\varpi_c f_c+\varpi_m f_m \tag{4.103}$$

where the subscripts m and c refer to the metal and ceramic constituents and f is the volume fraction of the phase. The symbol ϖ denotes a generic material property like the Young's modulus.

The volume fractions of the ceramic f_c and metal f_m corresponding to the power law are expressed as (Reddy [54, 127], Praveen and Reddy [128], Reddy and Chin [129])

$$f_c=\left(\frac{z}{h}+\frac{1}{2}\right)^n, \qquad f_m=1-f_c \tag{4.104}$$

where n is the volume fraction exponent which takes values greater than or equal to zero. The value of n equal to zero represents a fully ceramic shell. Conversely, we have a fully metal shell as n tends to infinity (Fig. 4.6).

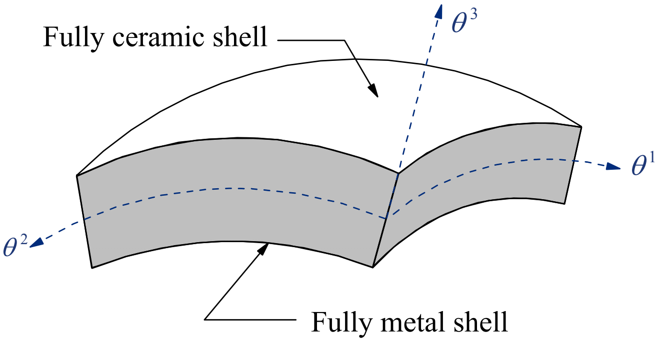

Fig. 4.5. Arbitrary functionally graded shell.

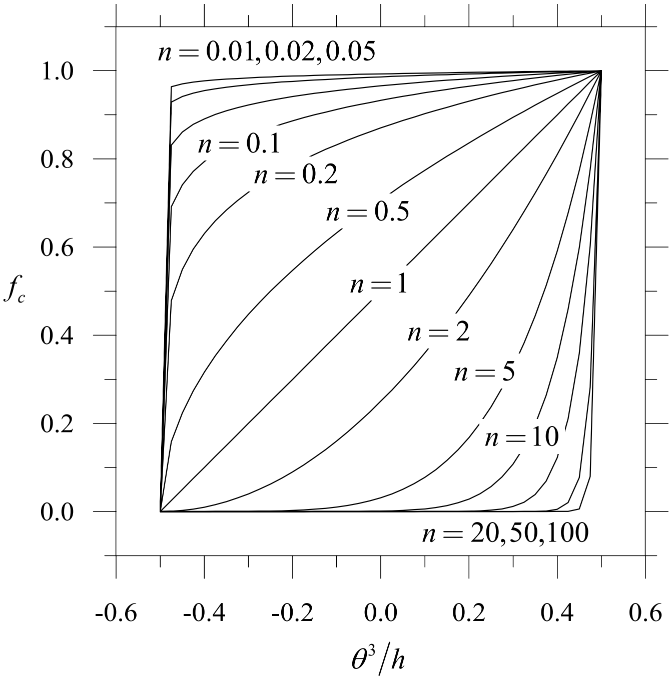

Fig. 4.6. Variation of the volume fraction function f_c through the dimensionless thickness for different values of n.

We consider the components of the elasticity tensor $C^{ijkl}\left(\theta^3\right)$ as a function of the thickness coordinate. They can be written in terms of the convected base vectors as

$$\mathbb{C} = C^{ijkl}\left(\theta^3\right)\mathbf{g}_i \otimes \mathbf{g}_j \otimes \mathbf{g}_k \otimes \mathbf{g}_l \tag{4.105}$$

which can be arranged in a matrix $\left[C^{ijkl}\right] \in \mathbb{M}^{6\times 6}$ such that

$$\left[C^{ijkl}\right] = \begin{bmatrix} C^{1111} & C^{1122} & C^{1133} & 0 & 0 & 0 \\ C^{1122} & C^{2222} & C^{2233} & 0 & 0 & 0 \\ C^{1133} & C^{2233} & C^{3333} & 0 & 0 & 0 \\ 0 & 0 & 0 & C^{2323} & 0 & 0 \\ 0 & 0 & 0 & 0 & C^{1313} & 0 \\ 0 & 0 & 0 & 0 & 0 & C^{1212} \end{bmatrix}_{6\times 6} . \tag{4.106}$$

The components C^{ijkl} at each θ^3 are functions of only two independent variables. then

$$\begin{aligned} C^{1111} &= C^{2222} = C^{3333} = \frac{E\left(\theta^3\right)(1-\nu)}{(1+\nu)(1-2\nu)} \\ C^{1122} &= C^{1133} = C^{2233} = \frac{E\left(\theta^3\right)\nu}{(1+\nu)(1-2\nu)} \\ C^{1212} &= C^{1313} = C^{2323} = \frac{E\left(\theta^3\right)}{2(1+\nu)} \end{aligned} \tag{4.107}$$

where $E\left(\theta^3\right) = E_c f_c + E_m f_m$. The Poisson's ratio ν is considered constant through the thickness. Thus

$$\nu\left(\theta^3\right) = \nu \tag{4.108}$$

and hence

$$\begin{aligned} C^{ijkl}\left(\theta^3\right) &= C_c^{ijkl} f_c + C_m^{ijkl} f_m \\ &= C_{cm}^{ijkl} f_c + C_m^{ijkl} \end{aligned} \tag{4.109}$$

where $C_{cm}^{ijkl} = C_c^{ijkl} - C_m^{ijkl}$ and f_c, f_m are given in (4.104).

G. The geometrically exact shell theory

We shall point out that, except assumptions 1 and 2, no further kinematic hypotheses were used in the derivation of the shell theory. Equation (4.46) and (4.47) are exact within the frame of the adopted kinematical model. Consequently, the present model allows the shell undergoes finite deformations (no restrictions on displacements and rotations).

We now consider briefly the geometrically exact shell theory (Simo and Fox [5], Fox [60], Sansour and Bednarczyk [93]). This formulation relies on the concept of a Cosserat continuum in which the reduction of the three-dimensional equations is carried out in a direct manner by considering the continuum to be a two-dimensional surface. We will show here that the geometrically exact shell theory can be derived from the three-dimensional continuum by adopting four assumptions. In that sense our present shell formulation is superior to the Cosserat shell theory which can be seen as a subset of the present approach.

The main assumption for the adopted Cosserat shell model is given next

Assumption 1: The position vector $\mathbf{x}\left(\theta^i\right)$ is considered as a linear expansion of the thickness coordinate around the midsurface. The normal strain in assumed to be zero, i.e.

$$\mathbf{x}\left(\theta^i\right)=\overline{\mathbf{r}}\left(\theta^\alpha\right)+\theta^3\overline{\mathbf{a}}_3\left(\theta^\alpha\right), \qquad \overline{\mathbf{a}}_3\cdot\overline{\mathbf{a}}_3=1. \tag{4.110}$$

Assumption 1 introduces the inextensibility condition to the kinematic equations of the shell (known as the Reissner-Mindlin inextensibility constraint). This assumption implies that the normal strain component $\varepsilon_{33}^{(0)}$ should be zero. Equation (4.41) and the last equation of (4.110) lead to

$$\varepsilon_{33}^{(0)} = \frac{1}{2}(\bar{\mathbf{a}}_3 \cdot \bar{\mathbf{a}}_3 - 1) = 0 . \tag{4.111}$$

The terms $\varepsilon_{33}^{(1)}$ and $\varepsilon_{33}^{(2)}$ also vanish since $\underline{\Psi} = \mathbf{0}$.

This hypothesis considers that the director vector $\mathbf{a}_3$ rotates to $\bar{\mathbf{a}}_3$ without changing its length. The constraint enforces the director to remain *straight* and *unstretched*. Most shell formulations describe the deformation of the director with the help of a rotation tensor $\mathbf{\Lambda}$. Namely

$$\bar{\mathbf{a}}_3 = \mathbf{\Lambda}\, \mathbf{a}_3 \tag{4.112}$$

for $\mathbf{\Lambda} \in \mathrm{SO}(3)$. Thus, the inextensibility condition $\| \mathbf{a}_3 \| = \| \bar{\mathbf{a}}_3 \|$ holds automatically.

Parametrizations of the rotation tensor $\mathbf{\Lambda}$ are crucial for the development of finite rotation theories based on assumption 1. Finite element formulations for shells require two independent rotational degrees of freedom in order to avoid rank-deficiency problems. The original three independent parameters needed to describe the proper tensor $\mathbf{\Lambda}$ is reduced to two parameters by neglecting the drilling rotation.

These formulations can be classified in two categories independent of the adopted rotational parametrizations: additive update structure and multiplicative update structure (Betsch et al. [111], Ibrahimbegovic [130]).

The first formulation relies on two successive rotations identified with spherical coordinates (Ramm [131]). Rotations of the shell elements are limited to 90° or in some cases to 180° because singularity problems may arise. However, the update of the configuration of the shell is additive which is suitable for finite element implementations.

The second one is based on the exact description of finite rotations by means of the Rodrigues formula and it is considered singularity-free (Simo and Fox [5]). We define the exponential map as $\exp : \hat{\mathbf{\Theta}} \in \mathrm{so}(3) \rightarrow \mathbf{\Lambda} \in \mathrm{SO}(3)$ such that

$$\boldsymbol{\Lambda} = \exp\left[\hat{\boldsymbol{\Theta}}\right] = \sum_{N=0}^{\infty} \frac{1}{N!} \hat{\boldsymbol{\Theta}}^{N} \tag{4.113}$$

where $\mathrm{so}(3) = \left\{\hat{\boldsymbol{\Theta}} \in \mathscr{T}^2 \middle| \hat{\boldsymbol{\Theta}} + \hat{\boldsymbol{\Theta}}^T = \mathbf{0}\right\}$.

Next, we introduce the Rodrigues formula

$$\boldsymbol{\Lambda} = \exp\left[\hat{\boldsymbol{\Theta}}\right] = \mathbf{1} + \frac{\sin\|\boldsymbol{\theta}\|}{\|\boldsymbol{\theta}\|} \hat{\boldsymbol{\Theta}} + \frac{1}{2} \frac{\sin^2\left(\|\boldsymbol{\theta}\|/2\right)}{(\|\boldsymbol{\theta}\|/2)^2} \hat{\boldsymbol{\Theta}}^2 \tag{4.114}$$

where $\boldsymbol{\theta} \in \mathscr{V}$ is the rotation vector associated to $\hat{\boldsymbol{\Theta}}$ (it can also be understood as an eigenvector of $\hat{\boldsymbol{\Theta}}$ such that $\hat{\boldsymbol{\Theta}}\boldsymbol{\theta} = \mathbf{0}$). For this case the update of the configuration of the shell is multiplicative which leads to a complex update algorithms.

In addition to assumption 1, kinematics of the shell may be substantially simplified. We introduce further assumptions in the model (see Büchter and Ramm [9]) arriving to the so-called geometrically exact shell theory.

Assumption 2: Quadratic and higher-order terms in θ^3 of the Green strain tensor components are neglected.

Assumption 3: The normal stresses in the thickness direction are neglected, i.e. $S^{33} = 0$. This assumption allows us to reduce the material law by condensation of the elasticity tensor.

Assumption 4: Let the shifter tensor $\boldsymbol{\mu}$ be approximated to the identity tensor. Then

$$\boldsymbol{\mu} \approx \mathbf{1}, \quad \mu = \det\left(\boldsymbol{\mu}\right) \approx 1. \tag{4.115}$$

This is comparable to assume $\hat{\mathbf{S}} \approx \mathbf{S}, \hat{\mathbf{E}} \approx \mathbf{E}$ in the virtual work statement.

The last assumption restrict the application of the formulation to thin shells where a relative error in the order of h/R is tolerated $(h/R \geq 20)$.

CHAPTER V

VARIATIONAL MODEL AND NUMERICAL SIMULATIONS

The purpose of this chapter is to develop the finite element formulation for the geometrically nonlinear shell theory presented in Chapter IV. We start by applying the principle of virtual work to derive the weak form of the equilibrium equations. These equations are already reduced to their two-dimensional form after performing the integration through the thickness of the components of the elasticity tensor. A consistent linearization is then carried out that yields the elemental tangent operator. The finite element discretization is introduced by approximating the parametric space of the midsurface and the covariant components of the kinematic variables. The highly nonlinear system of algebraic equations is solved by an incremental-iterative method. In particular, we utilize the incremental Euler-forward method and the iterative Newton-Raphson method. The cylindrical arc-length method is also implemented for cases in which the tangent matrix exhibits singularities. Finally, extensive numerical simulations are presented for finite deformation analysis of benchmark problems that include plates, cylindrical, spherical and hyperboloidal shells under static loading.

As it was established in the last chapter, we adopt the simplest possible shell kinematics which allows for a linear distribution of the transverse and normal strains over the shell thickness. Accordingly, we have assumed that the position vector of any point of the shell body is determined by the equation

$$\mathbf{x}\left(\theta^{\alpha}\right)=\overline{\mathbf{r}}\left(\theta^{\alpha}\right)+\theta^{3}\overline{\mathbf{a}}_{3}\left(\theta^{\alpha}\right)+(\theta^{3})^{2}\underline{\psi}\left(\theta^{\alpha}\right) \tag{5.1}$$

where the vector quantities $\overline{\mathbf{r}}$ and $\overline{\mathbf{a}}_3$ were defined in Chapter IV. Hence, the ordered triple $\left(\overline{\mathbf{r}},\overline{\mathbf{a}}_3,\underline{\psi}\right)$ characterizes the configuration space of the shell.

Instead of the triple $\left(\bar{\mathbf{r}}, \bar{\mathbf{a}}_3, \underline{\psi}\right)$ we may consider alternatively the triple of displacement vectors $\left(\mathbf{u}, \boldsymbol{\varphi}, \underline{\psi}\right)$ as defining the configuration space of the shell such that

$$\mathbf{v}\left(\theta^{\alpha}\right) = \mathbf{u}\left(\theta^{\alpha}\right) + \theta^{3}\boldsymbol{\varphi}\left(\theta^{\alpha}\right) + (\theta^{3})^{2}\underline{\psi}\left(\theta^{\alpha}\right) \tag{5.2}$$

where $\underline{\psi} = \psi_3 \mathbf{a}^3$. Thus, the abstract configuration of the shell is denoted by the set

$$\mathscr{C} = \left\{ \Phi \equiv \left(\mathbf{u}, \boldsymbol{\varphi}, \underline{\psi}\right) \middle| \Phi : \mathscr{A} \in \mathbb{R}^2 \to \mathbb{R}^3 \times \mathbb{R}^3 \times \mathbb{R} \right\}. \tag{5.3}$$

Note that $\Phi \in \mathscr{C}$ contains the same amount of three-dimensional information as (5.2) to locate at any time arbitrary points in the three-dimensional shell (Fig. 5.1).

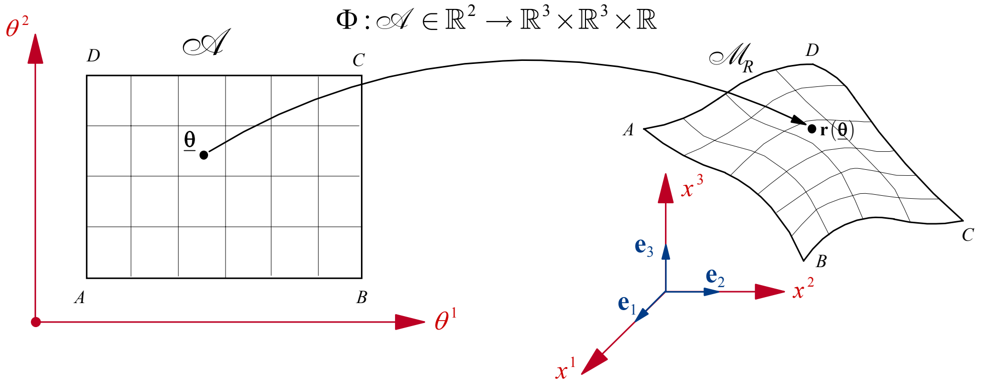

Fig. 5.1. Abstract configuration space of the shell.

A. The weak formulation

The finite element framework is based on the principle of virtual work. We confine our analysis to static cases (no inertial forces). It can be shown that the virtual work statement is precisely the weak form of the equilibrium equations and it is valid for linear and nonlinear stress-strain relations.

We now construct the space of kinematically admissible variations. Let Φ_{ε} represent a single parameter curve of configurations of the shell such that $\Phi_\varepsilon|_{\varepsilon=0} = \Phi$ and $\Phi_\varepsilon \in \mathscr{C}$ for all values of ε. Then, Φ_ε is given by

$$\Phi_\varepsilon = \left(\mathbf{u} + \varepsilon\mathbf{w}, \boldsymbol{\varphi} + \varepsilon\vartheta, \underline{\boldsymbol{\psi}} + \varepsilon\underline{\boldsymbol{\kappa}}\right) \tag{5.4}$$

which requires only linear operations (the space $\mathscr{C}$ is linear). The *Gâteaux* (directional) derivative, defined as

$$\delta(\circ) = \frac{d}{d\varepsilon}(\circ)_\varepsilon\Big|_{\varepsilon=0} \tag{5.5}$$

is used to describe elements of $\mathcal{T}\mathscr{C}$ (the tangent space of $\mathscr{C}$). That is

$$\delta\Phi = \frac{d\Phi_\varepsilon}{d\varepsilon}\Big|_{\varepsilon=0} = \left(\delta\mathbf{u}, \delta\boldsymbol{\varphi}, \delta\underline{\boldsymbol{\psi}}\right). \tag{5.6}$$

Therefore, the tangent space to $\mathscr{C}$ at a configuration Φ, denoted by $\mathcal{T}\mathscr{C}$, is given by triplets

$$\mathcal{T}\mathscr{C} = \left\{\left(\delta\mathbf{u}, \delta\boldsymbol{\varphi}, \delta\underline{\boldsymbol{\psi}}\right) : \mathscr{A} \rightarrow \mathbb{R}^3 \times \mathbb{R}^3 \times \mathbb{R}\right\}. \tag{5.7}$$

The space of kinematically admissible variations $\mathcal{V}$ follows immediately by restricting elements of $\mathcal{T}\mathscr{C}$ to be zero on those portions of the boundary where the kinematic variables are specified [60]. Thus

$$\mathcal{V} = \left\{\delta\Phi \equiv \left(\delta\mathbf{u}, \delta\boldsymbol{\varphi}, \delta\underline{\boldsymbol{\psi}}\right) \in \mathcal{T}\mathscr{C} \;\Big|\; \delta\mathbf{u}|_{\Gamma_D} = 0, \delta\boldsymbol{\varphi}|_{\Gamma_D} = 0, \delta\underline{\boldsymbol{\psi}}|_{\Gamma_D} = 0\right\} \tag{5.8}$$

where Γ_D is the Dirichlet boundary.

With the help of Eqs. (4.65) and (4.72) we express the weak formulation as

$$\mathcal{G}(\Phi, \delta\Phi) = \mathcal{G}_{\text{int}}(\Phi, \delta\Phi) - \mathcal{G}_{\text{ext}}(\Phi, \delta\Phi) = 0 \tag{5.9}$$

where

$$\mathcal{G}_{\text{int}}(\Phi, \delta\Phi) = \int_{\mathscr{M}_R} (\mathbf{M}^0 \cdot \delta\boldsymbol{\varepsilon}^0 + \mathbf{M}^1 \cdot \delta\boldsymbol{\varepsilon}^1)\, d\Omega \tag{5.10a}$$

$$\begin{aligned}\mathcal{G}_{\text{ext}}(\Phi,\delta\Phi) &= \int_{\mathcal{M}_R} (\mathbf{p}\cdot\delta\mathbf{u}+\mathbf{l}\cdot\delta\boldsymbol{\varphi}+\mathbf{k}\cdot\delta\underline{\boldsymbol{\psi}})\,d\Omega \\ &\quad+\int_{\partial\mathcal{M}_R} (\mathbf{p}^s\cdot\delta\mathbf{u}+\mathbf{l}^s\cdot\delta\boldsymbol{\varphi}+\mathbf{k}^s\cdot\delta\underline{\boldsymbol{\psi}})\,ds.\end{aligned} \tag{5.10b}$$

The expression shown above depends on the variation of the strains. These are easily computed as follows

$$\begin{aligned}\delta\boldsymbol{\varepsilon}^0 &= \operatorname{Sym}\left(\delta\mathbf{F}^{0^T}\mathbf{F}^0\right)\\ \delta\boldsymbol{\varepsilon}^1 &= \operatorname{Sym}\left(\delta\mathbf{F}^{0^T}\mathbf{F}^1+\delta\mathbf{F}^{1^T}\mathbf{F}^0\right)\end{aligned} \tag{5.11}$$

where $\delta\mathbf{F}^0$ and $\delta\mathbf{F}^1$ are given by (4.67). The operator $\operatorname{Sym}(\circ)$ takes the symmetric part a tensor.

The stress resultants $\mathbf{M}^n$ are obtained by integration through the thickness of the second Piola-Kirchhoff stress tensor, i.e.

$$\left[\mathbf{M}^0,\mathbf{M}^1\right]=\int_{-h/2}^{h/2}\left[1,\theta^3\right]\hat{\mathbf{S}}\mu\,d\theta^3. \tag{5.12}$$

This equation is valid for materials with constant properties or with properties varying continuously through the thickness of the shell. On the other hand, through-the-thickness integration of multilayered composites should be carried out at each lamina. Then, Eq. (5.12) becomes

$$\left[\mathbf{M}^0,\mathbf{M}^1\right]=\sum_{L=1}^{N}\int_{h_L}^{h_{L+1}}\left[1,\theta^3\right]\hat{\mathbf{S}}^{(L)}\mu\,d\theta^3. \tag{5.13}$$

For hyperelastic materials, the static part of the weak form of the equilibrium equations is the first variation of an elastic potential energy function. This statement is known as the principle of minimum potential energy [55, 119]. We define the elastic potential function $\Pi(\circ):\mathscr{C}\to\mathbb{R}$ as

$$\begin{aligned}\Pi(\Phi) &= \int_{\mathscr{B}_R}\rho_0\,\Psi\,dV-\int_{\mathcal{M}_R}(\mathbf{p}\cdot\mathbf{u}+\mathbf{l}\cdot\boldsymbol{\varphi}+\mathbf{k}\cdot\underline{\boldsymbol{\psi}})\,d\Omega\\ &\quad-\int_{\partial\mathcal{M}_R}(\mathbf{p}^s\cdot\mathbf{u}+\mathbf{l}^s\cdot\boldsymbol{\varphi}+\mathbf{k}^s\cdot\underline{\boldsymbol{\psi}})\,ds.\end{aligned} \tag{5.14}$$

We set $\Psi\left(\mathbf{E}\right)=\hat{\Psi}\left(\hat{\mathbf{E}}\right)$ and therefore

$$\hat{\mathbf{S}}\left(\hat{\mathbf{E}}\right)=\rho_0\frac{\partial\hat{\Psi}\left(\hat{\mathbf{E}}\right)}{\partial\hat{\mathbf{E}}}. \tag{5.15}$$

Let us introduce the two-dimensional function Ξ of elastic strain energy of the shell, measured per unit area of surface $\mathscr{M}_R$

$$\Xi=\int_{-h/2}^{h/2}\mu\hat{\Psi}\left(\hat{\mathbf{E}}\right)d\theta^3 \tag{5.16}$$

where $\Xi:=\Xi\left(\boldsymbol{\varepsilon}^0,\boldsymbol{\varepsilon}^1\right)$. After some manipulations Eq. (5.14) becomes

$$\begin{aligned}\Pi\left(\Phi\right)=&\int_{\mathscr{M}_R}\rho_0\,\Xi\left(\boldsymbol{\varepsilon}^0,\boldsymbol{\varepsilon}^1\right)d\Omega-\int_{\mathscr{M}_R}(\mathbf{p}\cdot\mathbf{u}+\mathbf{l}\cdot\boldsymbol{\varphi}+\mathbf{k}\cdot\underline{\boldsymbol{\psi}})\,d\Omega\\&-\int_{\partial\mathscr{M}_R}(\mathbf{p}^s\cdot\mathbf{u}+\mathbf{l}^s\cdot\boldsymbol{\varphi}+\mathbf{k}^s\cdot\underline{\boldsymbol{\psi}})\,ds\end{aligned} \tag{5.17}$$

which is a two-dimensional statement. The density ρ_0 is not a function of θ^3.

The first variation of the potential energy is obtained with the directional derivative defined by (5.5). Thus

$$\begin{aligned}\mathcal{G}\left(\Phi,\delta\Phi\right)=\delta\Pi\left(\Phi,\delta\Phi\right)&=\frac{d}{d\varepsilon}\Pi\left(\Phi_\varepsilon\right)\Big|_{\varepsilon=0}\\&=D\Pi\left(\Phi\right)\left[\delta\Phi\right]=\nabla\Pi\left(\Phi\right)\cdot\delta\Phi=0\,.\end{aligned} \tag{5.18}$$

Performing the variation of (5.17) we arrive to

$$\begin{aligned}\delta\Pi\left(\Phi,\delta\Phi\right)=&\int_{\mathscr{M}_R}\sum_{k=0}^{1}(\mathbf{M}^k\cdot\delta\boldsymbol{\varepsilon}^k)\,d\Omega-\int_{\mathscr{M}_R}(\mathbf{p}\cdot\delta\mathbf{u}+\mathbf{l}\cdot\delta\boldsymbol{\varphi}+\mathbf{k}\cdot\delta\underline{\boldsymbol{\psi}})\,d\Omega\\&-\int_{\partial\mathscr{M}_R}(\mathbf{p}^s\cdot\delta\mathbf{u}+\mathbf{l}^s\cdot\delta\boldsymbol{\varphi}+\mathbf{k}^s\cdot\delta\underline{\boldsymbol{\psi}})\,ds=0\end{aligned} \tag{5.19}$$

with a new definition of the stress resultants, i.e.

$$\mathbf{M}^0=\rho_0\frac{\partial\Xi}{\partial\boldsymbol{\varepsilon}^0},\quad\mathbf{M}^1=\rho_0\frac{\partial\Xi}{\partial\boldsymbol{\varepsilon}^1}\,. \tag{5.20}$$

Equation (5.19) is a set of highly nonlinear differential equations which are functions of the triple $(\mathbf{u}, \varphi, \underline{\psi})$ and the curvilinear coordinates $\{\theta^i\}$. Upon discretization, we solve this problem by the Newton-Raphson method.

B. Linearization and tangent operators

As it was mentioned in the last section, a common and simple technique to solve the nonlinear equations is to use the incremental/iterative solution technique of Newton's type. It is an efficient method that exhibits quadratic convergence rate near to the solution point. This procedure requires a consistent linearization of the weak form generating recurrence update formulas. The nonlinear problem is then replaced by a sequence of linear problems which are easy to solve at each iteration and load step.

Linearization is a systematic process that relies on the concept of directional derivatives (Hughes and Pister [132], Marsden and Hughes [120, p. 226], Bonet and Wood [133, p. 146]). We assume that the external forces are conservative (independent of Φ). Applying that procedure to equation (5.9) we obtain

$$\mathcal{L}\mathcal{G}(\Phi, \delta\Phi; \Delta\Phi) = \mathcal{G}(\Phi, \delta\Phi) \underline{+ D\mathcal{G}(\Phi, \delta\Phi)[\Delta\Phi]} + o(\Delta\Phi) \tag{5.21}$$

where the underlined term is called consistent tangent operator. Furthermore, we can write the tangent operator as

$$\begin{aligned} D\mathcal{G}(\Phi, \delta\Phi)[\Delta\Phi] &= \nabla\mathcal{G}(\Phi, \delta\Phi) \cdot \Delta\Phi \\ &= \nabla\left(\nabla\Pi(\Phi) \cdot \delta\Phi\right) \cdot \Delta\Phi \\ &= \nabla\left(\nabla\Pi(\Phi)\right) \Delta\Phi \cdot \delta\Phi \end{aligned} \tag{5.22}$$

since $\delta\Phi$ remains constant during the increment $\Delta\Phi$.

The term $\nabla(\nabla\Pi(\Phi))$ is nothing but the *Hessian operator* of the scalar field $\Pi(\Phi)$ which is always symmetric (Liu [134, p. 271]). Therefore, the tangent operator will be symmetric if there exists a total potential energy from which the weak form is derived (hyperelastic materials) and if the space of configuration of the shell $\mathscr{C}$ is linear. For other cases, e.g. geometrically exact shell theories, we should expect that the consistent tangent operator (Hessian operator) and the consistent linearization (second variation of the total potential energy) are not the same. For more a detailed explanation of this issue the reader can consult the excellent paper of Simo [135].

Next, the iterative solution procedure is discussed. The Newton-Raphson technique goes as follows: given a configuration $\Phi^k \in \mathscr{C}$, corresponding to iteration *k*, solve the linearized system

$$\mathcal{G}\left(\Phi^k, \delta\Phi\right) + \nabla\mathcal{G}\left(\Phi^k, \delta\Phi\right) \cdot \Delta\Phi^k = 0 \tag{5.23}$$

where $\Delta\Phi^k$ is the incremental change in the configuration of the shell. This increment is used to update the shell configuration $\Phi^k \to \Phi^{k+1} \in \mathscr{C}$. Namely

$$\Phi^{k+1} = \Phi^k + \Delta\Phi^k. \tag{5.24}$$

It is evident that the use of the triple $\left(\mathbf{u}, \varphi, \underline{\psi}\right)$ preserves the additive structure of the configuration update of the shell. With the new configuration, the value of $\mathcal{G}\left(\Phi^{k+1}, \delta\Phi\right)$ is calculated. Convergence of the iterative procedure is achieved when this value is zero for all $\delta\Phi \in \mathcal{V}$. More details of the incremental/iterative method utilized in the numerical solution are given in Section D.

The consistent tangent operator is decomposed in two parts: the material tangent operator and the geometric tangent operator. Thus

$$D\mathcal{G}\left(\Phi, \delta\Phi\right)\left[\Delta\Phi\right] = D_m\mathcal{G}\left(\Phi, \delta\Phi\right)\left[\Delta\Phi\right] + D_g\mathcal{G}\left(\Phi, \delta\Phi\right)\left[\Delta\Phi\right]. \tag{5.25}$$

The contribution of the external forces vanishes because they are conservative. The first term which is the material part is given by

$$D_m\mathcal{G}\left(\Phi, \delta\Phi\right)\left[\Delta\Phi\right] = \int_{\mathscr{M}_R} \sum_{n=0}^{1} (D\mathbf{M}^n \left[\Delta\Phi\right] \cdot \delta\boldsymbol{\varepsilon}^n)\, d\Omega \tag{5.26}$$

and the geometric part by

$$D_g\mathcal{G}(\Phi,\delta\Phi)[\Delta\Phi]=\int_{\mathscr{M}_R}\sum_{n=0}^{1}(\mathbf{M}^n\cdot D\delta\boldsymbol{\varepsilon}^n[\Delta\Phi])\,d\Omega. \tag{5.27}$$

The material part of the tangent operator results from the directional derivative of the stress resultants. Using (5.12) we obtain

$$\begin{aligned}D\mathbf{M}^i(\Phi)[\Delta\Phi]&=\Delta\mathbf{M}^i(\Phi,\Delta\Phi)\\&=\int_{-h/2}^{h/2}\mu(\theta^3)^i\,\Delta\hat{\mathbf{S}}\,d\theta^3\\&=\sum_{j=0}^{1}\int_{-h/2}^{h/2}\mu(\theta^3)^{i+j}\,\hat{\mathbb{C}}\cdot\Delta\boldsymbol{\varepsilon}^j\,d\theta^3\end{aligned} \tag{5.28}$$

where $D\hat{\mathbf{S}}(\hat{\mathbf{E}})[\Delta\hat{\mathbf{E}}]=\Delta\hat{\mathbf{S}}=\hat{\mathbb{C}}\cdot\Delta\hat{\mathbf{E}}$ and $\hat{\mathbb{C}}$ is the pull-back of the contravariant fourth-order elasticity tensor $\mathbb{C}$. Substituting (5.28) into (5.26) we arrive to

$$D_m\mathcal{G}(\Phi,\delta\Phi)[\Delta\Phi]=\int_{\mathscr{M}_R}\sum_{i=0}^{1}\sum_{j=0}^{1}(\delta\boldsymbol{\varepsilon}^i\cdot\mathbb{B}^{(i+j)}\cdot\Delta\boldsymbol{\varepsilon}^j)\,d\Omega \tag{5.29}$$

where $\Delta\boldsymbol{\varepsilon}^j$ is given by (5.11). The components of the tensor $\mathbb{B}^{(k)}$ are the material stiffness coefficients of the shell and are defined as

$$\mathbb{B}^{(k)}=\int_{-h/2}^{h/2}\mu(\theta^3)^k\,\hat{\mathbb{C}}\,d\theta^3,\qquad k=0,1,2\,. \tag{5.30}$$

For isotropic plates, the tensor $\mathbb{B}^{(1)}$ vanishes. This means that membrane and bending stress resultants are computed directly from membrane and bending strain resultants respectively. There are no coupled terms between both effects.

Two important facts are pointed out from Eq. (5.29): first, the material part of the tangent operator is symmetric whenever the tensor $\hat{\mathbb{C}}$ is symmetric; second, Eq. (5.29) is valid even for cases in which material nonlinearity occurs, i.e. assumption 3 (4.83) is not required.

The geometric part of the tangent operator results from the directional derivative of the variations of the kinematic quantities multiplying the stress resultants. We compute

$\Delta\delta\boldsymbol{\varepsilon}^i$ using (5.11). That is

$$\begin{aligned}\Delta\delta\boldsymbol{\varepsilon}^0 &= \mathrm{Sym}\left(\delta\mathbf{F}^{0^T}\Delta\mathbf{F}^0\right)\\ \Delta\delta\boldsymbol{\varepsilon}^1 &= \mathrm{Sym}\left(\delta\mathbf{F}^{0^T}\Delta\mathbf{F}^1 + \delta\mathbf{F}^{1^T}\Delta\mathbf{F}^0\right)\end{aligned} \tag{5.31}$$

which are symmetric tensors. The stress resultants are evaluated from the following equation

$$\mathbf{M}^i = \sum_{j=0}^{1} \mathbb{B}^{(i+j)}\boldsymbol{\varepsilon}^j, \qquad i = 0,1 \tag{5.32}$$

for a symmetric tensor $\mathbf{M}^i$. Then, we obtain

$$D_g\mathcal{G}(\Phi,\delta\Phi)[\Delta\Phi] = \int_{\mathscr{M}_R} \sum_{i=0}^{1}\sum_{j=0}^{1} (\Delta\delta\boldsymbol{\varepsilon}^i \cdot \mathbb{B}^{(i+j)} \cdot \boldsymbol{\varepsilon}^j)\, d\Omega\,. \tag{5.33}$$

The operator $D_g\mathcal{G}(\Phi,\delta\Phi)[\Delta\Phi]$ is evidently symmetric.

The derivation of virtual internal energy $\mathcal{G}_{\text{int}}$ (5.10a) and the tangent operator (5.25) is not a trivial task. Even for isotropic materials these expressions have an extremely complex form when displacements and rotations are large. To illustrate this fact we show in Table 5.1 the number of terms of the virtual strain energy for the present theoretical model and different laminated shell geometries.

C. Finite element discretization

Similar to the linear deformation cases (see Chapter III, Section C), we construct the finite-dimensional space of $\mathcal{V}$ called $\mathcal{V}^{hp}$ such that $\mathcal{V}^{hp} \subset \mathcal{V}$. Let $\mathscr{A}$ be the parametric space of the midsurface. In tensor-based finite element models, the domain $\mathscr{A}$ is discretized into NEL elements such that

$$\mathscr{A} = \bigcup_{e=1}^{\mathrm{NEL}} \mathscr{A}^e \tag{5.34}$$

for no overlapping subdomains $\mathscr{A}^e$ called finite elements.

Table 5.1. Number of terms of the virtual internal energy for different physical models and geometries.

Theory	Application	Kinematic variables	Virtual strain energy		
			Linear	Nonlinear	Total
Beam (Euler-Bernoulli)*	Moderate rotations	2	2	3	5
Navier-Stokes 2D equations**	-	3	10	4	14
Beam (Present)*	Finite deformations	5	13	109	122
Cylindrical shells (Sanders)	Moderate rotations	5	106	193	299
Rectangular plates (Present)	Finite deformations	7	136	2245	2381
Circular plates (Present)	Finite deformations	7	232	5197	5429
Cylindrical shells (Present)	Finite deformations	7	264	5474	5738
Spherical shells (Present)	Finite deformations	7	666	19630	20296
Hyperboloidal shells (Present)	Finite deformations	7	699	19424	20123

* Isotropic cases. **Newtonian fluid with constant viscosity.

The geometric quantities describing the shell surface (fields $b_{\alpha\beta}, a_{\alpha\beta}, a$) are taken exactly at every Gauss integration point. Therefore, there is no approximation of the midsurface. The natural coordinates θ^{α} are mapped on the biunit square, using high-order Lagrangian polynomials. Namely

$$\underline{\theta}(\xi,\eta)=\left(\sum_{j=1}^{m}(\theta^{\alpha})^{(j)}N^{(j)}(\xi,\eta)\right)\mathbf{e}_{\alpha} \tag{5.35}$$

where $\underline{\theta}=\theta^{\alpha}\mathbf{e}_{\alpha}$, m is the number of nodes of the element and $N^{(j)}(\xi,\eta)$ are Lagrangian interpolation functions at the node j.

Following the concept of isoparametric elements, we use the same Lagrangian polynomial degree for the interpolation of the covariant components of the kinematic variables, i.e.

$$\mathbf{u}^{hp}(\underline{\boldsymbol{\theta}})=\left(\sum_{j=1}^{m}u_i^{(j)}N^{(j)}(\xi,\eta)\right)\mathbf{a}^i,\quad \boldsymbol{\varphi}^{hp}(\underline{\boldsymbol{\theta}})=\left(\sum_{j=1}^{m}\varphi_i^{(j)}N^{(j)}(\xi,\eta)\right)\mathbf{a}^i$$
$$\underline{\boldsymbol{\psi}}^{hp}(\underline{\boldsymbol{\theta}})=\left(\sum_{j=1}^{m}\psi_3^{(j)}N^{(j)}(\xi,\eta)\right)\mathbf{a}^3 \tag{5.36}$$

where $(u_i^{(j)},\varphi_i^{(j)},\psi_3^{(j)})$ denote the nodal values at j of the kinematic variables. The Lagrangian polynomials are defined by (3.17) and (3.18).

The relations (5.36) are then substituted into equations (5.9) and (5.25) and the result into (5.23) arriving to a system of highly nonlinear algebraic equations which can be written in matrix form by means of the stiffness and tangent matrices. The actual computation of the entries of the stiffness and tangent matrices is carried out by symbolic algebra subroutines written in MAPLE. This program, which functions as a pre-processor for the FORTRAN program, allows us not only to generate these matrices in MAPLE language but also to convert them to FORTRAN statements for any adopted theoretical model and shell geometry.

D. Solution procedure

1. The incremental Newton-Raphson method

As mentioned before, The Newton-Raphson method is utilized for solving the system of nonlinear algebraic equations. Let $\hat{\Phi}$ be a configuration solution of the shell (vector quantity). The finite element method leads to a matrix equation of the form

$$\mathcal{R}\left(\hat{\Phi}\right)=\mathbf{0} \tag{5.37}$$

where the vector $\mathcal{R}\left(\hat{\Phi}\right)$ is called the residual (out of balance) force vector defined by

$$\mathcal{R}\left(\hat{\Phi}\right) = {}^{t+\Delta t}\mathbf{F}^{\text{int}}\left(\hat{\Phi}\right) - {}^{t+\Delta t}\mathbf{F}^{\text{ext}}\left(\hat{\Phi}\right). \tag{5.38}$$

The vector ${}^{t+\Delta t}\mathbf{F}^{\text{ext}}$ denotes the externally applied nodal loads and ${}^{t+\Delta t}\mathbf{F}^{\text{int}}$ is the vector of internal forces at the time $t+\Delta t$ (Bathe [68], Reddy [123]).

For a static analysis, the time variable t is a dummy variable used to describe the increment load application and corresponding solution vector. Equation (5.37) must be satisfied at each time t and it can be solved iteratively. We start from the initial configuration and then proceed incrementally. If the configuration at the iteration (i–1), ${}^{t+\Delta t}\Phi^{(i-1)}$ is known, we apply the linearization of the equilibrium equations (5.37) as

$$\mathcal{L}\mathcal{R}\left(\hat{\Phi}\right) = \mathcal{R}\left({}^{t+\Delta t}\Phi^{(i-1)}\right) + \left[\frac{\partial \mathcal{R}}{\partial \Phi}\right]_{{}^{t+\Delta t}\Phi^{(i-1)}} \Delta\Phi^{(i)} + \text{HOT} \tag{5.39}$$

where $\Delta\Phi^{(i)}$ is the incremental vector solution for the iteration *i*. We define the tangent matrix as

$${}^{t+\Delta t}\mathbf{K}_{\text{t}}^{(i-1)} = \left[\frac{\partial \mathcal{R}}{\partial \Phi}\right]_{{}^{t+\Delta t}\Phi^{(i-1)}} = \left[\frac{\partial \mathbf{F}^{\text{int}}}{\partial \Phi}\right]_{{}^{t+\Delta t}\Phi^{(i-1)}} \tag{5.40}$$

for external forces ${}^{t+\Delta t}\mathbf{F}^{\text{ext}}$ configuration independent. Finally, assuming that there is equilibrium at the configuration $\hat{\Phi}$ and neglecting higher-order terms, equation (5.39) becomes

$$\begin{aligned} {}^{t+\Delta t}\mathbf{K}_{\text{t}}^{(i-1)}\Delta\Phi^{(i)} &= -\mathcal{R}\left({}^{t+\Delta t}\Phi^{(i-1)}\right) \\ &= {}^{t+\Delta t}\mathbf{F}^{\text{int}}\left({}^{t+\Delta t}\Phi^{(i-1)}\right) - {}^{t+\Delta t}\mathbf{F}^{\text{ext}}. \end{aligned} \tag{5.41}$$

Considering that the configuration solution is known for the time *t*, a predictor is computed by a tangential incremental solution. Then, it is corrected by iterating equation (5.41) until an appropriate convergence criterion is satisfied (predictor-corrector method). At the time $t+\Delta t$ the initial conditions for starting the iterative scheme are the following

$$ {}^{t+\Delta t}\mathbf{K}_{\mathrm{t}}^{(0)} = {}^{t}\mathbf{K}_{\mathrm{t}}, \quad {}^{t+\Delta t}\mathbf{F}^{\mathrm{int}(0)} = {}^{t}\mathbf{F}^{\mathrm{int}}, \quad {}^{t+\Delta t}\Phi^{(0)} = {}^{t}\Phi. \tag{5.42} $$

The update of the configuration solution is

$$ {}^{t+\Delta t}\Phi^{(i)} = {}^{t+\Delta t}\Phi^{(i-1)} + \Delta\Phi^{(i)}. \tag{5.43} $$

The relations (5.41) and (5.43) constitute the full Newton-Raphson scheme. Notice that a tangent matrix is calculated at each iteration and a given load step. We should also expect that for sufficiently close predictor solution, the convergence rate is quadratic.

2. The arc-length method

The Newton-Raphson method is adequate for most nonlinear system of equations. However, for cases in which the equilibrium path contains limit points and bifurcation points (buckling of shells) the method fails. The response of the structure beyond the limit point is called postbuckling response. At that point the tangent matrix will be singular and the structure will be unstable.

To solve problems with limit and bifurcation points, an arc-length method can be used. The arc-length method was introduced by Riks [136, 137] and Wempner [138] with later modifications by Crisfield [139, 140] and Ramm [141] (see Reddy [123], Bathe [68] and Crisfield [142] for a detailed explanation of the method). The basic idea is to introduce a load multiplier that increases or decreases the intensity of the applied load. The load is assumed to vary proportionally during the response calculation. Equation (5.38) is rewritten as

$$ \mathcal{R}\left(\hat{\Phi}, \lambda\right) = {}^{t+\Delta t}\mathbf{F}^{\mathrm{int}}\left(\hat{\Phi}\right) - {}^{t+\Delta t}\lambda\,\mathbf{F}^{\mathrm{ext}} = \mathbf{0}. \tag{5.44} $$

Note that the load parameter λ becomes a variable. Equation (5.44) represents a system of n equations with $n+1$ unknowns. Hence, we need an additional equation which is used to determine the load multiplier. We introduce a spherical arc-length constraint. This is a constraint equation between the total displacement and load increments $\Phi^{(i)}$ and $\lambda^{(i)}$ at the time $t+\Delta t$, i.e.

$$\mathcal{K}\left(\Phi^{(i)},\lambda^{(i)}\right)=\Phi^{(i)}\cdot\Phi^{(i)}+\beta(\lambda^{(i)})^{2}\mathbf{F}^{\text{ext}}\cdot\mathbf{F}^{\text{ext}}-(\Delta L)^{2}=0 \tag{5.45}$$

where ΔL is the assumed arc-length for the step and β is a normalizing factor that takes care of the different dimension of the variables. The vector $\Phi^{(i)}$ and the scalar $\lambda^{(i)}$ are incremental (not iterative) quantities related to the last converged equilibrium state. It is implicitly understood that the total incremental quantities are referred to the time $t+\Delta t$. Consequently, they never use left superscripts (Fig. 5.2).

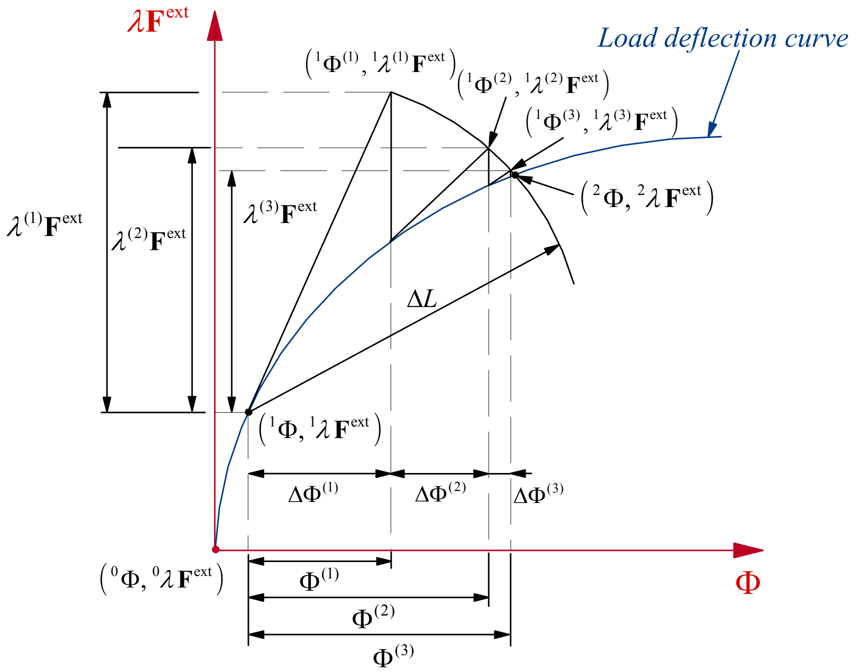

Fig. 5.2. Spherical arc-length procedure and notation for one degree of freedom system with $\beta=1$.

Within the load step $t+\Delta t$, the total increments $\Phi^{(i)}$ and $\lambda^{(i)}$ are defined by

$$\begin{aligned}\Phi^{(i)} &= {}^{t+\Delta t}\Phi^{(i)} - {}^{t}\Phi \\ \lambda^{(i)} &= {}^{t+\Delta t}\lambda^{(i)} - {}^{t}\lambda\,.\end{aligned} \tag{5.46}$$

The linearization of equation (5.44) is then applied around the configuration solution ${}^{t+\Delta t}\Phi^{(i-1)}$. This leads to

$$\mathcal{LR}\left(\hat{\Phi}\right)=\mathcal{R}\left({}^{t+\Delta t}\Phi^{(i-1)}\right)+\left[\frac{\partial\mathcal{R}}{\partial\Phi}\right]_{{}^{t+\Delta t}\Phi^{(i-1)}}\Delta\Phi^{(i)}+\left[\frac{\partial\mathcal{R}}{\partial\lambda}\right]_{{}^{t+\Delta t}\Phi^{(i-1)}}\Delta\lambda^{(i)}+\text{HOT}. \tag{5.47}$$

After some manipulations equation (5.47) becomes

$$\begin{aligned}{}^{t+\Delta t}\mathbf{K}_{\mathrm{t}}^{(i-1)}\Delta\Phi^{(i)} &= -\mathcal{R}\left({}^{t+\Delta t}\Phi^{(i-1)}\right)+\Delta\lambda^{(i)}\mathbf{F}^{\text{ext}} \\ &= ({}^{t+\Delta t}\lambda^{(i-1)}+\Delta\lambda^{(i)})\mathbf{F}^{\text{ext}}-\mathbf{F}^{\text{int}}\left({}^{t+\Delta t}\Phi^{(i-1)}\right)\end{aligned} \tag{5.48}$$

where $\Delta\Phi^{(i)}$ and $\Delta\lambda^{(i)}$ are the displacement and load increments at the iteration *i*.

To solve (5.48) we may rewrite this equation as

$$\begin{aligned}{}^{t+\Delta t}\mathbf{K}_{\mathrm{t}}^{(i-1)}\Delta\bar{\Phi}^{(i)} &= -\mathcal{R}\left({}^{t+\Delta t}\Phi^{(i-1)}\right) \\ {}^{t+\Delta t}\mathbf{K}_{\mathrm{t}}^{(i-1)}\Delta\tilde{\Phi}^{(i)} &= \mathbf{F}^{\text{ext}}\end{aligned} \tag{5.49}$$

and hence,

$$\Delta\Phi^{(i)}=\Delta\bar{\Phi}^{(i)}+\Delta\lambda^{(i)}\Delta\tilde{\Phi}^{(i)}\,. \tag{5.50}$$

The total displacement and load increments are computed as

$$\begin{aligned}\Phi^{(i)} &= \Phi^{(i-1)}+\Delta\Phi^{(i)} \\ &= \Phi^{(i-1)}+\Delta\bar{\Phi}^{(i)}+\Delta\lambda^{(i)}\Delta\tilde{\Phi}^{(i)} \\ \lambda^{(i)} &= \lambda^{(i-1)}+\Delta\lambda^{(i)}.\end{aligned} \tag{5.51}$$

Substituting (5.51) into the spherical arc-length constraint (5.45) gives a quadratic equation in $\Delta\lambda^{(i)}$ whose solution is the following

$$\mathcal{K}\left(\Phi^{(i)},\lambda^{(i)}\right)=a_1(\Delta\lambda^{(i)})^2+a_2\Delta\lambda^{(i)}+a_3=0 \tag{5.52}$$

where

$$\begin{aligned} a_1 &= \Delta\tilde{\Phi}^{(i)} \cdot \Delta\tilde{\Phi}^{(i)} + \beta \mathbf{F}^{\text{ext}} \cdot \mathbf{F}^{\text{ext}} \\ a_2 &= 2\Delta\tilde{\Phi}^{(i)} \cdot (\Phi^{(i-1)} + \Delta\bar{\Phi}^{(i)}) + 2\beta\lambda^{(i-1)} \mathbf{F}^{\text{ext}} \cdot \mathbf{F}^{\text{ext}} \\ a_3 &= (\Phi^{(i-1)} + \Delta\bar{\Phi}^{(i)}) \cdot (\Phi^{(i-1)} + \Delta\bar{\Phi}^{(i)}) - (\Delta L)^2 + \beta(\lambda^{(i-1)})^2 \mathbf{F}^{\text{ext}} \cdot \mathbf{F}^{\text{ext}} \end{aligned} \tag{5.53}$$

which can be solved for $\Delta\lambda^{(i)}$. Then, the update of the configuration of the shell (5.51) is completely defined.

Equation (5.52) yields two different solutions: $\Delta\lambda_1^{(i)}$ and $\Delta\lambda_2^{(i)}$. Hence, we arrive to two configuration of the shell, i.e.

$$\begin{aligned} \Phi_1^{(i)} &= \Phi^{(i-1)} + \Delta\bar{\Phi}^{(i)} + \Delta\lambda_1^{(i)} \Delta\tilde{\Phi}^{(i)} \\ \Phi_2^{(i)} &= \Phi^{(i-1)} + \Delta\bar{\Phi}^{(i)} + \Delta\lambda_2^{(i)} \Delta\tilde{\Phi}^{(i)}. \end{aligned} \tag{5.54}$$

We should choose a solution that lies closest to the previous total displacement increment $\Phi^{(i-1)}$. This procedure can be implemented by finding the solution of minimum angle α between $\Phi^{(i-1)}$ and $\Phi^{(i)}$. Namely

$$\cos\alpha = \frac{\Phi^{(i)} \cdot \Phi^{(i-1)}}{(\Delta L)^2} = \frac{a_4 + a_5\, \Delta\lambda^{(i)}}{(\Delta L)^2} \tag{5.55}$$

where

$$\begin{aligned} a_4 &= \Phi^{(i)} \cdot \Phi^{(i-1)} + \Phi^{(i)} \cdot \Delta\bar{\Phi}^{(i)} \\ a_5 &= \Phi^{(i)} \cdot \Delta\tilde{\Phi}^{(i)}. \end{aligned} \tag{5.56}$$

We now discuss the effect of the parameter β in the numerical solution. Crisfield [139] and Ramm [141] independently concluded that, for practical problems, the external load vector has a little influence on the final response. Therefore, we can set $\beta = 0$ which leads to a cylindrical rather than spherical constraint (5.45). This approach is called the cylindrical arc-length method.

At any initial load step, we shall assume a predictor solution. For the present cylindrical arc-length method the predictor solution is computed by the forward-Euler tangential method. That is

$$\begin{aligned}\Phi^{(1)} &= (\lambda^{(1)})\,{}^{t+\Delta t}\mathbf{K}_{\mathrm{t}}^{(0)^{-1}}\,\mathbf{F}^{\mathrm{ext}} \\ &= (\lambda^{(1)})\,{}^{t}\mathbf{K}_{\mathrm{t}}^{-1}\mathbf{F}^{\mathrm{ext}}.\end{aligned} \tag{5.57}$$

Note that $\Phi^{(1)} = \Delta\Phi^{(1)}$ and $\lambda^{(1)} = \Delta\lambda^{(1)}$. Substituting (5.57) into equation (5.45) with $\beta = 0$, we obtain

$$\lambda^{(1)} = \pm\frac{\Delta L}{\sqrt{\Delta\tilde{\Phi}^{(1)}\cdot\Delta\tilde{\Phi}^{(1)}}}. \tag{5.58}$$

The sign is taking positive if the tangent matrix ${}^{t}\mathbf{K}_{\mathrm{t}}$ is positive definite. Otherwise, for negative definite tangent matrix we take the negative value of $\lambda^{(1)}$.

Finally, the update of the configuration of the shell is calculated by

$$\begin{aligned}{}^{t+\Delta t}\Phi^{(i)} &= {}^{t+\Delta t}\Phi^{(i-1)} + \Delta\Phi^{(i)} \\ {}^{t+\Delta t}\lambda^{(i)} &= {}^{t+\Delta t}\lambda^{(i-1)} + \Delta\lambda^{(i)}\end{aligned} \tag{5.59}$$

or using the total increment

$$\begin{aligned}{}^{t+\Delta t}\Phi^{(i)} &= {}^{t+\Delta t}\Phi^{(0)} + \Phi^{(i)} = {}^{t}\Phi + \Phi^{(i)} \\ {}^{t+\Delta t}\lambda^{(i)} &= {}^{t+\Delta t}\lambda^{(0)} + \lambda^{(i)} = {}^{t}\lambda + \lambda^{(i)}\end{aligned} \tag{5.60}$$

at the time $t + \Delta t$. The additive relation (5.59) is valid for all degrees of freedom of the present finite element model. This is a great advantage over geometrically exact shell theories in which complex multiplicative update algorithms are required.

E. Numerical simulations

In this section, numerical simulations of the finite element approach for composite laminates and functionally graded shells are presented. An extensive verification is carried out for the present 7-parameter shell formulation by comparing our results with those found in the literature. In particular, we use the recent paper of Sze et al. [143] of popular benchmark problems for nonlinear shell analysis (because of the tabulated data). Furthermore, a parametric study is also done for bending behavior of multilayered composites and functionally graded ceramic-metal shells.

Regular meshes of $Q25$, $Q49$ and $Q81$ high-order elements with seven degrees of freedom per node were utilized in the finite element analysis (see Table 3.1). By increasing the p level or refining the finite element mesh, we mitigate locking problems. Therefore, there is no need to use tricky mixed interpolations techniques (for lower-order elements such as assumed strain elements or MITC elements) or reduced integration in the evaluation of the stiffness coefficients (i.e., full Gauss integration rule is employed in all examples).

1. Plates

a. Cantilever strip plate

The first example is a cantilever strip plate under end shear distributed force. The length L is set to be 10 and width $b = 1$ with ratio $L/h = 100$. For the analysis, a mesh of $4\times1Q25$ elements is enough to reach good convergence (Fig. 5.3). The material properties are prescribed to be

$$E = 1.0\times10^{7}, \quad \nu = 0.0$$

where E and ν are the Young's modulus and the Poisson's ratio, respectively.

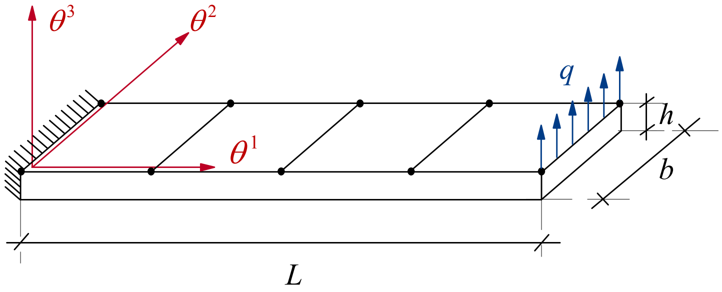

Fig. 5.3. Geometry of cantilever strip plate under end shear force.

Figure 5.4 shows the axial and transverse deflections of the tip of the plate versus the distributed shear loading q and compares the present results with those of Sze et al. [143]. Sze et al. use the ABAQUS commercial program for their examples which utilizes a bilinear element with hourglass stabilization (6 degrees of freedom per node). An excellent agreement is found between both formulations.

In Fig. 5.5 is illustrated the deformed configuration of the plate for different shear loading stages q. It is clearly seen that the plate undergoes large displacements. We do not consider in this problem a following loading (for that case the tangent operator would have another term due to the external load). The shear force remains in the same direction during the deformation.

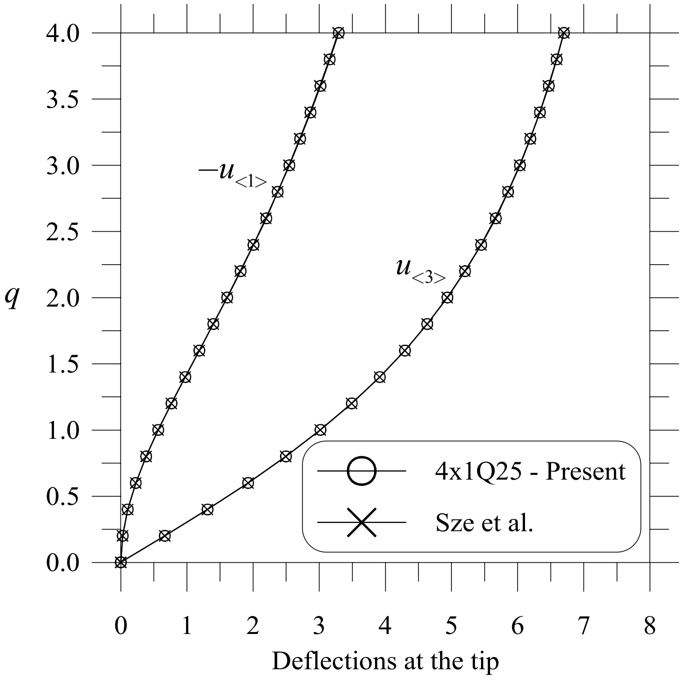

Fig. 5.4. Tip-deflection curves vs. shear loading q of the cantilever strip plate.

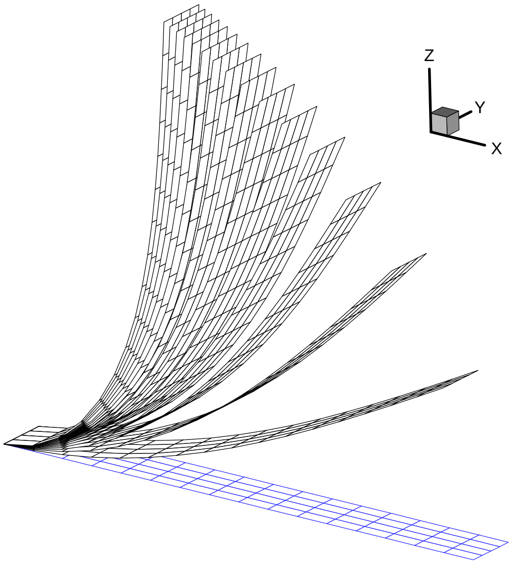

Fig. 5.5. Deformed configurations of the cantilever strip plate under end shear force (loading stages $q = 1, 2, \ldots, 15$).

Next, we consider a composite laminated plate with the same geometric data and loading conditions as the last example. The material properties of the lamina are as follows

$$\begin{aligned} &E_1 = 1.0\times10^6, E_2 = E_3 = 0.3\times10^6 \\ &G_{12} = G_{13} = 0.15\times10^6, G_{23} = 0.12\times10^6 \\ &\nu_{12} = \nu_{13} = 0.25, \nu_{23} = 0.25 \end{aligned}$$

for a transversely isotropic material.

The tip transverse deflection versus the distributed shear force is shown in Fig. 5.6 for different laminate schemes. As expected, the lay-up (90°/0°/90°) shows the most flexible response while the cross-ply laminate (0°/90°/0°) exhibits the stiffest response. It is observed that due to the non-symmetry of the angle-ply scheme (-45°/45°/-45°/45°) the plate displays lateral displacements in the direction θ^2 (Fig. 5.3). Nevertheless, the values are so small in comparison to the transverse displacements that can be neglected.

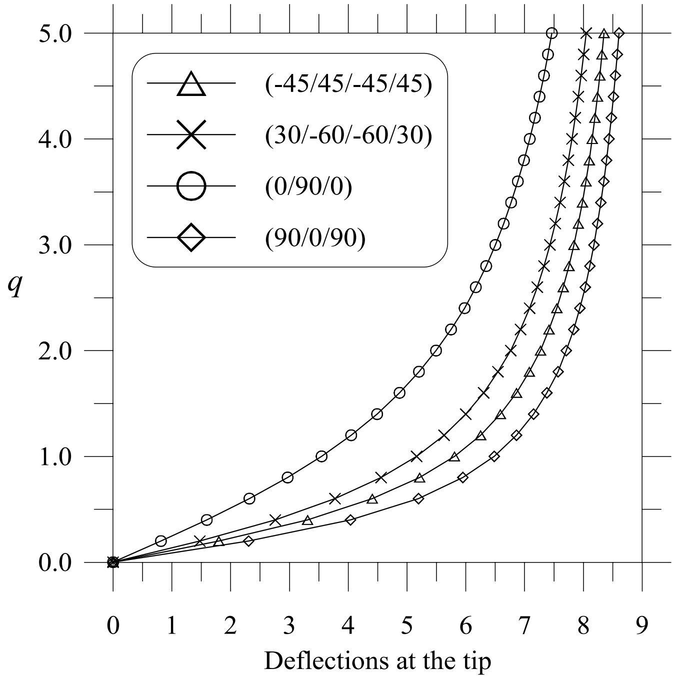

Fig. 5.6. Tip-deflection curves for laminate cantilever plate.

b. Roll-up of a clamped strip plate

A clamped strip plate is subjected to a bending distributed moment on the other end (Fig. 5.7). This is a classical benchmark problem for large deformation analysis and it has been considered in Refs. [92, 94, 111, 143]. In fact, this problem tests the capability of the finite element model to simulate finite rotations on shells. The analytical solution of this example corresponds to the classical formula $1/\rho = M/EI$. Thus, the tip deflections can be derived to be

$$\begin{aligned} \frac{u_{<1>}}{L} &= \frac{k}{M}\sin\left(\frac{M}{k}\right) - 1 \\ \frac{u_{<3>}}{L} &= \frac{k}{M}\left(1 - \cos\left(\frac{M}{k}\right)\right) \end{aligned} \qquad (5.61)$$

where $k = EI/L$. For $M_{\max} = 2\pi k$, the beam rolls up into a complete circle.

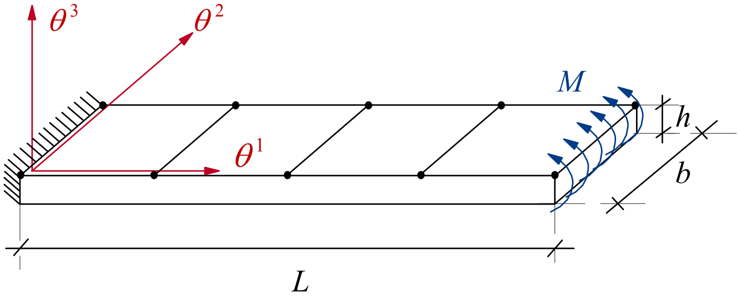

Fig. 5.7. Cantilever strip plate under end bending moment.

The material properties and geometry of the plate are chosen as

$$E = 1.2\times 10^6, \quad \nu = 0.0$$
$$L = 12.0, \quad b = 1.0, \quad h = 0.1\,.$$

Figure 5.8 depicts the tip displacement of the cantilever strip plate versus the end bending moment. For the present results a regular mesh of 8×1$Q25$ elements was utilized in the finite element discretization. The total loading is applied in 200 equal steps. The Newton method exhibits an excellent rate of convergence with less than 3 iterations per load step. The agreement between the present results and the computed analytical solution (5.61) is excellent.

Figure 5.9 shows the undeformed and deformed configuration of the strip plate for various load stages. The last two deformed configurations demonstrate the ability of the present approach to handle extreme rotations of the plate (up to 360° and 720° respectively). Geometrically exact shell models with parametrizations of the rotation tensor based on two independent angles or spherical coordinates (see Betsch et al. [111]) are not able to reach deformed configurations beyond 180° because the tangent stiffness matrix becomes rank-deficient.

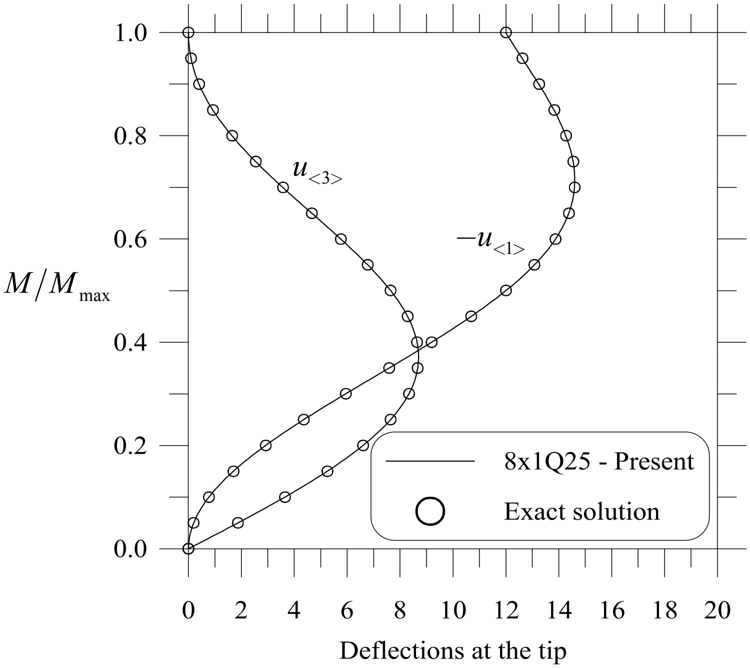

Fig. 5.8. Tip-deflection curves vs. end moment *M* of the cantilever strip plate.

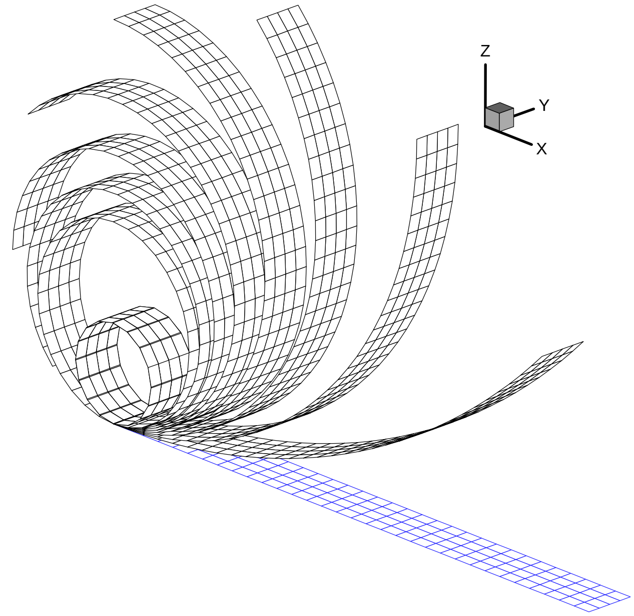

Fig. 5.9. Deformed configurations of the cantilever plate under end bending moment (loading stages $M/M_{\max} = 0.125, 0.25, \ldots, 1, 2$).

c. *Torsion of a clamped strip plate*

Similar to the last example, this problem exhibits large rotations and displacements. A torsional moment is applied to the end of an initially flat strip plate leading to torsional rotations up to 270° (Fig. 5.10). This example was analyzed by Simo et al. [92] (with the geometrically exact shell theory) and by Park et al. [144]. For the present case, we consider the following material properties and geometry

$$E = 12.0 \times 10^6, \quad \nu = 0.3$$
$$L = 10.0, \quad b = 1.0, \quad h = 0.1\,.$$

The torsional moment is an external loading which is treated as a secondary variable (related to a rotation θ) in finite element models with rotational degrees of freedom. Nevertheless, for the present approach the virtual work caused by the torsional moment T should be transformed into secondary variables related to the degrees of freedom φ_1 and φ_3, i.e.

$$T\delta\theta = M_1\delta\varphi_1 + M_3\delta\varphi_3 \tag{5.62}$$

where θ is the rotation around the axis θ^2 and M_i is a secondary variable related to φ_i.

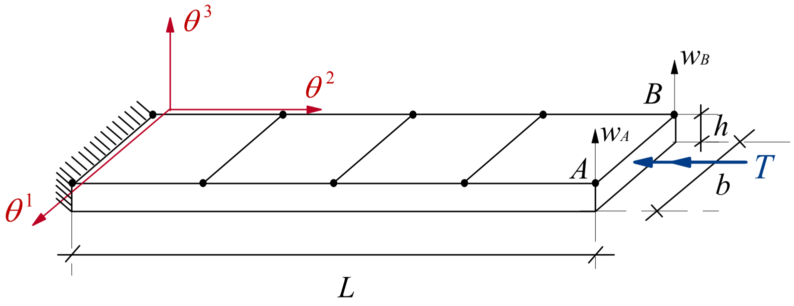

Fig. 5.10. Cantilever strip plate under end torsional moment.

The rotation θ can be expressed in terms of φ_1 and φ_3 by the relation

$$\tan\theta = \frac{\varphi_1}{(\varphi_3 + 1)}. \tag{5.63}$$

Applying the variation of (5.63) and substituting the result into (5.62) leads to

$$\begin{aligned} M_1 &= \frac{T(\varphi_3 + 1)}{\lambda^2} \\ M_3 &= -\frac{T\varphi_1}{\lambda^2} \end{aligned} \tag{5.64}$$

where $\lambda = \|\bar{\mathbf{a}}_3\| = \sqrt{\varphi_1{}^2 + (\varphi_3 + 1)^2}$.

At each iteration i and load step $t + \Delta t$, the secondary variables are computed by Eq. (5.64) using the previous configuration solution ${}^{t+\Delta t}\Phi^{(i-1)}$. Yet, the value of the moment M remains constant during the load step. This procedure should be applied to problems in which moments are involved as external loadings (e.g., the roll-up of a clamped beam).

Figure 5.11 shows the transverse deflections at the points A and B of the strip plate subjected to a torsional moment. The finite element simulation is performed with two different regular meshes of 1×8Q25 and 1×4Q81 elements in a full computational domain. The displacements at A and B are found to be equal but with opposite sign (maximum value of $b/2$).

Figure 5.12 depicts the deformed finite element mesh of the cantilever plate for various load stages. In the last configuration (for M = 1000), the plate displays rotations up to 270°. At that level of deformation convergence of the Newton-Raphson method is more difficult to achieve. The number of iterations of the Newton-Raphson method increases when the loading increases.

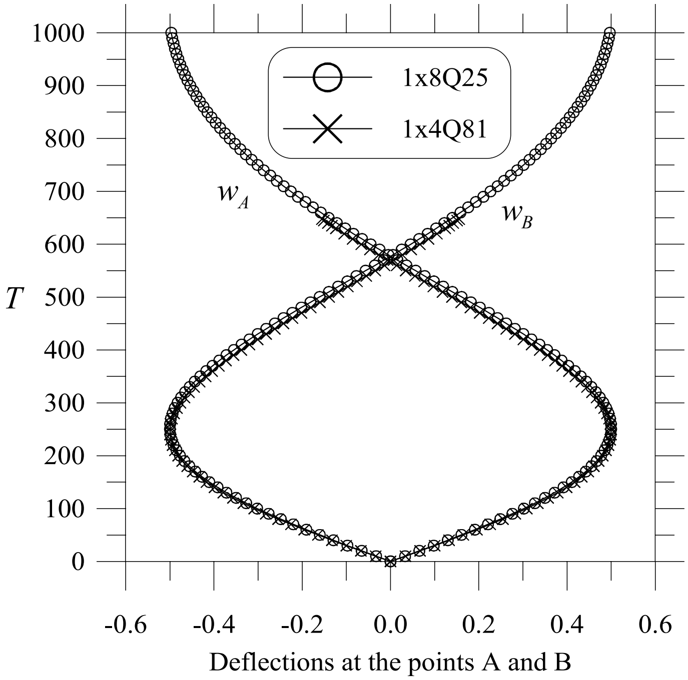

Fig. 5.11. Transverse deflection curves at points *A* and *B* vs. the torsional moment *T* of a cantilever strip plate.

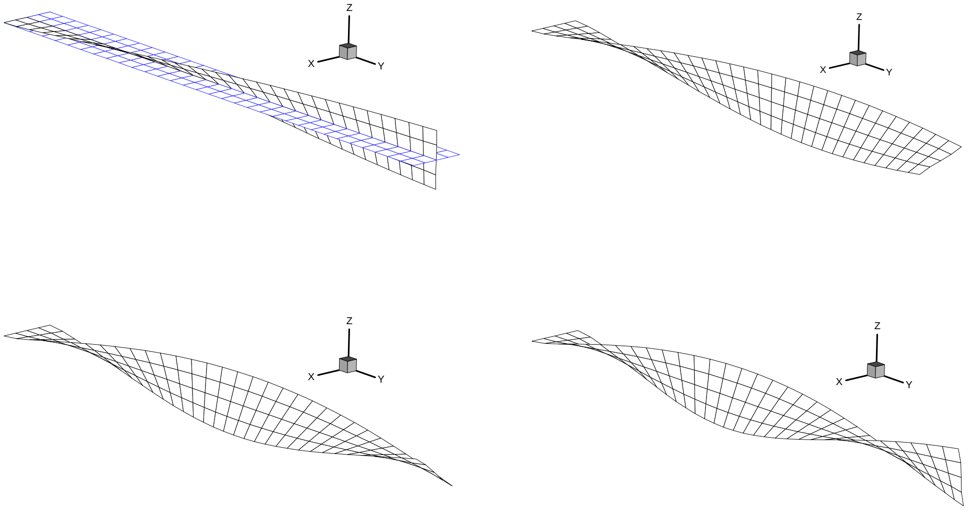

Fig. 5.12. Deformed configurations of the clamped strip plate under torsional moment (loading stages $T = 250, 500, 750, 1000$).

d. Postbuckling of a strip plate

We now consider bucking and postbuckling behavior of an isotropic plate subjected to compressive load (Fig. 5.13). This example shows the robustness of the present model to deal with pre-buckling and postbuckling response of shells. The following material properties and geometry, given by Massin and Al Mikdad [145], are used here

$$E = 2.0\times10^{11}, \quad \nu = 0.3$$
$$L = 0.5, \quad b = 0.075, \quad h = 0.0045$$

with moment of inertia $I_1 = 5.7\times10^{-10}$.

To activate the postbuckling equilibrium path we have to include a small perturbation in the system. Otherwise, only inplane displacements in the plate will occur (which is called the fundamental equilibrium path that beyond the critical load will be unstable). For the secondary path, we assume that the compressive load is applied with an imperfect angle of $1/1000$ $(0.0573°)$. That is, in addition to the inplane compressive load there is a small out of plane loading that causes the postbuckling response of the plate.

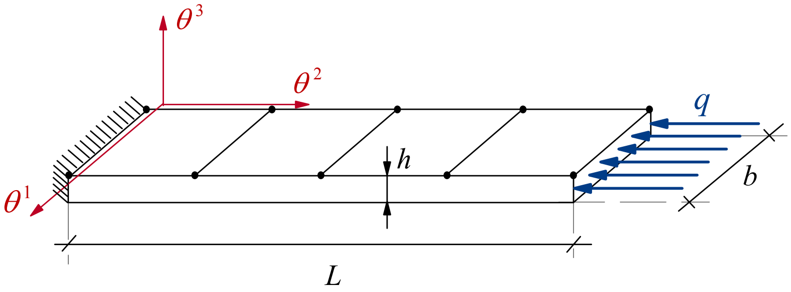

Fig. 5.13. Postbuckling of a strip plate under compressive load.

The tip displacement of the plate vs. the axial load is illustrated in Fig. 5.14. It is clearly observed a well-defined prebuckling stage ($F \le P_{cr}$) and postbuckling stage ($F \ge P_{cr}$). It is remarkable to see the accuracy of the critical load calculated by the present approach versus that obtained by Euler's formula ($P_{cr} = \pi^2 EI_1 / 4L^2$) which is $P_{cr} = 1124.2096$.

We also compare the present results with the analytical solution of Timoshenko [146]. We notice some differences (but still small) between both formulations, in particular, in the inplane displacement $u_{<1>}$. This can be attributed to the fact that the analytical solution of Timoshenko considers the plate inextensible while in the present formulation membrane deformations are taken into account. Finally, Fig. 5.15 shows various deformed configurations for the strip plate under axial compressive loading.

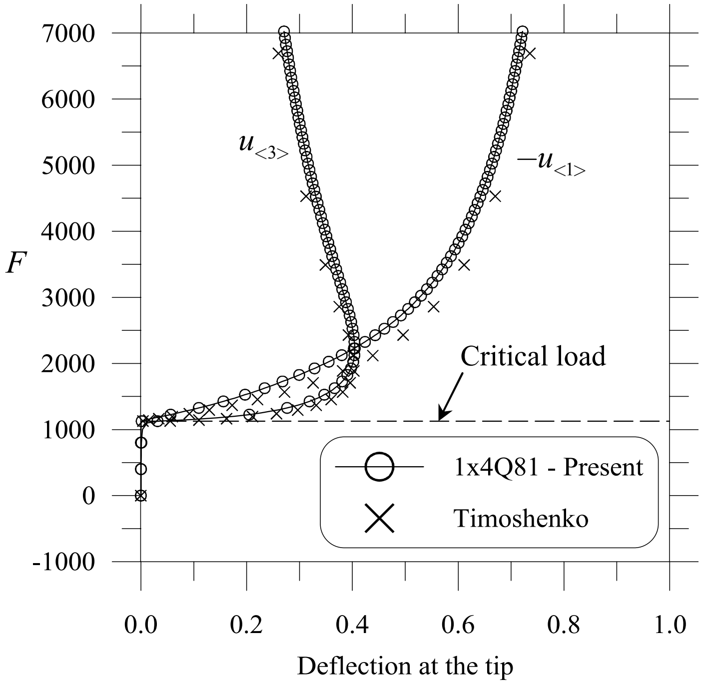

Fig. 5.14. Tip deflection curves vs. the compressive force $F = qb$ of a cantilever strip plate.

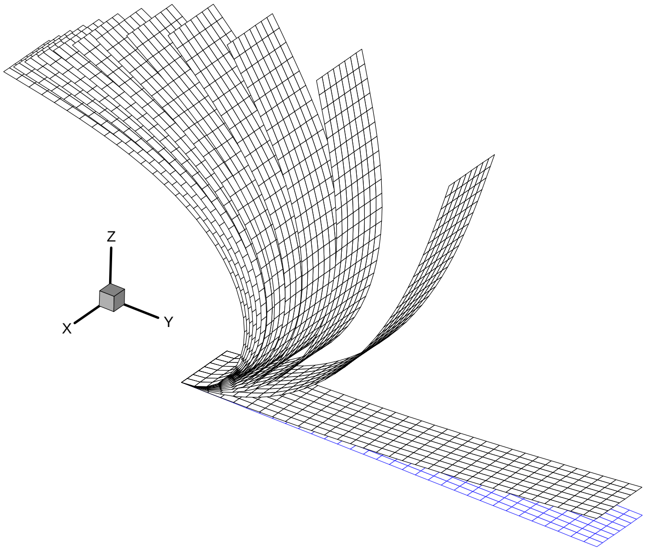

Fig. 5.15. Postbuckling configurations of the clamped strip plate under compressive load (loading stages $F = 1125, 1500, 2000, \ldots, 7000$).

e. Annular plate under end shear force

Next, we examine an annular clamped plate subjected to a distributed shear force (Fig. 5.16). This beautiful benchmark problem was considered by Büchter and Ramm [9], Sansour and Kollmann [112], Brank et al. [19] and Sze et al. [143], among others. The geometry and elastic material properties for the isotropic case are given by

$$E = 21.0 \times 10^6, \nu = 0.0$$
$$R_i = 6,\ R_e = 10,\ h = 0.03$$

for a maximum distributed force of $q_{\max} = 0.8$.

In the present simulation the plate is modeled by polar coordinates. However, the problem can be solved by using the standard Cartesian coordinates as well. A regular mesh of $1 \times 5Q49$ elements (p level equal to 6) is considered in the present analysis, because solutions obtained by the element $Q25$ are too stiff and suffer from locking.

Computation is performed by the Newton-Raphson method with 80 load steps (with equal load steps of 0.04). The standard convergence tolerance for the residual forces is set to be 1.0×10^{-6}.

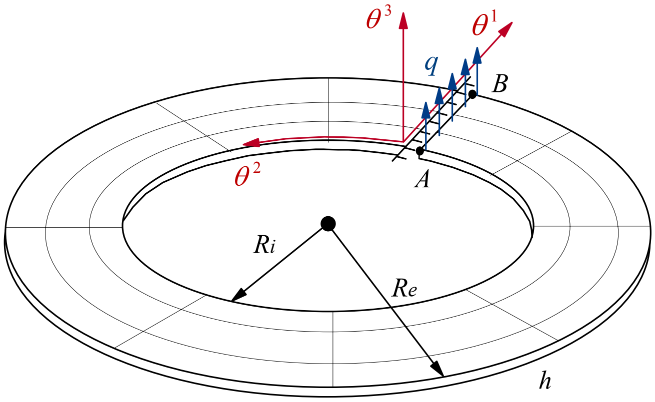

Fig. 5.16. Annular plate under end shear force.

The shear load versus displacement curves for two characteristic points are depicted in Fig. 5.17. Solutions obtained with the present formulation are in good agreement with those obtained by Sze et al. [143]. Figure 5.18 shows the deformed configuration of the isotropic annular plate for various load levels. It is seen that the plate undergoes large displacements at the corresponding loading of $F=3.2$.

We also study the bending behavior of the annular plate for multilayered composites with the same geometry as the isotropic case. The material properties of the lamina are as follows

$$\begin{aligned}&E_1=20.0\times10^6,\ E_2=E_3=6.0\times10^6\\&G_{12}=G_{13}=3.0\times10^6, G_{23}=2.4\times10^6\\&\nu_{12}=\nu_{13}=0.3, \nu_{23}=0.25\ .\end{aligned}$$

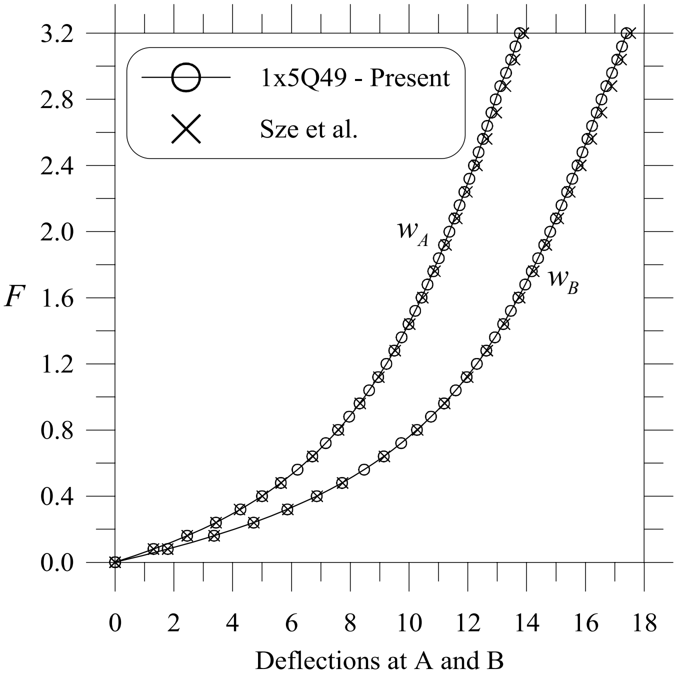

Fig. 5.17. Transverse displacement curves at points A and B vs. shear force $F = 4q$ of the cantilever annular plate.

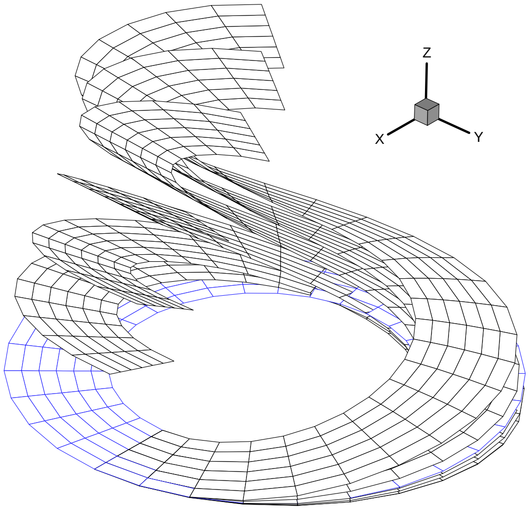

Fig. 5.18. Deformed configurations of the annular plate under end shear force (loading stages $F = 0.2, 0.4, 0.8, 1.6, 2.4, 3.2$).

The deflections at the point B versus the shear force are shown in Fig. 5.19 for different laminate schemes. Like the isotropic case, we consider for this problem full computational domain. We note that the laminate (-45°/45°/-45°/45°) exhibits the stiffest response. However, the plate still undergoes large displacements. Finally, Fig. 5.20 shows the deformed configuration for a composite angle-ply annular plate under a shear loading $F = 1.8$. From a qualitative standpoint, the deformed configuration for the laminated plate is quite similar to the corresponding configurations for isotropic plates.

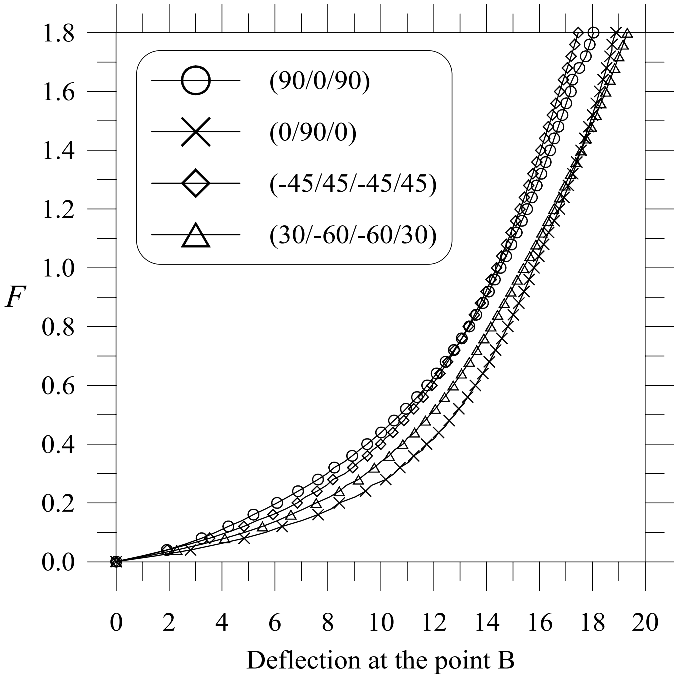

Fig. 5.19. Displacement at B vs. shear force $F = 4q$ of the annular plate for various laminate schemes.

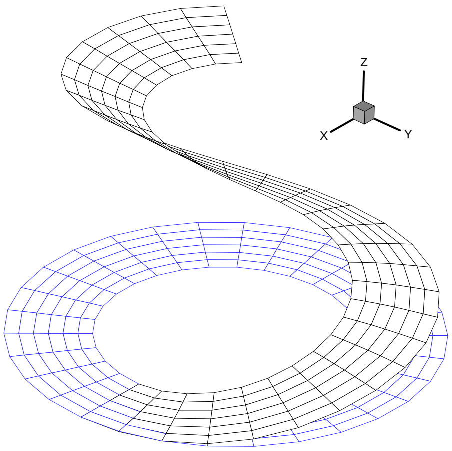

Fig. 5.20. Deformed configuration of the annular plate under end shear force. Anti-symmetric angle-ply (-45°/45°/-45°/45°), loading $F = 1.8$.

2. Cylindrical shells

a. Cylindrical panel under point load

We study the behavior of cylindrical panels under central point load (Fig. 5.21). This is a well-known benchmark problem for nonlinear analysis of cylindrical shells which is particularly popular due to the snapping behavior. The problem has been considered in Refs. [19, 92, 139, 141, 143, 147]. The cylindrical arc-length method is used to follow the nonlinear path because the response of the structure goes beyond the limit point. The following cases are analyzed here: an isotropic panel, two cross-ply composite panels with schemes (0°/90°/0°) and (90°/0°/90°), an angle-ply laminate (-45°/45°/-45°/45°), and a laminate (30°/-60°/-60°/30°). All plies in the same laminate are equal in thickness. The material properties for the isotropic case are

$$E = 3102.75 \text{ N/mm}^2, \quad \nu = 0.3$$

with geometrical data

$$a = 508\,\text{mm}, \quad R = 2540\,\text{mm}, \quad h = 25.4, 12.7, 6.35\,\text{mm}, \quad \alpha = 0.1\,rad.$$

The material properties for the multilayered composites studied here are

$$E_1 = 3300\ \text{N/mm}^2, E_2 = E_3 = 1100\ \text{N/mm}^2$$
$$G_{12} = G_{13} = 660\ \text{N/mm}^2, G_{23} = 440\ \text{N/mm}^2$$
$$\nu_{12} = \nu_{13} = 0.25, \nu_{23} = 0.25\ .$$

The panel is hinged at the edges $\theta^2 = \pm\alpha$ and free at $\theta^1 = \pm a/2$. Due to the symmetry of the structure, a quarter of the shell is taken as computational domain for symmetric laminates. The boundary conditions for this example are

At $\theta^1 = 0$ $\quad u_{<1>} = \varphi_{<1>} = 0$ (Symmetry)

At $\theta^2 = 0$ $\quad u_{<2>} = \varphi_{<2>} = 0$ (Symmetry)

At $\theta^2 = \alpha$ $\quad u_{<1>} = u_{<2>} = u_{<3>} = \varphi_{<1>} = 0$

At $\theta^1 = a/2$ $\quad$ Free .

For other cases (e.g. antisymmetric laminates), we analyze the full panel, i.e

At $\theta^1 = \pm a/2$ $\quad$ Free

At $\theta^2 = \pm\alpha$ $\quad u_{<1>} = u_{<2>} = u_{<3>} = \varphi_{<1>} = 0\ .$

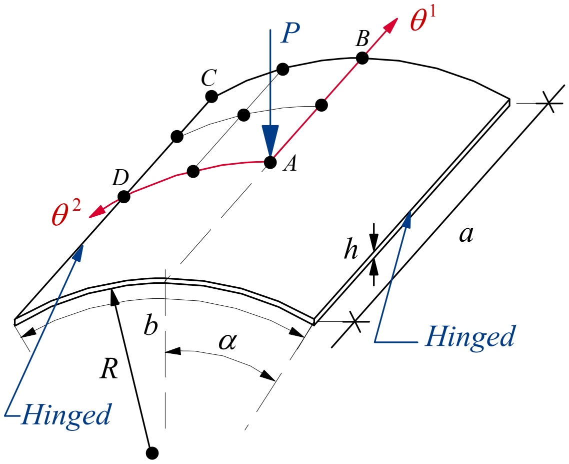

Fig. 5.21. Cylindrical shallow panel under point load.

In the following examples regular meshes of 4×4Q25 elements are used in a quarter of the shell. Figure 5.22 shows a comparison between the present central deflection results with those obtained by Sabir and Lock [147] for an isotropic shell with thickness h = 25.4 mm. They are in good agreement. Since there is no presence of limit points, this problem can be solved by the Newton-Raphson method.

If we reduce the thickness of the panel the response of the shell is dramatically different. Figures 5.23 and 5.24 show the load-deflection behavior of the shallow shell under point load with thickness $h = 12.7, 6.35\,\text{mm}$, respectively. In addition to the isotropic panel, two symmetric cross-ply laminates are included in the analysis, namely (90°/0°/90°) and (0°/90°/0°). Results obtained by Sze et al. are also reported for comparison reasons. The arc-length method is used in these examples.

We see from Fig. 5.23 that the structure, for the three studied cases, exhibits a limit point (the tangent matrix becomes singular). Beyond the limit point, the response of the panel will be unstable with possibility to occur a snap through. On the other hand, we observe from Fig. 5.24 a chaotic behavior of the panel, in particular, the corresponding load-deflection curve for the laminate (0°/90°/0°). For this laminate the response exhibits not only horizontal but also vertical tangents (8 in total). At some specific load level we can expect up to five different configuration solutions. The results shown in Fig. 5.23 and 5.24, obtained with the present formulation are in complete agreement with those reported in the literature [143].

We also notice that the level of deformation of the shell is still relatively small. No large displacements and rotations occur during the deformation. Therefore, we can obtain good approximations for this problem using simpler shell formulations (e.g. the theory of Sanders [148], the moderate rotation theory [95], etc).

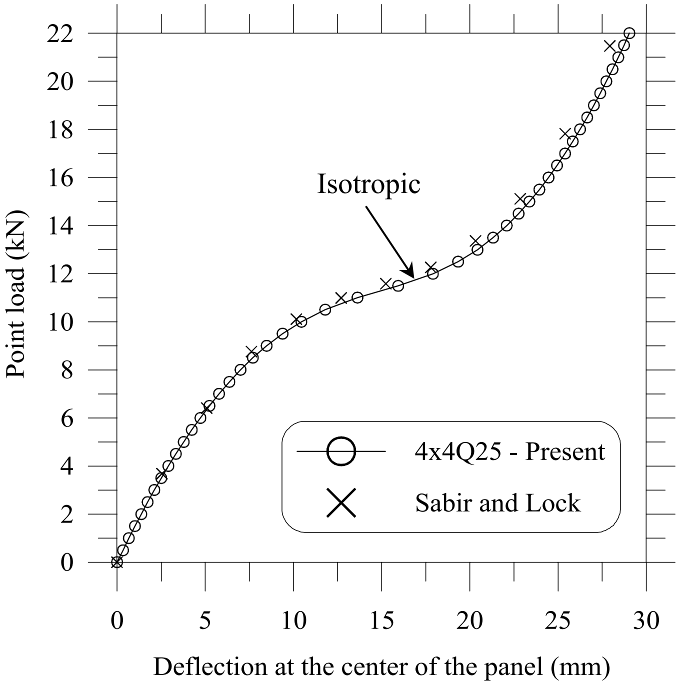

Fig. 5.22. Deflection at the center of the shallow panel under point load (*h* = 25.4mm).

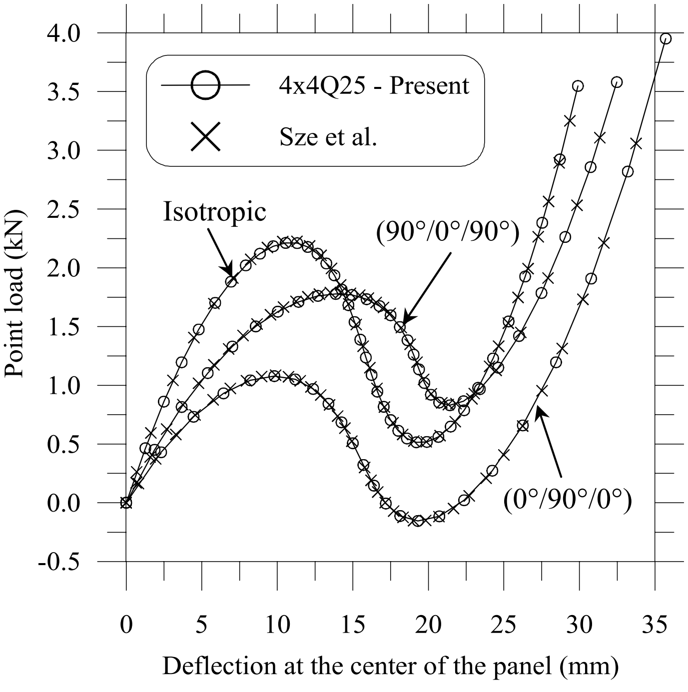

Fig. 5.23. Deflection at the center of the shallow panel under point load (*h* = 12.7 mm).

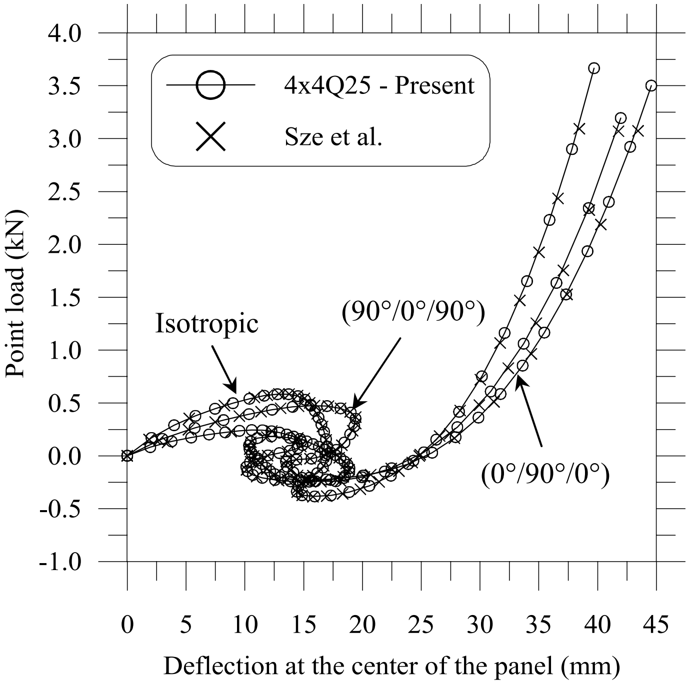

Fig. 5.24. Deflection at the center of the shallow panel under point load (*h* = 6.35 mm).

Next, we investigate the behavior of the cylindrical panel for two different stacking sequences: (-45°/45°/-45°/45°) and (30°/-60°/-60°/30°). Again, two thicknesses are considered in the analysis ($h = 12.7, 6.35\,\mathrm{mm}$) that leads to a thin panel with ratio $S = 200, 400$ (recall $S = R/h$). Since it is unknown the response of antisymmetric laminates, full panel is modeled with appropriate boundary conditions. A regular 8×8 mesh of *Q*25 elements (*p* level equal to 4) is used in the present analysis.

Numerical results concerning the central deflection at the point load are shown in Fig. 5.25 and 5.26. We see that the thicker panel exhibits standard limit points, whereas the thinner panel shows complex equilibrium paths with snap-through and snap-back behavior.

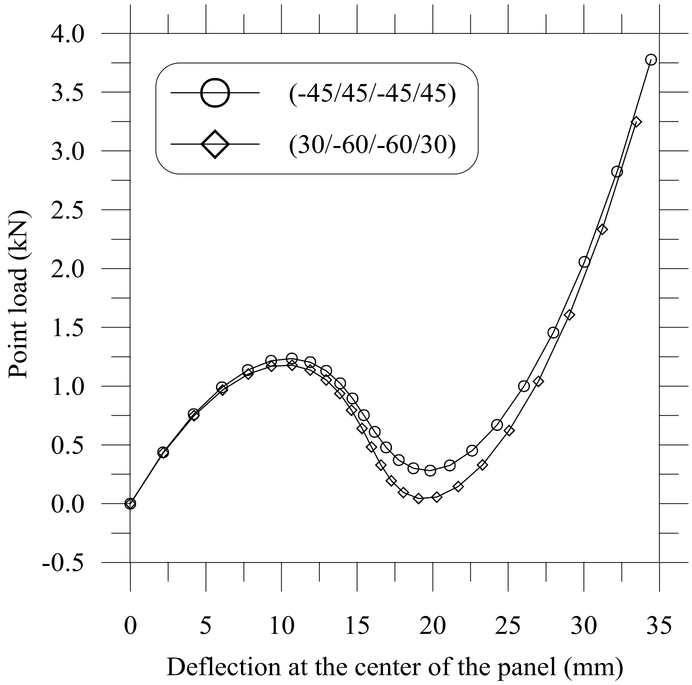

Fig. 5.25. Deflection at the center of the cylindrical panel under point load (Laminated shell, 8×8*Q*25, *h* = 12.7 mm).

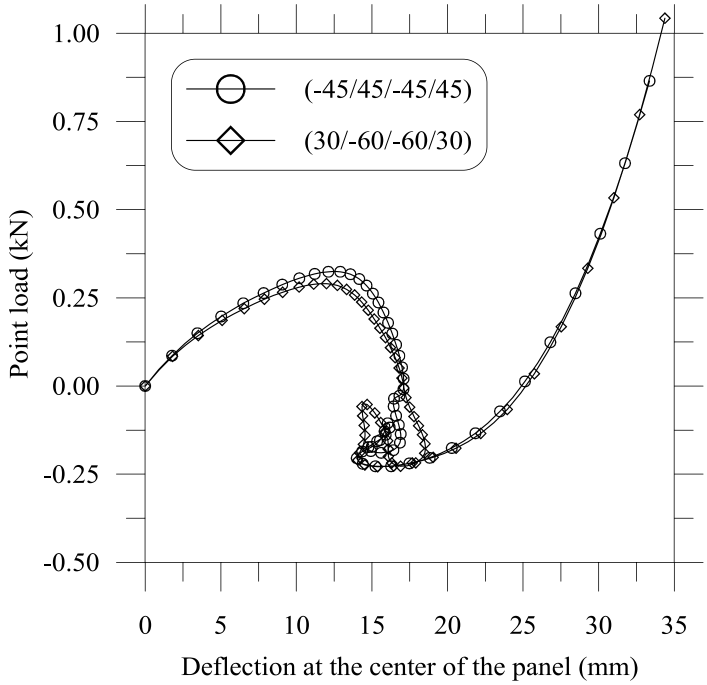

Fig. 5.26. Deflection at the center of the cylindrical panel under point load (Laminated shell, 8×8*Q*25, *h* = 6.35 mm).

b. Functionally graded panel under point load

We now consider nonlinear solutions for functionally graded shells. It is studied for the first time a shallow FGM panel under point load with the same geometry and boundary conditions as those of the last example. The material properties of the inhomogeneous panel vary continuously through the thickness of the shell. Yet, the shell is still isotropic with constant material properties in each surface. We use the rule of mixture to calculate the material properties from the ceramic and metal constituents. Young's modulus and Poisson's ratio for zirconia (ceramic material) and aluminium (metal material) are the following

$$\begin{aligned} E_c &= 151\,GPa, \quad \nu_c = 0.3 \\ E_m &= 70\,GPa, \quad \nu_m = 0.3\,. \end{aligned}$$

Note that the Poisson's ratio is constant.

In Fig. 5.27 and 5.28 we show central deflection vs. point load curves of the present 7-parameter formulation with different volume fraction exponent n (from fully metal to fully ceramic) for thicknesses $h = 12.7, 6.35\,\text{mm}$ respectively. We recall that fully ceramic behavior is achieved as $n = 0$ and fully metal as $n \to \infty$. Rectangular meshes of $4\times4Q25$ elements in a quarter of the panel are used in the analysis. As we expect, the pattern of the central deflection curves are similar to that of the isotropic and homogeneous shell (Fig. 5.23 and 5.24), i.e. standard limit points and complex equilibrium curves with snap-through and snap-back behavior. It is also found that the bending response of FGM shells lie in between that of the fully ceramic and fully metal shell.

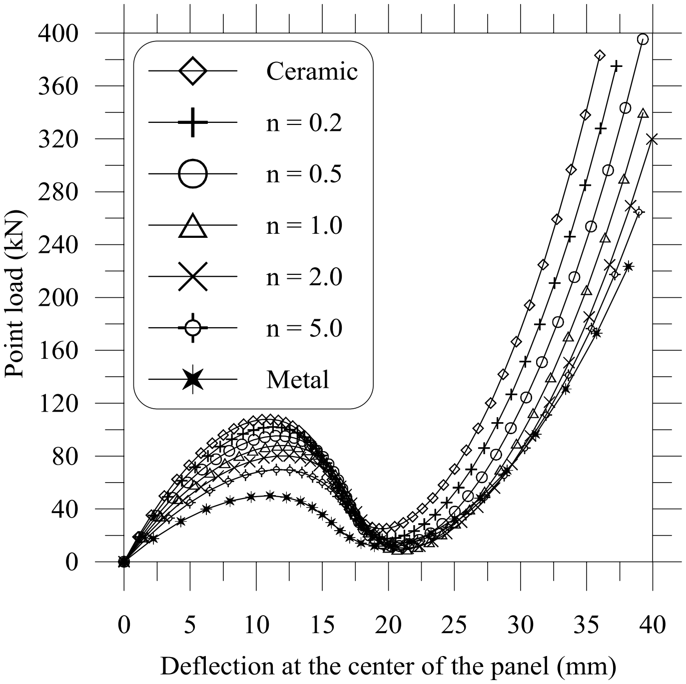

Fig. 5.27. Deflection at the center of the cylindrical panel under point load (FGM shell, 4×4*Q*25, *h* = 12.7 mm).

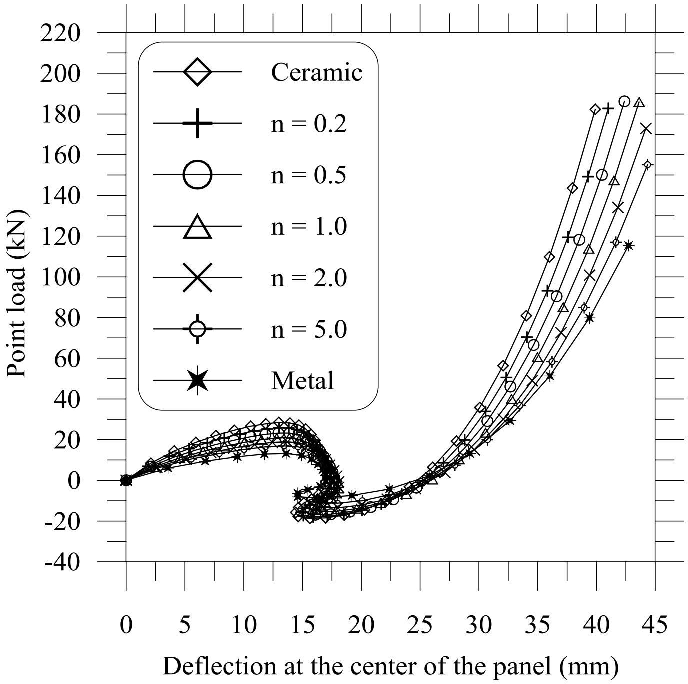

Fig. 5.28. Deflection at the center of the cylindrical panel under point load (FGM shell, 4×4*Q*25, *h* = 6.35 mm).

c. *Pull-out of an open-ended cylindrical shell*

The cylindrical shell with free ends is subjected to two opposite loads (see Fig. 5.29). The shell undergoes finite displacements and rotations, which provides a severe test for finite element formulations. This example was considered in Refs. [19, 112, 143, 144, 149] among others. The following material properties and geometrical data is used in the analysis

$$E = 10.5\times10^{6},\ \nu = 0.3125$$
$$L = 10.35,\ R = 4.953,\ h = 0.094\ .$$

Due to the symmetry conditions of the problem, only an octant of the shell is modeled using 2×2*Q*81 elements. Results obtained by *Q*25 element are too stiff and suffer from locking. The analysis is carried out by the Newton-Raphson method with 80 load steps (with equal load steps of 500). The adopted error tolerance for the residual was 1.0×10^{-6}.

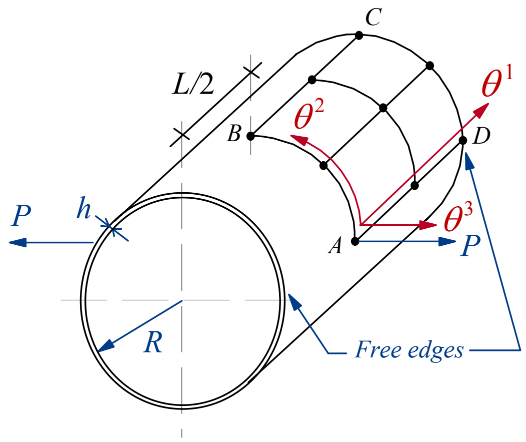

Fig. 5.29. Pull-out of a cylinder with free edges.

Figure 5.30 shows the radial displacements at the point *A*, *B* and *C* of the shell. It is noticed that the response of the shell has two different regions: the first is dominated by bending stiffness with large displacements; the second, at load level of $P = 20000$, is characterized by a very stiff response of the shell. Converged solutions obtained by the present model are compared with the results obtained by Sze et al. [143]. Our results agree well with the reference solution for the three curves considered. In Fig. 5.31 the undeformed and five different deformed configurations of the cylindrical shell are depicted.

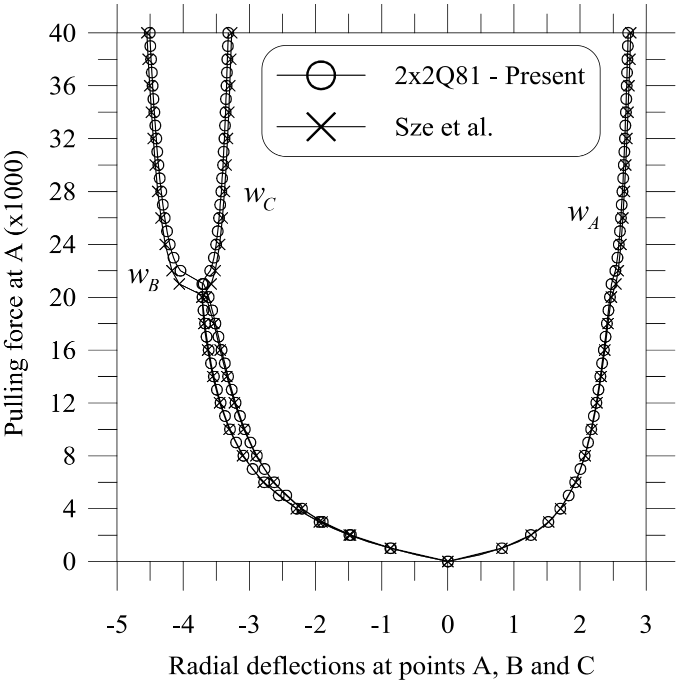

Fig. 5.30. Radial displacements at points *A*, *B* and *C* vs. pulling force of the cylinder with free edges.

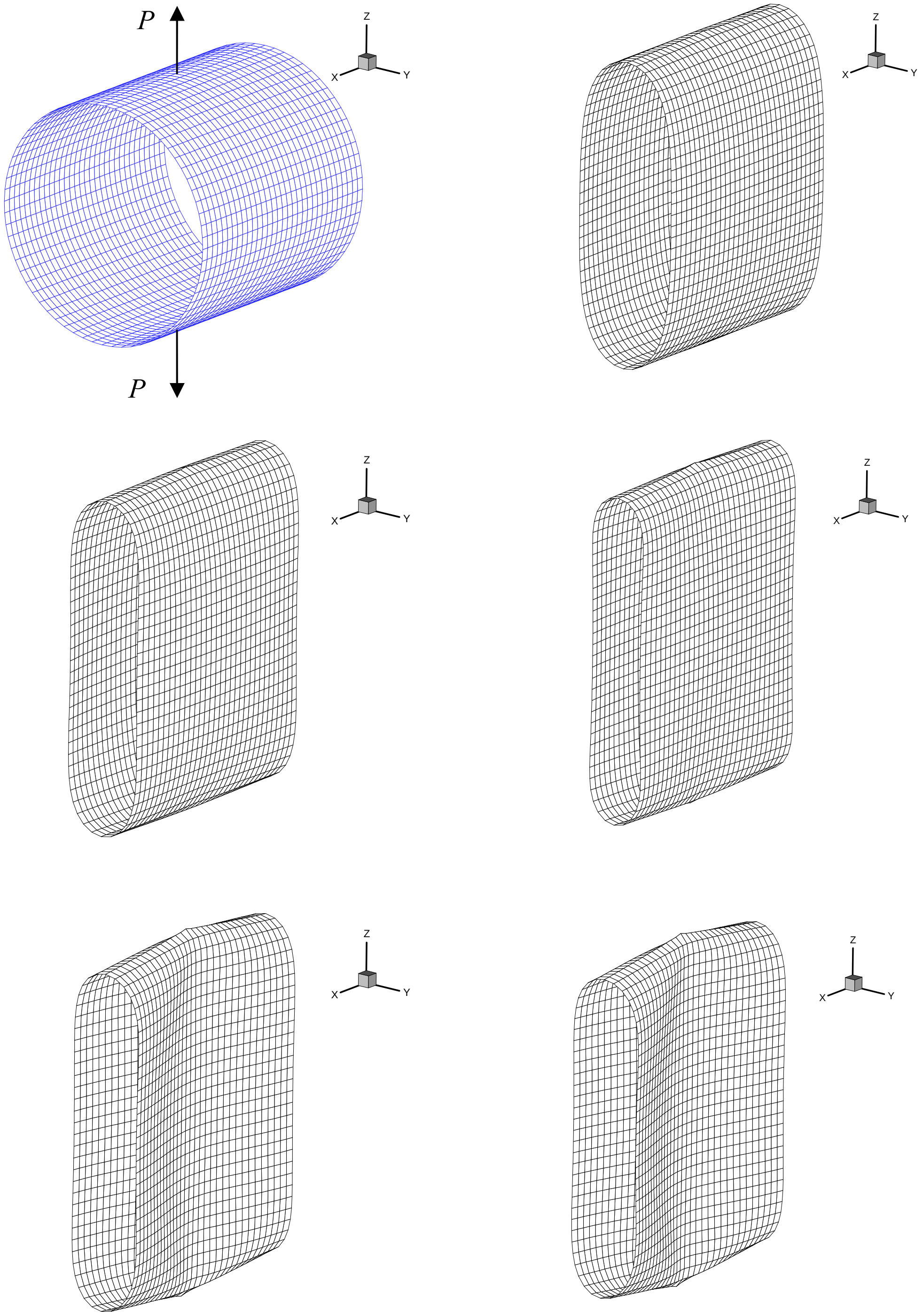

Fig. 5.31. Deformed configurations of the cylinder under pulling forces (loading stages $P = 5000, 10000, 20000, 30000, 40000$).

d. *Pinched semi-cylindrical shell*

Another well-known benchmark example for finite deformation is the semi-cylindrical shell under point load (Fig. 5.32). This problem has been investigated by Stander et al. [150], Balah and Al-Ghamedy [18] and Brank et al. [19] among others [143]. The length of the cylinder is L = 3.048, the thickness and radius are h = 0.03, R = 1.016 respectively. The analysis is carried out for isotropic and composite materials. The material properties are

$$E = 2.0685 \times 10^7, \nu = 0.3$$

for isotropic material and

$$\begin{aligned} &E_1 = 2068.5, E_2 = E_3 = 517.125 \\ &G_{12} = G_{13} = 795.6,\ G_{23} = 198.8942 \\ &\nu_{12} = \nu_{13} = 0.3,\ \nu_{23} = 0.3 \end{aligned}$$

for composites with geometrical data

$$L = 304.8, R = 101.6, h = 3.0\ .$$

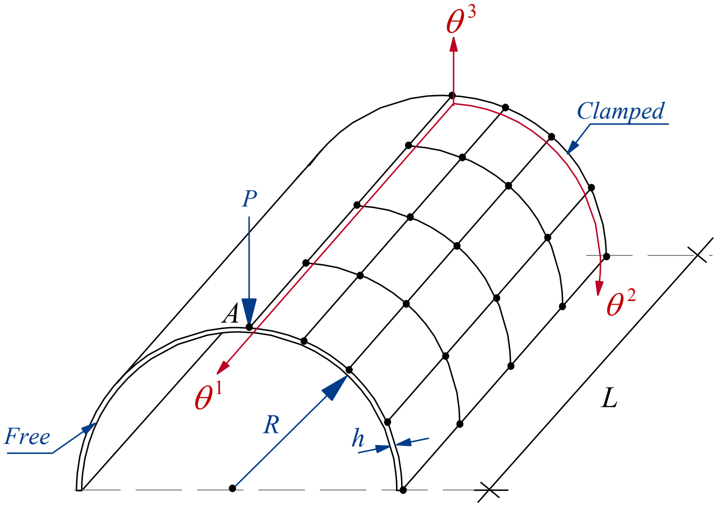

Fig. 5.32. Clamped semi-cylindrical shell under point load.

The problem is modeled using regular meshes of 4×4*Q*81 and 5×5*Q*81 elements to describe haft of the semi-cylinder. The load applied to the shell is increased (in 40 equal load steps) up to *P* = 2000. Figure 5.33 shows the deflection at the point *A* versus the point loading for the isotropic shell. Comparisons of the present results with those of Sze et al. are in close agreement. We see that the present results are slightly stiffer. Note that the corresponding solutions with a mesh of 4×4*Q*81 are quite involved with those of 5×5*Q*81. Figure 5.34 shows similar results for symmetric cross-ply shells. In this case, the agreement of the present solutions with those of Sze et al. is excellent. Finally, Fig. 5.35 depicts various deformed configurations for the isotropic shell while Fig. 5.36 shows the final configuration for the laminate (0°/90°/0°).

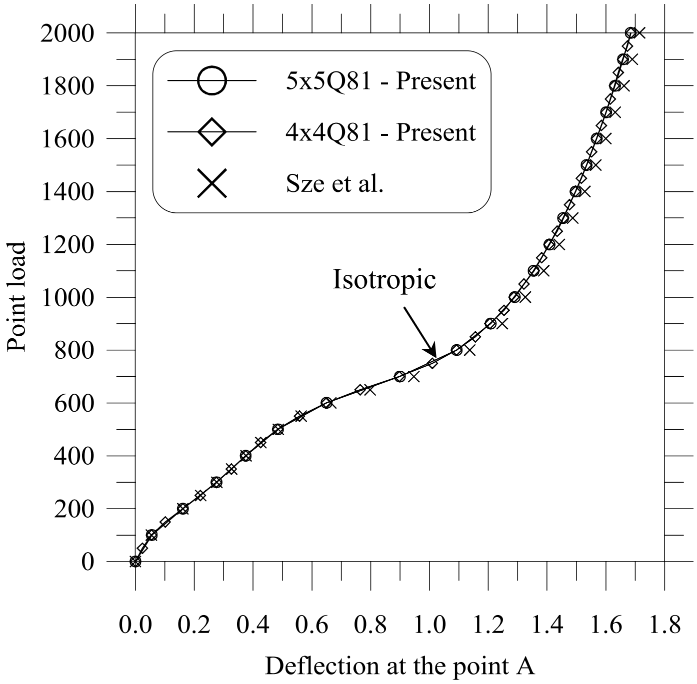

Fig. 5.33. Deflection at the point *A* of the clamped semi-cylindrical shell under point load (isotropic shell).

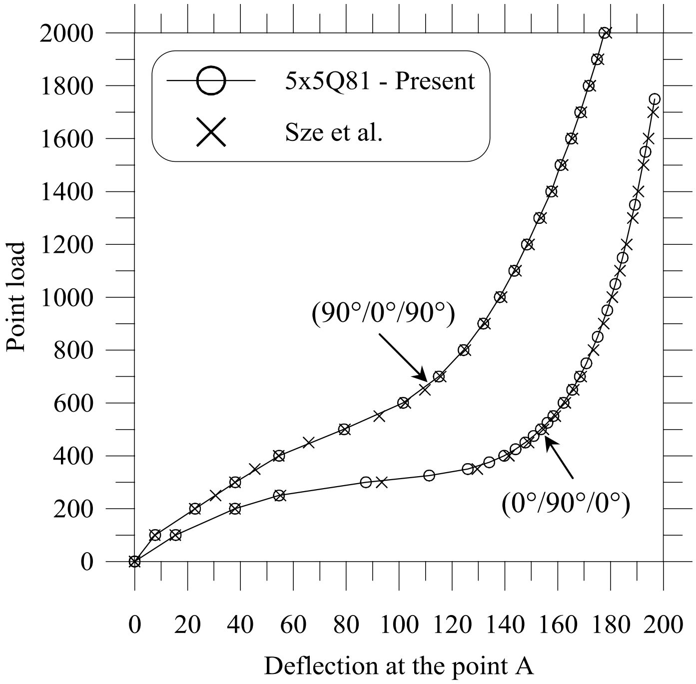

Fig. 5.34. Deflection at the point *A* of the clamped semi-cylindrical shell under point load (symmetric cross-ply laminated shell).

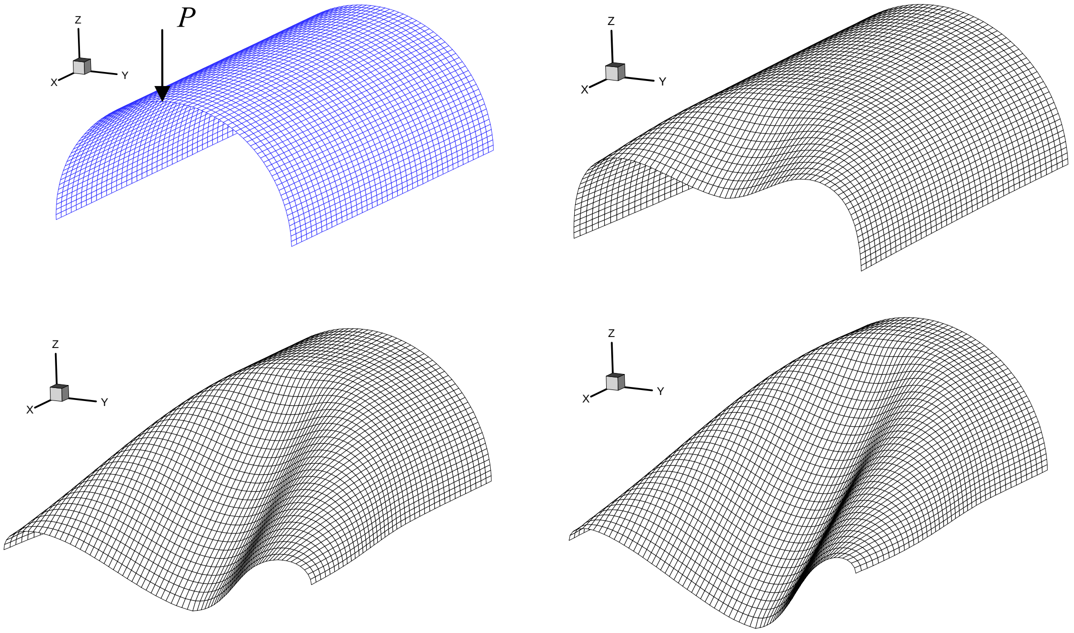

Fig. 5.35. Deformed configurations of the clamped semi-cylindrical shell under point load (isotropic shell, loading stages $P = 600, 1300, 2000$).

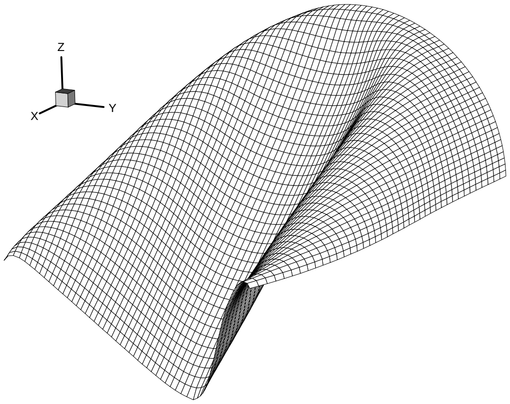

Fig. 5.36. Final configuration of the clamped semi-cylindrical shell under point load. Laminate (0°/90°/0°), $P = 2150$.

3. Spherical shells

a. Pinched hemisphere with 18° hole

The pinched hemispherical shell is considered as one of the most severe benchmark problem for nonlinear analysis of shells. It was treated before in Refs. [20, 92, 143, 149]. The shell has an 18° hole at the top and is subjected to two inward forces at 0° and 180° longitude on the equator, and two outward forces at 90° and 270° longitude on the equator, respectively (Fig. 5.37). The material and geometric properties are as follows

$$E = 6.825\times10^{7}, \nu = 0.3$$
$$R = 10.0, h = 0.04, P_{\max} = 400 .$$

We take advantage of the symmetry of the problem and only model one quadrant of the shell. The nonlinear analysis is performed by the Newton-Raphson method with a regular mesh of $8\times8Q25$ elements. The total load is applied in 80 equal load steps.

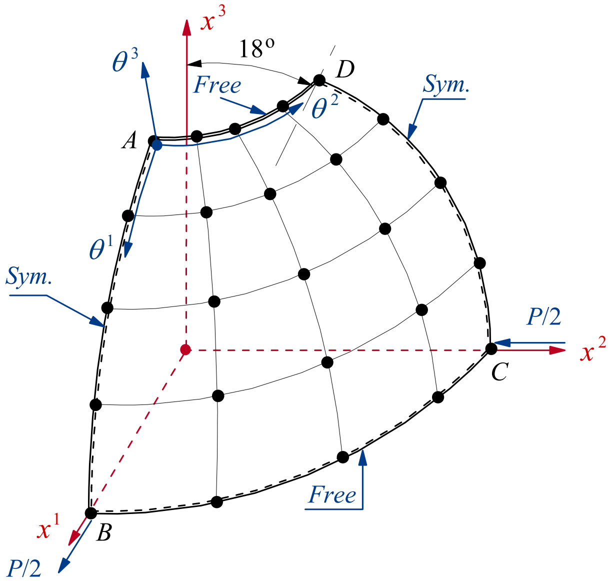

Fig. 5.37. Geometry of the pinched hemisphererical shell with 18° hole.

The boundary conditions for the problem were given in Chapter III section D-3 when we solved the linear problem. To avoid rigid body displacements in the response of the structure, we have to impose an additional condition at the point *B*

$$\text{At } \theta^1 = \pi/2,\, \theta^2 = 0 \qquad u_{<1>} = 0\,.$$

That is, the vertical displacement of *B* is zero.

Figure 5.38 shows a plot of the pinching load versus the radial deflection curves at the point *B* and *C*. The present solutions are compared with those of Sze et al. [143]. It is observed that our results are a little stiffer than solutions of Sze et al., but in general they are in good agreement. The rate of convergence of the Newton method is quite acceptable. The average of iterations per load step is 3. The final configuration of the pinched hemisphere without any magnification is shown in Fig. 5.39.

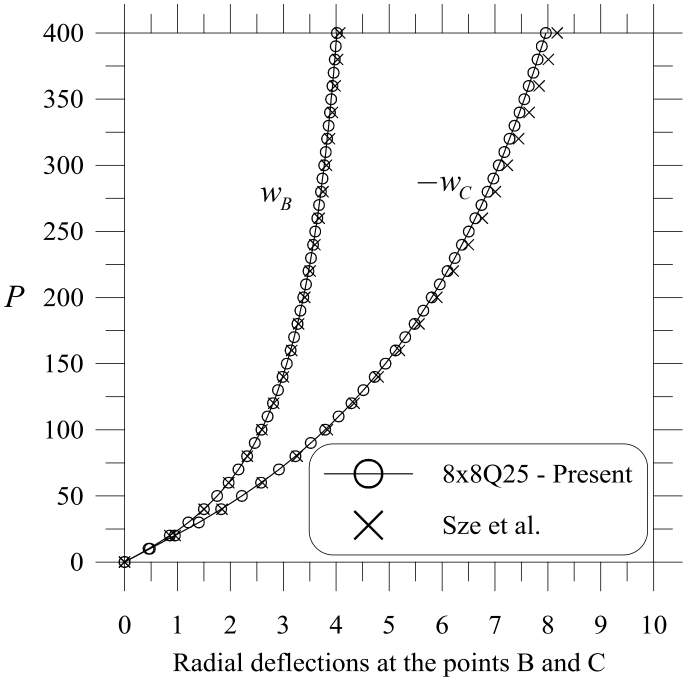

Fig. 5.38. Radial displacements at the points *B* and *C* of the pinched hemispherical shell with 18° hole.

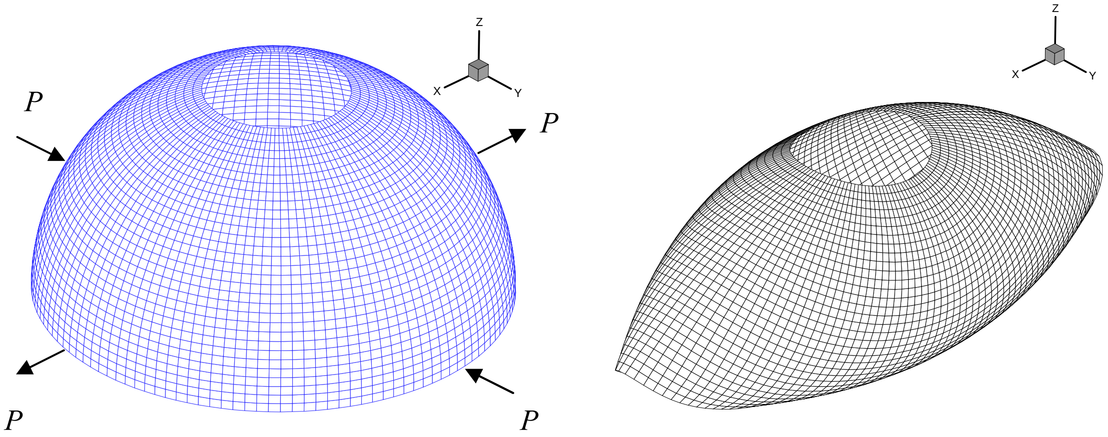

Fig. 5.39. Initial and final configurations of the pinched hemispherical shell with 18° hole, $P = 400$.

b. Full pinched hemisphere

The last numerical simulation in this section is the full pinched hemispherical shell under two inward and two outward opposite forces (Fig. 5.40). In this case, we consider a full hemisphere with no hole. Similar to the previous example, the shell is modeled by using spherical coordinates. The geometric data is as follows

$$R = 10.0,\, h = 0.04,\, P_{\max} = 400\ .$$

The nonlinear analysis is performed for an isotropic shell with material properties: $E = 6.825 \times 10^7, \nu = 0.3$ and two laminated shells with lamina properties

$$\begin{aligned} &E_1 = 6.0 \times 10^7, E_2 = E_3 = 2.0 \times 10^7 \\ &G_{12} = G_{13} = 1.125 \times 10^7, G_{23} = 0.7692 \times 10^7 \\ &\nu_{12} = \nu_{13} = \nu_{23} = 0.3 \end{aligned}$$

and stacking sequences (90°/0°/90°) and (0°/90°/0°).

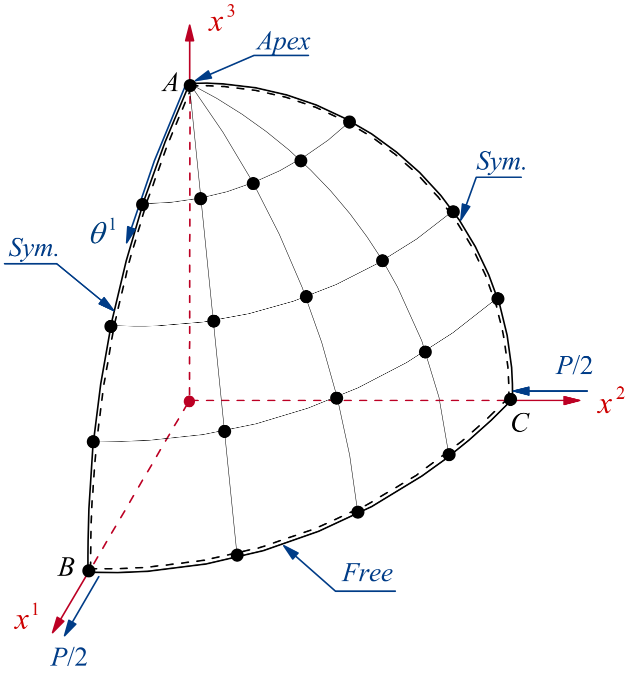

Fig. 5.40. Geometry of the full pinched hemispherical shell.

A regular mesh of 2×2Q81 elements is used in the analysis. Note that the one edge of the finite element mesh in the parametric space of the midsurface is shrunk into the apex (coerced mesh) in the Euclidean point space $\mathcal{E}$. This does not cause, however, any singularity problems in the solution.

Figure 5.41 shows the radial deflections at the point *B* and *C* versus the point loading for full pinched hemisphere. Besides the isotropic material, laminates with stacking sequences (0°/90°/0°) and (90°/0°/90°) are also considered. As expected we note that the laminate (0°/90°/0°) exhibits the most flexible response. Again we observe good rate of convergence of the Newton-Raphson method. The average of iterations per load step is 4.3 for a total of 20 load steps. The final configuration of the full pinched hemisphere is depicted in Fig. 5.42 for the laminate (0°/90°/0°).

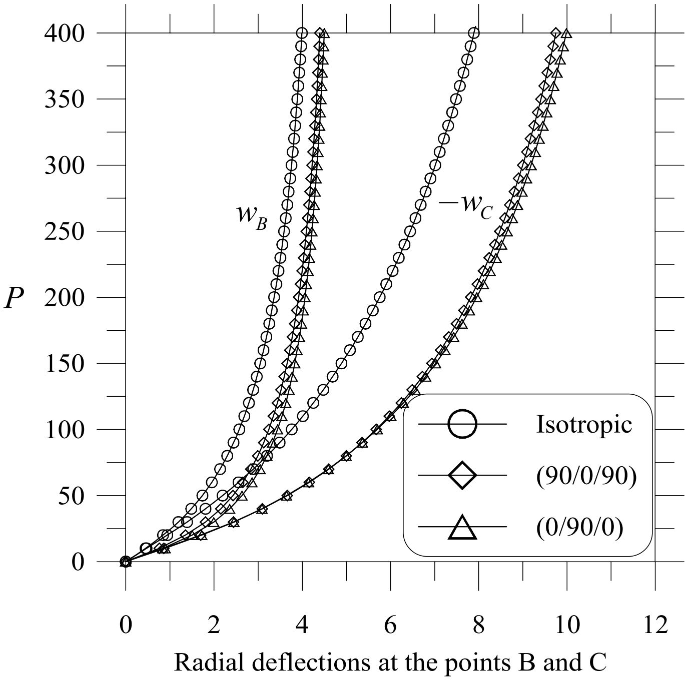

Fig. 5.41. Radial displacement curves at *B* and *C* of the full pinched hemispherical shell (2×2Q81).

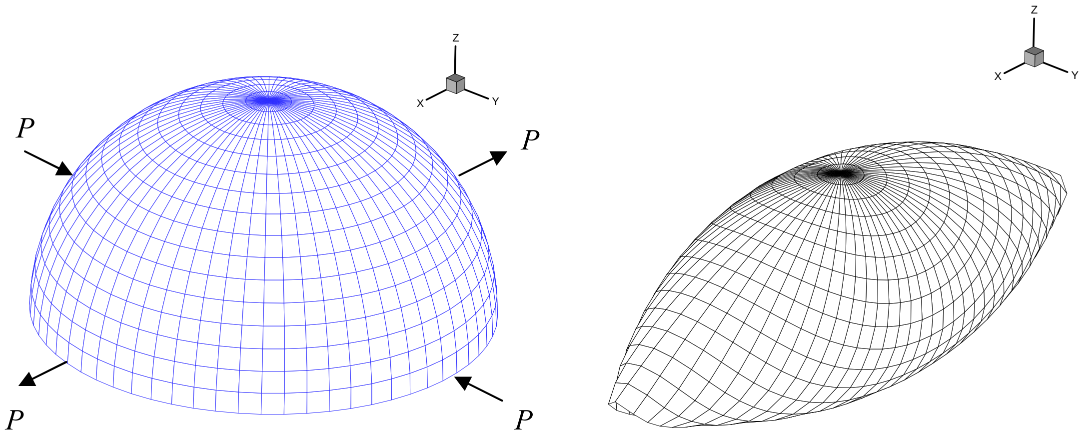

Fig. 5.42. Initial and final configurations of the full pinched hemispherical laminated shell (0°/90°/0°), $P = 400$.

4. Other shell geometries

a. *Composite hyperboloidal shell*

Next, we examine the behavior of a composite hyperboloidal shell under two inward and two outward point loads (Fig. 5.43). This beautiful example demonstrates the robustness of the present finite element model and its applicability to arbitrary shell geometries and very strong nonlinearities. The problem was considered by Başar et al. [106], Wagner and Gruttmann [151] and more recently by Balah and Al-Ghamedy [18]. The material properties of the lamina are

$$\begin{aligned} &E_1 = 40.0\times10^6, E_2 = E_3 = 1.0\times10^6 \\ &G_{12} = G_{13} =, G_{23} = 0.6\times10^6 \\ &\nu_{12} = \nu_{13} = \nu_{23} = 0.25 \end{aligned}$$

and geometry

$$R_1 = 7.5, R_2 = 15.0, L = 20.0, h = 0.04$$
$$R_0\left(x^3\right) = R_1\sqrt{1 + (x^3 / C)^2}$$

where $C = 20/\sqrt{3}$.

The analysis is carried out for two composite laminates (90°/0°/90°) and (0°/90°/0°) using the Newton-Raphson method. Due to the symmetry conditions only one octant of the shell has to be discretized. The loading is applied in 120 equal steps. In Fig. 5.44 and 5.45 we show the load deflection curves for the laminates (90°/0°/90°) and (0°/90°/0°) respectively. Meshes of 2×2Q81 and 4×4Q81 elements are utilized in the analysis. The present displacements for 4×4Q81 elements are larger than those reported by Başar et al. [106] or those reported by Balah and Al-Ghamedy [18]. Deformed configurations of the hyperboloidal shell for the two stacking sequences are illustrated in Fig. 5.46 (4×4Q81).

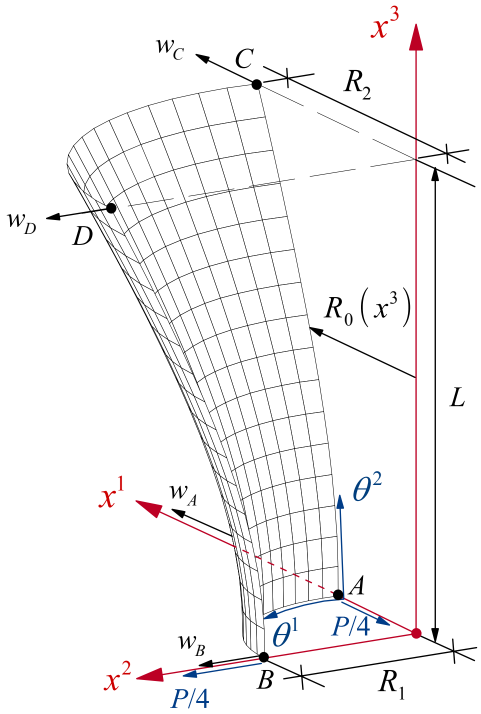

Fig. 5.43. Geometry and loading conditions of the composite hyperboloidal shell.

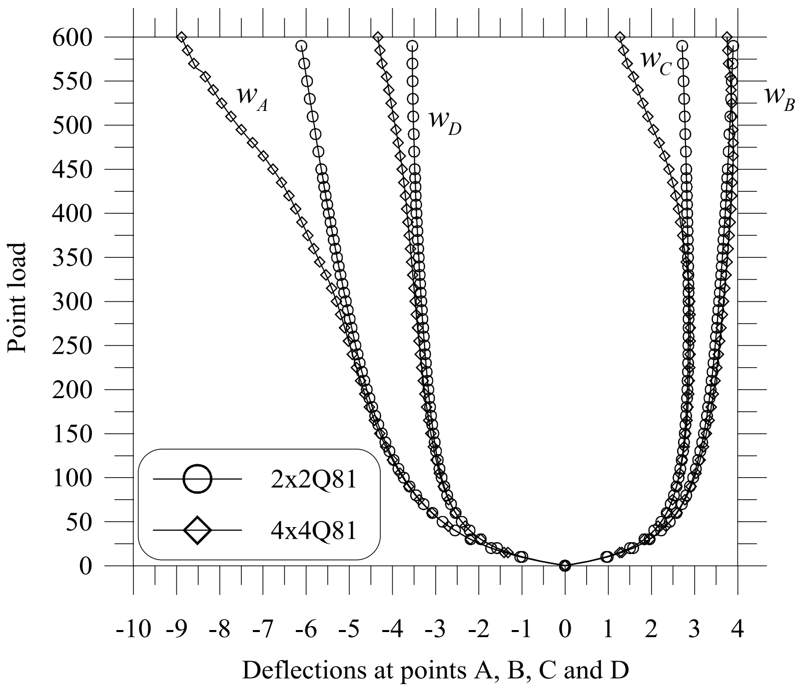

Fig. 5.44. Deflections at the points *A*, *B*, *C* and *D* of the pinched hyperboloidal shell. Laminate: (90°/0°/90°).

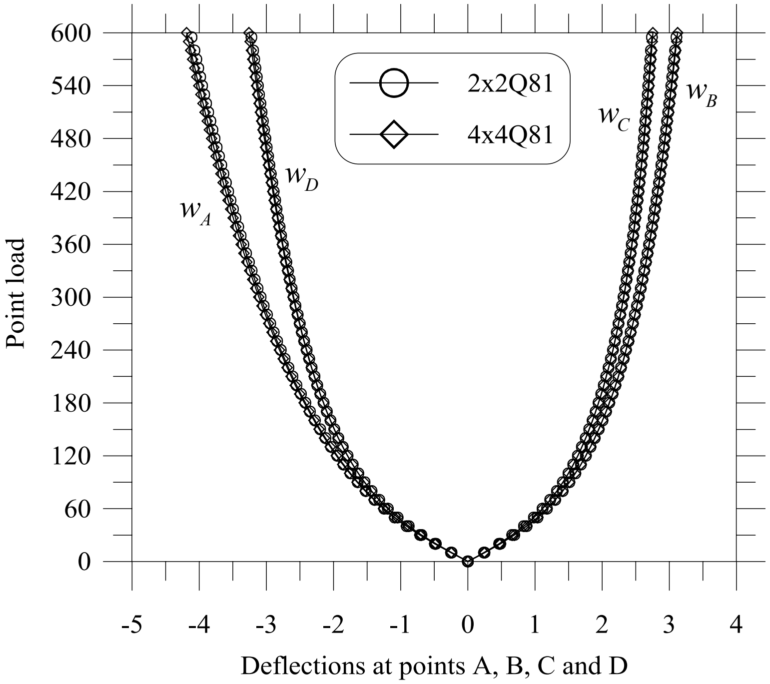

Fig. 5.45. Deflections at the points *A*, *B*, *C* and *D* of the pinched hyperboloidal shell. Laminate: (0°/90°/0°).

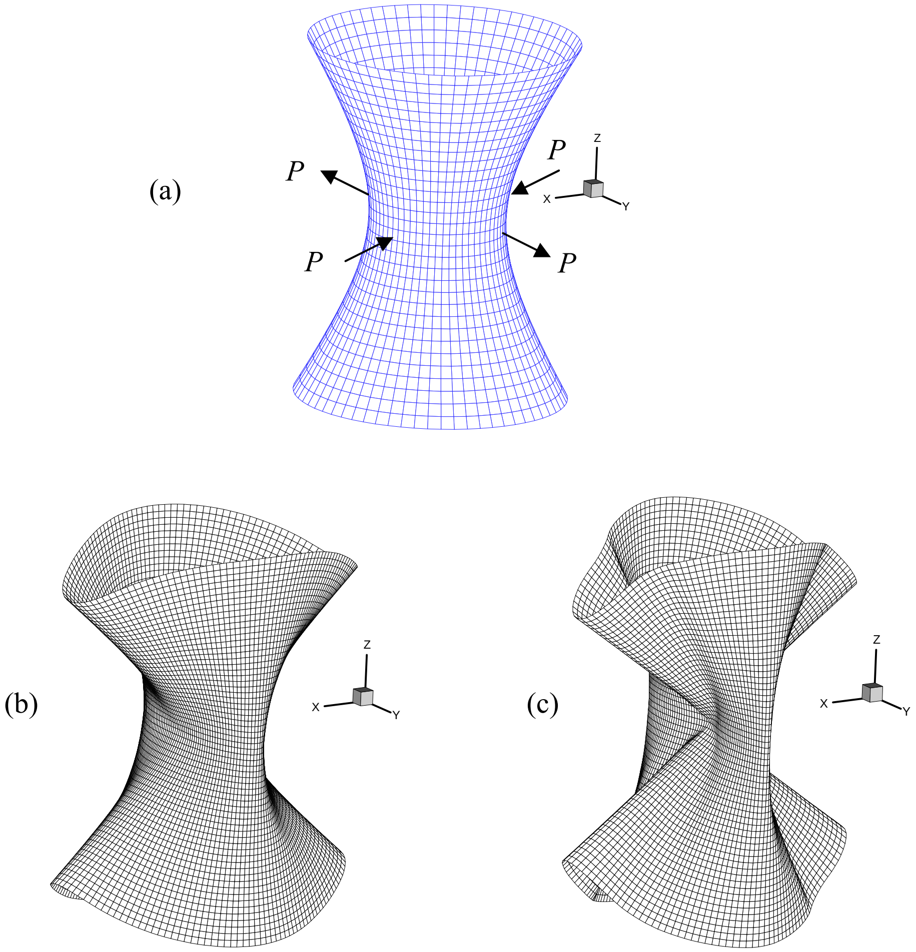

Fig. 5.46. Configurations of the pinched hyperboloidal laminated shell: (a) Undeformed state, (b) Deformed state for P = 600 and laminate (0°/90°/0°), (c) Deformed state for P = 495 and laminate (90°/0°/90°).

CHAPTER VI

CONCLUSIONS

A. Summary

In this dissertation we have proposed a tensor-based finite element model for the analysis of shell structures. Firstly, the formulation was applied to linear deformations based on a novel and consistent third-order shear deformation shell theory for bending of composite shells. The first-order shear deformation shell theory was also developed as a subset. In both theories derived herein, no simplification other than the assumption of linear elastic material is made in the computation of stress resultants and material stiffness coefficients. They are integrated numerically without any approximation in the shifter. A conforming high-order element was derived with C^0 continuity across the element boundaries in order to avoid locking problems. Applications of the model to laminated composites and functionally graded materials were presented to verify the validity of the approach.

Secondly, we consider a consistent shell formulation for the nonlinear analysis of multilayered composites and functionally graded shells. A simple tensor-based displacement finite element model was developed and a family of Lagrangian elements with high-order interpolation polynomials was employed. Again, the flexibility of this element precludes any possible membrane or shear locking. We perform applications of this element to finite deformations of shells. The first-order shell theory with seven parameters is derived with exact nonlinear deformations and under the framework of the Lagrangian description. This approach takes into account thickness changes and, therefore, 3D constitutive equations are required. Numerical simulations for plates, cylindrical and spherical shells showed the validity of the present approach and the accuracy of the developed shell element.

B. Concluding remarks

The main conclusions that we can draw from the numerical results obtained in this work are as follows:

1. The tensor-based finite element formulation described the mathematical shell model in a natural and simple way by using curvilinear coordinates. Complex matrix transformations to Cartesian coordinates were not required. Hence, the geometry of the midsurface was not approximated and no further errors were introduced in the model. The geometric parameters of the midsurface were computed exactly at each Gauss point.
2. The family of high-order elements with Lagrangian interpolations developed herein, showed to be free of membrane and shear locking. In particular, the element $Q81$ (with interpolation polynomials of eight degree) performed very well in the numerical examples for linear analysis. Even for extreme benchmark problems for finite deformations, the $Q81$ element demonstrated to be robust and efficient. The implementation of this element was also quite simple without any tricky interpolation techniques (as low-elements such as MITC and enhanced strain elements). Full integration rule was applied in all examples.
3. The consistent third-order shear deformation theory developed here showed an excellent performance to predict linear displacements and stresses of shells made of laminated composites and functionally graded materials. The cubic distribution of the displacement and strain field can describe the complex behavior of laminated shells with good accuracy when it is compared with analytical 3D

solutions. The zigzag effect in through-the thickness distributions of membrane displacements and stresses, which usually arises in thick shells, can be reproduced by this theory. In that aspect, it was observed that the third-order theory gave better results than first-order theories (based on the Reissner-Mindlin assumptions) for most problems examined.

4. An improved first-order theory that incorporates thickness stretching was elegantly and beautifully derived by using absolute tensor notation. This type of notation, which is index free, allowed us to present complicated equations in a compact and simple way without referring any coordinate system. The model has seven independent parameters with transverse normal strains being linear through the thickness of the shell. Therefore, the plane stress state was not enforced anywhere. Since thickness changes were included in the model, full 3D constitutive equations were utilized. The use of a rotation tensor was avoided by not considering rotational degrees of freedom. This is very attractive for implementation purposes since they circumvent complex rotation updates in the configuration of the shell. The extensive numerical simulations for different shell geometries as well as various kinds of materials, showed the accuracy of the formulation.
5. Regarding the numerical implementation, the use of symbolic computation allowed us to derive the stiffness and tangent matrices for the different models as well as geometries in this work. With simple subroutines written in MAPLE, we could generate functionals of complex structures and derive from them weak formulations of, virtually, any shell geometry. Furthermore, the stiffness and tangent matrices obtained with these subroutines were easily transformed to FORTRAN statements. The entries of these matrices were imported to the FORTRAN finite element code developed herein.

C. Recommendations

There are several areas for future research as possible continuation of this work. Among them we have:

1. From the point of view of engineering design and analysis, shells with intersections and cut-outs are of primary interest. For modeling that kind of structures powerful mesh generations are required. Due to the robustness and efficiency of quadrilateral high-order elements showed in this dissertation, it is interesting to develop high-order triangular elements using Lagrangian interpolations. This can bring together shell analyses and automatic meshing techniques available in various commercial codes.
2. Since large displacements and rotations are allowed in the model, it is probable that material nonlinearities will occur during the deformation of the shell. Therefore, to have a more realistic shell behavior, nonlinear material models need to be developed and incorporated in the present formulation.
3. Another important research direction is in developing a continuum damage mechanic (CDM) model for characterization of damage evolution and propagation in the shell using the present formulation. The finite element model has to be extended to include strong discontinuities in the displacement field. Crack and fatigue failures can be also investigated.

REFERENCES

[1] W.T. Koiter, J.G. Simmonds, Foundations of shell theory, in: E. Becker, G.K. Mikhailov (Eds.), Proceedings of the Thirteenth International Congress of Theoretical and Applied Mechanics, Springer-Verlag, Berlin, 1973.

[2] W. Pietraszkiewicz, Finite Rotations and Lagrangean Description in the Nonlinear Theory of Shells, Polish Scientific Publishers, Warszawa, 1979.

[3] D. Chapelle, K.J. Bathe, Fundamental considerations for the finite element analysis of shell structures, Comput. Struct. 66 (1) (1998) 19-36.

[4] S. Ahmad, B. Irons, O.C. Zienkiewicz, Analysis of thick and thin shell structures by curved finite elements, Int. J. Numer. Meth. Engrg. 2 (1970) 419-451.

[5] J.C. Simo, D.D. Fox, On a stress resultant geometrically exact shell model. Part I: Formulation and optimal parametrization, Comput. Methods Appl. Mech. Engrg. 72 (1989) 267-304.

[6] C. Chinosi, L. Della Croce, T. Scapolla, Hierarchic finite elements for thin Naghdi shell model, Int. J. Solids Struct. 35 (1998) 1863-1880.

[7] M. Cho, H.Y. Roh, Development of geometrically exact new elements based on general curvilinear coordinates, Int. J. Numer. Meth. Engrg. 56 (2003) 81-115.

[8] D. Chapelle, D.L. Oliveira, M.L. Bucalem, MITC elements for a classical shell model, Comput. Struct. 81 (2003) 523-533.

[9] N. Büchter, E. Ramm, Shell theory vs. degeneration - A comparison in large rotation finite element analysis, Int. J. Numer. Meth. Engrg. 34 (1992) 39-59.

[10] P.S. Lee, K.J. Bathe, Insight into finite element shell discretizations by use of the “basic shell mathematical model”, Comput. Struct. 83 (2005) 69-90.

[11] E. Hinton, H.C. Huang, A family of quadrilateral Mindlin plate elements with substitute shear strain fields, Comput. Struct. 23 (3) (1986) 409-431.

[12] E. Dvorkin, K.J. Bathe, A continuum mechanics based four-node shell element for general nonlinear analysis, Engrg. Comput. 1 (1984) 77-88.

[13] J.C. Simo, M.S. Rifai, A class of mixed assumed strain methods and the method of incompatible modes, Int. J. Numer. Meth. Engrg. 29 (1990) 1595-1638.

[14] Y. Leino, J. Pitkäranta, On the membrane locking of h-p finite elements in a cylindrical shell problem, Int. J. Numer. Meth. Engrg. 37 (1994) 1053-1070.

[15] J. Pitkäranta, Y. Leino, O. Ovaskainen, J. Piila, Shell deformation states and the finite element method: A benchmark study of cylindrical shells, Comput. Methods Appl. Mech. Engrg. 128 (1995) 81-121.

[16] H. Hakula, Y. Leino, J. Pitkäranta, Scale resolution, locking, and high-order finite element modelling shells, Comput. Methods Appl. Mech. Engrg. 133 (1996) 157-182.

[17] J.P. Pontaza, J.N. Reddy, Least-square finite element formulation for shear deformable shells, Comput. Methods Appl. Mech. Engrg. 194 (2005) 2464-2493.

[18] M. Balah, H.N. Al-Ghamedy, Finite element formulation of a third-order laminated finite rotation shell element, Comput. Struct. 80 (2002) 1975-1990.

[19] B. Brank, D. Perić, F.B. Damjanić, On implementation of a four node shell element for thin multilayered elastic shells, Comput. Mech. 16 (1995) 341-359.

[20] L. Vu-Quoc, X.G. Tan, Optimal solid shells for nonlinear analyses of multilayered composites. I. Statics, Comput. Methods Appl. Mech. Engrg. 192 (2003) 975-1016.

[21] J.N. Reddy, A simple higher-order theory for laminated composite plates, ASME J. Appl. Mech. 51 (1984) 745-752.

[22] J.N. Reddy, C.F. Liu, A higher-order shear deformation theory of laminated elastic shells, Int. J. Engrg. Sci. 23 (3) (1985) 319-330.

[23] C. Sansour, A theory and finite element formulation of shells at finite deformations involving thickness change: Circumventing the use of a rotation tensor, Arch. Appl. Mech. 65 (1995) 194-216.

[24] M. Bischoff, E. Ramm, Shear deformable shell elements for large strains and rotations, Int. J. Numer. Meth. Engrg. 40 (1997) 4427-4449.

[25] R.A. Arciniega, J.N. Reddy, Consistent third-order shell theory with application to composite circular cylinders, AIAA J. 43 (9) (2005) 2024-2038.

[26] J.N. Reddy, R.A. Arciniega, Shear deformation plate and shell theories: From Stavsky to present, Mech. Advanced Mater. Struct. 11 (2004) 535-582.

[27] Y. Stavsky, On the theory of symmetrically heterogeneous plates having the same thickness variation of the elastic moduli, in: D. Abir, F. Ollendorff, M. Reiner (Eds.), Topics in Applied Mechanics, American Elsevier, New York, 1965.

[28] P. Yang, C.H. Norris, Y. Stavsky, Elastic propagation in heterogeneous plates, Int. J. Solids Struct. 2 (1966) 665-684.

[29] N.J. Pagano, Exact solution for composite laminates in cylindrical bending, J. Compos. Mater. 3 (1969) 398-411.

[30] N.J. Pagano, Exact solution for rectangular bidirectional composites and sandwich plates, J. Compos. Mater. 4 (1970) 20-34.

[31] N.J. Pagano, S.J. Hatfield, Elastic behavior of multilayered bidirectional composites, AIAA J. 10 (1972) 931-933.

[32] J.M. Whitney, The effect of boundary conditions on the response of laminated composites, J. Compos. Mater. 3 (1969) 534-547.

[33] A.A. Khdeir, J.N. Reddy, Analytical solutions of refined plate theories of cross-ply composite laminates, ASME J. Pressure V. Tech. 113 (1991) 570-578.

[34] J.N. Reddy, A.A. Khdeir, Buckling and vibration of laminated composite plates using various plate theories, AIAA J. 27 (1989) 1808-1817.

[35] G. Simitses, J. Anastasiadis, Shear deformable theories for cylindrical laminates-equilibrium and buckling with applications, AIAA J. 30 (1992) 826-834.

[36] N.N. Huang, Influence of shear correction factors in the higher-order shear deformation laminated shell theory, Int. J. Solids Struct. 31 (1994) 1263-1277.

[37] S. Di, H. Rothert, Solution of laminated cylindrical shells using an unconstrained third-order theory, Compos. Struct. 32 (1995) 667-680.

[38] A.K. Nayak, S.J. Moy, R.A. Shenoi, Free vibration analysis of composite sandwich plates based on Reddy's higher-order theory, Compos. Part B: Engrg. 33 (2002) 505-519.

[39] J.N. Reddy, On refined computational models of composite laminates, Int. J. Numer. Meth. Engrg. 27 (2) (1989) 361-382.

[40] J.N. Reddy, A generalization of two dimensional theories of laminated composite plates, Communications Appl. Numer. Meth. 3 (1987) 173-180.

[41] J.N. Reddy, E.J. Barbero, J.L. Teply, A generalized laminate theory for the analysis of composite laminates, Dept. Engrg Sci. Mech., Report No. VPI-E-88.17, Virginia Tech, Blacksburg, 1988.

[42] J.N. Reddy, M. Savoia, Layer-wise shell theory for postbuckling of laminated circular cylindrical shells, AIAA J. 30 (1992) 2148-2154.

[43] M. Di Sciuva, An improved shear-deformation theory for moderately thick multi-layered anisotropic shells and plates, ASME J. Appl. Mech. 54 (1987) 589-596.

[44] M. Di Sciuva, Bending, vibration and buckling of simply supported thick multilayered orthotropic plates: an evaluation of a new displacement model, J. Sound Vibr. 105 (1986) 425-442.

[45] M. Di Sciuva, A refined transverse shear deformation theory for multilayered anisotropic plates, Atti Accademia delle Scienze di Torino, 118 (1984) 279-295.

[46] P.M. Naghdi, Theory of shells and plates, in: S. Flügge, C. Truesdell (Eds.), Handbuch der Physik, VIa/2, Springer-Verlag, Berlin, 1972.

[47] A.E. Green and W. Zerna, Theoretical Elasticity, Clarendon Press, Oxford, 2nd edition, 1968.

[48] P.M. Naghdi, Foundations of elastic shell theory, in: I.N. Sneddon, R. Hill (Eds.), Progress in Solid Mechanics, Vol. 4, North-Holland, Amsterdam, 1963.

[49] L. Librescu, Elastostatics and Kinetics of Anisotropic and Heterogeneous Shell-Type Structures, Noordhoff, Leyden, 1975.

[50] R. Schmidt, J.N. Reddy, A refined small strain and moderate rotation theory of elastic anisotropic shells, ASME J. Appl. Mech. 55 (1988) 611-617.

[51] W.T. Koiter, A consistent first order approximation in the general theory of thin elastic shells, in: W.T. Koiter (Ed.), The Theory of Thin Elastic Shells, North-Holland Pub. Co., Amsterdam, 1960.

[52] N. Büchter, E. Ramm, 3D-extension of nonlinear shell equations based on the enhanced assumed strain concept, in: C. Hirsch (Ed.), Computational Methods in Applied Sciences, Elsevier Publishers, Amsterdam, 1992.

[53] J.C. Simo, M.S. Rifai, D.D. Fox, On a stress resultant geometrically exact shell model. Part IV: Variable thickness shells with through-the-thickness stretching, Comput. Methods Appl. Mech. Engrg. 81 (1990) 53-91.

[54] J.N. Reddy, Mechanics of Laminated Composite Plates and Shells: Theory and Analysis, CRC Press, 2nd edition, Boca Raton, Florida, 2004.

[55] J.N. Reddy, Energy Principles and Variational Methods in Applied Mechanics, John Wiley & Sons Inc., 2nd edition, New York, 2002.

[56] G. Cantin, R.W. Clough, A curved cylindrical shell finite element, AIAA J. 6 (1968) 1057-1062.

[57] O.C. Zienkiewicz, The Finite Element Method, McGraw-Hill, New York, 1977.

[58] M.P. do Carmo, Differential Forms and Applications, Springer-Verlag, Berlin, 1994.

[59] R.L. Bishop, S.I. Goldberg, Tensor Analysis on Manifolds, Dover Publications Inc., New York, 1980.

[60] D.D. Fox, A geometrically exact shell theory, PhD dissertation, Applied Mechanics Division, Stanford University, 1990.

[61] M.S. Rifai, Static and dynamic finite element analysis of finite deformation geometrically exact shell models, PhD dissertation, Applied Mechanics Division, Stanford University, 1993.

[62] S.C. Brenner, L.R. Scott, The Mathematical Theory of Finite Element Methods, Springer-Verlag Inc., New York, 2002.

[63] M. Bernadou, P.G. Ciarlet, B. Miara, Existence theorems for two-dimensional linear shell theories, J. Elasticity 34 (1994) 111-138.

[64] P.G. Ciarlet, Mathematical Elasticity, Volume III: Theory of Shells, North-Holland, Amsterdam, 2000.

[65] D. Chapelle, K.J. Bathe, The mathematical shell model underlying general shell elements, Int. J. Numer. Meth. Engrg. 48 (2000) 289-313.

[66] D. Chapelle, K.J. Bathe, The Finite Element Analysis of Shells – Fundamentals, Springer-Verlag, Berlin, 2003.

[67] J.N. Reddy, An Introduction to the Finite Element Method, McGraw-Hill, 3rd edition, New York, 2005.

[68] K.J. Bathe, Finite Element Procedures, Prentice-Hall, New Jersey, 1996.

[69] I. Babuška, M. Suri, On locking and robustness in the finite element method, SIAM J. Numer. Anal. 29 (5) (1992) 1261-1293.

[70] J. Pitkäranta, The problem of membrane locking in finite element analysis of cylindrical shells, Numer. Math. 61 (1992) 523-542.

[71] O.C. Zienkiewicz, R.L. Taylor, J.M. Too, Reduced integration techniques in general analysis of plates and shells, Int. J. Numer. Meth. Engrg. 3 (1971) 275-290.

[72] H. Stolarski, H., T. Belytschko, Membrane locking and reduced integration for curve elements, ASME J. Appl. Mech. 49 (1982) 172-176.

[73] J.P. Pontaza, J.N. Reddy, Mixed plate bending elements based on least-squares formulation, Int. J. Numer. Meth. Engrg. 60 (2004) 891-922.

[74] J. Pitkäranta, Mathematical and historical reflections on the lowest-order finite element models for thin structures, Comput. Struct. 81 (2003) 895-909.

[75] M. Braun, Nichtlineare analysen von geschichteten, elastischen flächentragwerken, PhD dissertation, Bericht Nr. 19, Institut für Baustatik, Universität Stuttgart, 1995.

[76] M. Braun, M. Bischoff, E. Ramm, Nonlinear shell formulations for complete three-dimensional constitutive laws including composites and laminates, Comput. Mech. 15 (1994) 1-18.

[77] A.N. Palazotto, S.T. Dennis, Nonlinear Analysis of Shell Structures, AIAA Education Series, Washington D.C., 1992.

[78] C. Brebbia, J. Connor, Geometrically nonlinear finite element analysis, J. Engrg. Mech. 95 (2) (1969) 463-483.

[79] A.C. Scordelis, K.S. Lo, Computer analysis of cylindrical shells, J. A. Concrete Inst. 61 (5) (1964) 539-560.

[80] J.E. Gibson, The Design of Cylindrical Shell Roofs, Spon's Civil Engineering Series, London, 1961.

[81] D.G. Ashwell, Strain elements, with applications to arches, rings and cylindrical shells, in: D.S. Ashwell, R.H. Gallagher (Eds.), Finite Element for Thin Shells and Curved Members, John Wiley & Sons, New York, 1976.

[82] J.C. Simo, D.D. Fox, M.S. Rifai, On a stress resultant geometrically exact shell model. Part II: The linear theory, Comput. Methods Appl. Mech. Engrg. 73 (1989) 53-92.

[83] W. Flügge, Stresses in Shells, 2nd edition, Springer-Verlag, Berlin, 1973.

[84] I. Kreja, R. Schmidt, J.N. Reddy, Finite elements based on a first-order shear deformation moderate rotation theory with applications to the analysis of composite structures, Int. J. Nonlin. Mech. 32 (6) (1997) 1123-1142.

[85] G.R. Heppler, J.S. Hansen, A Mindlin element for thick and deep shells, Comput. Methods Appl. Mech. Engrg. 54 (1986) 21-47.

[86] T.K. Varadan, K. Bhaskar, Bending of laminated orthotropic cylindrical shells – An elasticity approach, Comput. Struct. 17 (1991) 141-156.

[87] Z.Q. Cheng, L.H. He, S. Kitipornchai, Influence of imperfect interfaces on bending and vibration of laminated composite shells, Int. J. Solids Struct. 37 (2000) 2127-2150.

[88] R.H. MacNeal, R.L. Harder, A proposed standard set of problems to test finite element accuracy, Fin. Elem. Analysis Des. 1 (1985) 3-20.

[89] J.L. Ericksen, C. Truesdell, Exact theory of stress and strain in rods and shells, Arch. Rat. Mech. Anal. 1 (1957) 295-323.

[90] A.E. Green, P.M. Naghdi, On the derivation of shell theories by direct approach, ASME J. Appl. Mech. 40 (1974) 173-176.

[91] A.E. Green, P.M. Naghdi, W.L. Wainwright, A general theory of a Cosserat surface, Arch. Rat. Mech. Anal. 20 (1965) 287-308.

[92] J.C. Simo, D.D. Fox, M.S. Rifai, On a stress resultant geometrically exact shell model. Part III: Computational aspects of the nonlinear theory, Comput. Methods Appl. Mech. Engrg. 79 (1990) 21-70.

[93] C. Sansour, H. Bednarczyk, The Cosserat surface as a shell model, theory and finite element formulation, Comput. Methods Appl. Mech. Engrg. 120 (1995) 1-32.

[94] J. Chróścielewski, I.J. Makovski, H. Stumpf, Genuinely resultant shell finite elements accounting for geometric and material nonlinearity, Int. J. Numer. Meth. Engrg. 35 (1992) 63-94.

[95] L. Librescu, Refined geometrically nonlinear theories of anisotropic laminated shells, Q. Appl. Math. 45 (1987) 1-22.

[96] L. Librescu, R. Schmidt, Refined theories of elastic anisotropic shells accounting for small strains and moderate rotations, Int. J. Nonlin. Mech. 23 (1988) 217-229.

[97] L. Librescu, M. Stein, Postbuckling of shear-deformable composite flat panels taking into account geometrical imperfections, AIAA J. 30 (1992) 1352-1360.

[98] L. Librescu, M.Y. Chang, Imperfection sensitivity and postbuckling behavior of shear-deformable composite doubly-curved shallow panels, Int. J. Solids Struct. 29 (1992) 1065-1083.

[99] A.F. Palmerio, J.N. Reddy, R. Schmidt, On a moderate rotation theory of laminated anisotropic shells, Part 1: Theory, Int. J. Nonlin. Mech. 25 (1990) 687-700.

[100] A.F. Palmerio, J.N. Reddy, R. Schmidt, On a moderate rotation theory of laminated anisotropic shells, Part 2: Finite element analysis, Int. J. Nonlin. Mech. 25 (1990) 701-714.

[101] W. Pietraszkiewicz, Geometrically nonlinear theories of thin elastic shells, Advan. Mech. 12 (1) (1989) 52-130.

[102] W. Pietraszkiewicz, J. Badur, Finite rotations in the description of continuum deformation, Int. J. Engrg. Sci. 21 (1983) 1097-1115.

[103] W. Pietraszkiewicz, Lagrangian description and incremental formulation in the nonlinear theory of thin shells, Int. J. Nonlin. Mech. 19 (1984) 115-140.

[104] Y. Başar, Finite-rotation theories for composite laminates, Acta Mech. 98 (1993) 159-176.

[105] Y. Başar, A consistent theory of geometrically nonlinear shells with an independent rotation vector, Int. J. Solids Struct. 23 (1987) 1401-1415.

[106] Y. Başar, Y. Ding, R. Schultz, Refined shear-deformation models for composite laminates with finite rotations, Int. J. Solids Struct. 30 (1993) 2611-2638.

[107] N. Büchter, E. Ramm, D. Roehl, Three-dimensional extension of nonlinear shell formulation based on the enhanced assumed strain concept, Int. J. Numer. Meth. Engrg. 37 (1994) 2551-2568.

[108] M. Bischoff, E. Ramm, On the physical significance of higher order kinematic and static variables in a three-dimensional shell formulation, Int. J. Solids Struct. 37 (2000) 6933-6960.

[109] B. Brank, J. Korelc, A. Ibrahimbegović, Nonlinear shell problem formulation accounting for through-the-thickness stretching and its finite element implementation, Comput. Struct. 80 (2002) 699-717.

[110] W.B. Krätzig, Best transverse shearing and stretching shell theory for nonlinear finite element simulations, Comput. Methods Appl. Mech. Engrg. 103 (1993) 135-160.

[111] P. Betsch, A. Menzel, E. Stein, On the parametrization of finite rotations in computational mechanics: A classification of concepts with application to smooth shells, Comput. Methods Appl. Mech. Engrg. 155 (1998) 273-305.

[112] C. Sansour, F.G. Kollmann, Families of 4-nodes and 9-nodes finite elements for a finite deformation shell theory. An assessment of hybrid stress, hybrid strain and enhanced strain elements, Comput. Mech. 24 (2000) 435-447.

[113] R.M. Bowen, C.C. Wang, Introduction to Vectors and Tensors, Vol. 2, Plenum Press, New York, 1976.

[114] C.A. Truesdell, A First Course in Rational Continuum Mechanics - Volume 1: General Concepts, Academic Press, 2nd edition, San Diego, 1991.

[115] P. Chadwick, Continuum Mechanics: Concise Theory and Problems, Dover Publications, 2nd edition, New York, 1999.

[116] R.M. Bowen, C.C. Wang, Introduction to Vectors and Tensors, Vol. 1, Plenum Press, New York, 1976.

[117] M.E. Gurtin, An Introduction to Continuum Mechanics, Academic Press, New York, 1981.

[118] Y. Başar, D. Weichert, Nonlinear Continuum Mechanics of Solids, Springer-Verlag, Berlin, 2000.

[119] G.A. Holzapfel, Nonlinear Solid Mechanics – A Continuum Approach for Engineering, John Wiley & Sons, New York, 2000.

[120] J.E. Marsden, T.J. Hughes, Mathematical Foundations of Elasticity, Prentice-Hall, Englewood Cliffs, New Jersey, 1983.

[121] L.M. Habip, Theory of elastic shells in the reference state, Arch. Appl. Mech. 34 (1965) 228-237.

[122] L.M. Habip, Theory of plates and shells in the reference state, PhD dissertation, Department of Engineering Science and Mechanics, University of Florida, 1964.

[123] J.N. Reddy, An Introduction to Nonlinear Finite Element Analysis, Oxford University Press, New York, 2004.

[124] C. Truesdell, W. Noll, The nonlinear field theories, in: S. Flügge, C. Truesdell (Eds.), Handbuch der Physik, III/2, Springer-Verlag, Berlin, 1965.

[125] M. Balah, Analysis of laminated general shells undergoing finite rotations and large motion, PhD dissertation, Dept. of Civil Engineering, King Fahd University of Petroleum and Minerals, 2000.

[126] S. Suresh, A. Mortensen, Fundamentals of Functionally Graded Materials, IOM Commun. Ltd, Cambridge, 1998.

[127] J.N. Reddy, Analysis of functionally graded plates, Int. J. Numer. Meth. Engrg. 47 (2000) 663-684.

[128] G.N. Praveen, J.N. Reddy, Nonlinear transient thermoelastic analysis of functionally graded ceramic-metal plates, Int. J. Solids Struct. 35 (1998) 4457-4476.

[129] J.N. Reddy, C.D. Chin, Thermomechanical analysis of functionally cylinders and plates, J. Thermal Stresses 21 (1998) 593-626.

[130] A. Ibrahimbegovic, On the choice of finite rotation parameters, Comput. Methods Appl. Mech. Engrg. 149 (1997) 49-71.

[131] E. Ramm, A plate/shell element for large deflections and rotations, in: K.J. Bathe, J.T. Oden, W. Wunderlich (Eds.), Formulations and Computational Algorithms in Finite Element Analysis, MIT Press, Cambridge, Massachusetts, 1997.

[132] T.J. Hughes, K.S. Pister, Consistent linearization in mechanics of solids and structures, Comput. Struct. 8 (1978) 391-397.

[133] J. Bonet, R.D. Wood, Nonlinear Continuum Mechanics for Finite Element Analysis, Cambridge University Press, Cambridge, 1997.

[134] I.S. Liu, Continuum Mechanics, Springer-Verlag, Berlin, 2002.

[135] J.C. Simo, The (symmetric) Hessian for geometrically nonlinear models in solid mechanics: Intrinsic definition and geometric interpretation, Comput. Methods Appl. Mech. Engrg. 96 (1992) 189-200.

[136] E. Riks, An incremental approach to the solution of snapping and buckling problems, Int. J. Numer. Meth. Engrg. 15 (1979) 524-551.

[137] E. Riks, The application of Newton's method to the problem of elastic stability, ASME J. Appl. Mech. 39 (1972) 1060-1066.

[138] G.A. Wempner, Discrete approximations related to nonlinear theories of solids, Int. J. Solids Struct. 7 (1971) 1581-1599.

[139] M.A. Crisfield, A fast incremental/iterative solution procedure that handles snap-through, Comput. Struct. 13 (1981) 55-62.

[140] M.A. Crisfield, An arc-length method including line searches and accelerations, Int. J. Numer. Meth. Engrg. 19 (1983) 1269-1289.

[141] E. Ramm, Strategies for tracing the nonlinear response near limit points, in: W. Wunderlich, E. Stein, K.J. Bathe (Eds.), Nonlinear Finite Element Analysis in Structural Mechanics, Spring-Verlag, Berlin, 1981.

[142] M.A. Crisfield, Nonlinear Finite Element Analysis of Solids and Structures, Vol. 1: Essentials, John Wiley & Sons, West Sussex, UK, 1991.

[143] K.Y. Sze, X.H. Liu, S.H. Lo, Popular benchmark problems for geometric nonlinear analysis of shells, Fin. Elem. Analysis Des. 40 (2004) 1151-1569.

[144] H.C. Park, C. Cho, S.W. Lee, An efficient assumed strain element model with six DOF per node for geometrically nonlinear shells, Int. J. Numer. Meth. Engrg. 38 (1995) 4101-4122.

[145] P. Massin, M. Al Mikdad, Nine node and seven node thick shell elements with large displacements and rotations, Comput. Struct. 80 (2002) 835-847.

[146] S. Timoshenko, Theory of Elasticity, McGraw-Hill, New York, 1936.

[147] A.B. Sabir, A.C. Lock, The application of finite elements to the large deflection geometrically nonlinear behavior of cylindrical shells, in: C.A. Brebbia, H. Tottenham (Eds.), Variational Methods in Engineering, University Press, Southampton, UK, 1972.

[148] J.L. Sanders, Nonlinear theories for thin shells, Q. Appl. Math. 21 (1963) 21-36.

[149] C. Sansour, H. Bufler, An exact finite rotation shell theory, its mixed variational formulation and its finite element implementation, Int. J. Numer. Meth. Engrg. 34 (1992) 73-115.

[150] N. Stander, A. Matzenmiller, E. Ramm, An assessment of assumed strain methods in finite rotation shell analysis, Engrg. Comput. 6 (1989) 58-66.

[151] W. Wagner, F. Gruttmann, A simple finite rotation formulation for composite shell elements, Engrg. Comput. 11 (1994) 145-176.

APPENDIX A

KINEMATIC RELATIONS

In this appendix, the explicit form of the kinematics of plates and shells for infinitesimal deformations is presented. For convenience, we express the equations in terms of the physical components of displacements and strains [48, 49]. Namely

$$\begin{aligned} \varepsilon_{<ij>} &= \frac{\varepsilon_{ij}}{\sqrt{g_{ii} g_{jj}}} \\ g_{ii} &= (\mu_i^i)^2 a_{ii} \qquad \text{(no sum)} \end{aligned} \tag{A.1}$$

and then, we define $\bar{\varepsilon}_{<ij>}$ as

$$\begin{aligned} \bar{\varepsilon}_{<ij>} &= \mu_i^i \mu_j^j \varepsilon_{<ij>} \\ &= \frac{\varepsilon_{ij}}{\sqrt{a_{ii} a_{jj}}} \qquad \text{(no sum).} \end{aligned} \tag{A.2}$$

A. Plates

1. First-order shear deformation theory

The strain field equations are

$$\begin{aligned} \bar{\varepsilon}_{<\alpha\beta>} &= \bar{\varepsilon}^{(0)}_{<\alpha\beta>} + \bar{\varepsilon}^{(1)}_{<\alpha\beta>} (\theta^3) \\ \bar{\varepsilon}_{<\alpha 3>} &= \bar{\varepsilon}^{(0)}_{<\alpha 3>} \end{aligned} \tag{A.3}$$

where

$$\begin{aligned} &\bar{\varepsilon}^{(0)}_{<11>} = u_{<1>,1} && \bar{\varepsilon}^{(0)}_{<22>} = u_{<2>,2} && 2\bar{\varepsilon}^{(0)}_{<12>} = u_{<1>,2} + u_{<2>,1} \\ &\bar{\varepsilon}^{(1)}_{<11>} = \varphi_{<1>,1} && \bar{\varepsilon}^{(1)}_{<22>} = \varphi_{<2>,2} && 2\bar{\varepsilon}^{(1)}_{<12>} = \varphi_{<1>,2} + \varphi_{<2>,1} \\ &2\bar{\varepsilon}^{(0)}_{<13>} = \varphi_{<1>} + u_{<3>,1} && 2\bar{\varepsilon}^{(0)}_{<23>} = \varphi_{<2>} + u_{<3>,2}. \end{aligned} \tag{A.4}$$

2. Third-order shear deformation theory

The strain-displacement equations are

$$\begin{aligned}
&\bar{\varepsilon}_{<\alpha\beta>} = \bar{\varepsilon}^{(0)}_{<\alpha\beta>} + \bar{\varepsilon}^{(1)}_{<\alpha\beta>}(\theta^3) + \bar{\varepsilon}^{(3)}_{<\alpha\beta>}(\theta^3)^3 \\
&\bar{\varepsilon}_{<\alpha 3>} = \bar{\varepsilon}^{(0)}_{<\alpha 3>} + \bar{\varepsilon}^{(2)}_{<\alpha 3>}(\theta^3)^2.
\end{aligned} \tag{A.5}$$

Now, we define the auxiliary functions

$$\begin{aligned}
&\psi_{<1>} = \varphi_{<1>} + u_{<3>,1} \\
&\psi_{<2>} = \varphi_{<2>} + u_{<3>,2}.
\end{aligned} \tag{A.6}$$

The membrane strain components are

$$\begin{aligned}
&\bar{\varepsilon}^{(0)}_{<11>} = u_{<1>,1}, && \bar{\varepsilon}^{(0)}_{<22>} = u_{<2>,2}, && 2\bar{\varepsilon}^{(0)}_{<12>} = u_{<1>,2} + u_{<2>,1} \\
&\bar{\varepsilon}^{(1)}_{<11>} = \varphi_{<1>,1}, && \bar{\varepsilon}^{(1)}_{<22>} = \varphi_{<2>,2}, && 2\bar{\varepsilon}^{(1)}_{<12>} = \varphi_{<1>,2} + \varphi_{<2>,1} \\
&\bar{\varepsilon}^{(3)}_{<11>} = k_1 \psi_{<1>,1}, && \bar{\varepsilon}^{(3)}_{<22>} = k_1 \psi_{<2>,2}, && 2\bar{\varepsilon}^{(3)}_{<12>} = k_1 (\psi_{<1>,2} + \psi_{<2>,1})
\end{aligned} \tag{A.7}$$

and the shear strain components are

$$\begin{aligned}
&2\bar{\varepsilon}^{(0)}_{<13>} = \varphi_{<1>} + u_{<3>,1}, && 2\bar{\varepsilon}^{(0)}_{<23>} = \varphi_{<2>} + u_{<3>,2} \\
&2\bar{\varepsilon}^{(2)}_{<13>} = 3k_1 \psi_{<1>}, && 2\bar{\varepsilon}^{(2)}_{<23>} = 3k_1 \psi_{<2>}\ .
\end{aligned} \tag{A.8}$$

B. Cylindrical shells

1. First-order shear deformation theory

The strain field equations are

$$\begin{aligned}
&\bar{\varepsilon}_{<\alpha\beta>} = \bar{\varepsilon}^{(0)}_{<\alpha\beta>} + \bar{\varepsilon}^{(1)}_{<\alpha\beta>}(\theta^3) \underline{+ \bar{\varepsilon}^{(2)}_{<\alpha\beta>}(\theta^3)^2} \\
&\bar{\varepsilon}_{<\alpha 3>} = \bar{\varepsilon}^{(0)}_{<\alpha 3>}
\end{aligned} \tag{A.9}$$

where the underlined term is neglected and

$$\bar{\varepsilon}^{(0)}_{<11>} = u_{<1>,1}, \quad \bar{\varepsilon}^{(0)}_{<22>} = \frac{1}{R} u_{<2>,2} + \frac{u_{<3>}}{R}, \quad 2\bar{\varepsilon}^{(0)}_{<12>} = \frac{1}{R} u_{<1>,2} + u_{<2>,1}$$

$$\begin{aligned}
&\bar{\varepsilon}^{(1)}_{<11>} = \varphi_{<1>,1}, \quad \bar{\varepsilon}^{(1)}_{<22>} = \frac{1}{R}\varphi_{<2>,2} + \frac{u_{<2>,2} + u_{<3>}}{R^2} \\
&2\bar{\varepsilon}^{(1)}_{<12>} = \frac{\varphi_{<1>,2}}{R} + \varphi_{<2>,1} + \frac{u_{<2>,1}}{R}, \quad \bar{\varepsilon}^{(2)}_{<11>} = 0 \\
&\bar{\varepsilon}^{(2)}_{<22>} = \frac{1}{R^2}\varphi_{<2>,2}, \quad 2\bar{\varepsilon}^{(2)}_{<12>} = \frac{1}{R}\varphi_{<2>,1}
\end{aligned} \tag{A.10}$$

with constant shear strains

$$\begin{aligned}
&2\bar{\varepsilon}^{(0)}_{<13>} = \varphi_{<1>} + u_{<3>,1} \\
&2\bar{\varepsilon}^{(0)}_{<23>} = \varphi_{<2>} + \frac{u_{<3>,2}}{R} - \frac{u_{<2>}}{R} \ .
\end{aligned} \tag{A.11}$$

2. Third-order shear deformation theory

The strain-displacement equations are

$$\begin{aligned}
&\bar{\varepsilon}_{<\alpha\beta>} = \bar{\varepsilon}^{(0)}_{<\alpha\beta>} + \bar{\varepsilon}^{(1)}_{<\alpha\beta>}(\theta^3) + \bar{\varepsilon}^{(2)}_{<\alpha\beta>}(\theta^3)^2 + \bar{\varepsilon}^{(3)}_{<\alpha\beta>}(\theta^3)^3 \underline{+\bar{\varepsilon}^{(4)}_{<\alpha\beta>}(\theta^3)^4} \\
&\bar{\varepsilon}_{<\alpha 3>} = \bar{\varepsilon}^{(0)}_{<\alpha 3>} + \bar{\varepsilon}^{(1)}_{<\alpha 3>}(\theta^3) + \bar{\varepsilon}^{(2)}_{<\alpha 3>}(\theta^3)^2 + \bar{\varepsilon}^{(3)}_{<\alpha 3>}(\theta^3)^3
\end{aligned} \tag{A.12}$$

where the underlined term is neglected. We define the auxiliary functions as

$$\begin{aligned}
&\psi_{<1>} = \varphi_{<1>} + u_{<3>,1} \\
&\psi_{<2>} = \varphi_{<2>} + \frac{1}{R}u_{<3>,2}.
\end{aligned} \tag{A.13}$$

The membrane strain components are

$$\begin{aligned}
&\bar{\varepsilon}^{(0)}_{<11>} = u_{<1>,1} \\
&\bar{\varepsilon}^{(0)}_{<22>} = \frac{1}{R}u_{<2>,2} + \frac{u_{<3>}}{R} \\
&2\bar{\varepsilon}^{(0)}_{<12>} = \frac{1}{R}u_{<1>,2} + u_{<2>,1} \\
&\bar{\varepsilon}^{(1)}_{<11>} = \varphi_{<1>,1} \\
&\bar{\varepsilon}^{(1)}_{<22>} = \frac{1}{R}\varphi_{<2>,2} + \frac{u_{<2>,2} + u_{<3>}}{R^2} \\
&2\bar{\varepsilon}^{(1)}_{<12>} = \frac{\varphi_{<1>,2}}{R} + \varphi_{<2>,1} + \frac{u_{<2>,1}}{R}
\end{aligned}$$

$$\begin{aligned}
&\bar{\varepsilon}^{(2)}_{<11>} = 0 \\
&\bar{\varepsilon}^{(2)}_{<22>} = k_2\left(\frac{1}{R}\psi_{<2>,2} - \frac{u_{<2>,2}}{R^2}\right) + \frac{1}{R^2}\varphi_{<2>,2} \\
&2\bar{\varepsilon}^{(2)}_{<12>} = k_2\left(\psi_{<2>,1} - \frac{u_{<2>,1}}{R}\right) + \frac{1}{R}\varphi_{<2>,1} \\
&\bar{\varepsilon}^{(3)}_{<11>} = k_1\psi_{<1>,1} \\
&\bar{\varepsilon}^{(3)}_{<22>} = k_3\left(\frac{1}{R}\psi_{<2>,2} - \frac{u_{<2>,2}}{R^2}\right) + \frac{k_2}{R}\left(\frac{1}{R}\psi_{<2>,2} - \frac{u_{<2>,2}}{R^2}\right) \\
&2\bar{\varepsilon}^{(3)}_{<12>} = k_1\frac{\psi_{<1>,2}}{R} + k_3\left(\psi_{<2>,1} - \frac{u_{<2>,1}}{R}\right) + \frac{k_2}{R}\left(\psi_{<2>,1} - \frac{u_{<2>,1}}{R}\right) \\
&\bar{\varepsilon}^{(4)}_{<11>} = 0 \\
&\bar{\varepsilon}^{(4)}_{<22>} = \frac{k_3}{R}\left(\frac{1}{R}\psi_{<2>,2} - \frac{u_{<2>,2}}{R^2}\right) \\
&2\bar{\varepsilon}^{(4)}_{<12>} = \frac{k_3}{R}\left(\psi_{<2>,1} - \frac{u_{<2>,1}}{R}\right)
\end{aligned} \tag{A.14}$$

and the shear strain components

$$\begin{aligned}
&2\bar{\varepsilon}^{(0)}_{<13>} = \varphi_{<1>} + u_{<3>,1} \\
&2\bar{\varepsilon}^{(0)}_{<23>} = \left(\varphi_{<2>} + \frac{1}{R}u_{<3>,2} - \frac{u_{<2>}}{R}\right) \\
&\bar{\varepsilon}^{(1)}_{<13>} = 0 \\
&2\bar{\varepsilon}^{(1)}_{<23>} = 2k_2\left(\psi_{<2>} - \frac{u_{<2>}}{R}\right) \\
&2\bar{\varepsilon}^{(2)}_{<13>} = 3k_1\psi_{<1>} \\
&2\bar{\varepsilon}^{(2)}_{<23>} = 3k_3\left(\psi_{<2>} - \frac{u_{<2>}}{R}\right) + \frac{k_2}{R}\left(\psi_{<2>} - \frac{u_{<2>}}{R}\right) \\
&\bar{\varepsilon}^{(3)}_{<13>} = 0 \\
&2\bar{\varepsilon}^{(3)}_{<23>} = \frac{2k_3}{R}\left(\psi_{<2>} - \frac{u_{<2>}}{R}\right).
\end{aligned} \tag{A.15}$$

C. Spherical shells

1. First-order shear deformation theory

The strain field equations are

$$\begin{aligned}\bar{\varepsilon}_{<\alpha\beta>} &= \bar{\varepsilon}^{(0)}_{<\alpha\beta>} + \bar{\varepsilon}^{(1)}_{<\alpha\beta>}(\theta^3) \underline{+ \bar{\varepsilon}^{(2)}_{<\alpha\beta>}(\theta^3)^2} \\ \bar{\varepsilon}_{<\alpha 3>} &= \bar{\varepsilon}^{(0)}_{<\alpha 3>}\end{aligned} \tag{A.16}$$

where the underlined term is neglected and

$$\begin{aligned}
\bar{\varepsilon}^{(0)}_{<11>} &= \frac{1}{R}u_{<1>,1} + \frac{u_{<3>}}{R} \\
\bar{\varepsilon}^{(0)}_{<22>} &= \frac{1}{R\sin(\theta^1)}u_{<2>,2} + \frac{u_{<3>}}{R} + \frac{\cot(\theta^1)u_{<1>}}{R} \\
2\bar{\varepsilon}^{(0)}_{<12>} &= \frac{1}{R\sin(\theta^1)}u_{<1>,2} + \frac{1}{R}u_{<2>,1} - \frac{\cot(\theta^1)u_{<2>}}{R} \\
\varepsilon^{(1)}_{<11>} &= \frac{1}{R}\varphi_{<1>,1} + \frac{1}{R}\left(\frac{u_{<1>,1} + u_{<3>}}{R}\right) \\
\bar{\varepsilon}^{(1)}_{<22>} &= \frac{1}{R\sin(\theta^1)}\varphi_{<2>,2} + \frac{\cot(\theta^1)\varphi_{<1>}}{R} \\
&\quad + \frac{1}{R}\left(\frac{1}{R\sin(\theta^1)}u_{<2>,2} + \frac{u_{<3>}}{R} + \frac{\cot(\theta^1)u_{<1>}}{R}\right) \\
2\bar{\varepsilon}^{(1)}_{<12>} &= \frac{\varphi_{<1>,2}}{R\sin(\theta^1)} + \frac{1}{R}\varphi_{<2>,1} - \frac{\cot(\theta^1)\varphi_{<2>}}{R} \\
&\quad + \frac{1}{R}\left(\frac{1}{R\sin(\theta^1)}u_{<1>,2} + \frac{1}{R}u_{<2>,1} - \frac{\cot(\theta^1)u_{<2>}}{R}\right) \\
\bar{\varepsilon}^{(2)}_{<11>} &= \frac{1}{R^2}\varphi_{<1>,1} \\
\bar{\varepsilon}^{(2)}_{<22>} &= \frac{1}{R}\left(\frac{1}{R\sin(\theta^1)}\varphi_{<2>,2} + \frac{\cot(\theta^1)\varphi_{<1>}}{R}\right) \\
2\bar{\varepsilon}^{(2)}_{<12>} &= \frac{1}{R}\left(\frac{\varphi_{<1>,2}}{R\sin(\theta^1)} + \frac{1}{R}\varphi_{<2>,1} - \frac{\cot(\theta^1)\varphi_{<2>}}{R}\right)
\end{aligned} \tag{A.17}$$

and the shear strain components

$$\begin{aligned} 2\bar{\varepsilon}^{(0)}_{<13>} &= \varphi_{<1>} + \frac{u_{<3>,1}}{R} - \frac{u_{<1>}}{R} \\ 2\bar{\varepsilon}^{(0)}_{<23>} &= \varphi_{<2>} + \frac{u_{<3>,2}}{R\sin(\theta^1)} - \frac{u_{<2>}}{R}\,. \end{aligned} \tag{A.18}$$

2. Third-order shear deformation theory

The strain-displacement equations are

$$\begin{aligned} \bar{\varepsilon}_{<\alpha\beta>} &= \bar{\varepsilon}^{(0)}_{<\alpha\beta>} + \bar{\varepsilon}^{(1)}_{<\alpha\beta>}(\theta^3) + \bar{\varepsilon}^{(2)}_{<\alpha\beta>}(\theta^3)^2 + \bar{\varepsilon}^{(3)}_{<\alpha\beta>}(\theta^3)^3 \underline{+\bar{\varepsilon}^{(4)}_{<\alpha\beta>}(\theta^3)^4} \\ \bar{\varepsilon}_{<\alpha 3>} &= \bar{\varepsilon}^{(0)}_{<\alpha 3>} + \bar{\varepsilon}^{(1)}_{<\alpha 3>}(\theta^3) + \bar{\varepsilon}^{(2)}_{<\alpha 3>}(\theta^3)^2 + \bar{\varepsilon}^{(3)}_{<\alpha 3>}(\theta^3)^3 \end{aligned} \tag{A.19}$$

where the underlined term is neglected. We define $\psi_{<\alpha>}$ as

$$\begin{aligned} \psi_{<1>} &= \varphi_{<1>} + \frac{1}{R}u_{<3>,1} \\ \psi_{<2>} &= \varphi_{<2>} + \frac{1}{R\sin(\theta^1)}u_{<3>,2}. \end{aligned} \tag{A.20}$$

The membrane strain components are

$$\begin{aligned} \bar{\varepsilon}^{(0)}_{<11>} &= \frac{1}{R}u_{<1>,1} + \frac{u_{<3>}}{R} \\ \bar{\varepsilon}^{(0)}_{<22>} &= \frac{1}{R\sin(\theta^1)}u_{<2>,2} + \frac{u_{<3>}}{R} + \frac{\cot(\theta^1)u_{<1>}}{R} \\ 2\bar{\varepsilon}^{(0)}_{<12>} &= \frac{1}{R\sin(\theta^1)}u_{<1>,2} + \frac{1}{R}u_{<2>,1} - \frac{\cot(\theta^1)u_{<2>}}{R} \\ \varepsilon^{(1)}_{<11>} &= \frac{1}{R}\varphi_{<1>,1} + \frac{1}{R}\left(\frac{u_{<1>,1}+u_{<3>}}{R}\right) \\ \bar{\varepsilon}^{(1)}_{<22>} &= \frac{1}{R\sin(\theta^1)}\varphi_{<2>,2} + \frac{\cot(\theta^1)\varphi_{<1>}}{R} \\ &\quad + \frac{1}{R}\left(\frac{1}{R\sin(\theta^1)}u_{<2>,2} + \frac{u_{<3>}}{R} + \frac{\cot(\theta^1)u_{<1>}}{R}\right) \end{aligned}$$

$$
\begin{aligned}
2\bar{\varepsilon}^{(1)}_{<12>} &= \frac{\varphi_{<1>,2}}{R\sin(\theta^1)} + \frac{1}{R}\varphi_{<2>,1} - \frac{\cot(\theta^1)\,\varphi_{<2>}}{R} \\
&\quad + \frac{1}{R}\left(\frac{1}{R\sin(\theta^1)}u_{<1>,2} + \frac{1}{R}u_{<2>,1} - \frac{\cot(\theta^1)\,u_{<2>}}{R}\right) \\
\bar{\varepsilon}^{(2)}_{<11>} &= \frac{1}{R^2}\varphi_{<1>,1} + \frac{k_2}{R}\left(\psi_{<1>,1} - \frac{u_{<1>,1}}{R}\right) \\
\bar{\varepsilon}^{(2)}_{<22>} &= \frac{1}{R}\left(\frac{1}{R\sin(\theta^1)}\varphi_{<2>,2} + \frac{\cot(\theta^1)\,\varphi_{<1>}}{R}\right) \\
&\quad + \frac{k_2\cot(\theta^1)}{R}\left(\psi_{<1>} - \frac{u_{<1>}}{R}\right) + \frac{k_2}{R\sin(\theta^1)}\left(\psi_{<2>,2} - \frac{u_{<2>,2}}{R}\right) \\
2\bar{\varepsilon}^{(2)}_{<12>} &= \frac{1}{R}\left(\frac{\varphi_{<1>,2}}{R\sin(\theta^1)} + \frac{1}{R}\varphi_{<2>,1} - \frac{\cot(\theta^1)\,\varphi_{<2>}}{R}\right) + \frac{k_2}{R\sin(\theta^1)}\left(\psi_{<1>,2} - \frac{u_{<1>,2}}{R}\right) \\
&\quad + \frac{k_2}{R}\left(\psi_{<2>,1} - \frac{u_{<2>,1}}{R}\right) - \frac{k_2\cot(\theta^1)}{R}\left(\psi_{<2>} - \frac{u_{<2>}}{R}\right) \\
\bar{\varepsilon}^{(3)}_{<11>} &= \frac{1}{R}\left(k_3 + \frac{k_2}{R}\right)\left(\psi_{<1>,1} - \frac{u_{<1>,1}}{R}\right) \\
\bar{\varepsilon}^{(3)}_{<22>} &= \frac{\cot(\theta^1)}{R}\left(k_3 + \frac{k_2}{R}\right)\left(\psi_{<1>} - \frac{u_{<1>}}{R}\right) + \frac{1}{R\sin(\theta^1)}\left(k_3 + \frac{k_2}{R}\right)\left(\psi_{<2>,2} - \frac{u_{<2>,2}}{R}\right) \\
2\bar{\varepsilon}^{(3)}_{<12>} &= \frac{1}{R\sin(\theta^1)}\left(k_3 + \frac{k_2}{R}\right)\left(\psi_{<1>,2} - \frac{u_{<1>,2}}{R}\right) + \frac{1}{R}\left(k_3 + \frac{k_2}{R}\right)\left(\psi_{<2>,1} - \frac{u_{<2>,1}}{R}\right) \\
&\qquad - \frac{\cot(\theta^1)}{R}\left(k_3 + \frac{k_2}{R}\right)\left(\psi_{<2>} - \frac{u_{<2>}}{R}\right) \\
\bar{\varepsilon}^{(4)}_{<11>} &= \frac{k_3}{R^2}\left(\psi_{<1>,1} - \frac{u_{<1>,1}}{R}\right) \\
\bar{\varepsilon}^{(4)}_{<22>} &= \frac{k_3\cot(\theta^1)}{R^2}\left(\psi_{<1>} - \frac{u_{<1>}}{R}\right) + \frac{k_3}{R^2\sin(\theta^1)}\left(\psi_{<2>,2} - \frac{u_{<2>,2}}{R}\right) \\
2\bar{\varepsilon}^{(4)}_{<12>} &= \frac{k_3}{R^2\sin(\theta^1)}\left(\psi_{<1>,2} - \frac{u_{<1>,2}}{R}\right) + \frac{k_3}{R^2}\left(\psi_{<2>,1} - \frac{u_{<2>,1}}{R}\right) \\
&\quad - \frac{k_3\cot(\theta^1)}{R^2}\left(\psi_{<2>} - \frac{u_{<2>}}{R}\right)
\end{aligned}
\tag{A.21}
$$

and the shear strain components

$$\begin{aligned}
&2\bar{\varepsilon}^{(0)}_{<13>} = \varphi_{<1>} + \frac{1}{R} u_{<3>,1} - \frac{u_{<1>}}{R}, \quad 2\bar{\varepsilon}^{(0)}_{<23>} = \varphi_{<2>} + \frac{1}{R\sin(\theta^1)} u_{<3>,2} - \frac{u_{<2>}}{R} \\
&2\bar{\varepsilon}^{(1)}_{<13>} = 2k_2\left(\psi_{<1>} - \frac{u_{<1>}}{R}\right), \qquad 2\bar{\varepsilon}^{(1)}_{<23>} = 2k_2\left(\psi_{<2>} - \frac{u_{<2>}}{R}\right) \\
&2\bar{\varepsilon}^{(2)}_{<13>} = \left(3k_3 + \frac{k_2}{R}\right)\left(\psi_{<1>} - \frac{u_{<1>}}{R}\right), \quad 2\bar{\varepsilon}^{(2)}_{<23>} = \left(3k_3 + \frac{k_2}{R}\right)\left(\psi_{<2>} - \frac{u_{<2>}}{R}\right) \\
&2\bar{\varepsilon}^{(3)}_{<13>} = \frac{2k_3}{R}\left(\psi_{<1>} - \frac{u_{<1>}}{R}\right), \qquad 2\bar{\varepsilon}^{(3)}_{<23>} = \frac{2k_3}{R}\left(\psi_{<2>} - \frac{u_{<2>}}{R}\right).
\end{aligned} \tag{A.22}$$

The constants k_1, k_2 and k_3 are given by

$$k_1 = -\frac{4}{3h^2}, \quad k_2 = \frac{4R}{(12R^2 - h^2)}, \quad k_3 = -\frac{16R^2}{(12R^2 - h^2)\,h^2}. \tag{A.23}$$

APPENDIX B

MATERIAL STIFFNESS COEFFICIENTS FOR FGM PLATES

In this appendix we present the exact values of the material stiffness coefficients for functionally graded plates. From equation (2.48) we have

$$\begin{aligned} \overset{k}{C}{}^{\alpha\beta\gamma\lambda} &= \int_{-h/2}^{h/2} C^{\alpha\beta\gamma\lambda}(\theta^3)^k \, d\theta^3, \qquad k = 0,1,2,3,4,6 \\ \overset{k}{C}{}^{\alpha 3\gamma 3} &= \int_{-h/2}^{h/2} C^{\alpha 3\gamma 3}(\theta^3)^k \, d\theta^3, \qquad k = 0,2,4\ . \end{aligned} \tag{B.1}$$

The coefficients $C^{\alpha\beta\gamma\lambda}$ and $C^{\alpha 3\gamma 3}$ are defined by

$$\begin{aligned} C^{\alpha\beta\gamma\lambda}\left(\theta^3\right) &:= C_{cm}^{\alpha\beta\gamma\lambda} f_c + C_m^{\alpha\beta\gamma\lambda} \\ C^{\alpha 3\gamma 3}\left(\theta^3\right) &:= C_{cm}^{\alpha 3\gamma 3} f_c + C_m^{\alpha 3\gamma 3} \end{aligned} \tag{B.2}$$

which are functions of θ^3. In the equation above f_c is the volume fraction function of the ceramic constituent and $C_{cm}^{\alpha\beta\gamma\lambda} = C_c^{\alpha\beta\gamma\lambda} - C_m^{\alpha\beta\gamma\lambda}$, $C_{cm}^{\alpha 3\gamma 3} = C_c^{\alpha 3\gamma 3} - C_m^{\alpha 3\gamma 3}$. The through-the-thickness integral (B.1) is solved analytically, i.e

$$\begin{aligned} \overset{0}{C}{}^{\alpha\beta\gamma\lambda} &= C_{cm}^{\alpha\beta\gamma\lambda}\left(\frac{h}{n+1}\right) + C_m^{\alpha\beta\gamma\lambda} h \\ \overset{1}{C}{}^{\alpha\beta\gamma\lambda} &= C_{cm}^{\alpha\beta\gamma\lambda}\left(\frac{nh^2}{2(n+1)(n+2)}\right) \\ \overset{2}{C}{}^{\alpha\beta\gamma\lambda} &= C_{cm}^{\alpha\beta\gamma\lambda}\left(\frac{(n^2+n+2)h^3}{4(n+1)(n+2)(n+3)}\right) + C_m^{\alpha\beta\gamma\lambda}\left(\frac{h^3}{12}\right) \\ \overset{3}{C}{}^{\alpha\beta\gamma\lambda} &= C_{cm}^{\alpha\beta\gamma\lambda}\left(\frac{(n^2+3n+8)nh^4}{8(n+1)(n+2)(n+3)(n+4)}\right) \\ \overset{4}{C}{}^{\alpha\beta\gamma\lambda} &= C_{cm}^{\alpha\beta\gamma\lambda}\left(\frac{(n^4+6n^3+23n^2+18n+24)h^5}{16(n+1)(n+2)(n+3)(n+4)(n+5)}\right) + C_m^{\alpha\beta\gamma\lambda}\left(\frac{h^5}{80}\right) \\ \overset{5}{C}{}^{\alpha\beta\gamma\lambda} &= C_{cm}^{\alpha\beta\gamma\lambda}\left(\frac{(n^4+10n^3+55n^2+110n+184)nh^6}{32(n+1)(n+2)(n+3)(n+4)(n+5)(n+6)}\right) \end{aligned} \tag{B.3}$$

$$\begin{aligned}\overset{6}{C}^{\alpha\beta\gamma\lambda} &= C_{cm}^{\alpha\beta\gamma\lambda}\left(\frac{(n^6+15n^5+115n^4+405n^3+964n^2+660n+720)h^7}{64(n+1)(n+2)(n+3)(n+4)(n+5)(n+6)(n+7)}\right)\\ &\quad +C_m^{\alpha\beta\gamma\lambda}\left(\frac{h^7}{448}\right)\end{aligned}$$

for bending-membrane material stiffness coefficients and

$$\begin{aligned}\overset{0}{C}^{\alpha 3\gamma 3} &= C_{cm}^{\alpha 3\gamma 3}\left(\frac{h}{n+1}\right)+C_m^{\alpha 3\gamma 3}h\\ \overset{2}{C}^{\alpha 3\gamma 3} &= C_{cm}^{\alpha 3\gamma 3}\left(\frac{(n^2+n+2)h^3}{4(n+1)(n+2)(n+3)}\right)+C_m^{\alpha 3\gamma 3}\left(\frac{h^3}{12}\right)\\ \overset{4}{C}^{\alpha 3\gamma 3} &= C_{cm}^{\alpha 3\gamma 3}\left(\frac{(n^4+6n^3+23n^2+18n+24)h^5}{16(n+1)(n+2)(n+3)(n+4)(n+5)}\right)+C_m^{\alpha 3\gamma 3}\left(\frac{h^5}{80}\right)\end{aligned}\tag{B.4}$$

for shear material stiffness coefficients. The constant *n* denotes the volume fraction exponent and *h* is the thickness of the shell.

VITA

Roman Augusto Arciniega Aleman was born in Lima and grew up in a middle-class Peruvian family. He attended the Faculty of Engineering at the University of Ricardo Palma where he received his bachelor's degree in civil engineering in December, 1990. He was awarded in 1994 with the CAPES scholarship from the Brazilian government to pursue his master's degree at the Department of Civil Engineering, Catholic University of Rio de Janeiro. He then worked in the industry for several years following his graduate education. As a civil engineer he participated in the design and supervision of different engineering projects working for La Pampilla Refinery, Andrade-Gutierrez Constructors and R. Rios J. Engineers. He was also a lecturer in structural analysis at the University of Ricardo Palma and Peruvian University of Applied Science. In January 2002, he began his Ph.D. studies at the Department of Mechanical Engineering, Texas A&M University and graduated in December 2005.

Mr. Arciniega has experience in the field of computational solid mechanics as well as material modeling. He is planning to work in the research and teaching area. He can be reached at the following address:

Department of Mechanical Engineering, Texas A&M University, College Station, TX 77843-3123. Email: rarciniegaa@hotmail.com